IMPLANTABLE DEPOTS FOR INTERSTITIAL DELIVERY OF RADIOLABELED GOLD NANOPARTICLES USING A BRACHYTHERAPY TECHNIQUE

BY

PRISCILLA LAI DREYER

A THESIS SUBMITTED IN CONFORMITY WITH THE REQUIREMENTS
FOR THE DEGREE OF DOCTOR OF PHILOSOPHY

Medical Biophysics
University of Toronto

Implantable Depots for Interstitial delivery of Radiolabeled Gold Nanoparticles using a Brachytherapy technique

Priscilla Lai Dreyer

Doctor of Philosophy

Department of Medical Biophysics
University of Toronto

2019

Abstract

Radiolabeled gold nanoparticles (AuNP) are emerging as a class of therapeutics for cancer due to their unique physical and chemical properties that differentiate them from other small or bulk materials, as well as other nanoscale particles. In the ideal condition their use as a radiotherapeutic agent is facilitated by preferential extravasation from the tumour vasculature and accumulation in the interstitial space as a result of the enhanced permeability and retention (EPR) effect, following systemic delivery. This delivery scenario was anticipated to reduce the accumulation of radiolabeled AuNP in normal tissues, thereby increasing the therapeutic ratio of tumour control to normal tissue complications. However, systemic delivery of AuNP has been challenged with the inability to escape phagocytic clearance by the reticuloendothelial system (RES) coupled with suboptimal accumulation of AuNP in the tumour. Furthermore, attempts at direct intratumoural delivery of radiolabeled AuNP to circumvent RES capture and increase tumour concentrations have encountered their own limitations such as clinical feasibility and unpredictable intratumoural radioactivity and dose distribution patterns. In contrast brachytherapy, the oldest form of internal radiotherapy, has well established methods to precisely deliver radioactive material. The use of radiolabeled AuNP in brachytherapy can be mutually beneficial, offering new opportunities for brachytherapy such as use of non-photon emitting radionuclides, potential for adjuvant therapies, and dose homogenization from AuNP redistribution in the tumour interstitial space. In this thesis, a delivery system for radiolabeled AuNP is developed by designing an implantable nanoparticle depot (NPD) compatible with traditional permanent brachytherapy techniques. The design of the NPD is validated in its ability to facilitate controlled release of AuNP, resulting in predictable AuNP distributions in breast cancer xenografts *in vivo*. Furthermore, micro-SPECT/CT (single-photon emission computed tomography/computed tomography) image based dosimetry techniques are applied to estimate the dose distribution surrounding NPD delivery of AuNP labeled with various electron emitting radionuclides. Finally, the efficacy and toxicity of lutetium-177-AuNP NPD is evaluated in two triple negative breast cancer mouse xenograft models. In summary, this thesis outlines the design, associated dosimetry and preclinical application of radiolabeled AuNP using electron emitting radionuclides, delivered by NPD and a permanent brachytherapy technique.

This thesis is dedicated to my husband

And my aunt, Jeamie, who lost the battle to cancer
But will live on in our hearts.

ACKNOWLEDGMENTS

To my previous and current supervisors Dr. Gregory Czarnota, Dr. Jean-Philippe Pignol, Dr. David Jaffray and Dr. Raymond Reilly, what a privilege it has been to be your student. I find myself struggling for the words that can truly reflect the amount of gratitude I have for each of you, because how can I sum up the years of support, and the countless hours of conversation that has steered me to this moment in my career and life – all in a few meagre sentences? – I can't! But I will give it my best shot. Greg, were it not for you I may not even be in research. You trusted me with more than I trusted with myself when I was a lowly undergraduate student, introduced me to a side of science that I had only ever read about, and sparked my interest in cancer research that has never faded nearly a decade later. JP, your enthusiasm and passion is contagious. Your endless wealth of creative ideas and knowledge is an inspiration and I hope that I never lose my curiosity or the courage to dream the seemingly impossible. David, in addition to your matchless ability to challenge my critical thinking and suggest ideas so far outside the box that I usually leave your office dumbstruck, you have been a model to me in many other ways. I remember once I asked you why you took so little time for yourself, you answered "We're only on this earth for so long – so why not make a difference while you're here". I hope to adopt your attitude of selflessness and dedication in my career. Lastly Ray, your unwavering support and confidence in me has left me speechless. Thank you for taking a leap of faith and welcoming me into your team. You have taught me to persevere through the many challenges in the last few years, and I hope to model your positivity and commitment to your students with those I encounter.

Along the road, I have been lucky enough to meet stellar researchers, work with great collaborators, and make amazing friends. If I were to list each person who has journeyed with me through the last 5 years, the length of this section would rival the length of this thesis, but to name a few; Zhongli Cai, you are a great researcher and more importantly an amazing person. It is an honor to have been mentored by you. Thank you for your tireless effort supporting my project, and working alongside me all those late nights. Elizabeth Huynh, your friendship through all these years has kept me sane and smiling through my undergraduate and graduate degrees. Members of the Reilly lab, thank you for the incredible memories and friendships – you welcomed me in as one of your own. Hadi Tadayyon, Golnaz Farhat, Anoja Giles, Azza Al-Mahrouki, Christina Kim, Eli Lechtman, and Shahram Mashouf from the Czarnota and Pignol labs, thank you for all the training and guidance in those initial years, but most of all thank you for being my Sunnybrook family. To the staff at STTARR, Teesha Komal and Deborah Scollard, your help has been invaluable, you deserve so much more recognition than you receive. To my many current and previous advisory committee members, Alex Vitkin, Gang Zheng, Michael Kolios, Martin Yaffe, and Shun Wong, thank you for your insight and encouragements, and for always making time for me. Lastly, I would especially like to thank Merle Casci for always making time to answer my questions, for helping me navigate the labyrinth of departmental policies, and for the personal support you provided as I transitioned downtown.

Most importantly I would like to thank my family. To my parents, thank you for the sacrifices you made so that I could have a better life. Mom, I will never forget all those late nights you spent staying up with me just to keep me company. My brother Calvin, thank you (and sorry) for the countless times I woke you in the night to recover work from a crashed computer – you are the best. I am sure you were relieved when I finally bought a new computer. To my other parents, Andy and Irene, thank you for your continued encouragements – I could not have asked for a better second family. Lastly to my husband, my best friend and anchor, you have stood by my side through it all. You have made me laugh when I felt like crying, and turned mountains into small hills. Thank you for making me the luckiest person in the world.

Lastly I would like to acknowledge the financial support I received from the Medical Biophysics department and other funding agencies, without which this work would not have been possible. These include; Queen Elizabeth II/Sunnybrook and Women's College Health Sciences Centre Scholarship in Science and Technology, Ontario Graduate Scholarship (OGS), NSERC Alexander Graham Bell Canada Graduate Scholarships-Doctoral (CGS D), Geoff Lockwood and Kevin Graham Medical Biophysics Graduate Award, Centre for Pharmaceutical Oncology (CPO) Scholarship, and other departmental and travel awards.

TABLE OF CONTENTS

LIST OF ABBREVIATIONS

% IA/g	Percent administered radioactivity per gram of tissue
% IA/organ	Percent administered radioactivity per organ
% ID/g	Percent injected dose per gram of tissue
^{103}Pd	Palladium-103
^{103}Rh	Rhodium-103
^{111}Cd	Cadmium-111
^{111}In	Indium-111
^{112}Cd	Cadmium-112
^{124}Xe	Xenon-124
^{125}I	Iodine-125
^{125}Te	Tellurium-125
^{125}Xe	Xenon-125
^{131}Cs	Cesium-131
^{153}Sm	Samarium-153
^{169}Yb	Ytterbium-169
^{177}Hf	Hafnium-177
^{177}Lu	Lutetium-177
^{188}Re	Rhenium-188
^{192}Ir	Iridium-192
^{198}Au	Gold-198
1D	One-dimensional
^{208}Pb	Lead-208
^{226}Ra	Radium-226
2D	Two-dimensional
^{32}P	Phosphorus-32
3D	Three-dimensional
3D-CRT	3-dimensional conformal radiation therapy
^{89}Sr	Strontium-89

^{90}Y	Yttrium-90
^{90}Zr	Zirconium-90
^{99m}Tc	Technecium-99m
a	Atomic radius
Ã	Cumulative activity
AAPM	American Association of Physicists in Medicine
AE	Auger electron
AF	Aggregation Factor
ALT	Alanine transaminase
ANOVA	Analysis of variance
ATCC	American type culture collection
Au	Gold
AUC	Area under the curve
AuNP	Gold nanoparticle
AUP	Animal user protocol
b	Impact parameter
BC	Breast cancer
Bcl-2	B-cell lymphoma 2
Bcl-xL	B-cell lymphoma-extra large
BCS	Breast conserving surgery
BN	Bombesin
Bq	Becquerel
BRCA1	Breast cancer 1
BRCA2	Breast cancer 2
BT	Breast tissue
BWI	Body weight index
CBC	Complete blood count
CBCF	Canadian Breast Cancer Foundation
CCAC	Canadian Council on Animal Care
CHO	Chinese hamster ovary
CI	Conformity index

CPM	Counts per minute
CPS	Counts per second
Cr	Creatinine
CS	Clonogenic survival
CSDA	Continuous slowing down approximation
CSS	Conventional sealed sources
CT	Computed tomography
CTAB	Hexadecylcetyltrimethylammonium bromide
d.dH2O	Double distilled water
D.p.i.	Days post injection
DEF	Dose enhancement factor
DHI	Dose homogeneity index
DLS	Dynamic light scattering
DLX2	Distal-less homeobox2
D_{max}	Maximum dose
DMEM	Dulbecco's modified eagle medium
D_{min}	Minimum dose
DNA	Deoxyribonucleic acid
DNR	Dose non-uniformity ratio
DOTA	1,4,7,10-tetraazacyclododecane-1,4,7,10-tetraacetic acid
DPBS	Dulbecco's phosphate buffered saline
DrVH	Dose rate volume histograms
DSB	Double strand break
DVH	Dose volume histograms
EBRT	External bean radiation therapy
EDTA	Ethylenediaminetetraacetic acid
EGCg	epigallocatechin-gallate
EGFR	Epidermal growth factor receptor
EGS4	Electron Gamma Shower Monte Carlo Code
EGSnrc	Electron Gamma Shower Monte Carlo Code
EPR	Enhanced permeability and retention

ER	Estrogen receptor
eV	Electron volts
FBS	Fetal bovine Serum
FWHM	Full width at half maximum
GEANT	Geometry and Tracking Monte Carlo Code
GLOBOCAN	Global Cancer Observatory
GLV	Gray level values
GPT	Glutamate-pyruvate transaminase
GRP-r	Gastrin-releasing peptide receptor
GTV	Gross tumour volume
Gy	Gray
H.p.i.	Hours post injection
Hb	Hemoglobin
HCl	Hydrogen chloride
Hct	Hematocrit
HDR	High dose rate
HER1	Human epithelial growth factor receptor-1
HER2	Human epithelial growth factor receptor-2
HVL	Half value layer
I.t.	Intratumoural
I.v.	Intravenous
IC	Internal conversion
ICRU	International Commission on Radiation Units and Measurements
ID/g	Injected dose per gram
IFF	interstitial fluid flow
IFP	interstitial fluid pressure
IMRT	Intensity modulated radiation therapy
ITS	Integrated TIGER Series
KURBUC	Kyushu University and Radiobiology Unit Code
LA	Lipoic acid
LABC	Locally advanced breast cancer

LD50	Lethal dose 50
LET	Linear energy transfer
MBq	Mega bequerel
MCL-1	Myeloid cell leukemia 1
MCNP5	Monte Carlo N-Particle 5
MIRD	Medical Internal Radionuclide Dose
MPS	Mononuclear phagocyte system
NIR	Near-infrared region
NOD	Non-obese diabetic
NP	Nanoparticle
NPD	Nanoparticle depot
NSERC	Natural Sciences and Engineering Research Council of Canada
OAR	Organs at risk
OLINDA/EXM	Organ Level Internal Dose Assessment/Exponential Modeling
OPSS	Ortho-pyridyl disulfide
P.i.	Post-injection
p53	Tumour suppressor protein p53
Pb	Lead
PBS	Phosphate buffer saline
PBSI	Permanent breast seed implantation
PDD	Percent depth dose
PE	Photoelectron
PEG	Polyethylene glycol
PENELOPE	Penetration and Energy Loss of Positrons and Electrons
PET	Positron emission tomography
PLGA	Poly (lactic-co-glycolic) acid
PLT	Platelet
PR	Progesterone receptor
PSA	Prostate specific antigen
PSI	Permanent seed implantation
PTT	Photothermal therapy

PTV	Planning target volume
RA	Rheumatoid arthritis
rad	Absorbed radiation dose unit
RBC	Red blood cells
RD	Relative difference
RES	Reticuloendothelial system
ROI	Regions of interest
RPMI	Rosewell Park Memorial Institute
RSE	Relative statistical errors
RTP	Radiotherapy treatment planning
RV	Relative volume
S value	Snyder value
s.c.	Subcutaneous
SCID	Severe combined immunodeficient
SD	Standard deviation
SEM	Standard error of the mean
SES	Silver enhancer staining
SPB	Surface plasmon band
SPECT	Single photon emission computed tomography
SPR	Surface plasmon resonance
SSD	Source to surface distance
$t_{1/2}$	Half-life
Tat	Trans-Activator of Transcription
TCP	Tumour control probability
$TD_{5/5}$	Tolerance dose resulting in 5% complication rate over 5 years
TDF	Time dose fractionation
TG-43	Task Group No. 43
TGI	Tumour growth index
TNBC	Triple negative breast cancer
TNF	Tumour necrosis factor
TNFα	Tumor necrosis factor alpha

UV	Ultra violet
V100	Volume of the PTV receiving at least 100% of the prescribed dose
V150	Volume of the PTV receiving at least 150% of the prescribed dose
V300	Volume of the PTV receiving at least 300% of the prescribed dose
VDK	Voxel dose kernels
VEL	Voxel edge length
VLV	Very low viscosity
VOI	Volume of interest
WBC	White blood cells
WBI	Whole breast irradiation
WHO	World health organization
Z	Atomic number
α	Alpha particle
β-/+	Beta minus/plus particle
γ	Gamma radiation

LIST OF MATHEMATICAL PARAMETERS

Parameters	Title	Description
$\tilde{A}(r_s, T_D)$ (Bq·s)	Cumulative activity	Time (T_D) integrated activity over the lifetime of the radionuclide within source organ (r_s)
$D(r_T,T_D)$ (Gy)	Absorbed dose	Absorbed dose to target organ (r_s) over total time during which decay takes place (T_D)
T_D (s)	Time of decay	Total time during which disintegration or decay takes place for calculation of absorbed dose using Snyder values
$S(r_T \leftarrow r_S)$ (mGy/MBq·s)	Snyder value	Snyder, or S, value for source organ, r_s, to target organ, r_T
r_s	Source organ	Source organ for determining Snyder value
r_T	Target organ	Target organ for determining Snyder value
I(x) (flux (ϕ) per steradian)	Photon intensity	Intensity of photons as a function of depth, x
I_0 (flux (ϕ) per steradian)	Initial photon intensity	Intensity of photons at depth x=0
μ (/cm)	Linear attentuation coefficient	Linear attenuation coefficient for calculation of photon attenuation as a function of depth
HVL (mm or cm)	Half value layer	The thickness of material required to reduce the intensity of photons by half
b	Impact parameter	Impact parameter relative to the classical atomic radius, a, describing the interaction of electrons with the orbital electron or nuclei of absorbing medium
a	Atomic radius	Classical atomic radius of absorbing medium for describing the interaction of electrons, with impact parameter b, with orbital electrons or nuclei
$S_{tot}(E)$ (MeV/cm^{2}g)	Mass stopping power	Rate of energy loss from radiative or collisional interactions per unit path length
R_{CSDA} (g/cm^2)	Continuous slowing down approximation range	Mean path length of a charged particle in an absorbing medium
dE (MeV)	Change in energy	Small incremental change in energy for calculation of R_{CSDA}
z_{max} (cm)	Depth of dose maximum	Gradual buildup in dose up to the depth of dose maximum, where charged particle equilibrium occurs
$t_{1/2}$ (h or d)	Radioactive half-life	The time required for radioisotope to decay to half its initial value
S_K (μGym^2/h)	Air kerma strength	Dosimetric parameter for TG-43 formalism. The product of air kerma rate at distance, d, in vacuo and the square of this distance, d^2

Λ (/cm^2)	Dose-rate constant	Dosimetric parameter for TG-43 formalism. The ratio of dose rate at the reference position and air kerma strength
G(r,θ)	Geometry function	Dosimetric parameter for TG-43 formalism, used to provide an inverse square-law correction of the spatial distribution around a point- and line-source
g(r)	Radial dose function	Dosimetric parameter for TG-43 formalism. Accounts for dose fall-off due to photon scattering and attenuation
$\phi_{an}(r)$	1 Dimension anisotropy function	Dosimetric parameter for TG-43 formalism, described as the ratio of the solid angle weighted dose rate at distance r, from the source, to the dose rate at r on the transverse plane
F(r, θ)	2 Dimension anisotropy function	Dosimetric parameter for TG-43 formalism, describing the change in dose as a function of polar angle
$\dot{D}$(r, θ) (cGy/h)	Dose rate (2D formalism)	Dose rate, from TG-43 2D formalism, as a function of distance, r, from line source and polar angle
$\dot{D}$(r) (cGy/h)	Dose rate (1D formalism)	Dose rate, from TG-43 1D formalism, as a function of distance, r, from point source
D_i (cm^2/s)	Diffusion coefficient	Rate of diffusion in a material resulting from passive particle transport
M_t	Mass of penetrant	Fickian model. Mass of penatrant (i.e. AuNP) in tunnel as a function of time, t
M_∞	Saturated mass of penetrant	Fickian model. Mass of penatrant (i.e. AuNP) in tunnel at saturation, or t=∞
L (mm)	Tunnel length	Fickian model. Length of tunnel L=2l
<r^2> (cm^2)	Root mean square displacement	The radial distance traveled by AuNP, calculated to be the boundary of infiltration
λ_{max} (nm)	Peak absorption wavelength	The peak absorption band for AuNP measured using UV-Vis spectroscopy
DHI	Dose homogeneity index	Parameter measuring the quality of dose distribution and describes proportion of treatment volume being overdose (by 150%)
CI	Conformity index	Parameter measuring the quality of dose distribution, describing the proportion of the planning target volume being treated with the prescibed dose
V100 (cm^3)	Volume 100	Volume of the PTV receiving at least 100% of the prescribed dose
V150 (cm^3)	Volume 150	Volume of the PTV receiving at least 150% of the prescribed dose
V300 (cm^3)	Volume 300	Volume of the PTV receiving at least 300% of the prescribed dose
PTV_{ref} (cm^3)	Reference planning target volume	Volume of the PTV receiving 100% or more of the prescribed dose

V_{PTV} (cm^3)	Planning target volume	Volume of the PTV
V_{ref} (cm^3)	Total treated volume	Total volume that is treated with 100% or more of the prescribed dose
$V_{95\%}$ (cm^3)	Volume 95	Volume enclosed by the 95% isodose line

LIST OF TABLES

LIST OF EQUATIONS

LIST OF FIGURES

CHAPTER 1

1 INTRODUCTION

1.1 CANCER

1.1.1 GLOBAL BURDEN OF CANCER

According to the World Health Organization (WHO), cancer is one of the top 10 leading causes of death worldwide, accounting for 8.8 million or 15.4% of deaths globally in 2015 (2017). The Global Cancer Observatory (GLOBOCAN) project, a WHO initiative aimed to provide estimates on the incidence, mortality and prevalence of 27 major cancers in 184 countries, reported that there were 14.1 million new cases and 8.2 million cancer related deaths in 2012 (Ferlay et al., 2015). Lung cancer remains the most common cancer worldwide for men and women combined, with an incidence of 1.8 million (12.9% of all cancers) and mortality of 1.6 million (19.4% of all cancers). The most common cancer diagnosed in women worldwide is breast cancer (BC), accounting for 25.2% of all cancer incidences and 14.7% of all cancer mortalities in women. The second most common cancer diagnosed in men worldwide is prostate cancer, accounting for 15.0% of all cancer incidences and 6.6% of all cancer mortalities in men, and is second only to lung cancer (16.7% of all cancers incidences and 23.6% of all cancer related mortalities). The incidence and mortality for a certain cancer differs nationally, and some cancers are more prevalent than others depending on whether the region is more or less developed (Fig. 1.1).

In Canada, cancer is the leading cause of death accounting for 30.2% of all deaths (Statistics, 2017). It has decreased in incidence in men but increased in incidence in women between 1988 and 2017, however cancer mortality rates have been declining steadily in both sexes. Prostate cancer in men (20.7%), and breast cancer in women (25.5%) are the predominant cancers diagnosed in Canadians. Female breast cancer incidence rates increased up until the 1990s due to increased availability of mammography screening and the implementation of provincial screening programs, however following 2004 incidence rates have stabilized. Prostate cancer incidence has been declining since 2007 by 5.3% per year possibly owed to revised guidelines against using prostate specific antigen (PSA) screening test levels as an indicator of prostate cancer (Statistics, 2017).

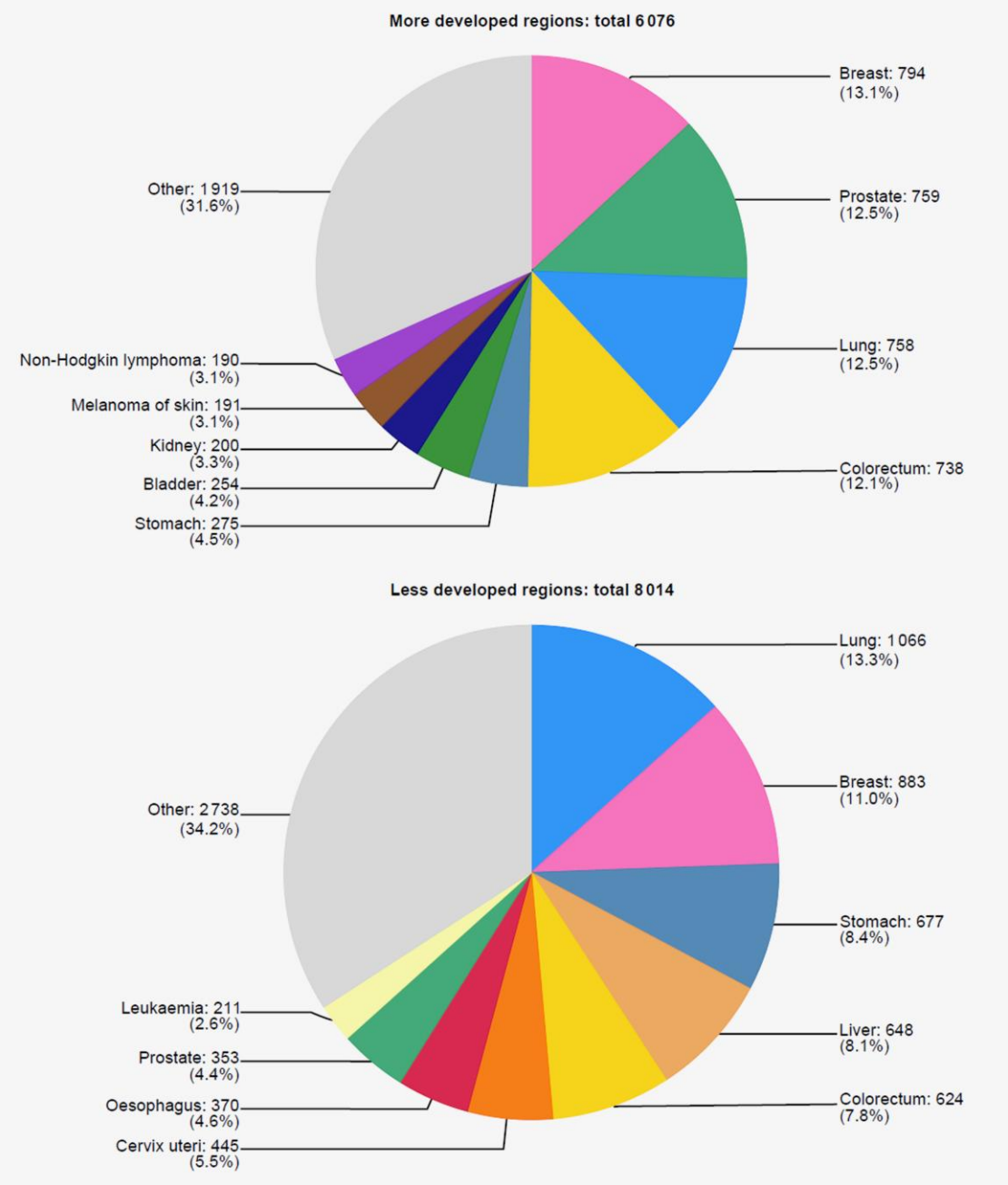

Figure 1.1 Estimated global numbers of new cases (thousands) with proportions for (a) more developed and (b) less developed regions, both sexes combined, by Ferlay et al. *Reprinted with permission.* (Ferlay et al., 2015)

1.1.2 BREAST CANCER

Breast cancer is currently categorized into five molecular subtypes based on the phenotype, each with distinctive clinical outcomes; luminal A, luminal B, triple-negative/basal-like, human epidermal growth factor receptor 2 (HER2)-enriched, and normal-like. The subtypes are classified based on the expression of estrogen receptors (ER), progesterone receptors (PR) and human epidermal growth factor receptor 1 and 2 (HER1/HER2). Luminal A breast

cancer is ER and/or PR positive, HER2 negative and exhibits low levels of Ki-67 protein responsible for controlling cell proliferation. Therefore, luminal A cancers exhibit slower growth and have the best prognosis of the subtypes. Luminal B breast cancer is ER and/or PR positive, can be HER1/HER2 positive or negative with high expression of Ki-67 protein, and thus has a faster growth rate and poorer prognosis than luminal A breast cancer. Triple-negative/basal-like breast cancer is ER/PR negative and HER2 negative, and has been found to be common in women with Breast Cancer 1 (*BRCA1*) genetic mutations. HER2-enriched breast cancer is ER/PR negative and HER2 positive, and exhibits a faster growth rate than luminal cancers. Both Triple-negative/basal-like and HER2-enriched subtypes have been associated with poorer prognosis. Normal-like breast cancer, is similar to normal breast tissue samples and has a similar gene expression to adipose tissue in the breast, namely lack of ER/PR and HER2 expression (Tang and Tse, 2016). Although, it is now speculated that this subtype of cancer may be the result of the contamination of samples with normal breast tissue (Prat et al., 2015, Tang and Tse, 2016).

1.1.3 TREATMENT AND MANAGEMENT OF BREAST CANCER BY RADIATION THERAPY

The aim of all breast cancer therapies is to achieve an optimal therapeutic index such that the dose of therapeutic agent is sufficient to achieve control of the disease and prevent local recurrence, while ideally causing minimal or no toxicity to normal tissues (Fig. 1.2). Of the various types of treatments available the most common are surgery, radiation therapy, and systemic therapy (i.e. hormonal therapies or chemotherapies), which are used in combination to treat breast cancers. In radiation therapy, the current standard of treatment for cancers of the breast is external beam radiation therapy (EBRT). Approximately 80% of patients in a radiation oncology department are treated with EBRT, while the remaining 20% are treated with other radiation techniques, such as brachytherapy. This treatment requires the use of a linear accelerator to generate a high energy photon beam that can be manipulated in shape to conform to the treatment volume. Typically, multiple beam projections are used to improve the homogeneity of the dose and escalate the dose to the treatment site while reducing the dose to normal critical tissues in the path of the beam. To improve the dose conformity, EBRT techniques such as 3-dimensional conformal radiation therapy (3D-CRT) (Olivotto et al., 2013) and intensity modulated radiation therapy (IMRT) (Jin et al., 2013), have been developed to improve normal tissue sparing of the heart and ipsilateral lung. The main advantage of EBRT is that it is a non-invasive form of treatment and the physical duration of the treatment is short. However, treatment regiments are often every day lasting several weeks.

An alternative form of radiation therapy is brachytherapy, which is best described as internal radiotherapy, as opposed to external radiation therapy. Brachytherapy utilizes sealed radioactive sources which are inserted interstitially or intracavitarily into the treatment site to irradiate the disease internally. The main advantage to EBRT is that the treatment schedule in brachytherapy is usually accelerated and the doses delivered are highly conformal to the treatment volume, however the procedure is invasive. The energy of the photons used are also much lower than EBRT

(keV versus MeV) which has advantages for normal tissue sparing and radioprotection. Although many types of brachytherapy now exist (i.e. high dose rate, pulsed dose rate, interstitial, intracavitary, low dose rate), treatment of some breast cancers are now carried out using permanent brachytherapy (Pignol et al., 2006). Permanent brachytherapy is the permanent placement of short lived and short ranged photon (X-ray or γ-ray) emitting radionuclide sources in the treatment site. This will be described in greater detail in section 1.3. Another form of internal radiotherapy is radionuclide therapy. Radionuclide therapy is a more recent technique in the nuclear medicine domain that shares the concept of internal radiation, however it is often administered systemically as an unsealed source unlike brachytherapy. Radionuclide therapy, usually administered in nuclear medicine, is defined as the use of radiopharmaceuticals targeted to the specific characteristics of a tumour using carrier molecules. The carrier molecule binds to the targeted cells allowing the radionuclide to deliver tumouricidal doses at the binding site. Unlike conventional external radiotherapy, radionuclides emitting short ranged radiation such as alpha (α) or beta (β) particles are the most appropriate as radiation exposure is confined to the target cells.

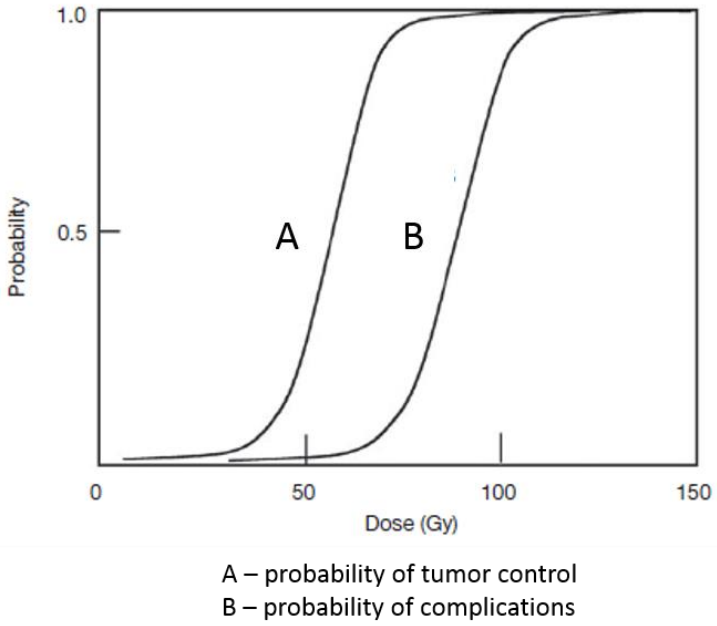

Figure 1.2 An illustration of the principle of therapeutic index adapted from Podgorsak (2005). Curve A represents the tumour control probability (TCP) and curve B the probability of complications or toxicity, both as a function of total dose (Gy). The ideal treatment delivers a dose resulting in the maximum probability of tumour control with minimal probability of complications, and therefore has a wide separation between curve A and B.

1.1.4 NEW STRATEGIES FOR BREAST CANCER TREATMENT: A BRIEF INTRODUCTION TO RADIATION NANOMEDICINE

New strategies for existing therapies are continually being developed, particularly in the field of radiation nanomedicine. Recently electron emitting radiolabeled gold nanoparticles (AuNP) have been proposed as a novel permanent brachytherapy technique for application in breast cancer therapy (Yook et al., 2016a, Yook et al., 2015b). The aim was to improve the therapeutic index by using intratumourally (i.t.) injected epidermal growth factor receptor (EGFR) targeted lutetium-177 (^{177}Lu) labeled AuNP dispersed in liquid to; (i) improve the dose homogeneity through small injections and peritumoural distribution of the AuNP, and (ii) use of a β emitter to increase dose conformity, thereby reducing exposure to normal tissues. Use of a β emitter also allows cross-firing effects which irradiates and kills cells not targeted by EGFR-^{177}Lu-AuNP. However this technique is challenged with heterogeneous distribution of the radiolabeled AuNP resulting in a heterogeneous dose distribution that is difficult to plan for cancer treatment.

1.2 IONIZING RADIATION

1.2.1 INTERACTIONS OF PHOTONS WITH MATTER

Ionizing radiation consists of photons or particles that have sufficient energy to liberate electrons, thereby ionizing the atoms or molecules in the material it transverses. Ionizing radiation is categorized into two groups: indirectly ionizing and directly ionizing radiation. Indirectly ionizing radiation, such as photons, can deposit energy in the material through a number of different interactions with the nuclei or the orbital electrons of the absorbing medium (Attix, 2004). The probability of a certain interaction occurring depends on the initial energy of the photon and the average atomic number of the absorbing medium, and is referred to as the cross section of reaction. Interactions with the nuclei can result in pair production or photodisintegration. Pair production can occur when the incident photon is near a nucleus and has an energy ≥ 1.02 MeV, which is the rest mass energy of an electron-positron pair (511 keV each). An electron-positron pair is created and emitted with a kinetic energy equivalent to the energy in excess of 1.02 MeV. The positron, an antiparticle, annihilates with an electron resulting in two photons of energy 511 keV, emitted at approximately 180° to one another. Photodisintegration is a direct interaction of the incident photon with the nucleus and is also known as a photonuclear reaction. In this interaction, the photon is absorbed by the nucleus resulting in the emission of a single or multiple neutrons. Photodisintegration occurs at much higher incident photon energies and the threshold energies represent the energy required to separate a neutron from the nucleus, which is dependent on the absorbing material (i.e. ^{208}Pb has a threshold energy of 7.4 MeV) (Podgorsak, 2006).

There are many different types of interactions photons can have with orbital electrons and only some of which will result in energy transfer: Compton scattering and photoelectric effect. In Compton scattering an incident photon interacts with a loosely bound orbital electron resulting in the production of a Compton recoil electron and scattered photon that has an energy which is lower than the incident photon. The kinetic energy of the electron is determined

as the difference in energy between the incident photon and scattered photon, assuming that the energy required to separate the electron from the atom is negligible. Unlike Compton scattering, the photoelectric effect occurs between an incident photon and a tightly bound orbital electron. In this interaction, the photon is entirely absorbed by the electron resulting in its ejection with a kinetic energy equivalent to the difference in the incident photon energy and binding energy of the electron. The photoelectron that is ejected leaves a vacancy which is filled by an upper shell electron, emitting a characteristic X-ray or Auger electron (AE) as it transitions to the lower energy shell. The Compton recoil electron, photoelectron (PE) and AE go on to deposit their energy in the medium through different interactions. (Podgorsak, 2006)

The interaction of photons with matter is probabilistic in nature and therefore they do not have a finite range. Instead, the intensity of photons (I(x)) in a material as a function of depth (x) is described by the process of attenuation, the progressive loss of energy from the photon beam where I_0 is the initial intensity and μ is the linear attenuation coefficient, which is exponential for monoenergetic beams (Eq. 1.1). Therefore as great distances are approached, the intensity can only ever approach zero.

$$I(x) = I_0 e^{-\mu x} \tag{1.1}$$

However, electronically produced photons are not monoenergetic rather the beam is made from a spectrum of photon energies. The attenuation is not purely exponential for polyenergetic photons since lower energy photons are attenuated at shorter distances, an effect known as beam hardening. Instead the penetration of polyenergetic photons is described by the half value layer (HVL), the thickness of material required to reduce the intensity of the photons by half (Eq. 1.2).

$$HVL = \frac{0.693}{\mu} \tag{1.2}$$

1.2.2 INTERACTIONS OF ELECTRONS WITH MATTER

Directly ionizing radiation is comprised of charged particles, such as electrons, which transfer energy to the material they transverse through direct Coulomb interactions with orbital electrons or nuclei of atoms in the medium. All charged particles are surrounded by an electric field and are subject to the Coulomb force, the strength of which depends on the magnitude of the charge of particles and the separation distance between the particles. Since an atom is composed of a positively charged nucleus, and negatively charged orbiting electrons the outcome of the energy transfer will differ depending on how the traversing electron interacts with the atom. These interactions are

categorized into: hard collision, soft collision and radiative collision, and can be described by the size of the impact parameter, b, relative to the classical atomic radius, a, of the absorbing atom. The impact parameter is best described as the minimum separation distance as the electron passes the nuclei of the absorbed atom with atomic radius, a. A hard collision occurs when the impact parameter is equivalent to the atomic radius (b≈a), and a soft collision occurs when the impact parameter is much larger than the atomic radius (b>>a). Both hard and soft collisions are interactions of the incident electron with the orbital electrons of the absorber, and result in energy transfer either through ionization or excitation of the orbital electrons. Radiative collision occurs when the impact parameter is much smaller than the atomic radius (b<<a) resulting in an interaction with the nuclei of the absorber. As the electron passes through the Coulomb field of the nucleus, it decelerates and the energy that is loss is emitted as bremsstrahlung radiation, or "braking radiation". Bremsstrahlung radiation is of great importance in radiation therapy since most external beam radiation are produced by decelerating electrons on a target to produce bremsstrahlung photons. For instance, the photons produced by a linear accelerator are bremsstrahlung photons.

Unlike photons, electrons have a finite range in the material they transverse since the likelihood of Coulomb interactions are not probabilistic, but definite. The length that an electron travels before coming to rest is dependent on its mass stopping power ($S_{tot}(E)$), the rate of energy loss from radiative or collisional interactions per unit path length, which is dependent on the atomic number, Z, of the material (Attix, 2004). The higher the average Z, the lower the stopping power of the electron and the lower the energy deposition in the medium over a given range. The path that the electron travels in a material is tortuous due to their low mass and large scattering angles, therefore their range in a material is typically less than their path length. The mean path length of a charged particle in an absorbing medium can be described by the continuous slowing down approximation (CSDA) range (Eq. 1.3), R_{CSDA}, where E_{ki} is the kinetic energy, however for electrons this value can be an overestimate of the true range by a factor of 2.

$$R_{CSDA} = \int_0^{E_{ki}} \frac{dE}{S_{tot}(E)} \tag{1.3}$$

1.2.3 RADIOBIOLOGICAL RESPONSES TO IONIZING RADIATION IN ONCOLOGY

Ionizing radiation is an effective therapy for management of cancer and has demonstrated success in a curative role as well as palliative role for symptom management in radiation oncology. Most often it is recommended as an adjuvant to surgery, which remains the primary form of treatment for operable cancers, however it has also been demonstrated as a monotherapy for various cancers such as the lung, prostate and skin (Fischbach et al., 1980, Potters et al., 2004, Timmerman et al., 2010, Henry et al., 2010). It is widely accepted that the primary target of radiation induced cell killing is DNA. In a study by Warters et al. Chinese hamster ovary cells (CHO) were labeled with ^{125}I-iododeoxyuridine for nuclear targeting and ^{125}I labeled monovalent concanavalin A for plasma membrane targeting (Warters et al.,

1978). Doses to the nucleus, plasma membrane and cytoplasm resulting in 50% cell kill, or lethal dose 50 (LD50), demonstrated that doses from DNA associated ^{125}I (LD50: 45 rad/0.45 Gy) were much more toxic than doses to the plasma membrane (LD50: 52 krad/520 Gy) and cytoplasm (LD50: 2470 rad/24.7 Gy). Their findings revealed that the contributions of cytoplasmic or membrane damage to radiation-induced cell death were minimal, and that nuclear damage was the primary target for radiation. The mechanism of damage to the DNA may occur through direct or indirect action. Direct action describes the interaction of radiation with the DNA or other critical targets resulting in ionization or excitation events in the DNA structure, or production of secondary electrons which interacts with the DNA. This is predominantly seen in high linear energy transfer (LET) radiations such as α-particles which are capable of generating highly dense ionization events along its path. The consequence of dense ionization events to the DNA is the production of double strand breaks (DSB) which are considered lethal due to the cells limited mechanism of repair for such extensive DNA damage. In indirect action radiation interacts with other molecules present in the cell, primarily water, to generate free radicals which in turn damages the DNA. Free radicals result from atoms or molecules that have been ionized, and therefore carry an unpaired electron causing it to become highly chemically reactive. The free radicals are capable of diffusing short distances within the cell to reach the DNA. For instance, the production of the hydroxyl free radical from water requires the production of an ion radical (H_2O^+) through ionization of a water molecule, and interaction of the ion radical with another water molecule to produce a hydroxyl radical (OH·):

$$2H_2O \xrightarrow{Radiation} H_2O^+ + e^- + H_2O^* \quad (1.4)$$
$$H_2O^* \rightarrow H + OH\cdot$$
$$H_2O^+ + H_2O \rightarrow H_3O^+ + OH\cdot$$

Direct and indirect damage to DNA will result in chromosomal aberrations that vary in repairability depending on the frequency of damage induction (dose rate and fractionation effects), the cells capacity for repair as cancerous cells often carry mutated genes responsible for damage detection and repair, and the complexity of the break, single stranded breaks being easier to repair than double stranded breaks. If repair does not occur, the cell will initiate cell death pathways resulting in; apoptosis, senescence, necrosis, autophagy or mitotic catastrophe. Of the various mechanisms of cell death, mitotic catastrophe is the dominant process following lethal radiation induced damage to DNA, and is recognized when the cell undergoes several more mitotic divisions before there is a permanent loss of replicative potential. Micronuclei containing chromosome fragments from double stranded breaks are often formed and do not partake in mitosis, resulting in the progressive loss of genetic information at each division. This form of cell death, or loss of replicative potential, is the most important consequence of radiation induced damage in radiation oncology (2009).

1.2.4 IMPACT OF DEPTH DOSE DISTRIBUTION

Photons are the most commonly used form of ionizing radiation in oncology for radiation therapy. They can be generated using an X-ray tube, a radioactive source, or a linear accelerator, to produce photons of varying energies allowing treatment of tissues at different depths. Photons, which have a greater penetrating depth than electrons, can liberate electrons deep within tissue through ionization events which then can deposit energy in the tissues locally. Therefore, external photon beam irradiation has become the primary standard of treatment for many forms of cancer due to its ability to reach deep seated tumours. In addition, photon beams can achieve high dose homogeneity in the target volume, however they often have poorer target conformity than charged particle therapies due to their longer range. Therefore multiple superimposing beams are typically used in external beam radiotherapy to achieve a more conformal dose distribution, and to minimize normal tissue exposure. Photon beams have a lower surface dose since dose deposition first requires interaction of the photons with electrons in the absorbing material, and thus have greater skin sparing effect (Fig. 1.3). Therefore, there is a gradual buildup in dose up to the depth of dose maximum, z_{max}, which occurs at a depth dependent on the photon beam energy. Beyond z_{max} the dose decreases exponentially due to attenuation of the photon beam as it transverses the material and by divergence of the beam at increasing distances, termed the inverse-square law (Podgorsak, 2006).

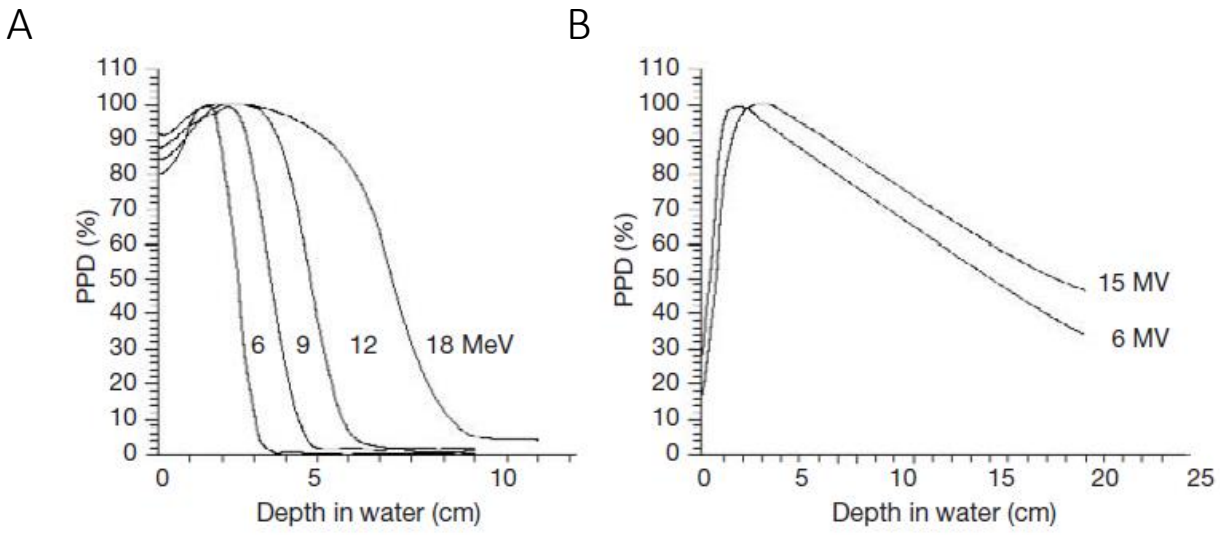

Figure 1.3 Percentage depth dose (PDD) (%) as a function of depth in water (cm) for (a) electron beams of energies 6, 9, 12, and 18 MeV, and (b) photon beams of energies 6 and 15 MV. Field size: 10x10 cm2. Source to Surface distance (SSD): 100 cm. *Printed with permission from Radiation Oncology Physics: A Handbook for Teachers and Students, ©IAEA, pg. 274* (2005)

Electrons have a much lower penetrating range due to their mechanism of interaction with matter, and therefore need to be localized directly at the target site. Due to their finite range, electron therapies are more conformal in depth making them an excellent option for treatment of lesions that are close to critical structures, or are superficial

to the body. Unlike photon beams, electron beams have a much greater surface dose that builds up to z_{max} at a depth dependent on the electron beam energy. The dose buildup region is attributed to the increase in scattering angle at greater depths with regard to the entry direction, resulting in an increase in electron fluence. Beyond z_{max}, the dose decreases rapidly into a bremsstrahlung photon tail that is produced from the electrons interaction with mechanical components within the accelerator.

1.3 PERMANENT BRACHYTHERAPY

1.3.1 BRIEF HISTORY AND GENERAL BACKGROUND

The concept of brachytherapy was first proposed by Pierre Currie who suggested, shortly after the discovery of radium by Marie Currie, that a small radium tube be inserted into the tumour. In 1903, Alexander Graham Bell suggested that a tiny fragment of radium sealed in a glass tube be inserted into the cancer site, and in 1904, Wickham and Derias performed the first intratumoural implantations using goose quills that had been sharpened (Devlin, 2007). Today permanent seed implantation (PSI) is a brachytherapy technique where sealed radioactive sources, or seeds, are implanted interstitially in order to treat cancerous tissues internally. It is offered as a treatment modality for a number of early stage localized carcinomas such as in the breast and prostate (Pignol et al., 2006, Pignol et al., 2009, Yu et al., 1999, Nag et al., 1999). The seeds used in PSI are typically made of a hollow titanium shell enclosing a substrate impregnated with a low energy and short lived radioactive material emitting (X/**γ**) photons, and a radiopaque metal fiducial for imaging (Reniers et al., 2002, Meigooni et al., 2003). There are no restrictions on the size or shape of a brachytherapy source, however a seed is defined as cylindrical in shape and having a length, L, less than or equal to 0.5 cm. The seeds are loaded into seeding needles or an applicator and implanted into the patient freehand or with the assistance of a template. Once implanted, the seeds irradiate the tissue continuously until the radioisotope is completely decayed and thereafter remain in the body permanently. The decayed seeds are not harmful to the patient nor do they typically cause any discomfort.

As with many brachytherapy modalities PSI enables highly conformal treatment of a target volume at the cost of increased dose heterogeneity in the treated volume. This heterogeneity is attributed to the highly localized attenuation of low energy radiation, which is desirable for radioprotection of patients and their families, but presents a challenge for generating homogeneous dose distributions (King, 2002). In clinical practice different loading patterns, such as uniform, modified uniform, nonuniform and peripheral loading, are used to achieve the most desirable dose distribution while sparing critical structures, such as the urethra and chest wall in prostate and breast brachytherapy, respectively. In PSI brachytherapy of the prostate seeds are implanted 5 mm or 10 mm apart and >100 seeds are implanted (Yu et al., 1999, Crook et al., 2002, Dicker et al., 2005), while treatment of the breast utilizes uniform loading of seeds 10 mm apart resulting in an average of 71 seeds to treat an average volume of 35 cc (Pignol and Keller, 2009a). The loading patterns are chosen based on the organ requiring treatment, surrounding organs at risk, and the

target volume. Seed and needle positions are determined using delineated ultrasound or computed tomography (CT) images of the target volume obtained for treatment planning.

1.3.2 RADIOISTOPES IN PERMANENT BRACHYTHERAPY

The earliest radioisotope used in interstitial brachytherapy was radium (^{226}Ra, $t_{1/2}$=1600 y, E=0.8 MeV), however today the selection of radioactive materials includes those emitting low energy photons that confine radiation exposure to the target tissue, and those with a sufficiently short half-life required for permanent implantation. Although the isotopes may contain other emissions, such as α or β radiation, the seeds are designed to absorb non-photon radiations such that the used portion of radiation fluence consists of γ and X radiation. Among the current isotopes used are iodine-125 (^{125}I, $t_{1/2}$=60 d, 28 keV), palladium-103 (^{103}Pd, $t_{1/2}$=17 d, 21 keV) and cesium-131 (^{131}Cs, $t_{1/2}$=9.7 d, 29 keV) which is less frequently used (Yu et al., 1999, Sahgal and Roach, 2007, Saito et al., 2007). Gold-198 seeds (^{198}Au, 2.7 d, 0.41 MeV) were also used in the past but have since been stopped due to unnecessary radiation exposure resulting from the higher energy photons (Porter et al., 1995).

The most common isotope used for permanent implant is ^{125}I which decays to tellurium-125 (^{125}Te) by electron capture, a process by which a proton rich nucleus absorbed an orbital electron changing the proton to a neutron (*refer to Appendix C for production and decay of radionuclides*), resulting in the emission of a maximum γ radiation energy of 35.5 keV (6.7%), and characteristic X-rays of 27-32 keV (93.3%) from internal conversion. Although the use of ^{125}I is most often seen in permanent brachytherapy of the prostate, there are several reports of its use for treatment of other cancers including carcinomas of the breast (Jansen et al., 2007), brain (Larson et al., 2004), liver (Martinez-Monge et al., 1999), skull and spine (Gutin et al., 1987). However, in a study conducted by Keller et al., use of ^{125}I (124 Gy) was not recommended for PSI of the breast due to the increased exposure and effective dose to the patient's partner (Keller et al., 2005). The HVL of ^{125}I in Pb is 0.02 mm, and in tissue is 17 mm, suggesting that implantation of ^{125}I can pose a risk to critical structures or organs adjacent to the target volume, or a risk to the public in the case of superficial implants.

Palladium-103 has recently increased in popularity due to its lower energy and therefore advantage for radioprotection (HVL in Pb/tissue: 0.01 mm/10 mm) and normal tissue sparing. It has a shorter half-life than ^{125}I and consequently delivers a higher initial dose rate which is advantageous for treatment of more aggressive fast growing tumours (Porrazzo et al., 1992). Palladium-103 decays by electron capture to rhodium-103 (^{103}Rh), resulting in the emission of characteristic X-rays of 20-23 keV in energy. Although ^{103}Pd was proposed for use as an interstitial source as early as 1958, it was not commercially available until 1987, and is therefore not as widely used as ^{125}I (Porrazzo et al., 1992). The most common application of ^{103}Pd is for treatment of prostate cancer, although it use has also been

reported for treatment of breast (Pignol and Keller, 2009b), lung (Martinez-Monge et al., 2008), and pancreas cancer (Nori et al., 1996).

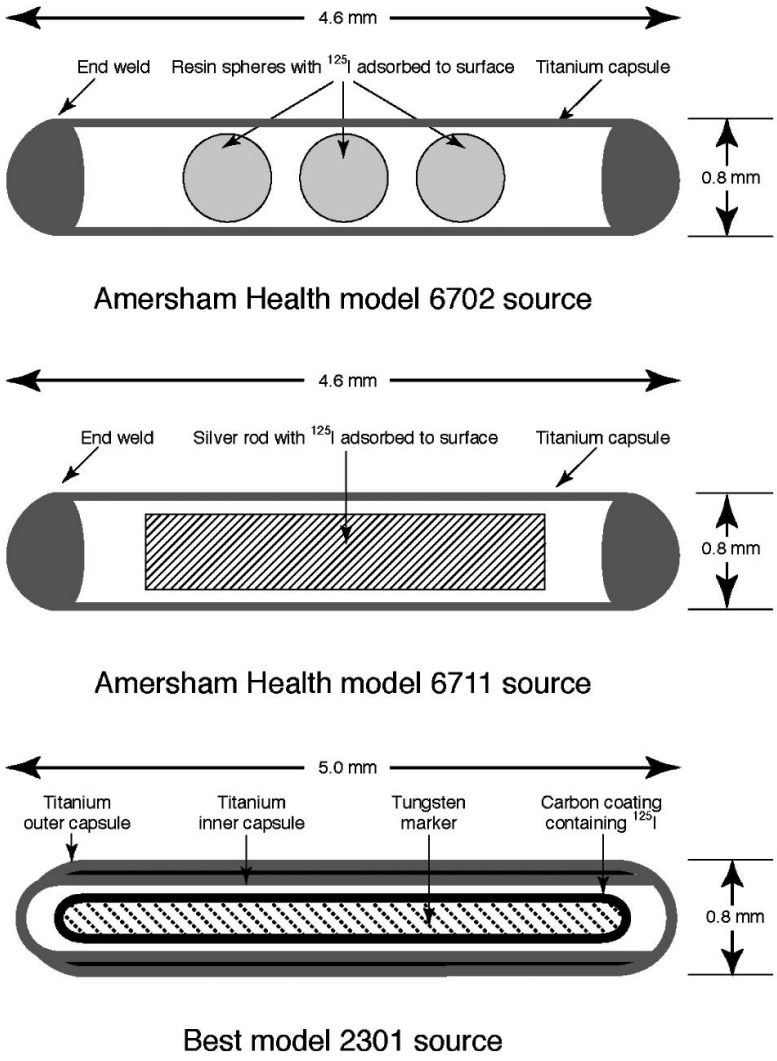

Figure 1.4 An illustration of the various brachytherapy seeds published in the Task Group No. 43 (TG-43) report demonstrating the different models and the variation in internal construction. *Adapted from Rivard* et al. (Rivard et al., 2004)

1.3.3 CONVENTIONAL BRACHYTHERAPY: TASK GROUP NO. 43 BASED DOSIMETRY

The most current method of calculation for dose-rate ($\dot{D}(r, \theta)$ or $\dot{D}(r)$, (cGy/h)) distributions around photon-emitting brachytherapy sources is outlined in the updated Task Group No. 43 (TG-43) protocol by the American Association of Physicists in Medicine (AAPM) (Rivard et al., 2004). The updated formalism applies dosimetric parameters (air-kerma strength (S_K, ($\mu Gym^2/h$)), dose-rate constant (Λ, (cm^{-2})), geometry function ($G(r,\theta)$), radial dose function ($g(r)$), 1D or

2D anisotropy function ($\phi_{an}(r)$ or $F(r, \theta)$)) that are specific to the source model, and therefore take into account manufacturer differences in construction and internal source design (Fig. 1.4). This was an important improvement from the previous calculation formalism, which was based on the apparent activity, equivalent mass of radium, exposure-rate constants, and tissue-attenuation coefficients, because the source construction varied between seed models resulting in changes to the dosimetric characteristics. For instance, the type of substrate used to absorb the radioactive material, the material and shape of the radio-opaque marker, and the capsules wall thickness and type of weld used to seal the source, will all contribute to modification of the source's emission spectrum. There are two formalisms: the general two-dimensional (2D) formalism (Eq. 1.5) which applies to sources that are cylindrically symmetric and the general one-dimensional (1D) formalism (Eq. 1.6) which approximates the seed as an isotropic point source. A detailed description of the dosimetric parameters and how they are determined is outlined in the TG-43 protocol and will not be mentioned here. The parameter, r, is the distance (cm) from the origin, or center of the seed, to the point of interest and θ is the angle between the vector, r, and the long axis of the source.

$$\dot{D}(r,\theta) = S_K \cdot \Lambda \cdot \frac{G_L(r,\theta)}{G_L(r_0,\theta_0)} \cdot g_L(r) \cdot F(r,\theta) \quad (1.5)$$

$$\dot{D}(r) = S_K \cdot \Lambda \cdot \frac{G_X(r,\theta_0)}{G_X(r_0,\theta_0)} \cdot g_X(r) \cdot \phi_{an}(r) \quad (1.6)$$

In the clinic, the dose distributions around interstitially implanted seeds are calculated using radiotherapy treatment planning (RTP) systems that apply 1D or 2D dose formalism calculations to individual seeds, the position of which are delineated by CT images. The contribution of dose-rate from each seed is summed to obtain a total dose rate. The resultant dose distribution is then displayed in 2D, as isodose lines overlaying the original CT image. The TG-43 calculations includes various assumptions including; lack of source-to-source shielding, water equivalence of tissues within 5 cm surrounding the seed, and a standardized patient scattering volume.

1.3.4 CURRENT LIMITATIONS OF PERMANENT BRACHYTHERAPY

The physical advantage of brachytherapy has always been the improved localized delivery of dose from the use of low energy photon sources. Low energy photon sources are additionally required for radioprotection purposes because patients return to their normal life after implantation of the radioactive sources. However, dose distributions in brachytherapy are inherently heterogeneous which is owed to highly localized attenuation of radiation and the inverse-square dose drop-off as a function distance from the source (Afsharpour et al., 2012). The consequence is overdosing in the planning target volume (PTV), with an average of 25.1% (range: 11.7%-46.2%) of the PTV receiving 200% of the prescribed dose (Pignol et al., 2006). As a result as many as 20% of patients receiving permanent breast

seed implantation (PBSI) develop induration of the breast compared to 5% for whole breast irradiation (WBI). Although this has no impact on the patient's health or quality of life, it may impact the resulting cosmesis. Permanent brachytherapy is currently limited to photon based radionuclides which poses radiation exposure risks to the hospital staff, public as well as the patient since photons do not have a finite range. In clinical practice, patients are discharged from the hospital only once the dose rate measured at 1 m from their body is below 0.5 mSv/h (Dauer et al., 2010). Another disadvantage is that use of permanent brachytherapy is limited to clinical cases where the tumour is well localized. This accounts for an average of 10-20% of patients requiring radiotherapy, although this percentage will differ based on the departments location, geography and access to resources. Many patients opt for brachytherapy for its convenience as most of the treatment is carried out after the patient is discharged from the hospital, and therefore does not require the several weeks of daily treatment characteristic of external beam radiotherapies (Blasko, 2000). However the procedure is invasive and requires technically trained physicians to accurately implant the sources to achieve the correct dosimetry. Even with correct positioning of the seeds at time of implantation, seeds have been reported to reposition post-implantation due to post-surgical edemas, which may cause seeds to drift to a different position or coalesce together as the swelling subsides, or in rare cases enter blood vasculature and travel to the lungs (Kono et al., 2010). To address these limitations, opportunities for radioisotope therapy as a novel form of brachytherapy has been investigated, particularly in the field of radiation nanomedicine (Yook et al., 2016a). Use of nanoparticles to deliver radiation therapy has been expected to reduce dose heterogeneities through the transport of radioactive nanoparticles through the tissue and eventual smoothing of the dose distribution. AuNP can also be labeled with a variety of different radionuclides, expanding the types of emissions (i.e. α, β+/-) and energies available for treatment. The potential role of radiation nanomedicine in permanent brachytherapy will be discussed in greater detail in the following section.

1.4 GOLD NANOPARTICLES

1.4.1 GOLD NANOPARTICLES IN MEDICINE

The use of gold as a therapeutic agent dates back thousands of years by various cultures including the Chinese and Egyptians, who ingested gold as a drug to cure various ailments or to increase longevity (Abraham, 2008). However it was not until 1857 that the first scientific report of colloidal gold, aqueous gold nanoparticles (AuNP), was published by Michael Faraday. Today AuNP are defined as particles with dimensions in the nanometer scale, 1-100 nm, composed of elemental gold (A=79). AuNP are most commonly made by reduction of Au(III) salts in a reducing agent, such as trisodium citrate, which acts as a stabilizing agent by preventing aggregation of the particles. Use of AuNP have been proposed in many medical applications including therapeutic and diagnostic applications due to their unique physical and chemical properties. These properties include optical absorption and scattering, biocompatibility, modifiable surface chemistry and labeling capacity, high surface to volume ratio, and differential biological uptake in tumours. In addition, the synthesis of AuNP is relatively uncomplicated and can be made in a variety of shapes, the most common being gold nanospehere, nanorods, nanoshells and nanocages, each of which have been designed for

unique applications (Dreaden et al., 2012). For the purpose of this thesis, references to AuNP will refer to gold nanospheres unless otherwise stated.

Currently, the only approved and proven application of gold as a therapeutic agent is in the form of gold colloids for the treatment of rheumatoid arthritis (RA). The first successful clinical application was documented by Abraham et al. in 1997, which reported a significant decrease in tenderness and swelling of the joints following oral administration of colloidal Au with no clinical evidence of toxicity in the patients (Abraham and Himmel, 1997). This served as a major achievement for the use of colloidal gold in therapy as the previous use of aurothiolates, or gold salts, for RA were found to be toxic causing hematologic abnormalities and pulmonary damage in patients (Abraham, 2008). More recently, Paciotti et al. reported the use of intravenously administered colloidal gold with surface bound tumour necrosis factor (PT-cAu-TNF) for treatment of colon cancer in mice, which demonstrated significant anti-tumour effects while being less toxic than administration of TNF alone (Paciotti et al., 2004). The agent now named Aurimmune (CyImmune Sciences), consisting of 27 nm AuNP coated with recombinant human tumour necrosis factor alpha (TNF-α) and polyethylene glycol (PEG), is under clinical trial for treatment of various advanced or metastatic cancers in patients, such as melanoma, pancreatic, ovarian and breast cancers (Giasuddin et al., 2012, Kim et al., 2010b).

1.4.2 CHARACTERISTICS OF GOLD NANOPARTICLES

1.4.2.1 OPTICAL PROPERTIES

The first report of the unique optical properties of gold nanoparticles was in 1857 by Michael Faraday, who described that the color of the aqueous colloidal gold solution was dependent on the particle size after observing the solution change from red to blue following precipitation of the AuNP (Abraham, 2008). Since then, our understanding of the optical properties of AuNP have advanced tremendously allowing for the development of many diagnostic and therapeutic applications. For instance, the dominating optical property of AuNP is their enhanced surface plasmon resonance (SPR), which is the collective oscillation of conduction electrons at the gold surface in the presence of an incident electromagnetic field, occurring at the resonant optical frequency or light wavelength (near 520 nm), that allows them to be strong absorbers and scatterers of visible light. The deep-red color of AuNP in water is attributed to this effect. Smaller AuNP (9 nm) are known to have a surface plasmon band (SPB) shifted slightly towards shorter wavelength (517 nm), while larger AuNP (99 nm) are shifted towards longer wavelengths (575 nm) (Daniel and Astruc, 2004). The SPB is also dependent on the particles shape, temperature and medium in which the AuNP are suspended. The ability of AuNP to interact with light has been fundamental to the use of AuNP in biomedical imaging, and now includes imaging techniques such as resonance scattering and two-photon luminescence confocal microscopy, which allow visualization of AuNP markers inside or on the surface of a cell. The most common method of bio-imaging using AuNP is dark field microscopy which relies on the resonance scattering of light laterally incident on sample containing

AuNP markers. The imaging capability of AuNP is owed to the intensity of SPR upon excitation with light, which results in an absorption and scattering cross section that is much greater than their geometric size (Hu et al., 2008). The AuNP are also more robust than conventional fluorescent probes used in dark field microscopy as they are not subject to photobleaching and can produce a stronger and more stable signal (Ueno et al., 2010). However, for many of these imaging techniques to be useful diagnostically, the AuNP must be conjugated with antibodies or other ligands to facilitate preferential binding to cell-surface proteins or receptors.

1.4.2.2 SURFACE CHEMISTRY

The ability to functionalize the surface of AuNP is of great importance as many of their proposed applications require their further modification. For instance, to exploit the optical properties of AuNP for biomedical imaging, the AuNP surface is bound with ligands to provide specific binding to a target which can then be imaged through excitation of the AuNP at the SPR wavelength of 520 nm. Modification of the AuNP surface is achieved by reaction with functional groups on the ligands such as thiols, phosphines and amines which have a high affinity for the AuNP surface. The most common of the functional groups is thiol (-SH group) which binds to the gold surface through coordinate covalent bonding, when a single atom contributes the shared pair of electrons instead of one from each atom (covalent bonding) (Hakkinen, 2012). The functional groups are used as an anchor for other moieties, such as ligands, proteins, antibodies and drugs, enabling AuNP to be applied towards a wide range of applications. For instance, the modification of AuNP surface with thiol-ending polyethylene glycol (PEG-SH) has been demonstrated to improve the stability of AuNP *in vivo* and decrease uptake by the reticular endothelial system (RES), a branch of the immune system that recognizes and captures foreign material in the blood which is then sequestered by the liver and spleen (Manson et al., 2011). Other modifications that change the net charge of the AuNP will impact the ability for cellular uptake which is important for the delivery of many therapeutic agents. Studies have demonstrated that cationic nanoparticles are more efficiently internalized than anionic nanoparticles due to the negatively charged cellular membrane, even if they are not functionalized with antibodies to facilitate endocytosis (Kim et al., 2010a). In addition to the easily modifiable surface, AuNP have high surface to volume ratio, which allows them to be ideal carriers as large quantities of material can be bound to their surface.

1.4.2.3 BIOCOMPATIBILITY, TOXICITY AND CLEARANCE

Elemental gold has been accepted as a biologically inert metal and as such has been used for implants in medicine such as for reconstruction of the middle ear, treatment of facial palsy, and various types of prostheses (Demann et al., 2005). However, it has been argued that colloidal metallic gold is not biologically inert. To date research on the toxicity of gold nanoparticles have generated conflicting results due to the wide range of experimental conditions such as the nanoparticles size, shape, charge, surface modifications, concentration, as well as the method of evaluating toxicity such as cytotoxicity, blood pharmacokinetics, kinetics of elimination, animal weight and behavioral

changes, organ function, or mortality. Cytotoxicity has been investigated in a number of different cell lines with a variety of surface functionalized AuNP. The conclusion of these studies are that an unmodified AuNP core greater than 2 nm in size is biologically inert, however AuNP below 2 nm in size are chemically reactive and can result in significant cytotoxicity by inducing oxidative stress and mitochondrial damage (Pan et al., 2009). Therefore it is suggested that AuNP used in medical applications be greater than 10 nm in size to reduce surface reactivity. The form and stability of surface modifications can also induce toxicity. Capping agents such as citrate, in the production of gold nanospheres, or hexadecylcetyltrimethylammonium bromide (CTAB), in the production of gold nanorods, are used as stabilizing agents. Citrate stabilized AuNP have not been found to be toxic, however free CTAB can be desorbed from the gold nanorod surface and is toxic (Ray et al., 2009). This demonstrates one of the challenges associated with evaluating cytotoxicity as the effects may be the result of free ligands or other modifying agents dissociated from the AuNP and not the AuNP itself.

The *in vivo* toxicity has been studied mainly as part of larger studies demonstrating the clinical potential of therapeutic nanoparticles, and therefore have generated varying conclusions due to differences in experimental conditions. In general, the level of toxicity depends on the route of administration, the most common being intravenous (i.v.), and the type of AuNP being studied (i.e. size, shape, labeled therapeutic agent) as the biodistribution and pharmacokinetics are influenced by these factors. A study by Chen et al. investigated the *in vivo* toxicity of citrate capped AuNP of varying sizes delivered intravenously and found that intermediate sizes of AuNP (8, 12, 17, 37 nm) induced toxicity in the form of fur colour change, weight loss, and lower median survival in mice, while small (3, 5 nm) and large (50, 100 nm) AuNP were well tolerated at the amounts delivered (Chen et al., 2009). Although the mechanism causing toxicity is not well understood, the study attributed it to accumulation of the AuNP in the liver and spleen resulting from adsorption of blood proteins onto the AuNP and recognition by the RES system. Another study by De Jong et al. demonstrated the size dependent tissue biodistribution of AuNP where smaller AuNP (10 nm) were more widely distributed in organs throughout the mouse body (i.e. liver, spleen, testis, lung, brain), while larger AuNP (250 nm) were limited to the liver and spleen (De Jong et al., 2008).

Clearance of AuNP from organs and their route of excretion from the body has also been demonstrated to be size dependent. Smaller AuNP (<5 nm) are capable of crossing filtration barriers in the kidney and can therefore be excreted into the urine. AuNP larger than 5 nm would be expected to be cleared from the liver via the hepatobiliary pathway, which involves endocytosis of the AuNP by hepatic cells, followed by enzymatic digestion of the cells, transfer into the bile and excretion from the body as fecal matter (Zhang et al., 2016b). This pathway depends strongly on the AuNP's interaction with hepatocytes which is influenced by the AuNP size, shape, charge and surface chemistry. Studies have reported that this process of excretion can be slow, requiring many months or longer (Sadauskas et al., 2009) and may therefore result in genetic changes and chronic toxicity to the liver (Balasubramanian et al., 2010). The alternate clearance pathway of AuNP >5 nm is by the RES, also known as the mononuclear phagocyte system (MPS),

where AuNP are removed from the blood by circulating phagocytic cells (i.e. Kupffer cells, splenic red pulp, machophages) and are sequestered in the liver and spleen. Once phagocytosed the AuNP remain in the cell to be decomposed, however since AuNP cannot be degraded by intracellular processes, the AuNP remains in the cell in the organ until it dies and is phagocytosed by other cells in the organ. The result is a bioaccumulation of AuNP in the liver and spleen, which can last over six months and lead to chronic toxicity (Balasubramanian et al., 2010). Despite these findings, many studies are still pursuing the systemic administration of functionalized AuNP as a therapeutic agent due to its other unique properties. It may be possible to minimize the accumulation of AuNP in the liver and spleen with proper optimization of the AuNP size, charge and surface modification, although more research in this field is required.

1.4.3 POTENTIAL APPLICATIONS OF GOLD NANOPARTICLES IN CANCER THERAPY

1.4.3.1 RADIATION ENHANCEMENT

Many studies have investigated the use of AuNP as enhancers for radiation therapy because the high atomic (Z) number of gold increases the photoelectric absorption of photons (Chithrani et al., 2010, Cui et al., 2017, Chattopadhyay et al., 2010). These studies have demonstrated preclinically that the presence of gold in the target volume during radiation treatment can result in significant dose enhancements and improve survival of tumour bearing mice. In a preclinical study, Hainfeld et al. demonstrated improved survival *in vivo* in mice bearing EMT-6 mammary tumours injected intravenously with 1.9 nm AuNP (Hainfeld et al., 2004). The one year survival was 20% with x-rays alone and 86% with AuNP enhanced radiation, using 250 kVp x-ray, although there is some controversy regarding the high concentrations of AuNP administered and whether that would be translatable to clinical practice. Similar results have been demonstrated *in vitro* by Rahman et al. on bovine aortic endothelial cells treated with photon and electron beams at various energies, and different concentrations of 1.9 nm AuNPs (Rahman et al., 2009). Dose enhancement factors (DEF) from 2.7 to 24.6 were recorded depending on the combination of AuNP concentration and radiation type. In the case of the DEF of 24.6, high concentrations of AuNP (1 mM) combined with 80 kVp energy X-rays were used to generate the dose enhancement effect.

There are several Monte Carlo-based dosimetry estimation studies that show significant dose enhancement from photoelectric absorption and subsequent release of lethal photoelectric products such as Auger electrons and photoelectrons (Cho et al., 2009). These studies have reported that there are greater advantages to using lower energy photon sources, such as ^{103}Pd, for dose enhancement rather than the high energy photons from EBRT. The Monte Carlo modeling study conducted by Lechtman et al. demonstrated radiosensitization using gold nanoparticles as a function of photon energy (Lechtman et al., 2011). The amount of photoelectric absorption was simulated for various clinical photon sources used in radiation therapy (6 MV, ^{192}Ir, 300 kVp, ^{169}Yb, ^{125}I, ^{103}Pd) and a 10^3 times increase was observed for ^{103}Pd in comparison to 6 MV. Additionally, Lechtman et al. states that the use of ~6 mg of

30 nm AuNP per gram of tumour can double the prescribed dose (Lechtman et al., 2011). A study conducted by Jones et al. compared similar clinical photon sources (6 MV, ^{192}Ir, 50 kVp, ^{169}Yb, ^{125}I, ^{103}Pd) (Jones et al., 2010). The results suggest that in order for radiation enhancement to be effective there must be adequate AuNP accumulation in the target volume which may be difficult to achieve *in vivo* in tumours. Radiosensitization is further enhanced when nanoparticles are internalized by target cells (Chithrani et al., 2010).

1.4.3.2 PHOTOTHERMAL THERAPY

As mentioned earlier AuNP have unique optical properties that allow them to absorb light, and if the light occurs in the near-infrared (NIR) region (700-900 nm) it can be converted to heat energy. This has led to the development of photothermal therapies (PTT) that utilize AuNP exposed to NIR lasers, which are capable of greater penetration in tissues before significant attenuation, as photosensitizers for treatment of cancer (Huang et al., 2008). With proper localization of the AuNP in the target site, thermal exposure producing local hyperthermia can result in cell death through irreversible damage to the cell membrane and protein denaturation (Riley and Day, 2017). Rapid heating of the AuNP may also result in formation of vapor bubbles that create highly localized damage to adjacent cells. The use of lasers allows the light to be focused at the treatment site which reduces damage to surrounding normal tissues. Focusing of the laser can be further improved through the use of fibre-optic waveguides inserted into the treatment site in interstitial laser hyperthermia. Due to the highly localized nature of gold nanoparticle mediated hyperthermia, researchers are exploring its use in combination with other therapeutic approaches to target metastasis or tumour lesions located beyond the irradiated site. For instance, *in vivo* studies have demonstrated successful therapy using AuNP induced hyperthermia in conjunction with radiation therapy, and have reported reductions in radiation doses required to achieve tumour control (Hainfeld et al., 2014). The overall success of PTT using AuNP as a monotherapy hinges on several factors. The SPB of AuNP occurs around 520 nm which makes them inefficient in the NIR range, however studies have demonstrated that aggregates of AuNP, which often form at the cell surface or once internalized, are very efficient and can reduce the laser intensity required by 20 times compared to PTT without AuNP (Huang et al., 2007). Therefore, aggregation of the AuNP is often desired. Sufficient accumulation of AuNP in the tumour is also necessary which can potentially be achieved by conjugation of AuNP to antibodies of markers overexpressed in tumour cells (El-Sayed et al., 2006). Lastly adequate delivery of radiation to the tumour, which may be located at depths beyond the penetration range (5-10 mm) of the laser, is required for generation of thermal effects.

1.4.3.3 DRUG DELIVERY AND TARGETING

AuNP have been demonstrated to passively accumulate in tumours by the enhanced permeability and retention (EPR) effect when delivered intravenously. In the EPR effect, nanoparticles are able to accumulate in tumours in greater quantities than in normal tissues as a result of defective tumour vascular physiology, elevated levels of vascular

permeability factors and substandard lymphatic drainage (Maeda et al., 2000). Studies have found AuNP accumulation ranging from to <1% to 7% injected dose per gram (ID/g) of tumour, depending on the AuNP size and surface modifications (Arnida et al., 2011, Zhang et al., 2009). The ability of AuNP to differentially accumulate in the tumour coupled with the high surface to volume ratio and modifiability of the AuNP surface, has triggered investigations on the use of AuNP in drug delivery systems. The advantage of using AuNP bound drugs as compared to free drugs is the potential to reduce toxicity while improving solubility, stability, biodistribution and pharmacokinetics (Ghosh et al., 2008). Conjugation of AuNP with antitumour agents such as tamoxifen and paclitaxel have been proposed for treatment of breast cancers (Dreaden et al., 2009, Gibson et al., 2007). Dreaden et al. demonstrated that drug transport is improved when bound to AuNP due to cellular uptake of AuNP which results in increased drug potency at the disease site as compared to free drugs (Dreaden et al., 2009). The ability to functionalize AuNP surfaces also provides opportunities for combined and targeted therapies. For instance, photothermal therapy using AuNP can be extended to photodynamic therapy through functionalization of the AuNP surface with photosensitizers, which inflict additional damage to tumour cells by photochemical generation of free radical species, and peptides or antibodies for cell targeting (Liu et al., 2010). The use of surface modifications with various targeting moieties have been demonstrated in AuNP which aims to provide specific targeting for certain tumour types and increase local AuNP concentrations (Kumar et al., 2013, Kumar et al., 2012). For instance, breast cancers with overexpression of HER2 have been effectively targeted and treated with trastuzumab (Herceptin) clinically, and could theoretically serve as a targeting agent for AuNP. Chattopadhyay et al. reported the biodistribution of trastuzumab labeled AuNP and found that the targeted AuNP improved internalization in HER2 positive tumour cells, but decreased tumour uptake due to rapid clearance from the blood following intravenous injection (Chattopadhyay et al., 2012a). Prolonging the blood circulation time to allow time for tumour uptake remains a challenge in targeted AuNP therapies, and studies have investigated surface modifications such as PEG to preserve their binding affinity while in blood (Paciotti et al., 2006).

1.4.3.4 RADIATION NANOMEDICINE AND RADIONUCLIDES

Advancements in surface modifiers containing chelators with the capacity to bind radionuclides have led to the development of radiolabeled AuNP as a vehicle for radiation delivery ("radiation nanomedicine"). Chelators, such as DOTA (1,4,7,10-tetraazacyclododecane- 1,4,7,10-tetraacetic acid) and EDTA (ethylenediaminetetraacetic acid), are agents that form multiple coordinate covalent bonds with a metal ion, including radiometals. Currently the radionuclides investigated for use in radiation nanomedicine include lutetium-177 (^{177}Lu, $t_{1/2}$=6.7 d, β_{max}=0.498 MeV, γ=0.208 MeV/0.113 MeV) (Yook et al., 2016a), indium-111 (^{111}In, $t_{1/2}$=2.8 d, γ=0.171 MeV/0.245 MeV) (Ehlerding and Cai, 2016, Cai et al., 2017), yttrium-90 (^{90}Y, $t_{1/2}$=2.8 d, β_{max}=2.28 MeV) (Lai et al., 2017), rhenium-188 (^{188}Re, $t_{1/2}$=16.9 h, β_{max}=2.12 MeV/1.96 MeV, γ=0.155 MeV) (Cao et al., 2004), and technetium-99m (^{99m}Tc, $t_{1/2}$=6.0 h, AE=0.9 keV, IC=15.4 keV, γ=0.14 MeV) (Jimenez-Mancilla et al., 2013), which are also already used clinically in nuclear medicine (*refer to Appendix C for production and decay of radionuclides: ^{177}Lu, ^{111}In and ^{90}Y*). These radionuclides typically have relatively short half-lives and short range emissions, such as beta particles and Auger electrons (AE), which deliver

highly localized dose to tissues in their immediate vicinity. Theoretically, binding of radionuclides to AuNP which have high surface to volume ratios could potentially increase the proportion of radioactivity accumulated in the tumour, facilitate cellular internalization of the radionuclide, and provide opportunities for targeting or adjuvant therapies by dual labeling the AuNP surface. Yook et al. reported the use of ^{177}Lu-labeled AuNP which were radiolabeled utilizing DOTA-PEG-lipoic acid which incorporated a DOTA chelator to complex ^{177}Lu and a thiol functional group for attachment to the AuNP, for treatment of locally advanced breast cancer (LABC) *in vitro* (Yook et al., 2015b) and *in vivo* in a xenograft mouse model (Yook et al., 2016a). The *in vitro* study compared the cytotoxicity of non-targeted ^{177}Lu-labeled AuNP and epidermal growth factor receptor (EGFR) targeted ^{177}Lu-panitumumab-AuNP in several BC cells expressing various levels of EGFR, and revealed reduced cell survival in BC with higher EGFR densities when treated with EGFR targeted ^{177}Lu-panitumumab-AuNP. The latter study compared the biodistribution and treatment efficacy of non-targeted ^{177}Lu-labeled AuNP and EGFR targeted ^{177}Lu-panitumumab-AuNP following intratumoural injection of the AuNP in suspension. However, the study demonstrated equivalent long term tumour retention, tumour growth arrest, and prolonged survival in mice treated with both targeted ^{177}Lu-AuNP and untargeted ^{177}Lu-AuNP. Jiménez-Mancilla et al. reported the use of dual ^{99m}Tc/^{177}Lu-labeled and gastrin-releasing peptide receptor (GRP-r) targeted AuNP (^{99m}Tc/^{177}Lu-AuNP-Tat-BN) for simultaneous radiotherapy and thermal ablation of prostate cancer *in vitro* (Jimenez-Mancilla et al., 2013). Following incubation of PC3 prostate cancer cells with ^{99m}Tc/^{177}Lu-AuNP-Tat-BN, cell proliferation was significantly inhibited in comparison to PC3 cells incubated without AuNP (^{99m}Tc-Tat-BN) and without GRP-r targeting (^{99m}Tc/^{177}Lu-AuNP) due to cellular internalization of the AuNP, allowing IC and AE inflicted damage on the cell nuclei from ^{99m}Tc and β-particle crossfire from ^{177}Lu.

1.4.4 ROUTES OF ADMINISTRATION OF RADIOLABELED AUNP AND ASSOCIATED CHALLENGES

1.4.4.1 INTRAVENOUS INJECTION OF RADIOLABELED AUNP IN SUSPENSION

One of the most appealing phenomenon of AuNP is their ability to differentially accumulate in tumours as a result of the enhanced permeability and retention (EPR) effect. However there are key issues regarding the dependence of nanoparticle delivery via the EPR effect such as; the insufficient accumulation of AuNP to produce a meaningful therapeutic effect, interference from immune cells, and the heterogeneity of EPR between and within tumours (Prabhakar et al., 2013, Maeda, 2012). For instance, passive targeting methods have resulted in low proportions of AuNP accumulation in the tumour due to capture by the RES and subsequent entrapment in the liver and spleen, combined with poor elimination of AuNPs from these organs (Balasubramanian et al., 2010, Chattopadhyay et al., 2012a). This limits the therapeutic potential of the AuNPs, in addition to increasing toxicity to healthy tissues. To increase accumulation in tumours AuNPs have been coated with various polymers such as PEG, which has allowed them to persist in circulation longer by preventing RES recognition, or modified with various polymers and targeting ligands to potentially improve retention of the gold in the tumour and encourage cellular uptake (Chattopadhyay et al., 2010). However, biodistribution results from intravenously administered surface-functionalized AuNP studies still

report significantly greater accumulation of AuNP in the liver and spleen in comparison to the tumour (~10 fold less AuNP) (Khlebtsov and Dykman, 2011). For instance, the *in vivo* study conducted by Chattopadhyay et al. reported that ~22% ID/g (% of injected dose/gram of tissue) of the injected HER2 targeted AuNP were sequestered by the liver and spleen, with only 1-2% accumulating in the tumour, after 48 hours. An additional challenge is that intravenously injected AuNP are not uniformly distributed within the tumour but rather are found in clusters near the tumour vasculature, and would therefore result in under dosing to regions of the tumour that are poorly vascularized (Diagaradjane et al., 2008, Hainfeld et al., 2004). These studies have found that the penetration of AuNP is limited to the vascular rich regions in the tumour, mainly in the peripheries. Therefore, infiltration of nanoparticles is largely dependent on tumour physiology, such as vascularity, stromal content, blood and interstitial pressure, which varies widely between individuals and even in different regions within the same tumour (Steichen et al., 2013).

1.4.4.2 INTRATUMOURAL INJECTION OF RADIOLABELED AUNP IN SUSPENSION

An alternative method to circumvent poor transport of AuNP in tumours from intravenous injections is direct intratumoural (i.t.) administration. The advantage of i.t. injection of AuNP in suspension is that AuNP delivery and distribution is not dependent on the EPR effect, high concentrations of AuNP in the tumour can be achieved, AuNP do not need complicated surface modifications to evade capture by the RES, and normal tissues are spared. Intratumoural administration has been demonstrated through single and multiple injections *in vivo* resulting in significant increase of AuNP concentrations in the tumour and reduction in the RES organs (Chattopadhyay et al., 2012a, Yook et al., 2016a, Ehlerding and Cai, 2016). For instance, the *in vivo* study conducted by Chattopadhyay et al. reported 30% ID/g accumulation in the tumour and 3.4% in the liver and spleen at 48 hours, following multiple i.t. injections of HER2 targeted ^{111}In-AuNP (Chattopadhyay et al., 2012a). In a study by Shukla et al., ^{198}AuNP-epigallocatechin-gallate (EGCg) was delivered via single i.t. injection into prostate cancer xenografts and over 70% ID was retained in the tumour at 24 h p. i. (Shukla et al., 2012). At 42 days p.i. 37% ID remained in the tumour, which resulted in effective tumour growth control, while liver accumulation was at 2.5 % ID.

Although pre-clinical studies on i.t. delivered radiolabeled AuNP have been successful in controlling tumour growth, i.t. administration is clinically impractical as multiple, precisely placed injections of radiolabeled AuNP would be required to deliver an even dose distribution in larger tumours. Additionally, the AuNP redistribute from the injection site randomly resulting in irregular dose distributions. This was demonstrated through micro-SPECT/CT imaging of i.t. injected ^{177}Lu-AuNP for treatment of LABC human breast cancer xenografts in mice in the *in vivo* study by Yook et al. (Fig. 1.5). Figure 1.5 illustrates representative 2-dimensional image-based radioactivity (right) and dose (left) distributions obtained from single i.t. injections into BC xenografts. The radioactivity distribution from targeted and non-targeted ^{177}Lu-AuNP display several regions containing high ^{177}Lu-AuNP concentration. These high radioactivity regions are not predetermined but receive a higher dose. Clinically, this will be problematic as the dose distribution

would depend on the unpredictable redistribution of radiolabeled AuNP within the tumour, and therefore be difficult to account for during treatment planning which has a direct impact on therapeutic response (Ehlerding and Cai, 2016).

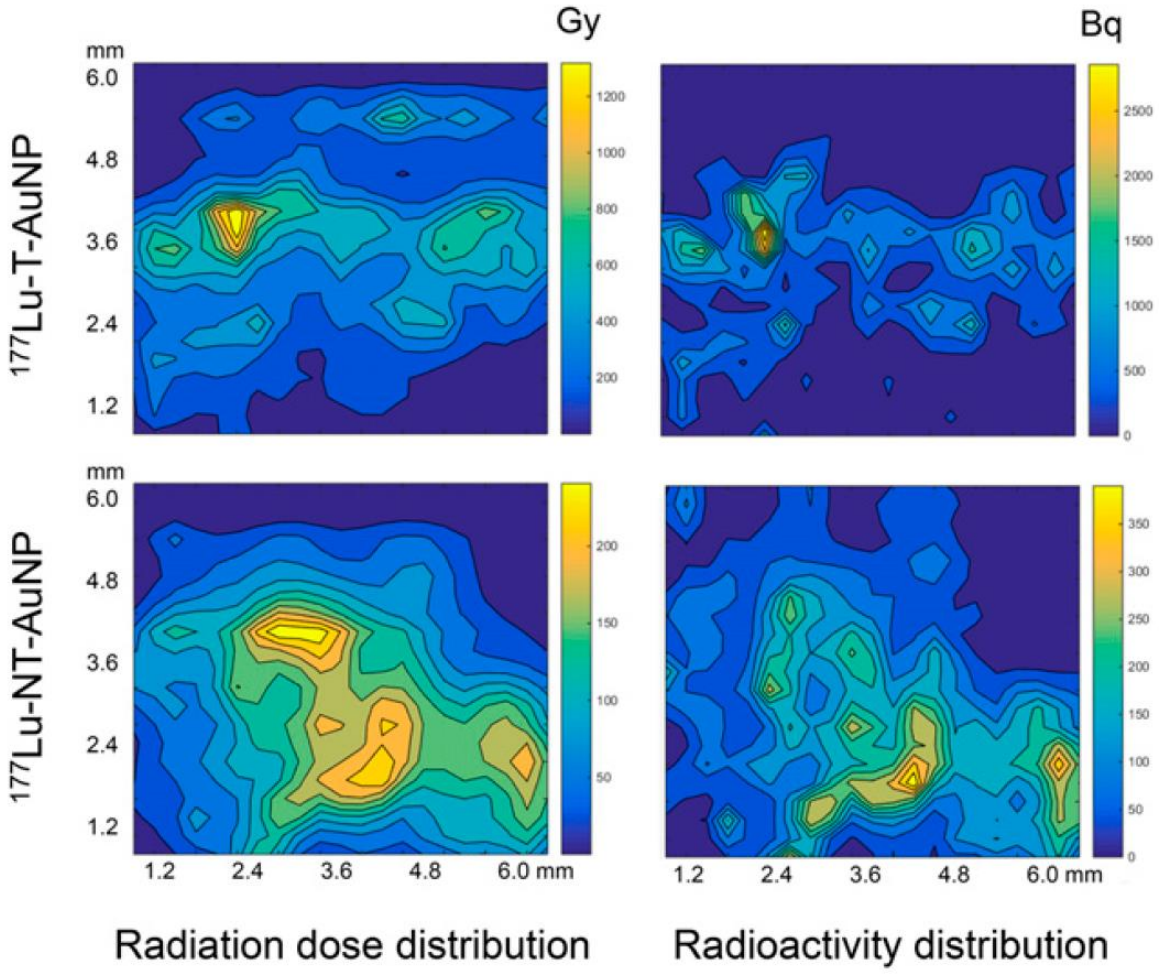

Figure 1.5 Representative dose (left) and radioactivity (right) distributions at 48 h post intratumoural injection of targeted (top) and non-targeted (bottom) ^{177}Lu-AuNP in BC tumour bearing mice. The boundary of the tumours are outside of the 6.0 mm by 6.0 mm region of interest. Note the heterogeneous distribution of radioactivity and dose regardless of the presence of targeting. *Originally published in JNM by Yook* et al. (Yook et al., 2016a)

1.4.5 GOLD NANOPARTICLES AND PERMANENT BRACHYTHERAPY

The heterogeneous dispersal of radiolabeled AuNP from i.v. and i.t. injections has revealed that a method for controlled delivery is necessary in order to adapt to more complex clinical scenarios where multiple injections of AuNP will be required for the treatment of larger tumours. To improve the feasibility of radiolabeled AuNP in future clinical studies I propose here in this thesis the use of implantable materials that are capable of slow release of AuNP, either

through their porosity or physical degradation, to be delivered by brachytherapy. The potential advantage of radiolabeled AuNP delivery using brachytherapy as to i.v. or i.t. injections of AuNP in suspension are; precise placement of the AuNP containing implants, controlled release of AuNP, predictable redistribution of AuNP in the tumour and therefore predictable dose distributions, and enhanced normal tissue sparing. Currently, the use of brachytherapy has been proposed only for delivery of AuNP for radiation enhancement and for other drug loaded nanoparticles (Sinha et al., 2015, Kumar et al., 2015). These studies have suggested combining nanoparticles into brachytherapy "spacers" that will facilitate their slow release after implantation. For instance, Kumar et al. described the design of poly (lactic-co-glycolic) acid (PLGA) brachytherapy seed spacers capable of releasing drug loaded silica nanoparticles through degradation of the spacers.

The use of radiolabeled AuNP can offer certain opportunities and improvements to permanent brachytherapy such as; dose enhancement from photoelectric absorption of AuNP, opportunity for adjuvant therapies from dual labeling (Yook et al., 2015b), the use of radionuclides with different emission types (β, AE, IC, α, etc.) (Jimenez-Mancilla et al., 2013, Ehlerding and Cai, 2016, Shukla et al., 2012), dose homogenization through the physical redistribution of radioactivity, and the natural elimination from the body following treatment. In the study conducted by Cho et al. the macroscopic dose enhancements from commonly used brachytherapy sources (^{125}I, ^{169}Yb, and ^{192}Ir) were simulated using Monte Carlo assuming a homogeneous distribution of AuNP in the treatment volume, and dose enhancements of >40% were reported depending on the dose of AuNP and radioisotope (Cho et al., 2009). However, there are very limited studies that have demonstrate the distribution of the AuNP over time, or their behaviour after implantation in detail. Additionally, there are no studies to date that use permanent brachytherapy techniques to deliver radiolabeled AuNP as a radiotherapeutic agent.

1.4.6 DOSIMETRY TECHNIQUES FOR RADIOLABELED AUNP: MIRD AND IMAGE BASED MONTE CARLO

The dosimetry techniques surrounding AuNP reported to date utilize either Monte Carlo simulations or organ level Snyder values, or S values, analogous to those used in nuclear medicine. Monte Carlo software such as Monte Carlo N-Particle Transport Code (MCNP), Geometry and Tracking (GEANT) Monte Carlo Code, or Electron Gamma Shower (EGSnrc), are designed to track particle transport and energy deposition in a virtual geometric space using source and target data specified by the user. Since all of the source and target information are inputted by the user, such as radionuclide decay probabilities and energy, emission types, material composition and density, and source and target dimensions, Monte Carlo based dosimetry is extremely versatile for investigating dose deposition for a wide range of scenarios provided there is sufficient time and computational power. In radionuclide therapy organ level S values (mGy/MBq·s), which describes the mean absorbed dose to the whole organ per unit of cumulative activity, are used to calculate the dose using software based on Medical Internal Radionuclide Dose (MIRD) formalism, such as Organ Level Internal Dose Assessment/Exponential Modeling (OLINDA/EXM) (Stabin, 1996, Stabin et al., 2005). The S values

used in programs such as OLINDA/EXM are pre-calculated by Monte Carlo simulation in phantoms that represent the average male or female body and assumes that the radioactivity is uniformly distributed throughout the target organs (Grimes and Celler, 2014). The dose, $D(r_T,T_D)$, to an organ, r_T, is determined by calculating the product of cumulative radioactivity, $\tilde{A}(r_S, T_D)$, or time-integrated activity over the lifetime of the radionuclide, where T_D represents the total time during which the disintegrations take place, occurring within itself and all source organs, r_S, with their corresponding S value, $S(r_T \leftarrow r_S)$, and taking the sum of the dose from all contributing organs (Eq. 1.11)

$$\boldsymbol{D(r_T, T_D) = \sum_{r_S} \tilde{A}(r_S, T_D) S(r_T \leftarrow r_S)} \quad (1.7)$$

The resulting dose is an estimate based on the assumption of uniform radioactivity distributions within the organ. In actuality, however, there are nonuniformities in the radioactivity distribution that occur temporally and spatially which leads to nonuniformities in the tissue absorbed dose. To improve visualization of regional sub-organ dose distribution studies have developed voxel based dosimetry techniques which are applied to SPECT or positron emission tomography (PET) images that can quantify and localize radioactivity with high spatial resolution (Full width at half maximum (FWHM) = 5-25 mm) (Jackson et al., 2013, Berenato et al., 2016). The temporal variations in radioactivity can be overcome through quantitative serial imaging therefore enabling mapping of dose distributions within organs. This image based technique for mapping dose distribution is ideal for radiolabeled AuNP which have nonuniform spatial distributions, change temporally, utilizing shorter range emitters, are highly localized within the tumour, and therefore require the high spatial resolution offered by SPECT or PET imaging. In this technique voxel dose kernels, a 3-dimensional (3D) space divided into millimeter to submillimeter sized cubic voxels containing S values, are generated from Monte Carlo simulations and convolved with 3D activity distributions to determine the imparted absorbed dose (Reiner et al., 2009, Lanconelli et al., 2012). A number of studies have published voxel-level S values including Amato et al. (^{32}P, ^{90}Y, ^{99m}Tc, ^{177}Lu, ^{131}I, ^{153}Sm, ^{186}Re, and ^{188}Re) using the GEANT4 Monte Carlo code (Amato et al., 2013), and Lanconelli et al. (^{89}Sr, ^{90}Y, ^{131}I, ^{153}Sm, ^{177}Lu, ^{186}Re, and ^{188}Re) using EGSnrc Monte Carlo code for 13 different voxel sizes (Lanconelli et al., 2012). However, the only study to date that has applied this method of dosimetry for radiolabeled AuNP was reported by Yook et al. who used micro-SPECT/CT imaging to determine the spatial distribution of i.t. injected ^{177}Lu-AuNP in a LABC xenograft model (Yook et al., 2016a).

1.5 HYPOTHESIS

The hybrid approach of brachytherapy using a nanoparticle depot (NPD) for delivery of radiolabeled nanoparticles can improve local concentrations, systemic control and reduce intrasubject distribution of radiation, thereby improving the therapeutic ratio. Furthermore, the NPD can enhance radiation distribution in the tumour as compared to conventional brachytherapy seeds which over-localizes dose.

1.6 AIMS

The objective of this research is to develop a novel delivery system for radiolabeled AuNP compatible with permanent brachytherapy technique for treatment of BC. The specific aims were:

1. To construct a biocompatible nanoparticle depot (NPD) capable of controlled release of AuNP *in vivo* and is implantable using permanent brachytherapy technique, and evaluate the intratumoural distribution of AuNP following implantation in a human BC xenograft mouse model.
2. To evaluate and compare the intratumoural dose distribution in simulation using voxel based dosimetry and MCNP Monte Carlo software for radiolabeled AuNP NPD and conventional sealed seeds using electron emitting radionuclides (^{111}In, ^{177}Lu, and ^{90}Y). To evaluate and compare the intratumoural dose distribution *in vivo* using micro-SPECT/CT imaging for NPD and i.t. injection of radiolabeled AuNP.
3. To evaluate the *in vivo* efficacy and toxicity of ^{177}Lu-AuNP delivered via a NPD implanted into two different human BC xenograft mouse models (MDA-MB-231 and MDA-MB-468), and using two different sizes of AuNP (5 nm and 15 nm).

The research described in this thesis is an extension of the current nanoparticle based radiation therapies being studied, with the aim to improve peritumoural AuNP distribution, dose homogeneity, administration and clinical translation of nanomedicines. The significance of this work is in its potential to deliver therapeutic nanoparticles through controlled release from eluting biocompatible hydrogels, implanted using existing permanent brachytherapy techniques. In combining radionuclide nanomedicine with brachytherapy the limitations of permanent brachytherapy and AuNP delivery will be addressed.

CHAPTER 2

2 DEPOT SYSTEM FOR CONTROLLED RELEASE OF GOLD NANOPARTICLES

Adapted from: Priscilla Lai, Eli Letchman, Shahram Mashouf, Jean-Philippe Pignol, Raymond M. Reilly (2016). Depot system for controlled release of gold nanoparticles with precise intratumoural placement by permanent brachytherapy seed implantation (PSI) techniques. *Int J Pharm,* 515**,** 729-739

2.1 ABSTRACT

We report the design of a NPD system for local delivery of AuNP that facilitates their controlled release and is implantable into tumours by permanent seed implantation (PSI) brachytherapy techniques. Various sizes (5, 15, 30, and 50 nm) of PEG coated AuNP and concentrations (6%, 8%, and 10% w/v) of calcium alginate used to form the NPD were studied. AuNP release rate, diffusion characteristics and spatial distribution were characterized in a tissue equivalent phantom model, and in a breast cancer tumour xenograft model and compared to a Fickian diffusion computational model, to identify the optimal NPD composition. In phantoms, 5 nm and 15 nm AuNP were released more rapidly than 30 nm or 50 nm AuNP but when implanted into tumour xenografts, AuNP exhibited slower release from NPD. Controlled prolonged release of AuNP was observed in tumour tissue over durations which were dependent on AuNP size. Maximum release and distribution in tumours was achieved using 5 nm AuNP incorporated into NPD. These results demonstrate the potential for the NPD as an effective local delivery system for AuNP-based therapies.

2.2 INTRODUCTION

Gold nanoparticles are receiving considerable attention for delivery of chemotherapeutic drugs (Liang et al., 2014), radionuclides (Yook et al., 2016a, Vilchis-Juarez et al., 2014) and photosensitizing drugs (Zhang et al., 2015) to tumours for cancer treatment. Furthermore, their ability to convert light to heat has led to interest in their application for photothermal therapy (Pekkanen et al., 2014, Liu et al., 2016, Bao et al., 2016) and their conversion of X-rays to more radiobiologically effective Auger and photoelectrons has generated interest in their use as sensitizers for radiation treatment of cancer (Chattopadhyay et al., 2013, Hainfeld et al., 2004, Huang et al., 2011). In almost all studies, AuNP were administered systemically by i.v. injection, based on extravasation of AuNP into tumours and their retention by the EPR effect (England et al., 2015). In some studies, AuNP were surface-modified with targeting ligands such as monoclonal antibodies or peptides to promote active uptake into tumours (Llevot and Astruc, 2012). Nonetheless, there remain significant challenges to the effective delivery of AuNP to tumours after i.v. injection, since they are

avidly recognized by the MPS which causes sequestration by the liver and spleen (Zhang et al., 2016a). Surface coating of AuNP with PEG chains minimizes MPS recognition and reduces liver and spleen uptake (Arnida et al., 2011). However, conjugation to targeting ligands may enhance MPS recognition resulting in diminished tumour uptake. For example, Chattopadhyay et al. previously reported that 30 nm diameter ^{111}In-labeled AuNP modified with trastuzumab to target subcutaneous (s.c.) HER2-positive MDA-MB-361 human BC xenografts in athymic mice exhibited 2-fold greater spleen uptake after i.v. injection than unmodified ^{111}In-AuNP [19.2 vs. 10.0 percent injected dose/g (% ID/g)] and tumour uptake was reduced compared to unmodified ^{111}In-AuNP by 2-fold (1.2 vs. 2.2% ID/g) (Chattopadhyay et al., 2012b). A recent article reviewed the delivery to tumours of a variety of nanoparticles including AuNP, by analysing data from 117 publications and concluded that a median of <1% of systemically administered nanoparticles were taken up by tumours in mouse xenograft models (Wilhelm et al., 2016).

One strategy to overcome these limitations of i.v. injected AuNP may be i.t. injection, particularly for tumours that are readily accessible, such as early stage BC which is confined mainly to the breast. We found that i.t. injected and trastuzumab-modified ^{111}In-AuNP yielded 25-fold higher tumour radioactivity (29.6% ID/g) than i.v. injected ^{111}In-AuNP and 10-fold lower spleen uptake (1.8% ID/g) and 1.7-fold lower liver accumulation (1.6% ID/g) (Chattopadhyay et al., 2012b). More recently, Yook et al. reported that very high tumour concentrations (>200% ID/g) were achieved for i.t. injected panitumumab-modified ^{177}Lu-labeled AuNP. These ^{177}Lu-AuNP deposited high radiation doses in s.c EGFR-positive MDA-MB-468 human BC xenografts (>30 Gy) in athymic mice with which arrested tumour growth (Yook et al., 2016a). Moreover, the retention of ^{177}Lu-AuNP in tumours minimized redistribution to normal organs resulting in low radiation doses (<1 Gy) that caused no normal tissue toxicity. These results are very promising for maximizing the radiotherapeutic effects of ^{177}Lu-AuNP on tumours while minimizing their effects on normal tissues. However, a practical obstacle to advancing this approach to human studies is the feasibility in precisely positioning AuNP in tumours by i.t. injection to obtain predictable radioactivity distribution and dose deposition, especially since patient tumours are much larger than the mouse tumour xenografts previously studied. Treatment of tumours in patients would require multiple i.t. injections that need to be spatially distributed with high accuracy in order to minimize regional heterogeneities in the radiation doses deposited in the tumour.

To address this challenge, we report here the design of a novel NPD system composed of a porous calcium alginate reservoir into which AuNP may be loaded, and which enables their controlled local release and diffusion in tumour tissues. The NPD were designed to have the same dimensions as brachytherapy seeds that are routinely used in patients for local radiation treatment of tumours, so that they can be precisely positioned into a tumour using the pre-loaded needle technique used for PSI (Hepel and Wazer, 2012). PSI brachytherapy techniques involve careful insertion of multiple radioactive seeds that are preloaded into seeding needles and guided into the tissue using a template system to assure precise placement. The template allows selection of the insertion depth in tissue and the distance between adjacent seeds such that seed positioning is accurate to within a few millimeters (Pignol and Keller, 2009b, Morton et al., 2016). Adapting the PSI technique for intra-tumoural placement of ^{177}Lu-AuNP would render

the approach practical for tumour treatment in BC patients. Moreover, the approach could potentially be extended to local treatment of other cancers for which brachytherapy is currently used (e.g. prostate cancer) (Nicolae et al., 2016). We studied the release of AuNP from the NPD as a function of calcium alginate concentration and AuNP size using an *in vitro* tissue-equivalent phantom model, by modeling the release by Fick's diffusion law, and experimentally *in vivo* in a BC tumour xenograft mouse model with the NPD inserted by PSI techniques (Fig. 2.1). To our knowledge, this report is the first to describe local delivery of AuNP in a tumour using a NPD system inserted by PSI techniques.

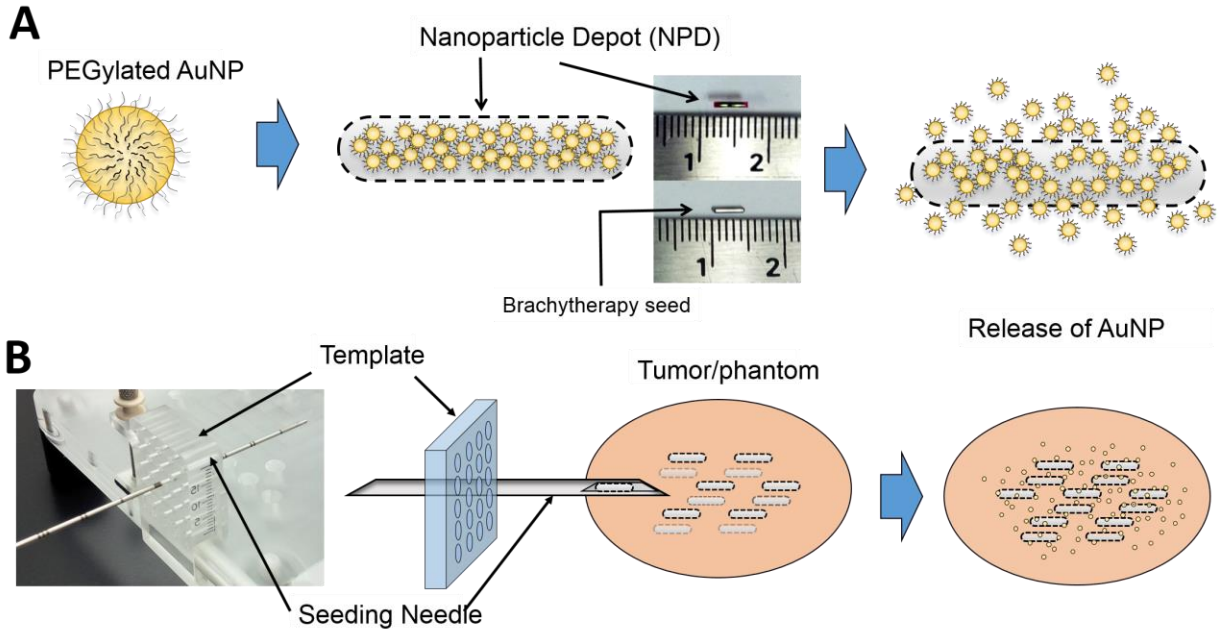

Figure 2.1 Conceptual illustration of NPD design and implantation. (a) The NPD is loaded with PEGylated AuNP and release of AuNP from the NPD occurs following implantation. A comparison of the dimensions of a NPD with those of a conventional titanium shell permanent brachytherapy seed is also shown. (b) The NPD is loaded in an 18 G seeding needle and deposited into a tissue-equivalent phantom or tumour xenograft in an athymic mouse using the template as a positioning guide. Once implanted, the NPD released AuNP into the surrounding phantom matrix or tumour tissue.

2.3 MATERIAL AND METHODS

2.3.1 GOLD NANOPARTICLE PEGYLATION

AuNP (5, 15, 30 and 50 nm; Ted Pella Inc., Redding, CA, USA) were PEGylated for 24 h at 4°C by incubation with 0.235g of mercaptopolyethylene glycol monomethyl ether (MeO-PEG-SH) (2 kDa; IRIS BioTech, Marktredwitz, Germany) in double distilled water (d.d. H_2O) per 500 mL of AuNP stock solution. The mean diameter and coefficient of variation (%) of the AuNP prior to PEGylation were 5.3 nm (≤15%), 14.4 nm (≤8%), 31.2 nm (≤8%) and 49.1 nm (≤8%) for 5, 15, 30 and 50 nm AuNP respectively. PEGylated AuNP were concentrated by ultracentrifugation (Eppendorf Centrifuge

5804 R, Hamburg, Germany) at 5,000 × g for 30 min and 15,000 × g for 60-120 min at 4˚C. The final AuNP concentration was measured by UV-Vis absorption at 525 nm (Nanodrop 2000, Thermo Scientific, Wilmington, DE, USA) by reference to a calibration curve.

2.3.2 NPD FORMATION AND INCORPORATION OF AUNP

Very low viscosity (VLV <20 mPa) ultrapure medical grade sodium alginate (Pronova NovaMatrix, Sandvika, Norway) was used to form the NPD. Alginate gels were first prepared by combining sodium alginate powder (6%, 8% and 10% w/v) with 0.5% NaCl aqueous solution. Gels were allowed to stabilize for 24 h before highly concentrated AuNP (~25-80 mg of AuNP/mL depending on AuNP size) in d.d. H_2O were added to the mixture to a final concentration of 0.2 mg of AuNP/5µL of gel. The AuNP/alginate solution was gently mixed using a vortex mixer for 1 min, then centrifuged for 7 min at a 1500 × g to collect any beading on the side of the vial during mixing. The AuNP/alginate gel mixture was injected into custom molds constructed from a block of polyacrylamide with cylindrical openings having the same dimensions as a conventional brachytherapy seed (0.8 mm diameter × 4 mm length). The molds were entirely submerged in a cross-linking solution of 10% calcium chloride in d.d. H_2O for 45 min then the NPD was removed from the mold using a trocar. A comparison of the NPD with a conventional brachytherapy seed is shown in Fig. 2.1a. To ensure the AuNP incorporated into the NPD were not aggregated as a result of the calcium alginate crosslinking process, NPD were submerged in d.d. H_2O. The UV-Vis absorbance spectrum of AuNP released from the NPD was obtained using the Nanodrop 2000 instrument. The peak absorption wavelength (λ_{max}) in the spectrum was compared to that of stock AuNP.

2.3.3 TISSUE-EQUIVALENT PHANTOM MODEL

Tissue-equivalent phantoms were made from 0.4% w/v ultrapure grade agarose (Bio-Rad Laboratories, Hercules, CA, USA) dispersed in a solution containing 10% Tris-Borate EDTA buffer (Sigma-Aldrich, St. Louis, MO, USA) and d.d. H_2O, which mimics the microstructure of soft tissues (Chen et al., 2002). Implantation into phantoms was carried out using a modified template device (Fig. 2.1b), designed and constructed by the Medical Physics Machine Shop (Sunnybrook Health Sciences Centre, Toronto, ON, Canada). The template was mounted to a stage to allow for finer template positioning. An 18 G seeding needle (Eckert & Ziegler, Oxford, CT, USA) was manually loaded with the NPD and the template was used to stabilize the needle during insertion. Phantoms were implanted with NPD composed of 6%, 8% or 10% (w/v) calcium alginate and incorporating 5, 15, 30 or 50 nm AuNP.

2.3.4 TUMOUR XENOGRAFT MOUSE MODEL

MDA-MB-231 human BC cells (ATCC, Manassas, VA, USA) were cultured at 37 °C in 5% CO_2 in RPMI-1640 medium (Sigma-Aldrich, St. Louis, MO, USA) supplemented with 5% penicillin/streptomycin and 10% fetal bovine serum.

Female severe combined immunodeficient (SCID) mice (Charles River Laboratories, Boston, MA, USA) were inoculated s.c. in the right hind leg with 2×10^6cells in 50µl of Mg^+/Ca^+ Dulbecco's Phosphate Buffered Saline (DPBS) using a 27 G needle. Tumours were permitted to grow to a diameter of 9 mm and were then implanted with NPD composed of 6% (w/v) calcium alginate and incorporating 5, 15, or 30 nm AuNP. During implantation, mice were anesthetized with 2% oxygen ventilated isoflurane. Mice were restrained on the stage and the needles positioned under ultrasound guidance (Sonix RP, Ultrasonix, Richmond, BC, Canada) such that the length of the NPD ran parallel to the leg and the NPD was centered in the tumour (Fig. 2.2). Only one NPD was implanted per tumour. Animals were sacrificed at 7 days post implantation and the tumours harvested and imaged by micro-CT. The Animal Use Protocol for this study was approved by the Sunnybrook Research Institute Animal Care Committee (SRI ACC) in accordance with the Canadian Council on Animal Care (CCAC) Guidelines.

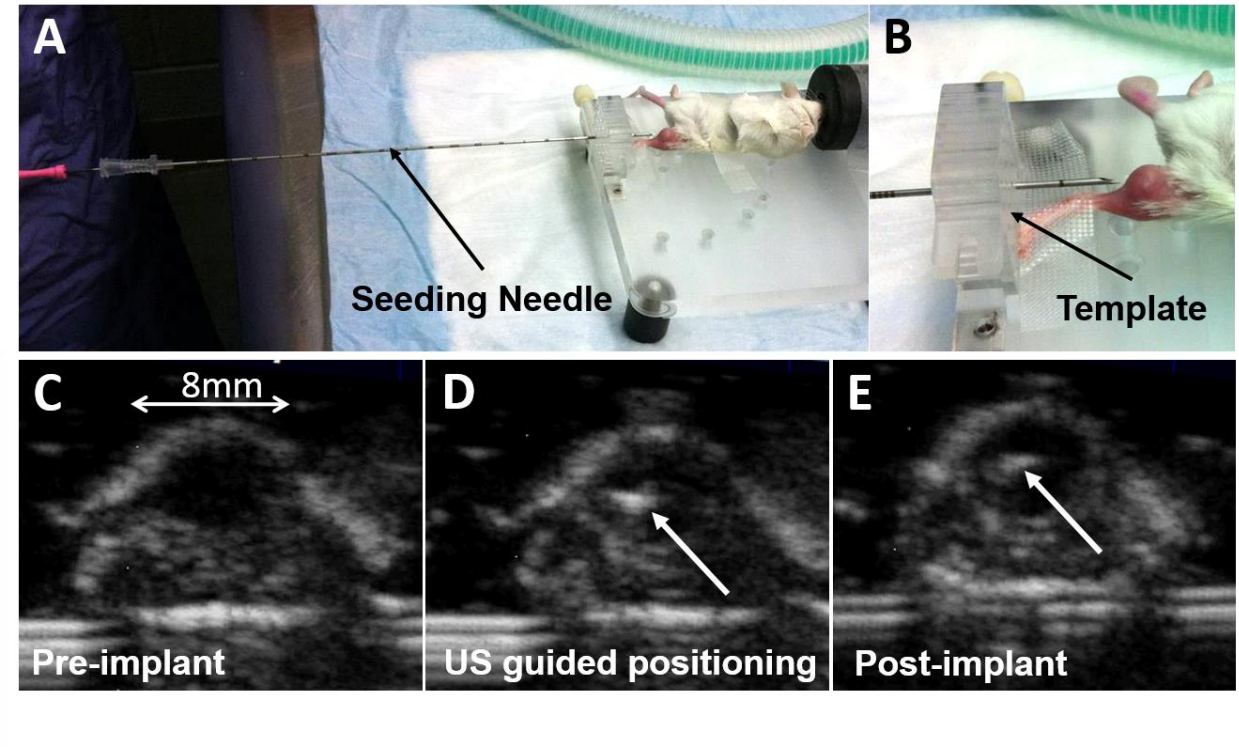

Figure 2.2 An image of the experimental setup and ultrasound guided implantation. (a) The seeding needle is centered at the tumour using the adjustable template shown in (b), while the mouse is restrained on the template stage. Ultrasound images collected (c) pre-implantation, (d) during implantation to verify positioning, and (e) post-implantation. The implanted NPD is indicated in panels (d) and (e) by the white arrow.

2.3.5 IMAGING OF AUNP RELEASE AND DISTRIBUTION

Release of AuNP from the NPD was analyzed by micro-CT (µCT100; Scanco Medical Bruttisellen, Switzerland). Images were acquired at 45 kVp (0.5 mm Al filtration), 200 µA, using a 20.5 mm field diameter and 20 µm × 20 µm × 20 µm

voxel size. Gray level values (GLV) were extracted from micro-CT DICOM images using MicroView GEHC (General Electric Health Care, Buckinghamshirem United Kingdom). GLV for various gold concentrations were collected using micro-CT scans of a calibration phantom containing water, air and known concentrations of AuNP in water. The GLV for the background (water) was subtracted and the results were used to generate a gold radiodensity curve of GLV values vs. AuNP concentrations (mg/mL). The gold concentrations within and surrounding the NPD were determined after subtracting the background GLV for the phantom. Release of AuNP from the NPD was analyzed using MATLAB (Mathworks, Natick, MA, USA). Images were imported into MATLAB and the total NPD volume decomposed into bins of GLV that corresponded to concentrations of gold. The mass of gold remaining after the allotted time, was determined by multiplying the number of voxels per bin, assuming 8×10^{-9} mL/voxel, by the corresponding AuNP concentration. The AuNP rate of release was calculated by dividing the mass of released AuNP by the amount of time elapsed at the time of imaging. Note that analysis of the release rate was derived only from AuNP retained within the volume of the NPD. The distribution of AuNP in the phantom was determined by measuring the diffused AuNP as a function of distance from the surface of the NPD. A combination of thresholding and manual contouring on ImageJ software (National Institutes of Health, Bethesda, Maryland, USA) was used to contour the NPD and successive regions of interest (ROI) 'rings' were created up to 2 cm radially from the NPD surface (see Results Fig. 2.4b). The average GLV was measured and converted to AuNP concentration as previously described.

Release of AuNP into tumour tissue was calculated as the ratio of the average GLV in the tumour to the average GLV in the NPD. This was done to avoid misinterpretation of AuNP in tumours from differences in GLV arising from inter-tumour variability. The average GLV was measured using manual thresholding and the Isosurface-to-ROI function in MicroView. As the AuNP concentrations reach equilibrium with the surrounding tumour tissue, the ratio approaches unity.

Tumour specimens were fixed immediately after imaging for 3 days at 4˚C using Carnoy's solution (95% ethanol, 5% acetic acid) to preserve the alginate gel and tissue. The samples were embedded into paraffin blocks and sectioned (5 µm thickness) and stained with silver enhancer staining (SES) (Silver Enhancer Kit, Sigma Aldrich) according to the manufacturer's instructions. Tumour sections were counterstained with Mayer's Hemotoxylin (Sigma-Aldrich). Tumour AuNP diffusion was calculated by manual contouring of the tumour section and measuring the percent positive staining in the contoured region using Imagescope (Leica Microsystems Inc., Concord, ON, Canada).

2.3.6 FICKIAN MODELING OF AUNP DIFFUSION AND SPATIAL DISTRIBUTION

Diffusion of AuNP (5, 15, 30 and 50 nm) from the NPD into the phantom was also predicted from experimentally derived diffusion coefficients, D_i (cm^2/s), to assess the validity of computational models for assessing nanoparticle distribution. The measured diffusion coefficients were used to calculate the root mean square displacement and the change in AuNP distribution over time. In this model, a tunnel with dimensions 20 mm × 5 mm × 3 mm ($L \times W \times H$)

was constructed using polyacrylamide. The tunnel was filled with tissue-equivalent medium, then submerged in a well of AuNP solution (Kim et al., 2010a). Diffusion of AuNP occurred from the exposed ends of the tunnel towards the center. Images of AuNP diffusion into the tunnel of length $L = 2l$, taking advantage of their red color, were collected using a digital camera (Canon PowerShot SD1400 IS Digital ELPH, Canon Inc. Tokyo, Japan), and the intensity profile along the length L, of the tunnel was extracted from the digital images using ImageJ software. The data was fitted to Fick's diffusion model (2.1).

$$\frac{\partial c}{\partial t} = \frac{\partial}{\partial x}\left[D\frac{\partial c}{\partial x}\right] \tag{2.1}$$

The solution used for this model in terms of concentration was developed by Crank et al. to give the mass of penetrant in the tunnel, M_t, as a function of time, t, compared to the saturation mass, M_∞ (2.2) (Crank, 1975, Comyn, 1985). Using this model the diffusion coefficients were determined from the slope of the line, m, when M_t/M_∞ vs. $t^{1/2}$ was plotted.

$$\frac{M_t}{M_\infty} = \frac{2}{l}\left(\frac{D}{\pi}\right)^{1/2} t^{1/2} \qquad where\ \frac{2}{l}\left(\frac{D}{\pi}\right)^{1/2} = m \tag{2.2}$$

The spatial distribution of AuNP was calculated using the experimentally derived diffusion coefficients. The radial distance traveled, or root mean square displacement, $\langle r^2 \rangle$, was calculated to determine the boundary of infiltration (2.3).

$$\langle r^2 \rangle = 6Dt + C \tag{2.3}$$

Estimations of AuNP diffusion were modeled for different times after implantation, and assumed uniform radial diffusion from the NPD. The distribution of AuNP was modeled using MATLAB's *pdepe* function to solve (2.1). In this model, the distribution is dependent on the release rates of AuNP from the NPD (*from Section 2.3.5*), the experimental diffusion coefficients for different AuNP sizes, and the duration of AuNP release. The initial conditions and boundary conditions assumes that at $t=0$, the concentration of AuNP outside the NPD is zero ($c(x, 0)=0$), the decrease in the initial concentration of the NPD is linear (c_0-*(release rate)*t*), and that the concentration and flux at the outer boundary of the volume is zero ($c(x_{max}, t)=0$, $\delta c/\delta x=0$).

2.3.7 STATISTICAL ANALYSIS

Significance was determined using an unpaired t-test with unequal variances ($P<0.05$).

2.4 RESULTS

2.4.1 UV-VIS SPECTROSCOPY

The λ_{max} expected for non-aggregated AuNP is 520 ± 10 nm depending on size (Amendola and Meneghetti, 2009). A shift towards longer wavelengths, or a shoulder in the spectrum is indicative of AuNP aggregation or shape anisotropy (Shankar et al., 2003). The absorption bands from released AuNP are compared to those for the stock AuNP in Table 1. The results indicate that the AuNP did not aggregate as a result of incorporation into the calcium alginate NPD. Absence of aggregation was also indicated by the lack of a shoulder in the spectrum compared to the stock AuNP spectrum (Fig. 2.3).

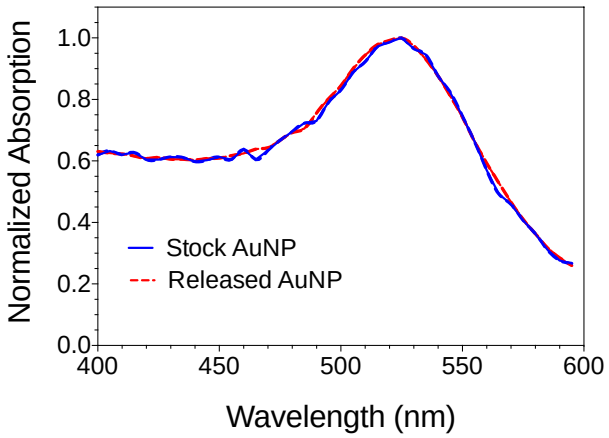

Figure 2.3 The UV-visible absorption spectrum for stock and NPD released AuNP. The normalized absorption, as a function of wavelength (nm), is plotted for 15 nm PEGylated stock AuNP (solid line) and AuNP released from a NPD composed of 6% w/v calcium alginate (dashed line).

Table 2.1 Absorption bands (λ_{max}) for stock AuNP and AuNP released from a nanoparticle depot (NPD). NPD were composed of 6% w/v calcium alginate.

AuNP size (nm)	Stock AuNP λ_{max} (nm)	Released AuNP λ_{max} (nm)
5	514.5 ± 0.2	516.0 ± 0.3
15	520.4 ± 0.2	520.8 ± 0.1
30	528.3 ± 0.1	527.5 ± 0.1
50	529.5 ± 0.5	527.0 ± 1.0

.

2.4.2 AUNP RELEASE IN A TISSUE-EQUIVALENT PHANTOM

Micro-CT was used to image the release of AuNP at different times from NPD composed of 6%, 8% or 10% w/v calcium alginate and incorporating 5, 15, 30 or 50 nm AuNP (9.5×10^{10}-9.5×10^{13} nanoparticles depending on AuNP size)

inserted into a tissue-equivalent phantom (Fig. 2.4a). The released AuNP concentration (mg/mL) was determined based on background corrected GLV with reference to a calibration curve (Fig. 2.4c). Representative micro-CT images of 30 nm AuNP in a NPD composed of different concentrations of calcium alginate with the GLV segmented by intensity (color scale) reveal differences in release rates at 7 days after insertion into the phantom (Fig. 2.4d). The release rates for each concentration of calcium alginate and AuNP size determined from the retention of AuNP within the NPD are compared in Fig. 2.5.

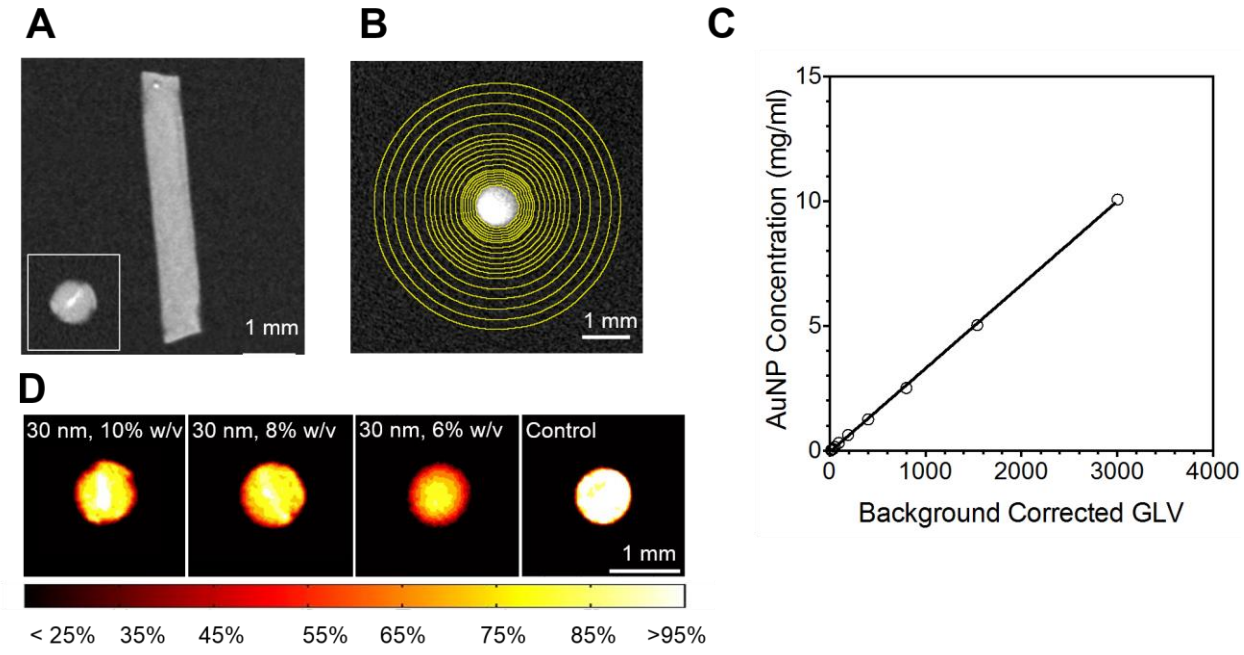

Figure 2.4 Evaluation of AuNP release from the NPD. (a) Micro-CT cross-sectional image of a 10% (w/v) calcium alginate NPD containing 30 nm AuNP at 7 days post implantation in a tissue-equivalent phantom. (b) A transverse cross-section of a 30 nm NPD illustrating region of interest (ROI) segmentation for measurement of diffused AuNP as a function of radial distance from the NPD. (c) A radiodensity curve obtained from scans of a calibration phantom containing air, water and increasing concentrations of AuNP, used to convert GLV to AuNP concentrations (mg/mL). (d) Cross sectional images of NPD (10%, 8% and 6% w/v calcium alginate) incorporating 30 nm AuNP at 7 days post implantation, after segmenting the GLV into radiodensity bins. The regions within the NPD containing different concentrations of AuNP are indicated by the color scale, where 100% represents the initial concentration (36.6 mg/mL). Note the difference in color between the control and 10%, 8% and 6% w/v calcium alginate NPD at 7 days. Difference between the use of 10%, 8% and 6% w/v calcium alginate appear minor.

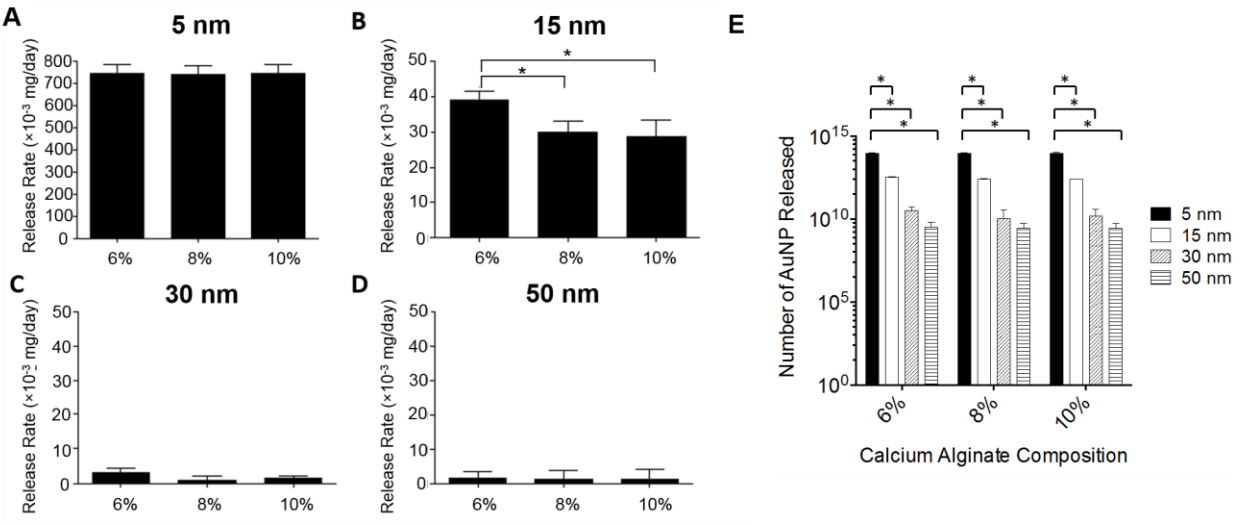

Figure 2.5 AuNP release rates (mg/day) for 6%, 8% or 10% w/v calcium alginate NPD for (a) 5 nm, (b) 15 nm, (c) 30 nm, or (d) 50 nm AuNP. Values shown represent the mean ± SEM (n=3) release rate (mg/day × 10^{-3}). Significant differences are indicated by the asterisks. Note the different y-axis scale for panel (a). The number of AuNP released at 3 days post implantation is also shown in (e) for the combinations of AuNP sizes and calcium alginate concentrations. Note the logarithmic y-axis scale. Significant differences ($P<0.05$) are indicated by asterisks.

NPD composed of lower concentrations of calcium alginate and smaller sized AuNP exhibited higher release rates (Fig. 2.5 a-d). The highest rate of release of gold was found for 5 nm AuNP incorporated into NPD with no significant differences between 6%, 8% or 10% w/v calcium alginate compositions (744 ± 41 ×10^{-3} vs. 743 ± 41 ×10^{-3} vs. 740 ± 41 ×10^{-3} mg/day). The NPD with the lowest release rates were those incorporating 50 nm AuNP (1.1 ± 2.7 ×10^{-3} mg/day to 1.3 ± 2.1 ×10^{-3} mg/day) which were not influenced by the calcium alginate concentration. Some significant differences were found for 15 nm AuNP incorporated into 6% vs. 8% and 6% vs. 10% w/v calcium alginate NPD. There were no significant differences between the release rates caused by varying the alginate concentration in NPD incorporating 30 nm AuNP. The initial number of AuNP loaded into the NPD were: 5 nm (9.5×10^{13} particles), 15 nm (3.5×10^{12} particles), 30 nm (4.4×10^{11} particles) and 50 nm (9.5×10^{10} particles). Based on the total number of AuNP released at 3 d (Fig. 2.5d), approximately 100%, 98%, 7% or 3.3% release of the total AuNP loaded into the NPD were released over this time period for 5 nm, 15 nm, 30 nm or 50 nm AuNP, irrespective of the alginate composition. These results indicated that AuNP release was controlled mainly by particle size.

2.4.3 AUNP SPATIAL DISTRIBUTION IN A TISSUE-EQUIVALENT PHANTOM

The diffusion of AuNP from the NPD into a tissue-equivalent phantom was modeled by Fick's diffusion law. To measure the diffusion coefficients, D_i, a series of images were obtained at various times with a digital camera of AuNP diffusing into a gel tunnel (Fig. 2.6a). Diffusion occurred inward from the ends of the tunnel, towards the center. Using Fick's

diffusion law (Fig. 2.6b), the D_i (Table 2) were determined by extracting M_t/M_∞ from the intensity profiles for different AuNP sizes in the tissue-equivalent gels (Fig. 2.6c). The results indicate that D_i decreases with increasing AuNP size.

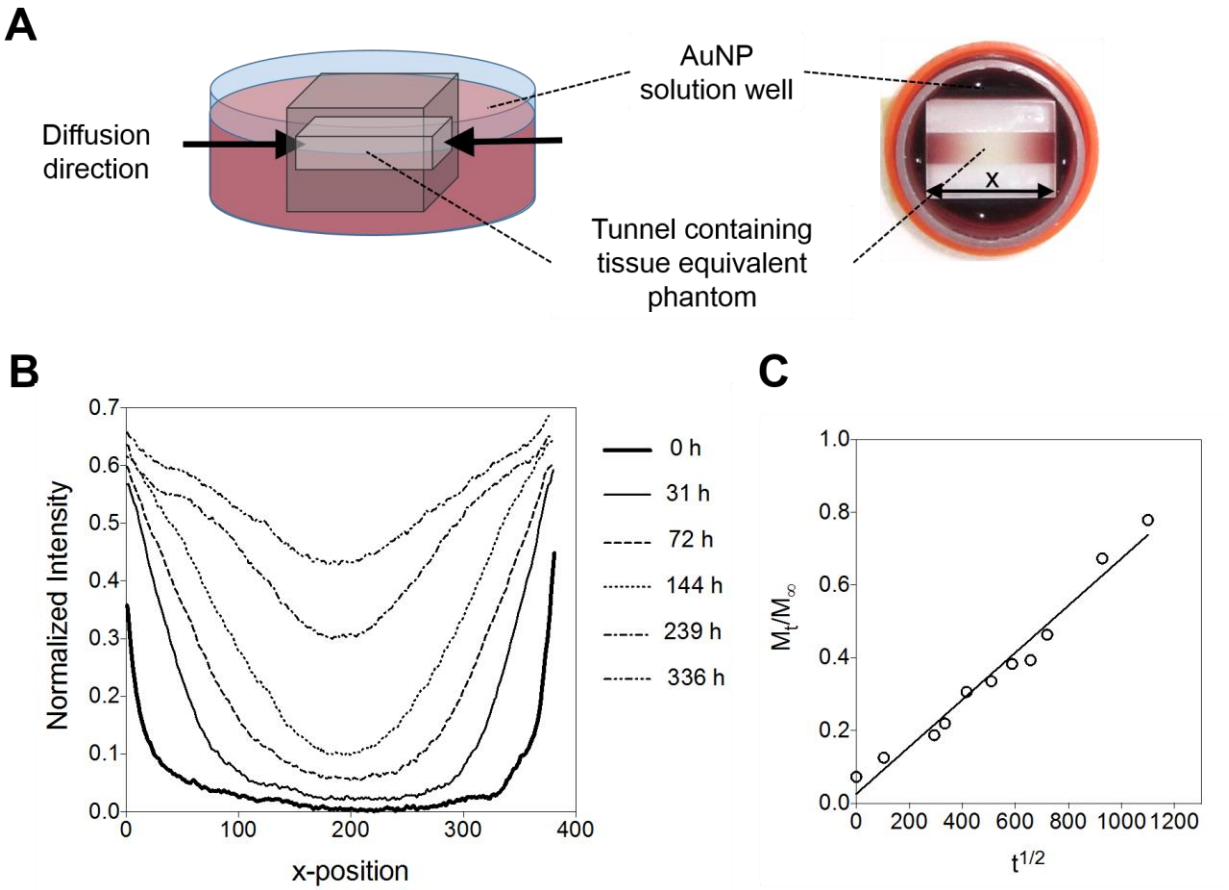

Figure 2.6 Overview of Fickian diffusion model. (a) Diffusion of AuNP into a tunnel in a tissue-equivalent gel phantom following submerging the tunnel in a well of AuNP solution. Digital images were obtained of the AuNP diffusing into the tunnel at various times. The color intensity profile of the tunnel at each time point was extracted using ImageJ software. (b) The intensity profile for Fickian diffusion modeling of 5 nm AuNP in a tissue-equivalent phantom, comparing normalized intensity vs. position (x-axis) along the tunnel at various times. The intensities were normalized to the maximum intensity. (c) The corresponding plot of M_t/M_∞ vs. $t^{1/2}$ for 5 nm AuNP (r=0.97). M_t is the mass of sorbed penetrant in the tunnel as a function of time (secs), t, compared to the saturation mass, M_∞. The diffusion coefficients (Table 2.2) were determined from the slope of the line using equation 2.3.

Table 2.2 Diffusion coefficients [D_i (cm^2/s)] for AuNP in a tissue equivalent phantom at 20°C.

AuNP size (nm)	D_i (cm^2/s)
5 nm	3.29×10^{-7}
15 nm	3.13×10^{-7}
30 nm	0.616×10^{-7}
50 nm	0.0445×10^{-7}

NPD inserted into the tissue-equivalent phantom are shown at days 1 and 7 after implantation. Released AuNP (red color) diffused into the phantom matrix are visualized surrounding the NPD at day 7. The radial distance of diffused AuNP released from the NPD was determined using D_i to approximate the boundary of AuNP infiltration into the phantom (Fig. 2.7b). Since conventional brachytherapy seeds are implanted into tissues about 1 cm apart, the minimum distance required for AuNP from two adjacent seeds to diffuse and occupy the space between two seeds is 5 mm. For the NPD incorporating 50 nm AuNP, the time for released particles to bridge this distance was very long (95 days) and not feasible, whereas smaller AuNP (5 nm and 15 nm) diffused to this radial distance in 3 days and 7 days, respectively (Fig. 2.7c) which are compatible with use of the NPD as delivery systems for AuNP. With sufficient time, AuNP diffused up to 4 cm from the surface of the NPD (Fig. 2.7b).

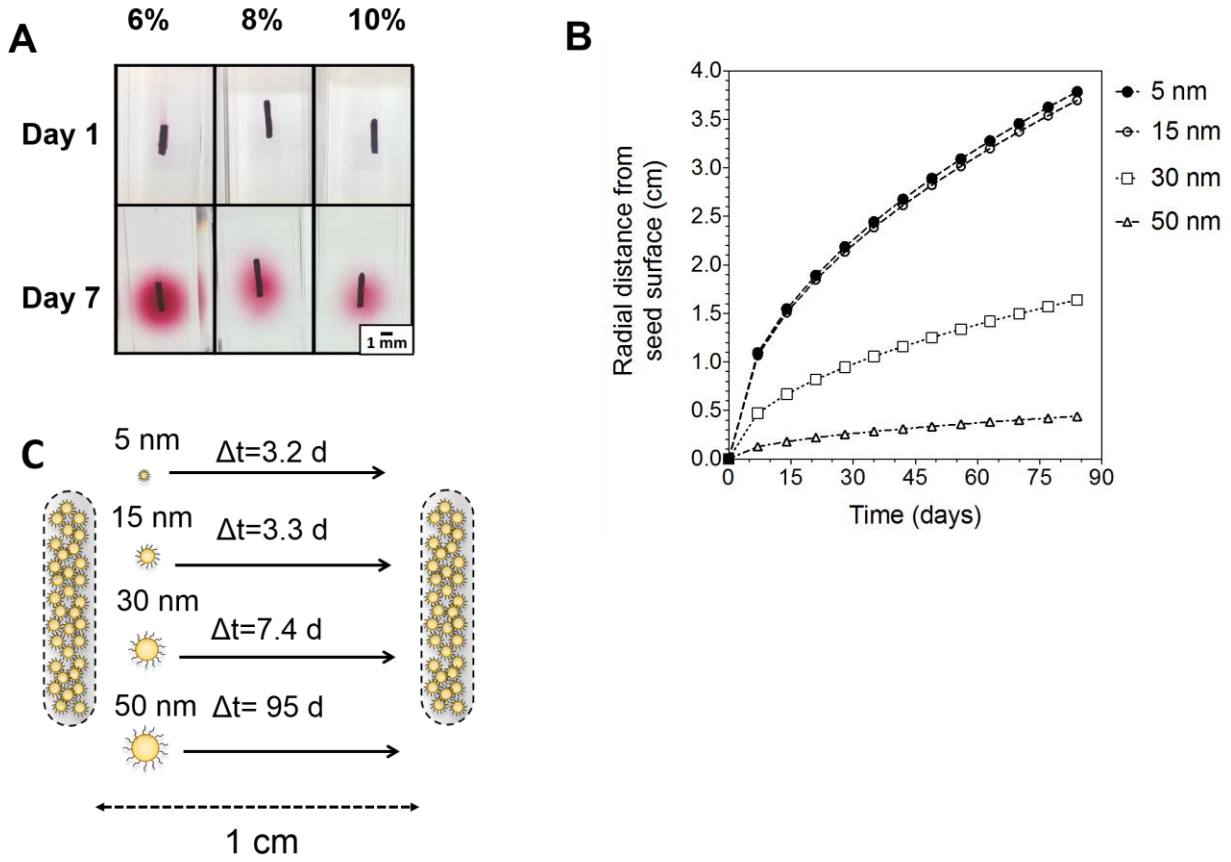

Figure 2.7 (a) Images of a NPD composed of 6%, 8%, and 10% w/v calcium alginate and incorporating 30 nm AuNP at day 1 and day 7 after implantation into a tissue-equivalent phantom. AuNP released from the NPD and diffused into the phantom matrix are evident by the red color surrounding the NPD at day 7. (b) The radial distance (cm) diffused by AuNP released from the NPD as a function of time (days) for 5 nm, 15 nm, 30 nm or 50 nm AuNP. (c) An illustration comparing the duration of time, Δt, required by AuNP of different sizes to diffuse half the distance (5 mm) between two adjacent NPD placed 1 cm apart.

The concentrations of AuNP diffused from the surface of the NPD in the phantom were determined by micro-CT image analysis using the average GLV to estimate gold concentrations in selected ROI (Fig. 2.4b) with reference to a radiodensity curve (Fig. 2.4b). These were compared to those calculated numerically by solving the Fickian diffusion model with the *pdepe* function in MATLAB using the experimentally-determined release rates and diffusion coefficients. The experimental and modeled results are shown in Figure 2.8. The concentration distribution of AuNP is represented in 1-dimension as a function of radial distance, where x=0 is the surface of the NPD. The times for which concentration profiles were analysed were 3 h for 5 nm, 45 h for 15 nm, and 7 days for 30 nm and 50 nm AuNP. While the 50 nm AuNP distributions were modeled correctly by Fick's diffusion law, there were some differences between modeled and experimental distributions for 5 nm, 15 nm, and 30 nm AuNP. This was most evident for the 5 nm AuNP for which Fick's law greatly under-predicts diffusion. The results suggest that computational modeling of diffusion may not be sufficient to predict the distribution of AuNP released from the NPD in a tissue-equivalent phantom, especially for small AuNP.

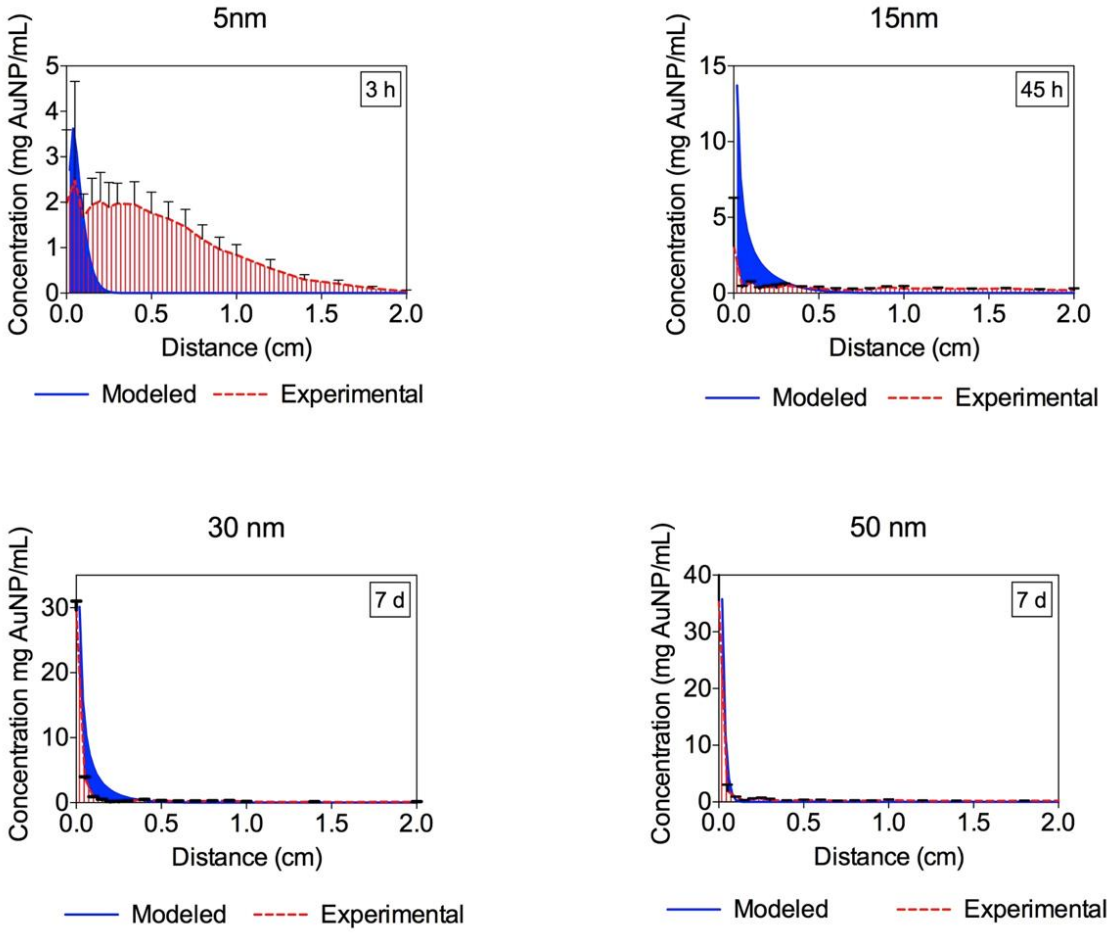

Figure 2.8 The concentration distribution of AuNP represented in 1-dimension as a function of radial distance. The experimentally determined distribution of AuNP measured by micro-CT (red vertical line filled curve) released from a 6% w/v calcium alginate NPD, expressed in AuNP concentration (mg/mL) at selected time points as a function of distance (cm) from the surface of the NPD (x=0) for AuNP sizes of (a) 5 nm, (b) 15 nm, (c) 30 nm, and (d) 50 nm. The

distribution modeled by Fick's law (blue solid filled curve) is shown for comparison using a reverse y-axis. Note that the only AuNP size where the experimental concentration distribution is well represented by the Fickian model is 50 nm.

2.4.4 AUNP RELEASE AND DIFFUSION IN A TUMOUR XENOGRAFT MODEL

NPD made from 6% (w/v) calcium alginate and incorporating 5 nm, 15 nm or 30 nm AuNP were implanted using the PSI technique into s.c. MDA-MB-231 human BC tumour xenografts in SCID mice (Fig. 2.2). The tumours were excised and imaged *ex vivo* using a micro-CT at 7 days post-implantation (Fig. 2.9a). AuNP release rates (Fig. 2.9b) were determined as described in section 3.2. The release rates in the tumour followed the same trend as in the phantoms, with 5 nm AuNP demonstrating the most rapid release followed by 15 nm and 30 nm AuNP. However, AuNP release from the NPD implanted into tumours occurred much slower than in the phantom model (64.3 times, 7.0 times and 2.6 times slower for 5 nm, 15 nm and 30 nm AuNP, respectively). The percentage of AuNP release for each concentration of calcium alginate and AuNP size determined from the retention of AuNP within the NPD when implanted into phantoms and into tumours are compared in Figure 2.10. The uptake ratio of AuNP in the tumours, calculated as the ratio of the average GLV in the tumour to the average GLV in the NPD, were 1.0 ± 0.0, 0.65 ± 0.03, and 0.353 ± 0.003 for 5 nm, 15 nm and 30 nm respectively. An uptake ratio of 1.0 indicates that the average AuNP concentrations in the nandepot and surrounding tumour tissue are equivalent and have reached equilibrium with maximal AuNP release. Thus, concentrations of AuNP in the NPD and tumour tissue equilibrated more rapidly for 5 nm AuNP than 15 nm or 30 nm AuNP. Silver enhancer staining (SES) was used to assess the local regional distribution of AuNP in the tumour. The distributions of AuNP in representative tumours are shown in Figure 2.9c for 5 nm, 15 nm or 30 nm AuNP incorporated into a 6% calcium alginate NPD. Based on the staining observed, there was heterogeneous intratumoural distribution of AuNP, unlike that found in the phantom model. The percent positive staining in tumour sections is summarized in Figure 2.9d. Tumours implanted with a NPD incorporating 5 nm AuNP demonstrated the highest percentage of staining and most homogeneous staining, although not all of the tumour area was occupied by AuNP.

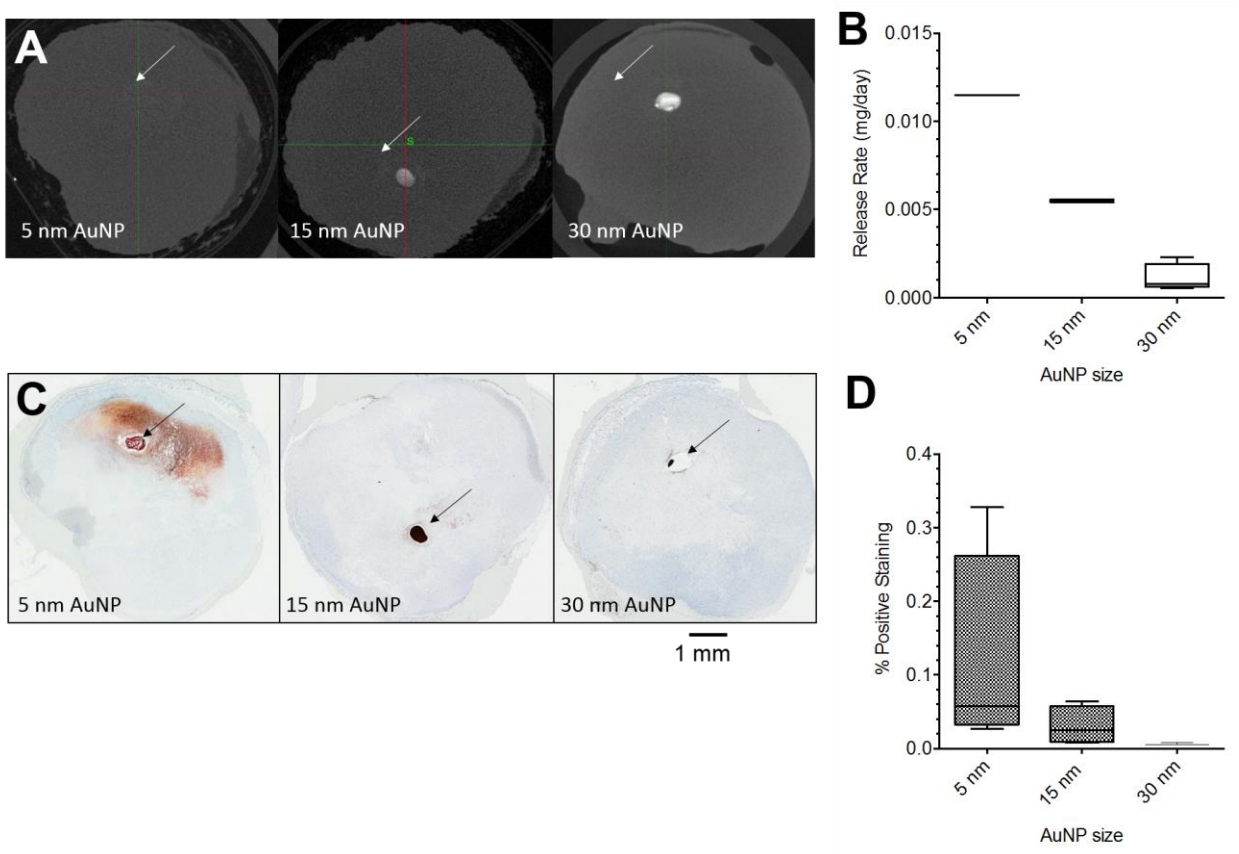

Figure 2.9 AuNP release and distribution *in vivo*. (a) Micro-CT cross sectional image of a tumour implanted with a NPD incorporating 5 nm, 15 nm or 30 nm AuNP (left to right). For sections with the NPD incorporating 15 nm or 30 nm AuNP the NPD was visualized as a bright radiodense focus due to retention of the AuNP, whereas due to release of the 5 nm AuNP, the NPD is not observed. (b) The release rate of AuNP (mg/day) for each AuNP size. (c) Silver enhancer staining (SES, brown color) of sections from tumours implanted with a NPD incorporating 5 nm, 15 nm or 30 nm AuNP (left to right). (d) Percent of tumour section exhibiting positive staining by SES. Error bars represent the standard deviation. Note the difference in AuNP distribution, as indicated by staining in (c), in tumours implanted with 5 nm, 15 nm and 30 nm AuNP.

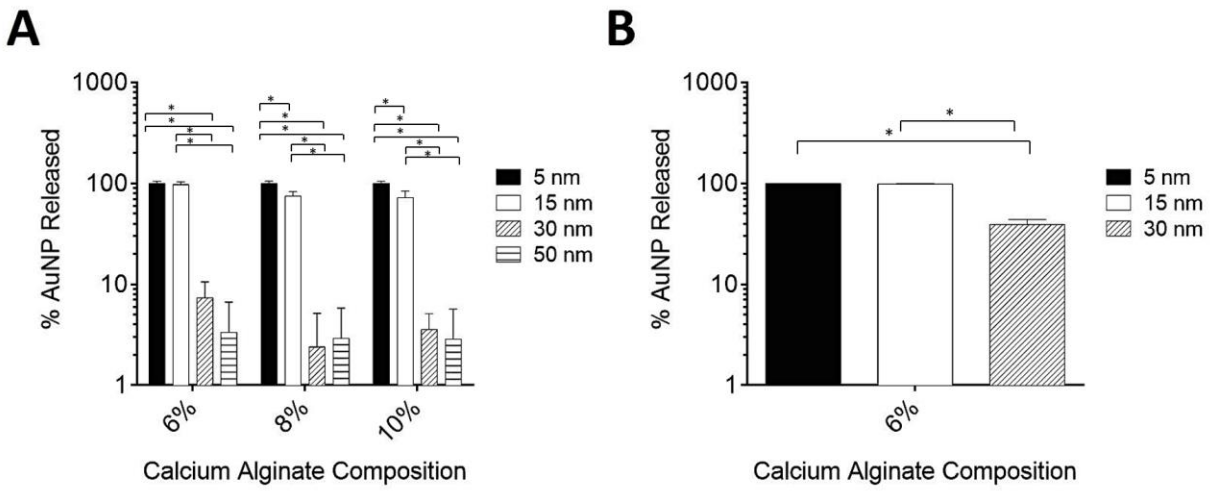

Figure 2.10 Percentage of AuNP released in a phantom and *in vivo*. (a) Percentage of AuNP release for NPD composed of 6%, 8% or 10% w/v calcium alginate for 5 nm, 15 nm, 30 nm, and 50 nm AuNP at 7 d post implantation in a tissue equivalent phantom. (b) Percentage of AuNP release for 6% w/v calcium alginate NPD for 5 nm, 15 nm, and 30 nm AuNP at 7 d post implantation in a tumour xenograft in a mouse. The error bars represent the standard deviation and significance is denoted by the asterisks ($P<0.05$). Note that there were no observable differences between 6%, 8% or 10% w/v calcium alginate composition, indicating that AuNP size is the main determinant influencing AuNP release.

2.5 DISCUSSION

We report here for the first time, the design and evaluation of a NPD system that provides controlled local release of AuNP and permits precise implantation into a tumour by adapting existing clinically used PSI brachytherapy techniques. NPD were constructed from different concentrations of calcium alginate (6%, 8% or 10% w/v) and incorporated a wide range of AuNP sizes (5 nm, 15 nm, 30 nm or 50 nm). The release of AuNP from the NPD and their local diffusion was studied in a tissue-equivalent phantom by micro-CT and modeled by Fick's diffusion law, as well as examined experimentally in a human BC tumour xenograft mouse model following implantation by PSI techniques. The results of the phantom study revealed that the calcium alginate concentration used to construct the NPD was not a major factor influencing AuNP release, but release was highly dependent on AuNP size. The highest release rates were noted for 5 nm and 15 nm AuNP and very slow release rates were found for 30 nm and 50 nm AuNP (Figs. 2.5 and 2.7). These results suggest that the microstructure of the NPD may be similar at all concentrations of calcium alginate studied. No previous reports have examined the release of AuNP from a calcium alginate matrix, but the release rate of other encapsulated materials is dependent on the matrix porosity and molecular weight of the materials (Huguet and Dellacherie, 1996). The pore size for matrices formed of 3-7% w/v calcium alginate has been reported to range from 12-16 nm (Klein et al., 1983). The slow release of 30 nm and 50 nm AuNP from the NPD in our study which were composed of 6-10% w/v calcium alginate, suggests that the pore size may be similar, permitting rapid release of 5 nm or 15 nm AuNP, but restricting the release of larger sized AuNP. It may be possible to further modify the release of 5 nm and 15 nm AuNP by decreasing the concentration of calcium alginate, which has been

demonstrated in other studies increase the pore-length and number of pores available (Cheetham et al., 1979) while maintaining the pore diameter (Hannoun and Stephanopoulos, 1986).

In addition to release rate, an important consideration is the diffusion and spatial distribution of AuNP released from the NPD. In the tissue-equivalent phantom, modeling of AuNP diffusion revealed a major decrease in gold concentrations at distances >0.5 cm from the NPD for all sizes of AuNP (Fig. 2.8). Nonetheless, the 5 nm AuNP diffused the greatest distance, while 30 nm and 50 nm AuNP exhibited only minor diffusion from the surface of the NPD. These results are similar to those reported by Sinha et al., who created a theoretical model to study the intratumoural distribution of AuNP delivered by PLGA brachytherapy spacers following implantation into a tumour (Sinha et al., 2015). PLGA spacers are intended to be implanted during PSI brachytherapy, similar in concept to NPD, to facilitate release of AuNP but with the aim of providing enhancement for external beam radiation therapy. They showed that 10 nm AuNP diffused less than 5 mm from the PLGA spacer at 1 day or 5 days after implantation. Nonetheless, they predicted sufficient gold concentrations at 5 mm to achieve at least 20% dose-enhancement.

Modeling is often the primary approach to achieve an understanding of AuNP distribution in a tumour (Kim et al., 2013) but it oversimplifies the complexity of the diffusion process. We compared the modeled AuNP distribution to the experimental AuNP distribution measured by micro-CT in a tissue-equivalent phantom (Fig. 2.8). The experimental distribution showed a decrease in AuNP concentration with increasing distance as predicted by Fick's diffusion law, but the distribution displayed some major differences, especially for 5 nm AuNP (Fig. 2.8a), and there were some heterogeneities noted by the non-smooth distribution of the 15 nm AuNP (Fig. 2.8b) suggesting that there are added complexities in AuNP transport that were not accounted for in the diffusion model. The tissue-equivalent phantom used in this study is a well-established surrogate for examining the diffusion of drugs and nanoparticles in human tissues (Chen et al., 2002, Salloum et al., 2008) but our results suggest that further evaluation in an *in vivo* tumour model is warranted to fully understand the spatial distribution of AuNP.

The intra-tumoural transport of AuNP is expected to vary depending on the physiological and morphological characteristics of the tumour and surrounding stroma (Netti et al., 2000). These may affect the percolation of AuNP within the tumour interstitial space. The results from the *in vivo* study conducted here revealed 2.6-64.4 fold slower release rates for AuNP in a tumour compared to the tissue-equivalent phantom as well as some heterogeneities in AuNP distribution around the NPD visualized by SES, especially for 5 nm AuNP (Fig. 2.9). These heterogeneities reflect the complexity of tumour tissue and how transport of AuNP may not be accurately modeled by simple diffusion. In fact, several studies investigating systemic administration of nanoparticles suggest that the main mechanism of particle transport is convection from interstitial fluid flow, which is highly dependent on the interstitial fluid pressure (IFP) (Stapleton and Milosevic, 2013, Stapleton et al., 2013, Eikenes et al., 2005). In addition, heterogeneities in IFP have been found in tumours, contributing to non-uniform nanoparticle distribution (Stapleton et al., 2015). Sykes et

al. demonstrated that parameters such as extracellular matrix content, vascularity, and cell density, all affect AuNP transport into tumours following systemic administration, and they proposed that the properties of AuNP, in particular their size should be tailored to the tumour physiology to optimize their transport (Sykes et al., 2016). The NPD described here provides an opportunity to study the effect of AuNP characteristics and tumour physiology on the local diffusion of AuNP *in vivo* in a tumour xenograft mouse model, following implantation by PSI techniques.

Based on the more rapid (Fig. 2.5) and complete release of 5 nm AuNP (Fig. 2.10) and greater and more homogeneous diffusion of these particles from the NPD surface (Fig. 2.8), we believe that this size of AuNP would be most feasible for local intratumoural delivery with the NPD system. Since the calcium alginate concentrations did not influence the release characteristics of AuNP from the NPD, concentrations ranging from 6% to 10% w/v are suitable for constructing the NPD. All of these concentrations provided sufficient stiffness for the NPD to be implanted into a phantom or tumour by PSI techniques. Our previous studies of panitumumab-modified ^{177}Lu-AuNP injected i.t. for local treatment of tumours (Yook et al., 2016a) employed 30 nm AuNP. However, it should be possible to decrease the size of these ^{177}Lu-AuNP for incorporation into the NPD, since Jiménez-Mancilla et al. radiolabeled 5 nm AuNP conjugated to bombesin peptides with ^{99m}Tc or ^{177}Lu (Jimenez-Mancilla et al., 2013). The time required for 5 nm AuNP to traverse the distance between two NPD placed 1 cm apart (3.2 days; Fig. 2.7c) to maximize homogeneity in tissue diffusion is compatible with the physical half-life of ^{177}Lu (6.6 days). Implantation of multiple NPD into tumours in patients combined with local release of ^{177}Lu-AuNP will minimize any heterogeneities in radiation dose deposition

2.6 CONCLUSION

We conclude that a NPD system composed of 6% to 10% calcium alginate and incorporating 5 nm AuNP provides the most rapid release and diffusion of AuNP in a tissue-equivalent phantom *in vitro* or *in vivo* in a human BC tumour xenograft model. Modeling of the release and diffusion of AuNP using Fick's diffusion law did not accurately predict the diffusion of AuNP from the NPD in a tissue-equivalent phantom and did not predict heterogeneities observed experimentally in the phantom or in a tumour. The precise intratumoural placement of the NPD using clinically used PSI techniques should enable advancement of local treatment of tumours with ^{177}Lu-labeled AuNP provided that the size of these AuNP is decreased to 5 nm. The NPD system should be widely applicable to local tumour treatment using other AuNP-based therapeutic agents.

2.7 ACKNOWLEDGEMENTS

This study was supported by a grant from the Canadian Breast Cancer Foundation (CBCF), Ontario Region, to R.M. Reilly and J.P. Pignol. P. Lai is supported by an Alexander Graham Bell Canada Graduate Scholarship from the Natural Sciences and Engineering Research Council of Canada (NSERC). The authors would like to acknowledge Emily Wong, Sai Bala, and Ahmed El-Falou from the laboratory of Dr. Gregory Czarnota, as well as Harry Easton from the Medical Physics Machine Shop at Sunnybrook Health Sciences Centre for their contributions to this study.

CHAPTER 3

3 MONTE CARLO SIMULATION OF RADIATION TRANSPORT AND DOSE DEPOSITION FROM GOLD NANOPARTICLES LABELED WITH ^{111}IN, ^{177}LU OR ^{90}Y

Adapted from: Priscilla Lai, Zhongli Cai, Jean-Philippe Pignol, Eli Lechtman, Shahram Mashouf, Yijie Lu, Mitchell A. Winnik, David A. Jaffray, Raymond M. Reilly. (2017) Monte Carlo simulation of radiation transport and dose deposition from locally released gold nanoparticles labeled with ^{111}In, ^{177}Lu or ^{90}Y incorporated into tissue implantable depots. *Phys Med Biol,* 62**,** 8581-8599.

3.1 ABSTRACT

Permanent seed implantation brachytherapy is a highly conformal form of radiation therapy but is challenged with dose inhomogeneity due to its utilization of low energy radiation sources. Gold nanoparticles conjugated with electron emitting radionuclides have recently been developed as a novel form of brachytherapy and can aid in homogenizing dose through physical distribution of radiolabeled AuNP when injected i.t. in suspension. However, the distribution is unpredictable and precise placement of many injections would be difficult. Previously, we reported the design of a NPD that can be implanted using PSI techniques and which facilitates controlled release of AuNP. We report here the 3D dose distribution resulting from a NPD incorporating AuNP labeled with electron emitters (^{90}Y, ^{177}Lu, ^{111}In) of different energies using Monte Carlo based voxel level dosimetry. The MCNP5 Monte Carlo radiation transport code was used to assess differences in dose distribution from simulated NPD and conventional brachytherapy sources, positioned in breast tissue simulating material. We further compare these dose distributions in mice bearing subcutaneous human breast cancer xenografts implanted with ^{177}Lu labeled AuNP (^{177}Lu-AuNP) in a NPD, or injected i.t. with ^{177}Lu-AuNP in suspension. The radioactivity distributions were derived from registered SPECT/CT images and time-dependent dose was estimated. Results demonstrated that the dose distribution from NPD reduced the maximum dose 3-fold when compared to conventional seeds. For simulated NPD, as well as NPD implanted *in vivo*, ^{90}Y delivered the most homogeneous dose distribution. The tumour radioactivity in mice i.t. injected with ^{177}Lu-AuNP redistributed while radioactivity in the NPD remained confined to the implant site. The dose distribution from radiolabeled AuNP NPD were predictable and concentric in contrast to i.t. injected radiolabeled AuNP, which provided irregular and temporally variant dose distributions. The use of NPD may serve as an intermediate between PSI and radiation delivered by radiolabeled AuNP by providing a controlled method to improve delivery of prescribed doses as well as homogenize dose from low penetrating electron sources.

3.2 INTRODUCTION

Radiation treatment of BC is important for preventing progression of early stage disease and recurrence (Early Breast Cancer Trialists' Collaborative et al., 2011). Although the current standard of care for breast radiotherapy is external beam radiation, brachytherapy has proven to be an effective alternative with nearly equivalent long term survival rates (Strnad et al., 2016, Smith et al., 2012, Pignol et al., 2015) and the added benefit of convenience due to the accelerated treatment time (Smith et al., 2009). Permanent brachytherapy sources, or seeds, conventionally comprises low energy photon emitting radioisotopes encapsulated in titanium housing. The resulting dose distribution is highly conformal allowing dose escalation while maintaining normal tissue sparing. However, dose conformity allowed by the localized attenuation of photons inherently results in regions of high dose particularly for tissues in close proximity to the seed, which is disadvantageous if the exposed tissues involve critical structures.

An innovative approach that has been proposed to extend current BC brachytherapy is the use of radiolabeled AuNP that can be deposited locally in tissues. In this proposed treatment, radiolabeled AuNP in suspension are i.t. injected. Radiotherapeutic AuNP may improve the therapeutic window of brachytherapy (tumour control ratio to normal tissue toxicity) by allowing the use of more conformal radiations (i.e. electrons, α particles) as well as provide opportunities to exploit individual cancer phenotypes by AuNP surface modifications with targeting ligands (Ehlerding and Cai, 2016, Vilchis-Juarez et al., 2014, Yook et al., 2015b). In addition, due to the ability of radiolabeled AuNP to migrate through tissue, the dose distribution from brachytherapy can be homogenized by lowering high dose regions. There is considerable preclinical evidence that supports local i.t. administration of radiolabeled AuNP as a novel form of cancer treatment (Yook et al., 2016a, Ehlerding and Cai, 2016, Vilchis-Juarez et al., 2014). In a recent study by Yook et al. single i.t. injections of EGFR targeted ^{177}Lu-AuNP (4-5 MBq) were administered in mice bearing MDA-MB-468 s.c. tumours dramatically decreasing tumour growth by 30-fold compared to controls (Yook et al., 2016a). However, this study also showed heterogeneous intratumoural distribution of i.t. injected ^{177}Lu-AuNP resulting in large variation in dose deposition, revealing that a method for precise placement and controlled intratumoural delivery of radiolabeled AuNP is necessary to minimize these heterogeneities and improve clinical applicability (Yook et al., 2016a). Clinical treatment of human tumours, which are much larger, would require multiple injections of radiolabeled AuNP that may distribute unpredictably. This would not be feasible during dose planning and could have an impact on therapeutic response if some tumour regions receive lower than the prescribed dose (Ehlerding and Cai, 2016). To improve the feasibility of brachytherapy treatment of tumours using radiolabeled AuNP, we recently reported the design of a NPD into which AuNP can be incorporated and which can be precisely positioned using PSI techniques, where the NPD enables slow release of AuNP into the surrounding tumour (Lai et al., 2016). These NPD formed from calcium alginate have dimensions and shape similar to conventional permanent brachytherapy seeds and were used to incorporate AuNP of various sizes (5, 15, 30 and 50 nm). In tissue equivalent phantoms and *in vivo* in tumour xenografts in mice, these NPD demonstrated highly localized and concentric distributions of AuNP. In the context of dosimetry, the NPD provides a way to spatially design and administer prescription doses of radiolabeled AuNP,

allowing for the precision of conventional brachytherapy while offering the potential advantage of homogenizing dose through local diffusion of radioactivity.

There are two components that influence the dose deposition from NPD: the distribution of nanoparticles through tissue, and the transport of radiation from the nanoparticles. The first objective of the present study was to compare differences in dose distributions between simulated single NPD and conventional brachytherapy seeds, and multi NPD/seed arrays that replicate clinical seed loading approaches in brachytherapy, resulting from AuNP redistribution. The second objective was to compare electron emitters of varying energies and penetration range (^{90}Y: 0.93 MeV (mean, β^-), 1.1 cm penetration range, ^{177}Lu: 0.13 MeV (mean, β^-), 0.17 cm penetration range, and ^{111}In: 0.18 MeV (mean, internal conversion electron), 0.93 keV (mean, Auger electron), 0.06 cm penetration range) using Monte Carlo generated voxel dose kernels (VDK) and previously modeled distributions of AuNP released from the NPD (Lai et al., 2016). Three dimensional dosimetry was also performed on radioactivity distributions derived from SPECT images of mice bearing s.c. MDA-MB-231 human breast cancer xenografts implanted i.t. with a single NPD incorporating ^{177}Lu-AuNP, or directly injected i.t. with ^{177}Lu-AuNP. This is the first time that the dose distribution from radiolabeled AuNP released locally from a NPD has been modeled using Monte Carlo methods and image-based biodistribution data from *in vivo* mouse tumour xenograft models.

3.3 MATERIALS AND METHODS

3.3.1 CONSTRUCTION OF ^{177}LU-AUNP AND NPD

^{177}Lu-AuNP were constructed by coating 15 nm AuNP (Ted Pella, Redding, CA) with a diblock copolymer containing a polyethylene glycol (PEG; 2 kDa) block and a block of polyglutamide with 8 pendant 1,4,7,10-tetraazacyclododecane-1,4,7,10-tetraacetic acid (DOTA) chelators for complexing ^{177}Lu and 4 terminal lipoic acid (LA) groups [PEG-*p*Glu(DOTA)$_8$-LA$_4$] that permitted multithiol conjugation to the AuNP surface (Yook et al., 2016b). PEG-*p*Glu(DOTA)$_8$-LA$_4$ (3 μg) was labeled by incubation with 10 MBq of ^{177}LuCl$_3$ (PerkinElmer, Akron, OH) in 1 mL of 1 M sodium acetate buffer (pH 5.5) at 80˚C for 30 mins. PEG-*p*Glu(DOTA)$_8$-LA$_4$-^{177}Lu was then linked to AuNP (1 mL, 1.40×10^{12} particles) by incubation at 60˚C with gentle shaking for 1 h in low binding microcentrifuge tubes (Axygen Scentific, Union City, CA). ^{177}Lu-AuNP were purified from unconjugated PEG-*p*Glu(DOTA)$_8$-LA$_4$-^{177}Lu by ultracentrifugation at 15,000 × g for 45 min at 4˚C, carefully removing the supernatant and resuspending in 1 mL of d.d. H_2O. This procedure was repeated twice. NPD that incorporated ^{177}Lu-AuNP were formed as previously reported using very low viscosity (VLV <20 mPa) ultrapure medical grade sodium alginate (Pronova™ NovaMatrix, Sandvika, Norway) with high guluronate (G) residue content, crosslinked in 10% calcium chloride in d.d. H_2O (Lai et al., 2016). The final radioactivity contained in each NPD, incorporating 0.12 mg (3.52×10^{15} particles) of ^{177}Lu-AuNP, was 2-3 MBq. The PEGylation density of ^{177}Lu-AuNP was approximately 57 PEG-*p*Glu(DOTA)$_8$-LA$_4$-^{177}Lu per AuNP and was determined as previously reported by Yook *et alet al* (Yook et al., 2016b).

3.3.2 ANIMAL MODEL

The MDA-MB-231 human breast adenocarcinoma cell line (ATCC, Manassas, VA) was cultured at 37 °C in 5% CO_2 in DMEM supplemented with 5% penicillin/streptomycin antibiotics and 10% fetal bovine serum (Gibco-Invitrogen, Carlsbad, CA). Approximately 2×10^6 cells suspended in 50 µL of PBS were injected s.c. into the right flank of female CB-17 scid mice (Charles River Laboratories, Boston, MA) using a 1 mL syringe fitted with a 27 gauge (27G) needle. Tumour xenografts were permitted to grow to a diameter of 10 mm prior to implantation of a single NPD incorporating ^{177}Lu-AuNP or direct i.t. injection of ^{177}Lu-AuNP. NPD implantation into the tumours was carried out as previously reported using a template mounted stage (Lai et al., 2016). During implantation and i.t. injection, mice were anesthetized using 2% oxygen ventilated isoflurane. For i.t. injection, ^{177}Lu-AuNP (2-3 MBq, 3.52×10^{15} particles) suspended in 50 µL of d.d. H_2O were injected using a 28G½" 1 mL insulin syringe. Injections were carried out slowly and pressure placed on the injection site to reduce backflow. Mice requiring NPD implantation were restrained on the template mounted stage (see (Lai et al., 2016) for details). Briefly, an 18G seeding needle (Eckert & Ziegler. Oxford, CT) was manually loaded with a single NPD and the template was used to stabilize the needle during NPD insertion. Seeding needles were positioned such that the length of the NPD ran parallel to the leg, and the NPD was centered in the tumour. Only one NPD was implanted per tumour. All animal studies were conducted in compliance with Canadian Council on Animal Care (CCAC) regulations and were performed under a protocol approved by the Animal Care Committee at the University Health Network (AUP #2780).

3.3.3 SMALL ANIMAL SPECT/CT IMAGING

Mice bearing s.c. MDA-MB-231 tumour xenografts were imaged using a small animal SPECT/CT (NanoSPECT tomograph; Bioscan, Washington, DC) at 1, 24, 48 h and 7 d post implantation of the NPD incorporating ^{177}Lu-AuNP or post i.t. injection of ^{177}Lu-AuNP. The acquisition time was increased from 150 s/projection at 1 h p.i. to 309 s/projection at 7 d p.i. to compensate for radionuclide decay. SPECT images were collected using a 0.3 mm × 0.3 mm × 0.3 mm voxel size (82 projections, 10% energy window at 208 keV/113 keV/57 keV, 4 subsets (per each detector), OSEM reconstruction, no attenuation correction, and noise suppression). Cone-beam CT images were collected using a 0.2 mm × 0.2 mm × 0.2 mm voxel size (45 kVp, 126 projections (1 s/projection), Fast Cone Beam FBP reconstruction, FBP filter was Shepp-Logan with 50% cutoff frequency). The SPECT and CT (DICOM) images were registered using InvivoScope software (Bioscan). The SPECT images between each time point were registered using a combination of manual and automatic rigid registration methods on Inveon Research Workplace software (Siemens Healthcare GmbH, Henkestraße, Germany). The linearity of radioactivity measurement by volume-of-interest (VOI) analysis of the SPECT images was verified by examining the number of counts detected in the VOI and the known radioactivity of ^{177}Lu. This was achieved by imaging serial dilutions of ^{177}Lu in 0.5 mL Eppendorf tubes containing 30 µL of a solution of known amounts of radioactivity under the same conditions, over a wide range that included the radioactivity used in the experiments.

3.3.4 MONTE CARLO SIMULATION

The transport and energy deposition of radionuclide emissions was simulated using Monte Carlo N-Particle software (MCNP 5, Los Alamos National Security, New Mexico) and voxel based geometry methods. The ITS (Integrated TIGER Series) energy indexing mode (DCBN 18 card = 1) was used. The accuracy of MCNP calculations using ITS mode has been demonstrated in a number of other studies (Chibani and Li, 2002, Reynaert et al., 2002). The continuous-slowing-down-approximation (CSDA) range, denoted here by R_{CSDA}, is the average path length travelled by the electrons. Three radionuclides were chosen to represent long-range (^{90}Y, R_{CSDA}=1.1 cm), mid-range (^{177}Lu, R_{CSDA}=0.17 cm) and short-range (^{111}In, R_{CSDA}=0.06 cm) electron emitters, however all radiation types (photons, β, Auger electron (AE), and internal conversion electron (IE)) were considered for each radionuclide. A detailed summary of the emission spectra for ^{90}Y, ^{177}Lu, and ^{111}In is included in the Supplemental Material (Table B 1). The radiation spectra for these radionuclides were obtained from Medical Internal Radiation Dose (MIRD) Radionuclide Data (Eckerman and Endo, 2008). VDK were calculated as the sum of the contributions from each radiation type, weighted by the abundance of each radiation type emitted per decay.

The cubic voxel geometry used for simulation was comprised of voxel sizes of 0.3×0.3×0.3 mm^3, or 0.3 mm voxel edge length (VEL) for our application, and 3.0×3.0×3.0 mm^3, or 3 mm VEL for validation of the Monte Carlo model by comparison to S values published by Bolch et al. (^{90}Y) in MIRD pamphlet no. 17 and by Lanconelli *et alet al* (^{90}Y and ^{177}Lu) (Lanconelli et al., 2012, Bolch et al., 1999). Note that the ^{111}In VDK was not compared with these methods due to a lack of published data. For the 0.3 mm VEL geometry, the VDK were calculated out to distances such that the range of the kernel would contain over 99.9% of the energy deposition by the source (1.1 cm). The 3 mm VEL dose kernels were depicted up to distances of 2.6 cm from the source for comparison with published data (Lanconelli et al., 2012, Bolch et al., 1999). The source voxel (coordinates (i, j, k) = (0, 0, 0)), modelled as isotropic, was homogenously distributed with ^{90}Y, ^{177}Lu, or ^{111}In. The region inside of the cubic geometry was filled with breast tissue (BT) material (ρ=1.02 g/cm^3) (ICRU, 1989). The region outside of the cubic geometry was a larger cube of BT centered at the origin, sufficient to allow for particle backscatter. A total of 100 million particles were tracked and the energy deposition (MeV) in each voxel per particle was tallied. The S values were determined by converting the energy deposition per particle (MeV/particle) in each voxel to mGy/MBq·s. Relative statistical errors (RSE) as low as 0.01% were achieved and the mean RSE was 8.25% for the 0.3 mm VEL kernels, and 11.4% for the 3 mm VEL kernels. For electron energies below 1 keV energy cut-off, the energy deposition was assumed to occur entirely within the source voxel.

Additionally, for MCNP calculations using 0.3 mm VEL, a material composition of 0.3% gold (Au) and 99.7% BT (ICRU) (Au + BT) (1.077 g/cm^3) was used in place of BT alone to simulate the potential effects of the presence of the Au on radiation transport and dose deposition. The percentage of Au used was selected from the concentration of AuNP in the NPD (37.5 mg AuNP/mL, equivalent to 0.3% Au) and represents a maximum effect scenario in which these high concentrations of AuNP are located in every voxel. Practically, the concentrations of AuNP will vary based on the

location of the voxel relative to the NPD due to release and tissue diffusion of AuNP. Our previous study demonstrated that tissue concentrations of AuNP were much lower than in the NPD, decreasing to 0.03% Au, or 10% of the NPD concentration, at 0.1 cm from the NPD surface. Every voxel (S_r) (mGy/MBq·s) in each kernel was normalized to the corresponding source voxel (S_0) (mGy/MBq·s), and averaged with other voxels with the same source-to-voxel distance (r). The relative difference (RD) was calculated using the formula $100\times(S_{r,Au+BT} - S_{r,BT})/S_{r,BT}$, where $S_{r,Au+BT}$ is the voxel value at distance r, in the Au + BT kernel and $S_{r,BT}$ is the corresponding voxel value in the BT kernel.

3.3.5 NPD AND CONVENTIONAL SEED SIMULATION

To study the temporal dependence of dose distribution from transport of AuNP released from the NPD, a 21×21×21 array (6.3×6.3×6.3 mm^3 volume) was created containing a simulated NPD at the center with dimensions of 2×2×13 voxels (0.6×0.6×3.9 mm^3) using MATLAB (Mathworks, Natick, MA). The spatial distribution of radioactivity inside and around the NPD at various times (0, 14, 28, 42, and 56 h) was simulated using our previously published AuNP concentration profiles (Lai et al., 2016). One-dimensional AuNP concentration profiles (mg/mL of AuNP per unit distance) were converted to discretized radioactivity spatial distributions by assuming isotropic AuNP distribution and pre-defined specific activities of AuNP for ^{90}Y (14.9 MBq/mg AuNP), ^{177}Lu (20.8 MBq/mg AuNP), and ^{111}In (209.5 MBq/mg). These corresponded to 1.8, 2.5, and 25.1 MBq for ^{90}Y, ^{177}Lu, and ^{111}In, respectively, incorporated into the NPD. These initial radioactivity values were chosen such that the average integral dose delivered by each radionuclide in the simulated volumes would be the same (120 Gy). A conventional seed was also simulated using the same activity of ^{90}Y and dimensions of the NPD, but all radioactivity remained within the dimensions of the seed at all time points. The spatial distribution of dose rate at each time point was determined by convolving the VDK with the radioactivity spatial distributions, and was plotted in one dimension (dose-rate vs. distance). The total dose delivered to each voxel was calculated by integrating the dose rate (Gy/s) in each voxel as a function of time, t, from t=0 to t=56 h using the trapezoidal rule, and then integrating from t=56h to t=∞, assuming only radioactive decay.

A multi-NPD and multi–seed array was also created with four NPD/seeds spaced 4.5 mm apart (center-to-center) in a square formation, to simulate the radioactivity and dose distributions from multiple sources. The total dose deposited was calculated, as described above, by convolving the radioactivity distributions with the voxel dose kernel. The total volume was 9.6×9.6×9.6 mm^3. A 2D dose map was then generated from the center axial slice (Z=11). Cumulative dose volume histograms (DVH), which indicate the fraction of voxels, or volume fraction (0-1.0), receiving a specific absorbed dose, were created for each simulated volume.

3.3.6 DOSE DISTRIBUTIONS IN TUMOURS

To predict the *in vivo* dose distribution in a tumour, a 6.3×6.3×6.3 mm volume of interest (VOI) corresponding to a 21×21×21 array was selected using MATLAB from SPECT images of tumours in mice which had been injected i.t. with

^{177}Lu-AuNP or implanted with NPD containing ^{177}Lu-AuNP. The measured counts in each voxel were converted to radioactivity (MBq) by applying a conversion factor determined from dividing the simulated radioactivity from section 2.6 (1.8, 2.5, and 25.1 MBq for ^{90}Y, ^{177}Lu, and ^{111}In, respectively) by the sum of the counts in the VOI. To calculate the dose rate distribution, the radioactivity array was convolved by the VDK determined from MCNP5. The images of the dose rate distributions were generated from the center axial slice (Z=11) using MATLAB. The model assumed homogeneous tissue density throughout the tumour, and uniform radioactivity distribution within the voxels. Since the VOI length (6.3 mm) is smaller than the kernel length (11 mm), which was surrounded by BT allowing for backscatter, the assumption is that the boundary of the tumour is well beyond the edge of the VOI to allow for the same backscatter. Dose rate volume histograms (DrVH), which indicate the fraction of voxels in the VOI exposed to a specific dose rate, were created for each radionuclide in the simulation and are included in the Supplemental Materials (*Appendix B*). The total dose was calculated by integrating the dose rate (Gy/s) in each voxel as a function of time, t, from t=0 to t=7 d using the trapezoidal rule, and then integrating from t=7 d to t=∞, assuming that the dose rate in the voxel changed only due to radioactive decay.

3.3.7 STATISTICAL ANALYSIS

Results were expressed as mean ± standard deviation (SD; n = 3-4) and tested for statistical significance using one-way ANOVA (P<0.05), or a paired t-test (P<0.05) using Prism 6.01 (Graphpad, San Diego, CA) software.

3.4 RESULTS

3.4.1 SMALL ANIMAL SPECT/CT IMAGING

SPECT/CT images of mice obtained at 1, 24, and 48 h and 7 d post implantation of the NPD incorporating ^{177}Lu-AuNP or post i.t. injection of ^{177}Lu-AuNP are shown in Figure 3.1. At 1 h, the tumour radioactivity in mice injected i.t. with ^{177}Lu-AuNP appeared to be distributed over a slightly larger volume while ^{177}Lu-AuNP incorporated into the NPD remained confined to the depot implant site. However, the radioactivity signal intensity in the tumour in mice implanted with the NPD or injected i.t. decreased with time. Since the images were normalized to the initial signal intensity immediately after implantation of the NPD or i.t. injection of ^{177}Lu-AuNP, by acquiring subsequent images over an appropriately increased time to compensate for radioactive decay, we interpret these changes in signal intensity as re-distribution of ^{177}Lu within the tumour or to other organs. Within the range of radioactivity tested (0-37.5 MBq) and under the specified imaging parameters (Section 3.3.3), the number of counts in the VOI analysis of the SPECT images increased linearly with radioactivity (Fig. 3.2). The conversion factor between counts and radioactivity was 159±10 cps/MBq.

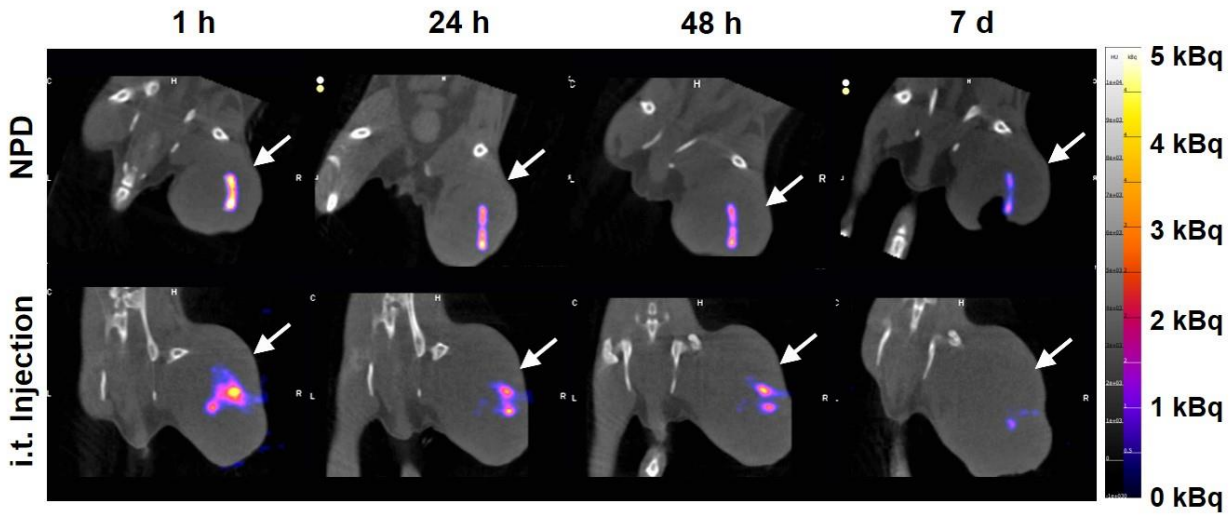

Figure 3.1 SPECT/CT images of the right flank of representative mice bearing MDA-MB-231 tumour xenografts (white arrow). Images were collected at 1 h, 24 h, 48 h and 7 d following i.t. injection of ^{177}Lu-AuNP or ^{177}Lu-AuNP incorporated into a NPD and then implanted i.t. Intensity bar indicates radioactivity. Images at later time points were normalized to the 1 h images to correct for radioactive decay. Note the difference in ^{177}Lu emission patterns from the NPD and i.t. injections, with the i.t. injected ^{177}Lu-AuNP demonstrating greater distribution heterogeneity.

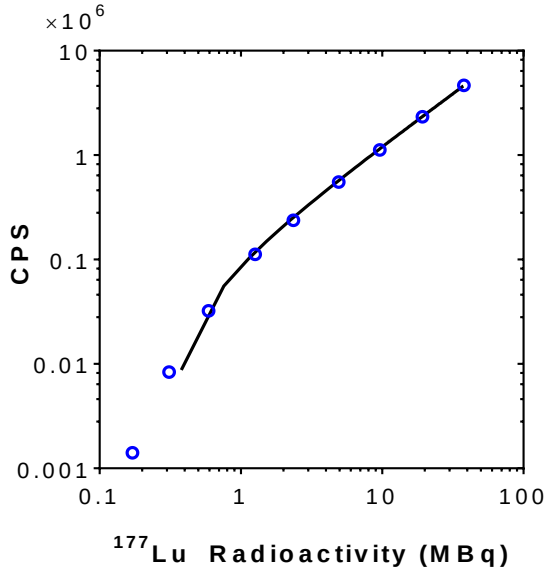

Figure 3.2 Linearity of measurement of radioactivity. VOI analysis of SPECT images by calibration of the counts per second (CPS) detected per unit of ^{177}Lu radioactivity (MBq). Serial dilutions of ^{177}Lu were imaged under the same conditions as the *in vivo* experiments, over a radioactivity range that included the amounts used in these experiments. The log-log plot results in an inflection in the curve at radioactivity <1 MBq but the relationship between CPS and radioactivity was linear (R^2=0.99).

3.4.2 MONTE CARLO SIMULATION AND VALIDATION

The normalized VDK (S_r/S_0) for ^{90}Y, ^{177}Lu, and ^{111}In, generated using 100% BT vs. 0.3% Au/99.7% BT for 0.3 mm VEL as a function of distance from the source are shown in Figure 3.3. The shape of the dose kernel plots without Au were coincident with those with the addition of Au, with slight divergences observed for ^{90}Y at increasing distances from the source (Fig. 3.3a). For ^{177}Lu (Fig. 3.3b) and ^{111}In (Fig. 3.3c), both dose kernel curves calculated from BT alone and BT + Au were in good accordance and demonstrated a steep decrease due to primary electron energy loss up to the CSDA range (0.17 cm for ^{177}Lu, and 0.06 cm for ^{111}In), the maximum projected range of the electrons. Beyond the CSDA range, the contributions to dose deposition in voxels were from primary photons (γ-rays and X-rays) and secondary photons (bremsstrahlung X-rays). The CSDA range of ^{90}Y is 1.1 cm which is at the upper limit of the kernel range, therefore the photon-only portion of the kernel is not included in our calculations. However, ^{90}Y primary photons only contribute to 0.15% of all emissions and the kernel range of 1.1 cm captures over 99.99% of the energy deposition.

The relative difference, or RD, as a function of distance from the source voxel, r, calculated using $100*(S_{r,Au+BT} - S_{r,BT})/S_{r,BT}$, between $S_{r,BT}$ (for BT alone) vs. $S_{r,Au+BT}$ (0.3% Au/99.7% BT) are shown in Figure 3.3d. For all curves, the difference in the kernel calculated in 0.3% Au/99.7% BT was +3.5% to +5.5% compared to BT at the source voxel. The RD decreased to a minimum (-85.9%, -37.3%, and -14.5% for ^{90}Y, ^{177}Lu, and ^{111}In respectively) at distances approaching the CSDA range. The greatest RD was observed for ^{90}Y at the CSDA range but at distances where the modeled high concentration of Au was relevant (<0.1 cm), based on our previous study (Lai et al., 2016), the RD was only 5.3 ± 0.2%. Thus, the absence of Au in the calculations resulted in an underestimation of dose deposition from 0-0.04 cm and overestimation at distances >0.04 cm, thus having a greater impact on the doses from ^{177}Lu and ^{111}In.

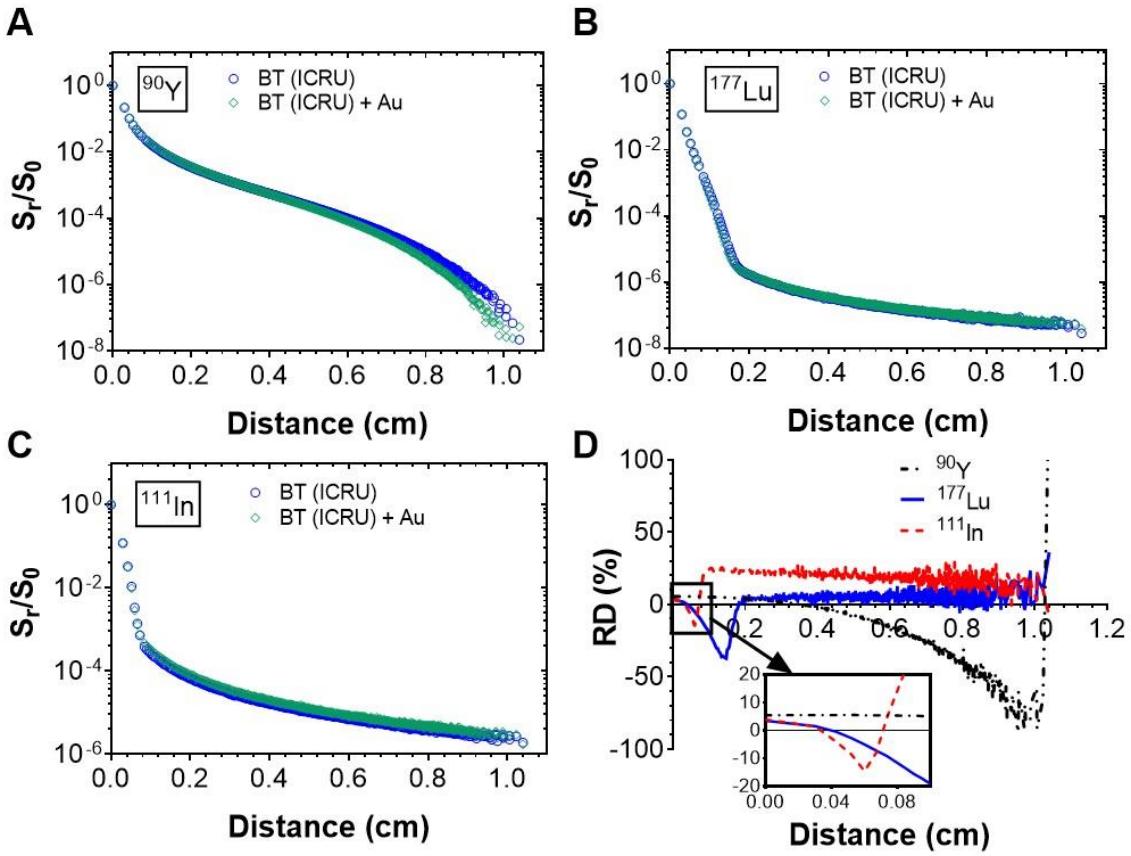

Figure 3.3 Voxel dose kernels (VDK) with 0.3 mm edge length. VDK, containing normalized S values plotted as a function of distance (cm), were generated from a source voxel (0, 0, 0) containing homogeneously distributed (a) ^{90}Y, (b) ^{177}Lu, and (c) ^{111}In. VDK were calculated for ICRU breast tissue (BT) only and for a homogeneous medium containing 99.7% BT and 0.3% Au. (d) A comparison between VDK from the two media is made for each radionuclide and shown as the relative difference (RD) as a function of distance. Note that the RD at the distances where the high Au concentrations would be relevant is low (<5%).

To validate the dose estimates provided by the MCNP model, the VDK with 3 mm voxel edge length were compared to published S values by Bolch et al. for ^{90}Y (Bolch et al., 1999), and Lanconelli et al. for ^{90}Y and ^{177}Lu (Lanconelli et al., 2012). The VDK curves reported for ^{90}Y (Fig. 3.4a) and ^{177}Lu (Fig. 3.4b) were in good agreement with those from our MCNP simulation. While our dose kernel curves were almost indistinguishable with those obtained by Lanconelli *et alet al*, small divergences were observed for the ^{90}Y curves at distances beyond the CSDA range, particularly from 1-2 cm when compared to the curves generated by Bolch et al. A comparison of the calculated S values for the source voxel (0, 0, 0) and voxel position (5, 5, 5) for ^{90}Y and ^{177}Lu, with the corresponding voxels published by Lanconelli et al. is summarized in Table 1. An additional comparison of S values was made with and without contributions from Auger electrons (AE) and internal conversion electrons (IC) to allow for a more direct comparison between models because the dose kernels calculated by Lanconelli et al. did not include AE and IC emissions in their spectrum. The S values

generated in our study when contributions from these particles were omitted were closer to the published S values for ^{177}Lu (RD = 1.4%) than when they were included (RD = 10.4%), since AE and IC contributed to 33.2% of the total number of emissions per decay. However, due to their ultrashort range (maximum R_{CSDA} = 0.091 cm), omission of these electrons did not affect the S values at 2.6 cm (voxel (5, 5, 5). Similarly, no difference in S values were observed for the ^{90}Y source voxel (0, 0, 0), as AE and IC only contribute 0.14% of the total emissions.

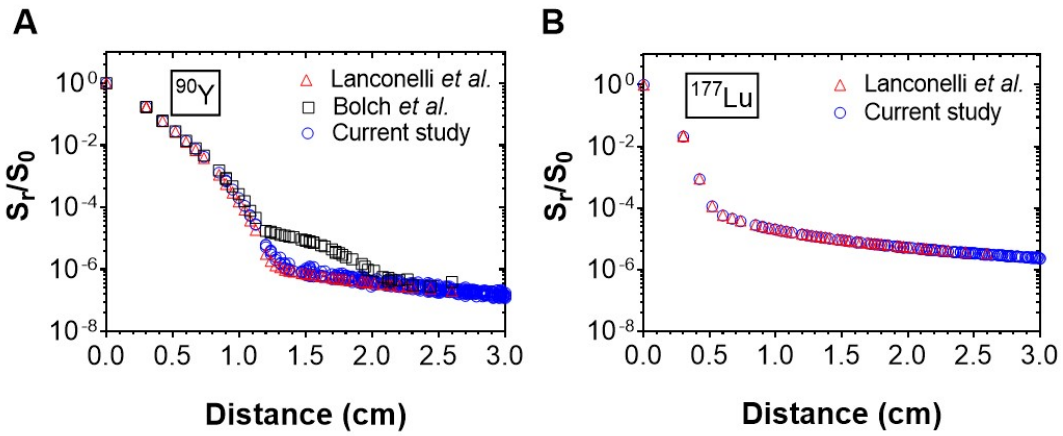

Figure 3.4 Validation of voxel dose kernels (VDK) with 3 mm edge length. VDK, containing normalized S values plotted as a function of distance (cm), were generated from a source voxel (0, 0, 0) containing homogeneously distributed (a) ^{90}Y and (b) ^{177}Lu. The normalized kernels for ^{90}Y are compared with those reported by Lanconelli et al. (Lanconelli et al., 2012) and Bolch et al. (Bolch et al., 1999) while those for ^{177}Lu were compared only to Lanconelli et al. Note the good agreement between the current study VDK and those published by Lanconelli et al.

Table 3.1 S values (mGy/MBq·s) at voxel locations (0, 0, 0) and (5, 5, 5), calculated in the current study and compared to those from Lanconelli et al. (Lanconelli et al., 2012). S values for the current study were also calculated without AE and IC emission contributions, which were omitted in the Lanconelli study, to allow for a direct comparison. The relative difference (RD) between the S values shown were calculated relative to values published by Lanconelli et al.

Position		(0, 0, 0)			(5, 5, 5)	
	Current study S values (mGy/MBq·s)	Lanconelli et al. S values (mGy/MBq·s)	RD[a] (%)	Current study S values (mGy/MBq·s)	Lanconelli et al. S values (mGy/MBq·s)	RD[a] (%)
^{90}Y	1.58 ± 0.0002		0.64	2.98 (±0.3) ×10^{-7}		7.45
^{90}Y$_{(-)\ AE/IC}$[a]	1.58 ± 0.0001	1.59	0.64	2.98 (±0.3) ×10^{-7}	3.22×10^{-7}	7.45
^{177}Lu	7.65 (±0.0008) ×10^{-1}		10.38	2.39 (±0.05) ×10^{-6}		4.82
^{177}Lu$_{(-)\ AE/IC}$[a]	6.83 (±0.0008) ×10^{-1}	6.93×10^{-1}	1.44	2.39 (±0.05) ×10^{-6}	2.28×10^{-6}	4.82

[a] Auger electron (AE), internal conversion electron (IE), and relative difference (RD).

3.4.3 NPD SIMULATION

A simulated NPD containing radiolabeled AuNP, which permits local diffusion of radioactivity due to release of the nanoparticles, was created using MATLAB to illustrate the temporal diffusion-dependent dose distributions. The discrete radioactivity (kBq) and dose rate (mGy/s) as a function of voxel positions (mm) are illustrated for the NPD incorporating AuNP labeled with ^{90}Y, ^{177}Lu or ^{111}In (Fig. 3.5) at several time points (0, 14, 28, 42, and 56 h). In Figure 3.5a-c, the change between NPD radioactivity profiles at each time point is the result of both diffusion of released radiolabeled AuNP as well as radioactive decay. The release of AuNP from the NPD and their diffusion, simulated using our previously published AuNP concentration profiles (Lai et al., 2016), is noted by the horizontal spread of radioactivity at the periphery (located at positions 3.0 and 3.3 mm). The distribution of radioactivity has direct impact on the dose rate distribution, which is presented as a function of voxel position (mm) in Figure 3.5d-f, at the same time points. The total dose deposited within and around the NPD, calculated by integrating the dose rate in each voxel as a function of time ($t = 0 \rightarrow \infty$), is shown in the dose maps in Figure 3.5e and 3.5f respectively. Note the difference in the scale resulting from the different initial radioactivity. The discrete radioactivity, dose rate and total dose deposited for a conventional seed containing non-diffusing ^{90}Y is shown in Figure 3.6. A comparison of the dose maps in Figure 3.5g, for ^{90}Y-AuNP in a NPD, and Figure 3.6c, for ^{90}Y in a conventional seed, demonstrates a 3-fold decrease in maximum dose for the NPD.

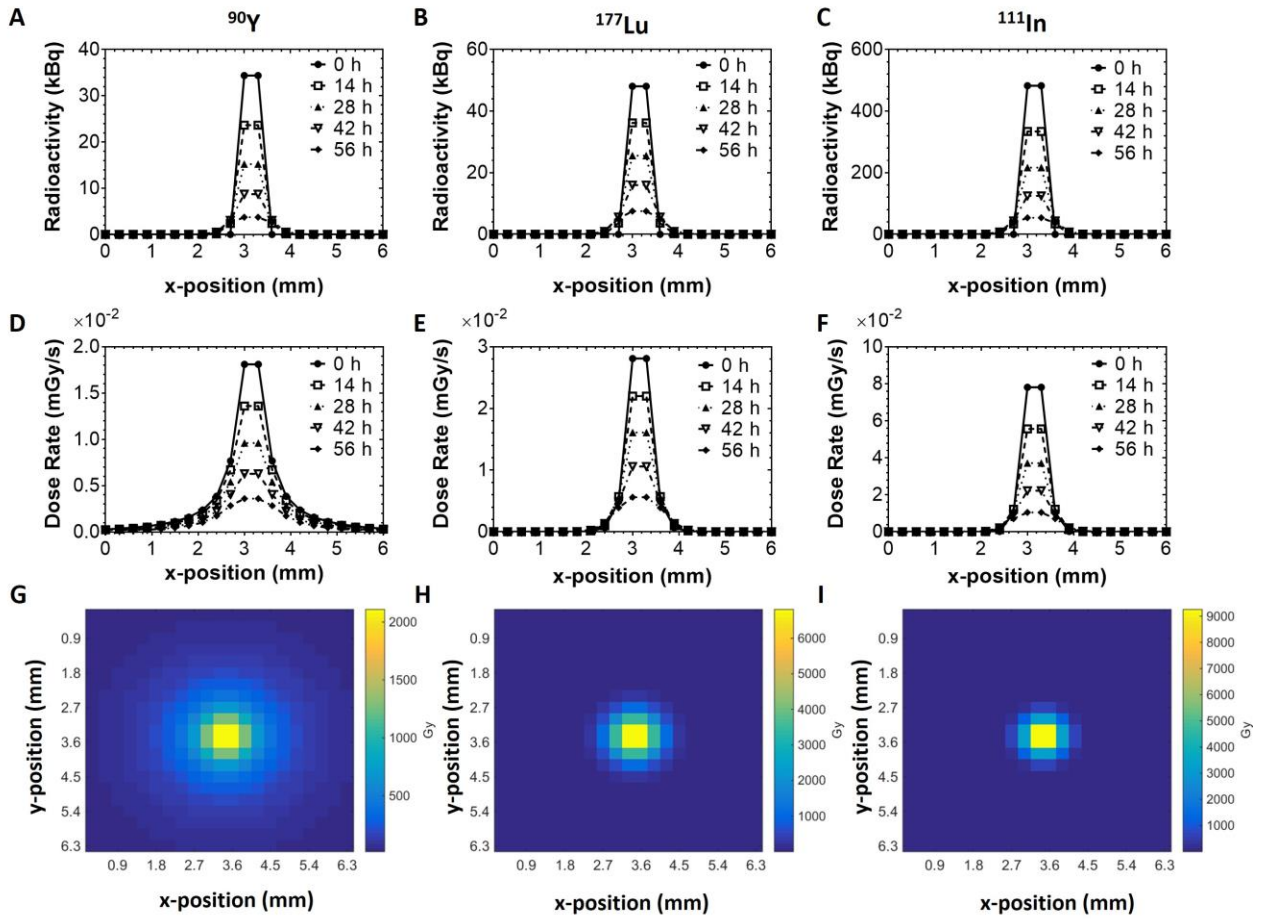

Figure 3.5 1D radioactivity and dose rate distributions and 2 D dose distributions. Profiles of radioactivity (kBq) as a function of voxel position (mm) for NPD incorporating (a) ^{90}Y-AuNP, (b) ^{177}Lu-AuNP, or (c) ^{111}In-AuNP. Discrete dose rate (mGy/s) as a function of voxel position (mm) for (d) ^{90}Y-AuNP, (e) ^{177}Lu-AuNP, and (f) ^{111}In-AuNP. Dose map (Gy) for NPD containing (g) ^{90}Y-AuNP, (h) ^{177}Lu-AuNP, and (i) ^{111}In-AuNP generated from a cross section (slice z=11) of the 3-dimensional dose distributions. Note the difference in the dose intensity scales. Note the difference in maximum dose between (g), (h), and (i).

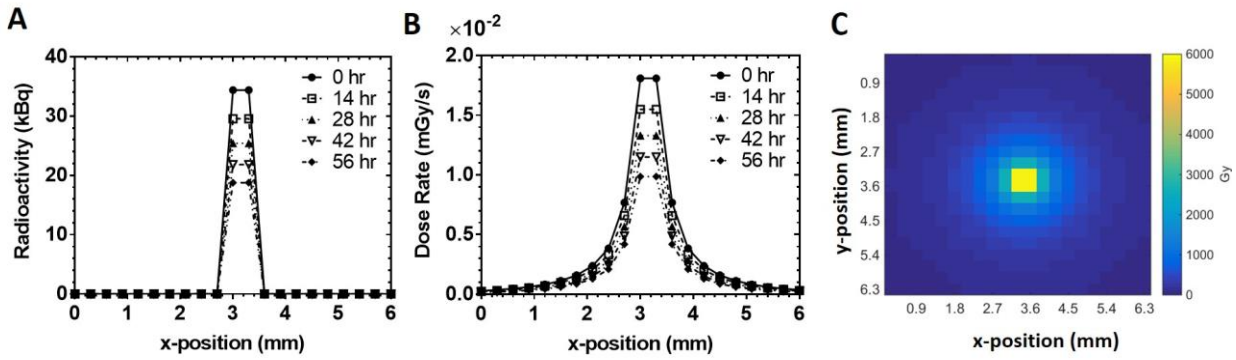

Figure 3.6 Radioactivity and dose distributions from a conventional sealed source incorporating ^{90}Y. (a) Profiles of radioactivity (kBq) as a function of voxel position (mm), (b) Discrete dose rate (mGy/s) as a function of voxel position (mm), and (c) corresponding dose map (Gy) generated from a cross section (slice z=11) of the 3-dimensional dose distribution for a conventional non-diffusive seed incorporating ^{90}Y. Note the difference in maximum dose (c) between the conventional seed and the NPD (Fig. 3.5g).

A volume containing 4 NPD or conventional seeds spaced 4.5 mm apart (center-to-center) in a square formation was simulated to replicate multiple placements of radioactive sources which would be required for patient treatment. The dose maps for the multiple NPD are shown in Figure 3.7 and for the conventional seeds are shown in Figure B 1 in the Supplemental material (Appendix B). For NPD containing AuNP labeled with 1.8 MBq of ^{90}Y (Fig. 3.7a), 2.5 MBq of ^{177}Lu (Fig. 3.7b), and 25.1 MBq of ^{111}In (Fig. 3.7c) respectively, the corresponding maximum doses located at the NPD were 2,100 Gy, 6,800 Gy and 9,300 Gy. The maximum doses for the conventional seeds containing the same activities of ^{90}Y, ^{177}Lu, and ^{111}In were a factor of 2.8 (5,900 Gy), 3.4 (23,000 Gy) and 2.7 (25,000 Gy) higher than the NPD. The respective minimum doses at the VOI periphery for the NPD were 21.8 Gy, 0.12 Gy, and 2.2×10^{-3} Gy, versus 44.8 Gy, 0.19 Gy and 3.4×10^{-3} Gy for the conventional seeds. Evaluation of the DVH (Fig. 3.8) also demonstrates that use of the NPD delivers a more homogeneous dose, with larger volumes receiving higher doses than with conventional seeds. A comparison of the radionuclides revealed that 80-90% of the volume fraction treated with ^{177}Lu containing sources (NPD or seed), and 87-95% of the volume fraction treated with ^{111}In containing sources received an absorbed dose of 0 ± 0.005% of the maximum dose (0 ± 0.34 Gy and 0 ± 0.46 Gy, respectively). Concerning ^{90}Y, none of the volume received doses between 0 ± 0.005% of the maximum dose.

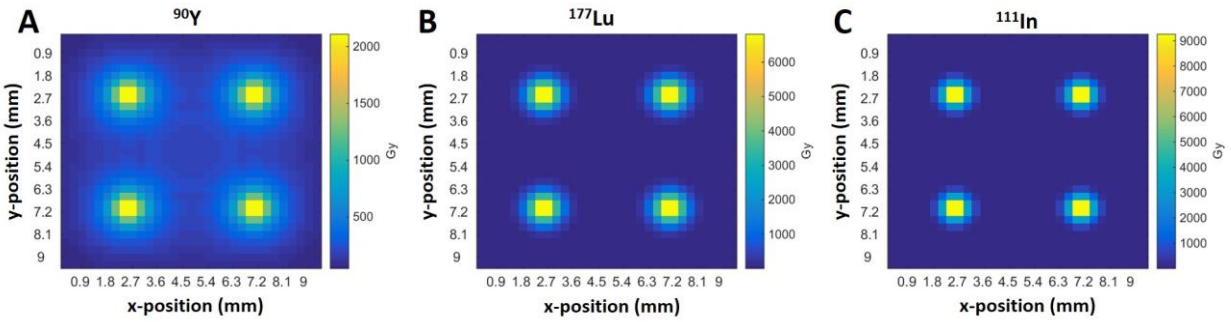

Figure 3.7 Dose maps of 4 NPD spaced 4.5 mm apart (center-to-center) in a square formation. The NPD contained AuNP labeled with either (a) ^{90}Y, (b) ^{177}Lu, or (c) ^{111}In. Dose maps were generated from axial cross sections (slice z=11) of the 3-dimentional dose distributions. Note the difference in the dose intensity scales.

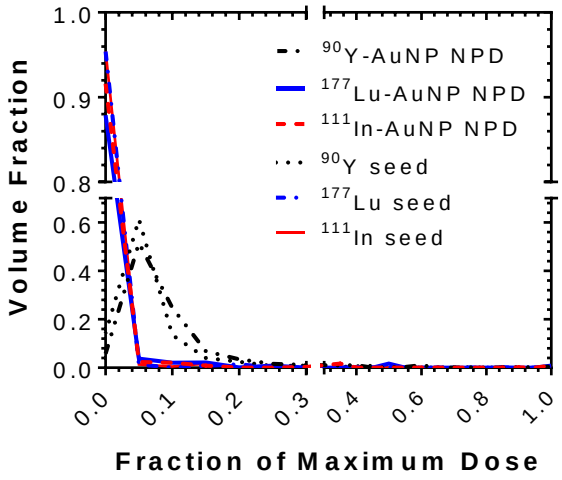

Figure 3.8 Histogram of dose distribution within VOI. The volume fraction is plotted as a function of the fraction of maximum dose. The curves correspond to the dose distributions of ^{90}Y, ^{177}Lu, and ^{111}In-labeled AuNP incorporated into 4 NPD or the same radionuclides in conventional seeds.

3.4.4 DOSE RATE AND DOSE DISTRIBUTIONS FROM SPECT IMAGES

The dose rate distributions for ^{90}Y, ^{177}Lu, and ^{111}In were calculated using the radioactivity distribution measured in representative SPECT images of ^{177}Lu-AuNP incorporated into a NPD inserted i.t. or ^{177}Lu-AuNP directly injected i.t. (Fig. B 2). The dose rates were calculated by convolving the radioactivity distributions derived from SPECT images with the corresponding VDK obtained from MCNP simulations (Fig. 3.3). For the dose rate distribution results of NPD and i.t. injected radiolabeled AuNP, see the Supplemental materials (Appendix B).

The dose distributions (Fig. 3.9) were obtained by registering the SPECT images of an implanted NPD incorporating ^{177}Lu-AuNP at various times to determine the cumulative radioactivity distribution, and convolving a VOI with the various VDK. Similar to the simulated NPD, use of ^{90}Y resulted in greater penetration and a more homogenous distribution of dose (max: 3600 Gy, min: 7.0 Gy) when compared to ^{177}Lu (max: 11000 Gy, min: 0.06 Gy), and ^{111}In (max: 14000 Gy, min: 9.8×10^{-4} Gy). The corresponding DVH for Figure 3.9 is shown in Figure 3.10. Examination of the DVH supports these findings as 88.5% of the volume fraction received an absorbed dose of 0 ± 0.005% of the maximum dose (0 ± 0.55 Gy) for the volume containing an NPD incorporating ^{177}Lu-AuNP, and 90.3% of the volume fraction received an absorbed dose of 0 ± 0.005% of the maximum dose (0 ± 0.73 Gy) for the volume containing an NPD incorporating ^{111}In-AuNP. However for the NPD incorporating ^{90}Y-AuNP, none of the volume fraction received no absorbed dose (0 ± 0.005% of the maximum dose or 0 ± 0.18 Gy).

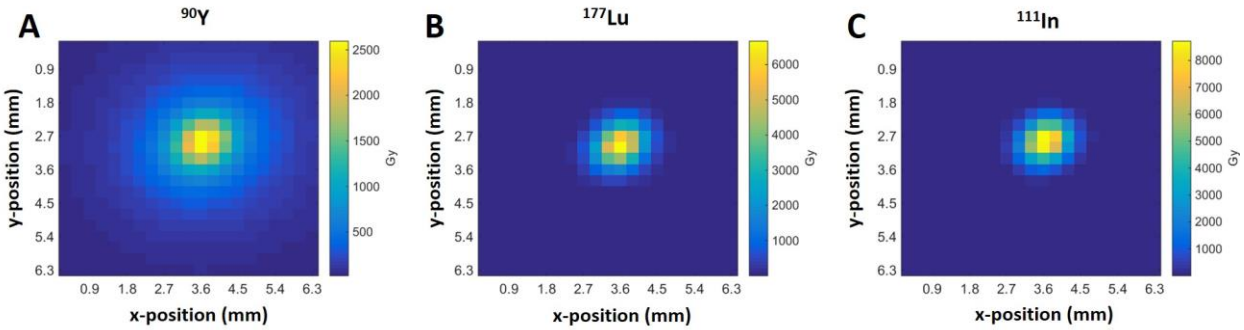

Figure 3.9 2D in vivo dose distributions. Dose distributions of (a) ^{90}Y-, (b) ^{177}Lu-, and (c) ^{111}In-labeled AuNP incorporated into a NPD and implanted i.t. into breast cancer xenografts in mice. Dose distributions were generated using cumulative radioactivity distributions determined from registered SPECT images of a tumour implanted with a NPD incorporating ^{177}Lu-AuNP obtained at 1 h, 24 h, 48 h, and 7 d, and convolving with ^{90}Y, ^{177}Lu or ^{111}In VDK generated from MCNP5. The dose distributions shown are representative slices of the calculated 3D dose distribution. Note the difference in the dose intensity scales.

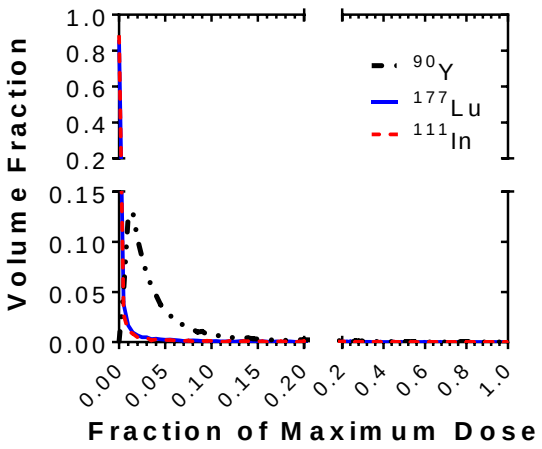

Figure 3.10 Histogram of dose distribution within VOI. The volume fraction is plotted as a function of the fraction of maximum dose. The curves correspond to the dose distributions of ^{90}Y-, ^{177}Lu-, and ^{111}In-AuNP incorporated into a NPD and implanted i.t. into a human breast cancer xenograft in a mouse.

3.5 DISCUSSION

In this study, we demonstrate for the first time the dose distribution, determined using MCNP5, from radiolabeled AuNP delivered using a novel nanoparticle depot (NPD) system as an intermediate between conventional brachytherapy seeds and i.t. injections of suspended radiolabeled AuNP. The resultant dose distribution was comparably more uniform than direct i.t. injection of radiolabeled AuNP and delivered a lower maximum dose than conventional seeds suggesting that NPD may offer a solution to tissue overdose in permanent brachytherapy. In our comparison of electron emitters of varying energies and tissue penetrating ranges (^{90}Y, ^{177}Lu, and ^{111}In), the modelled dose distributions from radiolabeled AuNP revealed that higher energy electron emitters (^{90}Y) are capable of partially compensating for heterogeneities in radioactivity distribution. These findings were consistent for dose distributions from simulated arrangements consisting of a single NPD implanted into tissue or an array of 4 NPD used to simulate the larger radiation field of patient tumours. The *in vivo* dose distributions calculated from SPECT images (Fig. 3.9) of tumours implanted with a single NPD incorporating ^{177}Lu-AuNP were comparable to the dose distributions predicted by the simulated NPD (Fig. 3.5g-i), and supported the use of a higher energy electron emitter, ^{90}Y.

The MCNP simulations compared the energy deposition in a cubic volume containing BT and 0.3% Au+ 99.7% BT material from a source voxel containing homogeneously distributed radionuclides (Fig. 3.3). The percentage of Au used was selected to represent a maximum effect scenario in which the high concentrations of AuNP within the NPD were also located in all other voxels. However, our previous study (Lai et al., 2016) demonstrated that tissue concentrations of AuNP were much lower than in the NPD, decreasing to 0.03% Au at 0.1 cm from the NPD surface. The percent difference in energy deposition (Fig. 3.3d) between the two materials as a function of distance demonstrated that in regions where the Au concentrations were high (0.3%) there was an underestimation of dose

by 3.5%-5.5% in the immediate vicinity of the radioactivity source. The lower dose deposition in the Au+BT material is attributed to the dependence of electron collisional stopping power on the atomic number, Z, of the material (Attix, 2004). The higher the average Z, the lower the collisional stopping power of the electron and the lower the energy deposition in the medium over a given range. Subsequent calculations performed in this study were conducted using VDK from BT only, which were justified by the fact that only a small portion of the voxels contained 0.3% Au and that the discrepancy in dose deposition would decrease greatly as the Au concentration decreased.

AuNP are expected to have an additional local effect by absorbing photons and electrons and converting them into a more localized cascade of low energy electrons capable of increased biological damaged, which may have important therapeutic consequences. The contributions to dose enhancement at the cellular level has been investigated by Lechtman et al., Mcmahon et al., and Brown et al., and will be incorporated into the current model in future work (Lechtman et al., 2011, Brown and Currell, 2017, McMahon et al., 2011). However, their work demonstrates an overarching need for more detailed Monte Carlo simulation models at higher spatial resolution, to elucidate the impact of AuNP radioenhancement on cellular biophysical functions (Nikjoo et al., 2016). Other Monte Carlo track structure codes, such as KURBUC for biophysical modelling (Nikjoo et al., 1998), PENELOPE (Lechtman et al., 2011), and Geant4 (Sakata et al., 2016, Bernal et al., 2015) amongst many others which have been reviewed by Nikjoo et al. (Nikjoo et al., 2006) and Zygmanski and Sajo. (Zygmanski and Sajo, 2016) are useful for low energy emitters, Auger cascade transport simulations, and self-absorbed fraction calculations for different types of nanoparticles.

The MCNP model was validated by comparing the VDK obtained from the current study to those published by Lanconelli et al. and Bolch et al. (Fig. 3.4). The percentage difference between Lanconelli et al. and the current study for ^{90}Y and ^{177}Lu, were lower for the source voxel dose (0, 0, 0) (0.64% and 1.44% respectively) and higher at 2.6 cm (5, 5, 5) (7.45% and 4.82% respectively) when AE and IC were omitted to allow for a more direct comparison between models because the dose kernels calculated by Lanconelli et al. did not include AE and IC emissions. In addition, the discrepancy in S values between Lanconelli et al. and the current study may be attributed to the use of soft tissue (ρ=1.04 g/cm^3) from Cristy and Eckermann (Cristy and Eckerman, 1987a) as compared to BT (ρ=1.02 g/cm^3) from ICRU-44 (ICRU, 1989) in our study. The VDK from Bolch et al. were generated using the EGS4 Monte Carlo code. The discrepancy in the VDK at 1-2 cm has been documented in other studies (Reiner et al., 2009, Lanconelli et al., 2012) but the effect on dose distribution should be minimal since the contribution to dose beyond 1.1 cm is <0.001%.

The use of diffusible AuNP released from the NPD may be advantageous compared to conventional sources in permanent seed brachytherapy, which commonly deliver unnecessarily high local doses to tissues adjacent to the seed (Ravi et al., 2011). During treatment planning, conventional seeds are arranged in 3D to deliver 100% of the prescription dose to the entire clinical target volume. For instance, in the study by Ravi et al., 90 Gy was delivered to patients receiving PSI of the breast with 97% target volume coverage at 100% of the prescription dose. However, 61% of the target volume received 150% of the prescription dose and 15% of the target volume received 200% of the

prescription dose, demonstrating that significant volumes of tissue received well beyond the prescribed doses. In the present study, we demonstrated a 3-fold decrease in the maximum dose compared to a conventional seed incorporating the same radionuclide and radioactivity, which is attributed to the release of radiolabeled AuNP from the NPD over the course of treatment. There is an additional advantage to using NPD when these regions of overdose are near critical structures, such as the skin or chest wall for breast cancers (Lin et al., 2008), and ureter and rectum for prostate cancers (Zelefsky et al., 2003), which will improve normal tissue sparing.

Three different electron emitting radionuclides (^{90}Y, ^{177}Lu, and ^{111}In) were used in the NPD simulations to determine the influence of electron range combined with radioactivity distributions on dose delivery. The radioactivity profiles from a single simulated NPD (Fig. 3.5) incorporating ^{90}Y-AuNP resulted in lower absorbed dose to tissue in close proximity to the NPD in comparison to ^{177}Lu, and ^{111}In, and a higher absorbed dose at further distances due to greater penetration of the higher energy electrons. Similarly, simulation of 4 NPD implants (Fig. 3.7) positioned 4.5 mm apart demonstrated that the use of the longer range electron emitter, ^{90}Y, delivered more homogenous dose distribution, as indicated by the DVH (Fig. 3.8). Although it is possible to decrease the implantation distance between NPD to improve the dose homogeneity when using ^{177}Lu, and ^{111}In, smaller distances will become clinically impractical for larger treatment volumes due to the number of NPD that may be required to minimize dose heterogeneities. For instance, in PSI brachytherapy of the prostate, seeds are implanted 5 mm or 10 mm apart depending on the loading approach (uniform, peripheral, modified uniform/peripheral), and typically >100 seeds are implanted (Dicker et al., 2005, Yu et al., 1999, Crook et al., 2002). Permanent brachytherapy in the breast uses the uniform loading approach requiring that seeds are placed 10 mm apart, center-to-center, resulting in a median of 71 seeds (33-102 seeds) to cover a median volume of 35 cc (14.7-66.6 cc) (Pignol and Keller, 2009a).

An alternate solution is to improve the release characteristics and tissue diffusion rate of radiolabeled AuNP incorporated into the NPD, by decreasing their size (Lai et al., 2016) such that a larger proportion of the dose is delivered further from the NPD. In a previous study we demonstrated that smaller AuNP (5 nm, 15 nm) were released more completely and had improved distribution in MDA-MB-231 tumour xenografts in mice than larger AuNP (30 nm, 50 nm), which were mostly retained by the NPD, resulting in much more localized intratumoural distribution. For example, 5 nm AuNP demonstrated nearly complete release within 3 days and diffused up to several millimeters from the NPD (< 5mm) (Lai et al., 2016). The improved diffusion properties of smaller (5 nm) AuNP may help to address the heterogeneities in dose distribution observed in the current study using 30 nm AuNP. This represents a major advantage of using radiolabeled AuNP incorporated into the NPD as opposed to conventional brachytherapy seeds, in that the AuNP may be designed to be released by the NPD at different rates and exhibit different diffusion distances within the tissue to minimize dose heterogeneities.

To verify the results from simulated NPD, three dimensional dosimetry was performed using radioactivity distributions determined from registered SPECT images of mice bearing s.c. MDA-MB-231 breast cancer xenografts implanted with

a NPD incorporating ^{177}Lu-AuNP. The observed dose distribution (Fig. 3.9) and DVH (Fig. 3.10) were in agreement with those from the simulated NPD, with ^{90}Y delivering the most homogenous dose distribution. To increase the therapeutic efficacy of ^{111}In-AuNP or ^{177}Lu-AuNP, the dose distribution could be made more homogeneous by using smaller nanoparticles to improve the dispersal of AuNP released from the NPD in tissue, as previously discussed (Lai et al., 2016). This may also further reduce the maximum dose and alleviate the dose burden to overdosed tissues. The comparison of the therapeutic efficacy of various sizes of radiolabeled AuNP will be included in future work and will build on the dosimetry models developed in the current study.

Fitting of the radioactivity vs. time curve to obtain the cumulative radioactivity introduces additional error in the final absorbed dose estimates from radiolabeled AuNP due to the inherent inaccuracies of the trapezoidal rule and the need to assume physical decay as the only factor causing decreased radioactivity from the final SPECT image, since redistribution of the radiolabeled AuNP from the tumour may also occur as previously demonstrated by i.t. injection studies (Yook et al., 2016a). There are additional factors that influence the accuracy of dose rate distributions calculated in this study. Firstly, the use of SPECT imaging for quantifying spatial distributions of radioactivity adds a source of error since the radioactivity is averaged over the voxel volume which is limited by the spatial resolution of the system. It is accepted that SPECT image quality presents the largest source of error in radioactivity quantification and many studies have focused on improving the accuracy of SPECT reconstruction techniques to aid in 3D dosimetry (Dewaraja et al., 2005, Pacilio et al., 2015, Ljungberg et al., 2002). Secondly, our study employed the low abundance γ-emissions from ^{177}Lu to quantify radioactivity distributions on SPECT images, but ^{177}Lu is also a β^- emitter, and in the present study we estimated that i.t. implantation of a NPD incorporating 2.5 MBq of ^{177}Lu-AuNP deposits a dose of ~120 Gy in the tumour volume. It has been demonstrated by Stapleton et al. that the effects of radiation influences the transport of nanoparticles in tissue (Stapleton et al., 2017). Further investigation on the subject of the effects of radiation on nanoparticle transport are required to understand this potential source of error.

3.6 CONCLUSION

Use of the NPD may provide an opportunity to homogenize dose by lowering dose to tissues adjacent to the sources that are commonly overdosed in conventional brachytherapy, as well as allow the use of electron emitters with different energies and ranges to deposit doses at different distances from the NPD. Comparison of electron emitters with varying penetrating ranges incorporated into a NPD implanted into a tumour xenograft in mice revealed that the higher energy electron emitter, ^{90}Y, delivered a more homogenous tumour dose distribution than the lower energy electron emitters, ^{177}Lu and ^{111}In, and could compensate for heterogeneities in radioactivity distribution. Dose modelling of simulated multiple NPD implantation predicted that the dose distribution from ^{177}Lu and ^{111}In would be suboptimal as large volumes would receive no dose at 4.5 mm implantation distances and closer distances may be impractical clinically. However, the properties of radiolabeled AuNP, particularly size may be optimized to provide more rapid and complete release from the NPD as well as greater diffusion within tissues (Lai et al., 2016), which may address dose heterogeneity. The dose rate distribution *in vivo* from a NPD incorporating radiolabeled AuNP and

implanted into a tumour xenograft in a mouse remained concentric around the NPD, while i.t. injected radiolabeled AuNP resulted in irregularly shaped dose rate distributions that were spatially variant with time. Thus, NPD are clinically more feasible than i.t. administration as a brachytherapy because they provide a more predictable dose distribution. Despite the challenges, the high doses delivered locally by radiolabeled AuNP incorporated into a NPD and the potential to further design this system to minimize dose heterogeneities warrants further investigation of NPD as a solution to improving brachytherapy strategies for cancer treatment.

3.7 ACKNOWLEDGEMENTS

This research was supported by a grant from the Canadian Breast Cancer Foundation (CBCF), Ontario Region to R.M. Reilly and J.P. Pignol. P. Lai is supported by an Alexander Graham Bell Canada Graduate Scholarship from the Natural Sciences and Engineering Research Council of Canada (NSERC). Dr. David Jaffray holds that Orey and Mary Fidani Family Chair in Radiation Physics at Princess Margaret Cancer Foundation. The authors would also like to acknowledge Deborah Scollard and Teesha Komal at the Spatio-temporal Targeting and Amplification of Radiation Response (STTARR) Innovation Centre, University Health Network.

CHAPTER 4

4 EFFECTIVENESS AND TOXICITY OF ^{177}LU-LABELED GOLD NANOPARTICLES DELIVERED VIA A NANOPARTICLE DEPOT FOR TREATMENT OF HUMAN BREAST CANCER XENOGRAFTS IN MICE

Priscilla Lai, Zhongli Cai, Jean-Philippe Pignol, David A. Jaffray, Raymond M. Reilly. Submitted to Journal of Brachytherapy.

4.1 ABSTRACT

Radiolabeled gold nanoparticles (AuNP) have recently been proposed as a novel form of permanent brachytherapy with the aim of homogenizing dose distribution through local AuNP redistribution after intratumoral deposition. The objective of this work was to evaluate the dose homogeneity, therapeutic efficacy and normal tissue toxicity of ^{177}Lu labeled AuNP, delivered using a nanoparticle depot (NPD) implanted by permanent brachytherapy techniques, for treatment of subcutaneous (s.c.) breast cancer xenografts in mice. Five nm and 15 nm ^{177}Lu-AuNP NPD were constructed and implanted into radiation-resistant MDA-MB-231 or radiation-sensitive MDA-MB-468 tumor bearing mice. Small animal SPECT/CT imaging was conducted and image-based dose distributions were calculated using previously reported Monte Carlo methods. Tumor growth and body weight were monitored (15-78 days) before animals were euthanized and the organs and blood collected for biodistribution. Tumor and organ doses were calculated using OLINDA and organ based S-values. Treatment with 5 nm and 15 nm ^{177}Lu-AuNP NPD resulted in significant tumor growth delay in MDA-MB-231 or MDA-MB-468 breast cancer xenografts as compared to PEGylated AuNP NPD and untreated control. There were no normal tissue toxicities as indicated by no decreases in body weight. Dose distributions from the 5 nm ^{177}Lu-AuNP NPD were more homogeneous than 15 nm ^{177}Lu-AuNP NPD, but radioactivity retention in the tumors were similar. Tumor radioactivity for the 5 nm and 15 nm ^{177}Lu-AuNP NPD treatment group at 1 day was 71-73 %IA/tumor, and decreased by 3-15% at 15 days to 60-71 %IA/tumor. Normal tissue uptake was highest in the liver (2.1±2 %IA/organ) for the animals treated with 15 nm ^{177}Lu-AuNP NPD and in the kidney (0.4±0.1 %IA/organ) for animals treated with 5 nm ^{177}Lu-AuNP NPD. Treatment using ^{177}Lu-AuNP NPD was highly effective for arresting the growth of MDA-MB-468 tumors in mice, but was less effective for inhibiting the growth of MDA-MB-231 tumors at the amounts of radioactivity administered. Overall, this study demonstrates that radiolabeled AuNP delivered using an NPD can successfully treat tumours with minimal exposure to normal tissues, and reduced dose heterogeneities particularly when using 5 nm AuNP.

4.2 INTRODUCTION

Permanent seed brachytherapy represents one of the most conformal radiation delivery techniques available, allowing dose escalation to the target tumor volume while sparing normal tissues (Nag et al., 2001). However, brachytherapy seeds often use low energy photon sources (e.g. ^{103}Pd; 21 keV or ^{125}I; 28 keV) that result in heterogeneous dose distributions, and concern for high doses deposited in normal tissues adjacent to the seed. Brachytherapy has been employed for local treatment of several cancers (Huang et al., 2009, Pignol et al., 2015) including breast cancer (BC) where it has been studied as an adjuvant therapy for early stage BC after lumpectomy (Pignol et al., 2015). Pignol et al., treated women who received breast conserving surgery (BCS) with adjuvant permanent breast seed implant (PBSI) brachytherapy using palladium-103 seeds (Pignol et al., 2006). The seeds, measuring 0.8 mm in diameter and 4 mm in length, were implanted into the breast using a template guided system and seeding needles, and were spaced 1 cm apart according to treatment plans generated to achieve the best dose coverage (90 Gy to the treatment volume). However, some women developed telangiectasia, a painless late effect of radiation damage from implants near the skin that manifests as dilated vasculature in the skin, but may be physically disfiguring and psychologically distressing for patients (Pignol et al., 2015). Therefore, although permanent brachytherapy is advantageous for highly localized dose deposition in tumors, heterogeneity arising from high dose regions near the seed makes any slight misplacement of seeds near critical structures undesirable. Conversely, conventional external beam radiation therapy (EBRT), the current gold standard for treatment of BC, delivers a more homogeneous dose distribution (dose homogeneity index, DHI=0.8-0.95 with 1 being perfectly homogeneous), when compared to permanent brachytherapy (DHI=0.4) (Patel et al., 2007, Keller et al., 2012, Bovi et al., 2007), but has poorer tissue sparing resulting in higher exposure to organs at risk (OAR) such as the heart, lungs and skin (Lettmaier et al., 2011). Therefore the ideal radiotherapy would have the dose homogeneity of EBRT and conformity of brachytherapy, although to date none such therapy exists.An alternative strategy being explored by our group to address the limitations of dose heterogeneities in conventional permanent brachytherapy relies on the use radiolabeled gold nanoparticles (AuNP) delivered in suspension by direct intratumoral (i.t.) injection ("radiation nanomedicine"). This approach homogenizes the dose through local diffusion of radiolabeled AuNP, from the intratumoral site of injection, thereby leveling high and low dose regions. In addition, radiolabeled AuNP enable the delivery of a variety of radionuclides that can be electron, photon, and possibly α-emitting, extending the type and range of radiation energies and relative biological effectiveness used in brachytherapy. Preclinical studies in mice with s.c. human BC xenografts have shown promising results with Auger electron emitting ^{111}In or β-particle emitting ^{177}Lu labeled AuNP (Yook et al., 2016a, Cai et al., 2016, Cai et al., 2017). Yook et al. demonstrated tumor growth arrest up to 90 days with no normal tissue toxicities from ^{177}Lu-AuNP after delivering 22 Gy from 30 nm ^{177}Lu-AuNP to s.c. MDA-MB-468 human BC tumors in mice (Yook et al., 2016a). However, direct injection of radiolabeled AuNP is difficult to implement clinically in patients, due to larger treatment volumes which would require multiple injections with unpredictable dose distributions from injected radiolabeled AuNP in suspension due to variable intratumoral transport (Yook et al., 2016a, Lai et al., 2017). To address these practical limitations, we recently reported the design of a nanoparticle depot (NPD) into which radiolabeled AuNP are incorporated and released locally following tissue

insertion using permanent brachytherapy seed implantation (PSI) techniques (Lai et al., 2016). The NPD allowed precise placement and controlled release of 15 nm radiolabeled AuNP in s.c. MDA-MB-231 human BC xenografts in NOD/SCID mice, and resulted in a predictable concentric dose distribution (Lai et al., 2016). Monte Carlo simulations of the NPD dose distribution determined from radioactivity distributions obtained by SPECT imaging of ^{177}Lu-AuNP incorporated into a NPD and implanted into a tumor *in vivo* demonstrated a 3-fold decrease in the maximum dose as compared to a conventional sealed source of the same radioactivity. This reduction in maximum dose was accompanied by a negligible change to the minimum dose, indicating improved dose homogeneity. A more homogenous dose from brachytherapy has been associated with a lower risk of late toxicities and improved cosmetic outcome (Kramer et al., 1999). A comparison was also made between moderate energy β-particle emitting ^{177}Lu (mean β^- energy = 0.13 MeV; 0.17 cm penetration range), low energy Auger and internal conversion (IC) electron emitting ^{111}In (mean Auger electron energy = 0.93 keV and IC electron energy = 0.18 MeV, 0.06 cm penetration range) and high energy β^-particle emitting ^{90}Y (mean β^- energy = 0.93 MeV, 1.1 cm penetration range). These comparisons revealed that the use of a longer range electron emitting radionuclide such as ^{90}Y, or moderate range electron-emitter such as ^{177}Lu coupled with smaller AuNP (i.e. 5 nm) which we found exhibited enhanced local release from the NPD and greater dispersal within the tumor, would improve the dose distribution (Lai et al., 2016).

The current work examines the effectiveness and toxicity of ^{177}Lu-AuNP delivered via a NPD implanted into two human BC xenograft mouse models (MDA-MB-231 and MDA-MB-468), and uses two sizes of AuNP (5 nm and 15 nm). MDA-MB-231 and MDA-MB-468 cell lines were chosen to represent BC xenografts with lower and higher radiosensitivity, respectively (Cai et al., 2008, Yook et al., 2015b). Three dimensional dosimetry was performed using image derived SPECT images of mice bearing s.c. MDA-MB-231 xenografts to verify correct NPD implantation and to determine if 5 nm ^{177}Lu-AuNP resulted in a more homogeneous dose distribution then 15 nm ^{177}Lu-AuNP (Lai et al., 2017). Tumor growth was monitored and general toxicity was assessed by monitoring body weight. Similar to direct i.t. administration of radiolabeled AuNP, the NPD may allow migration of some AuNP released from the NPD site in the tumor to re-distribute to other organs resulting in normal tissue exposure. Therefore, tissue biodistribution studies were performed to evaluate the extent of ^{177}Lu-AuNP redistribution and its effect on the absorbed doses to normal organ doses. To our knowledge, our report is the first to describe brachytherapy of human BC tumor xenografts in mice using radiolabeled AuNP incorporated into a NPD.

4.3 MATERIAL AND METHODS

4.3.1 PREPARATION OF ^{177}LU-AUNP AND NPD

^{177}Lu-AuNP were synthesized as reported (Yook et al., 2015a, Lai et al., 2017). Briefly, a diblock copolymer with a polyethylene glycol (PEG) (2 kDa) block, and a block of polyglutamide with 8 pendant 1,4,7,10-tetraazacyclododecane-1,4,7,10-tetraacetic acid (DOTA) chelators and 4 terminal lipoic acid (LA) groups [PEG-*p*Glu(DOTA)$_8$-LA$_4$] was

synthesized (Yook et al., 2015b). PEG-*p*Glu(DOTA)$_8$-LA$_4$ (3 µg) was radiolabeled by incubation with $^{177}LuCl_3$ (7-25 MBq) (PerkinElmer) in 1 M sodium acetate buffer (10 µL, pH 5.5) at 80˚C for 30 mins. ^{177}Lu-AuNP were constructed by incubating PEG-*p*Glu(DOTA)$_8$-LA$_4$-^{177}Lu with 5 nm (1.9 mL) or 15 nm (1 mL) AuNP (Ted Pella; 5.0 ×10^{13} or 1.4 ×10^{12} particles/mL, respectively) at 60˚C on a shaker for 1 h in low binding microcentrifuge tubes (Axygen). Unlabeled 5 nm or 15 nm PEGylated AuNP were constructed by incubation with PEG-*p*Glu(DOTA)$_8$-LA$_4$. Radiolabeled and PEGylated AuNP were rinsed twice by suspending in d.d. H_2O, then recovered by ultracentrifugation at 15,000 × g for 1 h (5 nm) or 45 min (15 nm) at 4˚C. NPD were constructed as reported (Lai et al., 2016) using very low viscosity (VLV <20 mPa) ultrapure sodium alginate (Pronova™, NovaMatrix) reconstituted in 0.5% NaCl for 45 min (6% w/v) to form a gel, then mixing with radiolabeled AuNP to a final concentration of 0.12 mg of AuNP/3 µL of gel (9.5 × 10^{13} 5 nm size and 3.5 × 10^{12} 15 nm size). The resulting AuNP-gel mixture was injected into molds that produced NPD with dimensions similar to a conventional brachytherapy seed (0.8 mm × 4 mm). The alginate NPD were crosslinked in 10% $CaCl_2$ in d.d. H_2O.

4.3.2 CELL CULTURE AND TUMOUR XENOGRAFT MOUSE MODELS

MDA-MB-468 and MDA-MB-231 human BC cells (ATCC, Manassas, VA, USA), which exhibit greater and lower sensitivity in vitro to γ-radiation respectively (Cai et al., 2008), were cultured at 37 °C in 5% CO_2 in DMEM supplemented with 5% penicillin/streptomycin and 10% fetal bovine serum (FBS, Gibco-Invitrogen). MDA-MB-468 or MDA-MB-231 cells were recovered by trypsinization and 2 × 10^6 cells were suspended in 50 µL of sterile PBS and injected subcutaneously (s.c.) into the right flank of female non-obese diabetic severe combined immunodeficient (NOD/SCID) mice (Charles River). Tumors were allowed to grow to a diameter of 8 mm prior to NPD implantation.

4.3.3 BRACHYTHERAPY AND NORMAL TISSUE TOXICITY ASSESSMENT

Mice bearing MDA-MB-231 xenografts were randomized into treatment groups (n=7) as follows: (i) untreated (ii) PEGylated AuNP, (iii) 15 nm ^{177}Lu-AuNP (8.5 MBq), and (iv) 5 nm ^{177}Lu-AuNP (15 MBq). All AuNP were delivered via implantation of a NPD. Similarly, mice bearing MDA-MB-468 xenografts were randomized into these treatment groups (n=7) with the exception that 5 nm ^{177}Lu-AuNP (15 MBq) were not studied. The radioactivity dose for treatment was based on our report of local treatment of MDA-MB-468 tumors (6 mm diameter) in mice with ^{177}Lu-AuNP but scaled for the larger tumor size (8 mm diameter) in the current study (0.04 MBq/mm^3) (Yook et al., 2016a). NPD implantation into the tumors was carried out under anesthesia (isoflurane in 2% O_2) as reported using a template mounted stage and an 18G seeding needle (Eckert & Ziegler BEBIG, Inc. Oxford, CT) (Lai et al., 2016). Only one NPD was implanted per tumor. Mice bearing MDA-MB-468 xenografts were monitored for tumor growth for 71 days or until the tumor size reached the humane endpoint (>15 mm) as specified by the animal care protocol, when they were euthanized. The survival of mice bearing MDA-MB-468 xenografts were followed for 78 days. Mice bearing MDA-MB-231 xenografts were monitored for 14 days due to their more rapid growth rate, then euthanized for blood collection and hematology analysis, when tumor size in most mice was nearing the humane endpoint. The tumor volume (V) was measured every 3-7 days by two independent observers using calipers and calculated as V = (length×width^2)/2. The tumor growth index (TGI) was calculated by dividing the tumor volume at each time point by the initial tumor volume

prior to treatment. Body weight was monitored and the body weight index (BWI) was calculated by dividing the body weight at the measured time point by the initial body weight, in order to assess the general toxicity of the treatment. At the 14 days end-point for mice with MDA-MB-231 tumors, blood from control and ^{177}Lu-AuNP treated mice were collected by cardiac puncture and a complete blood cell (CBC) count was obtained using a Hemavet 950FS analyzer (DRE Scientific Ltd., Oxford, CT, USA). Hematology analysis included white blood cell (WBC), red blood cell (RBC), and platelet (PLT) counts, and hematocrit (Hct) and haemoglobin (Hb). Serum alanine aminotransferase (ALT) and creatinine (Cr) were also measured at this time point using Infinity Creatinine and Infinity ALT/GPT clinical chemistry kits (Fisher Diagnostics, Middletown, VA, USA).

4.3.4 SPECT/CT IMAGING AND TUMOUR DOSIMETRY

Mice with s.c. MDA-MB-231 tumors administered 15 nm or 5 nm ^{177}Lu-AuNP were imaged using a microSPECT/CT tomograph (NanoSPECT, Bioscan) at 1, 24, 48 h and 7 days post implantation of the NPD to verify the location of the implant and estimate the dose distribution. The acquisition time was increased from 150 s/projection at 1 h p.i. to 309 s/projection at 7 days p.i. to compensate for radioactive decay and obtain images with comparable intensities. SPECT images were collected using a 0.3×0.3×0.3 mm^3 voxel size and cone-beam CT images were collected using a 0.2×0.2×0.2 mm^3 voxel size. SPECT and CT images were co-registered using InvivoScope software (Bioscan) and SPECT images were registered temporally using manual and automated rigid registration techniques on Inveon Research Workplace software (Siemens). Dose distributions were determined by voxel based convolution dose kernel methods using Monte Carlo N-Particle software (MCNP 5, Los Alamos National Security) (Lai et al., 2017). A voxel dose kernel (VDK) for ^{177}Lu, comprising of voxel level S-values, was created using a cubic geometry and voxel sizes of 0.3×0.3×0.3 mm^3. A 6.3×6.3×6.3 mm^3 volume of interest (VOI) corresponding to a 21×21×21 array was selected using MATLAB (Mathworks) from each SPECT image to obtain a 3D radioactivity distribution at each time point. Each radioactivity distribution was convolved by the VDK and each voxel of the distribution integrated over all of the time points to infinity to obtain the final dose distribution. The radiation spectrum for ^{177}Lu was obtained from Medical Internal Radiation Dose (MIRD) radionuclide data (Eckerman and Endo, 2008) and breast tissue composition (ρ = 1.02 g cm^{-3}) was from the International Commission on Radiation Units & Measurements (ICRU) (ICRU, 1989).

4.3.5 BIODISTRIBUTION AND NORMAL ORGAN DOSIMETRY

Mice bearing MDA-MB-231 xenografts (n=4) were implanted with a NPD containing 3.0 MBq of ^{177}Lu-AuNP (9.5×10^{13} particles for 5 nm size and 3.5×10^{12} particles for 15 nm size). At 1, 3, 8, and 14 days post-implantation, the mice were sacrificed and the tumor, samples of blood and normal tissues were collected and the radioactivity (CPM) in each measured in a γ-counter (Wizard Model 1480, PerkinElmer) and converted to Bq by applying a conversion factor (0.19 Bq/CPM). Tissue radioactivity concentrations were expressed as percent administered radioactivity per gram of tissue (%IA/g) which was corrected for radioactive decay for evaluation of biodistribution. For organ dosimetry, the %IA/organ was obtained by multiplying the %IA/g results from biodistribution measurements (at 1, 3, 8, and 14 days)

by the standard organ weights for mice (Bitar et al., 2007). The average tumor weight (g) from the biodistribution study was used to estimate the tumor volume for dosimetry, assuming a density of 1 g/cm^3. The cumulative radioactivity (Ã$_S$ = Bq × s) for each source organ was determined by calculating the area under the radioactivity vs. time curve between 0-7 days using the Trapezoidal Rule, incorporating radioactive decay for each of the values. The cumulative radioactivity from 7 days to infinity (Bq × s) was calculated by dividing the final radioactivity at 7 days (Bq) by the decay constant for ^{177}Lu (1.2×10^{-6} s^{-1}), thus assuming further elimination only by physical decay. The absorbed dose to target normal organs was calculated using the MIRD formalism by multiplying the cumulative radioactivity in each source organ by the corresponding S-value for mice, obtained from Bitar et al. (Bitar et al., 2007). The dose deposited in the tumor was calculated using OLINDA/EXM software (Vanderbilt University) and a sphere model (8 mm diameter) to generate an S-value for a tumor with assumed density of 1 g/cm^3. All animal studies were conducted in compliance with Canadian Council on Animal Care (CCAC) guidelines and were performed under a protocol approved by the Animal Care Committee at the University Health Network (AUP # 2780.9).

4.3.6 STATISTICAL ANALYSIS

Results were expressed as mean ± standard deviation (SD) and tested for statistical significance (P<0.05) using two way ANOVA, paired t-tests, and Mantel-Cox test using Prism 6.01 (Graphpad) software.

4.4 RESULTS

4.4.1 BRACHYTHERAPY AND NORMAL TISSUE TOXICITY

The TGI was monitored for mice with MDA-MB-231 or MDA-MB-468 tumors treated with 15 nm ^{177}Lu-AuNP (8.5 MBq, 3.52×10^{12} particles) or 15 nm PEGylated AuNP, or for mice with MDA-MB-231 tumors treated with 5 nm ^{177}Lu-AuNP (15 MBq, 9.52×10^{13} particles) only. All AuNP were incorporated into a NPD. TGI was compared to the untreated control group or mice treated with unlabeled PEGylated AuNP (Fig. 4.1). The TGI curve for mice treated with PEGylated AuNP was not significantly different than the TGI curve for untreated control mice (P=0.8) for both MDA-MB-468 (Fig. 4.1a) and MDA-MB-231 tumors (Fig. 4.1b). Treatment with 15 nm ^{177}Lu-AuNP resulted in tumor growth arrest for the MDA-MB-468 tumors and tumor growth inhibition for MDA-MB-231 tumors, when compared to the final TGI time points for untreated mice (P=0.7 and P=0.002, respectively) or mice treated with PEGylated AuNP (P=0.02 and P=0.02, respectively). The tumor growth inhibitory effect of 15 nm ^{177}Lu-AuNP was greater in mice with more radiation sensitive MDA-MB-468 tumors, resulting in tumor growth arrest with minimal regrowth up to 71 days compared to the PEGylated AuNP treated group. At 71 days, the mean TGI in mice with MDA-MB-468 tumors treated with 15 nm ^{77}Lu-AuNP (TGI=1.5±1.3) was 3.2 fold significantly lower than in mice treated with PEGylated AuNP (TGI=4.8±1.3) (P<0.02). At 43 days, when the untreated control mice reached the humane tumor size endpoint, the mean TGI in mice treated with 15 nm ^{177}Lu-AuNP (TGI=1.4±0.9) was 1.6-fold significantly lower than for untreated control mice

(TGI=2.2±0.5; P<0.0001). For mice with MDA-MB-231 tumors, the growth inhibition at 14 days for tumors treated with 15 nm ^{177}Lu-AuNP resulted in a mean TGI (TGI=2.8±0.09) that was 1.3 fold significantly lower than untreated mice (TGI=3.7±1.0; P=0.02) or mice treated with PEGylated AuNP (TGI=3.8±1.0; P=0.002). Groups of mice with MDA-MB-231 tumors were treated with 5 nm ^{177}Lu-AuNP (15 MBq). These mice exhibited a mean TGI (TGI=2.4±0.2) that was 1.6-fold significantly lower than untreated mice (P<0.0001) or mice with MDA-MB-231 tumors treated with PEGylated AuNP (P<0.0001). The TGI in MDA-MB-231 tumor bearing mice were not statistically different for 15 nm ^{177}Lu-AuNP (8.5 MBq) and 5 nm ^{177}Lu-AuNP (15 MBq) treated groups, despite the higher administered radioactivity in the 5 nm ^{177}Lu-AuNP group (P=0.4). At 14 days, the tumor size in mice bearing MDA-MB-231 xenografts reached the humane endpoint (>15 mm diameter) as specified by the animal care protocol and these mice were euthanized, so monitoring of tumor growth beyond this time point was not possible.

^{177}Lu-AuNP at the amounts administered (15 MBq, 9.5×10^{13} particles for 5 nm size and 8.5 MBq, 3.5×10^{12} particles for the 15 nm size) were not generally toxic as indicated by no body weight loss in treated mice compared to mice treated with PEGylated AuNP or untreated mice (Fig. 1c,d). The mean BWI at 71 days in MDA-MB-468 tumor bearing mice treated with 15 nm ^{177}Lu-AuNP (BWI=1.0±0.02) was not significantly different than mice treated with PEGylated-AuNP (BWI=1.1±0.003; P=0.6). The mean BWI for untreated mice (BWI=1.0±0.02) with MDA-MB-468 tumors at 43 days when these tumors reached the human tumor size endpoint, was not significantly different than mice treated with the 15 nm ^{177}Lu-AuNP (BWI=1.0±0.07; P=0.6) or PEGylated-AuNP (BWI=1.1±0.06; P=0.9). The mean BWI at 14 days in mice with MDA-MB-231 tumors treated with 15 nm ^{177}Lu-AuNP (BWI=1.1±0.05) was not significantly different than control untreated mice (BWI=1.0±0.03; P=0.7) or mice receiving PEGylated AuNP (BWI=1.1±0.03; P=0.7) (Fig. 1d). The absence of toxicity was confirmed in hematology, kidney and liver function results from blood collected at 14 days post implantation, for mice bearing MDA-MB-231 xenografts and treated with 8.5 MBq of 15 nm ^{177}Lu-AuNP NPD or 15 MBq of 5 nm ^{177}Lu-AuNP NPD as compared to the unlabeled PEGylated AuNP NPD and untreated control groups (Table 4.1). There were no significant differences in RBC, Hb, Hct, PLT, Cr and ALT between the 5 nm or 15 nm ^{177}Lu-AuNP treated groups or between mice treated with ^{177}Lu-AuNP and mice receiving unlabeled PEGylated AuNP or control untreated mice, although WBC results were inconclusive. Kaplan-Meier curves were plotted to compare the survival of mice with MDA-MB-468 tumors treated with ^{177}Lu-AuNP and PEGylated-AuNP to untreated mice (Fig. 4.2). MDA-MB-468 tumor bearing mice receiving 15 nm ^{177}Lu-AuNP NPD had a significantly prolonged median survival of 73 days when compared to untreated mice for mice (34 days) (P=0.02) and a non-significantly trend towards increased survival compared to mice treated with PEGylated AuNP NPD (49 days) (P=0.09). At 78 days, there were 3/7 mice treated with 15 nm ^{177}Lu-AuNP surviving while there were 0 mice surviving that were treated with PEGylated AuNP or untreated mice. Complete regression of the tumor was observed in 1/7 mice treated with ^{177}Lu-AuNP. Long term survival analysis was not performed on mice bearing MDA-MB-231 tumors due to the rapid rate of tumor growth resulting in animals reaching endpoint by 14 days, and the requirement for euthanization at 14 days for blood collection and hematology analysis.

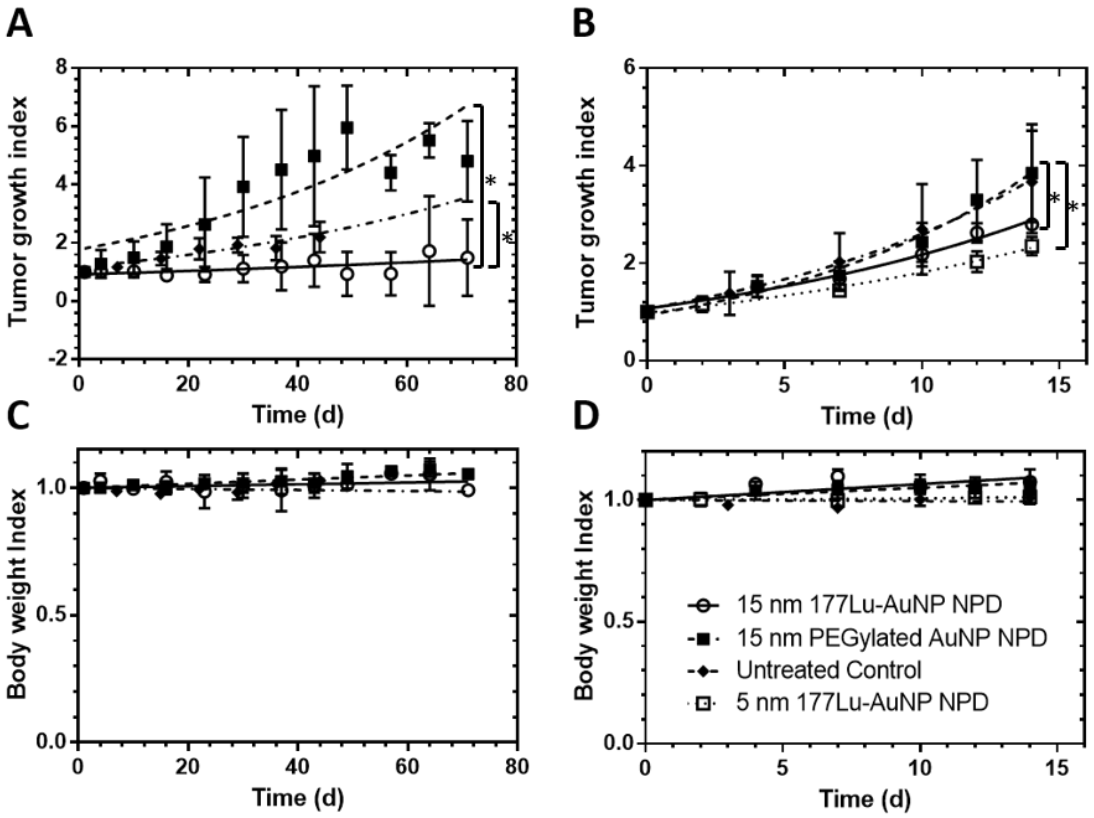

Figure 4.1 Tumour growth and body weight indices as a function of time. Tumour growth index (TGI) vs. time (days) for NOD/SCID mice (n=7) bearing s.c. (a) MDA-MB-468 or (b) MDA-MB231 human BC xenografts treated with a NPD incorporating 15 nm ^{177}Lu-AuNP (8.5 MBq, 3.52×10^{12} particles), 15 nm PEGylated AuNP or in mice receiving no treatment. Groups of mice with MDA-MB-231 xenografts were also treated with 5 nm ^{177}Lu-AuNP (15 MBq, 9.52×10^{13} particles). Body weight index (BWI) for mice with (c) MDA-MB-468 or (d) MDA-MB-231 tumours receiving these treatments. Note the tumor growth arrest in MDA-MB-468 tumor bearing animals treated with 15 nm ^{177}Lu-AuNP (a).

Table 4.1 Hematology and serum creatinine (Cr) and alanine aminotransferase (ALT) at 14 days post treatment with a NPD incorporating ^{177}Lu-AuNP in mice with s.c. MDA-MB-231 human breast cancer xenografts. Values are normalized with respect to the untreated control and errors (±) represent standard deviations.

MDA-MB-231	Untreated Control	15 nm ^{177}Lu-AuNP	15 nm PEGylated AuNP	5 nm ^{177}Lu-AuNP
WBC	1	1±1.5	0.8±0.5	1±1
RBC	1.00±0.03	1.0±0.1	0.93±0.08	0.86±0.06
Hb	1.00±0.03	1.00±0.09	0.95±0.07	0.85±0.05
Hct	1.00±0.04	1.0±0.2	0.91±0.08	0.86±0.06
PLT	1.0±0.6	0.6±0.9	0.2±2	1.0±0.6
Cr	1.0±0.5	1.3±0.4	1.3±0.4	0.9±0.5
ALT	1.0±0.3	0.8±0.9	0.8±0.3	1.0±0.2

*White blood cell (WBC), red blood cell (RBC), hemoglobin (Hb), Hematocrit (Hct), platelet (PLT), creatinine (Cr), and alanine aminotransferase (ALT).

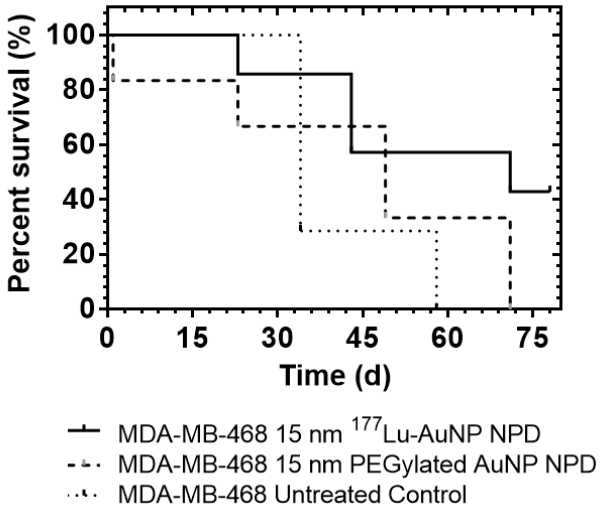

Figure 4.2 Percentage survival of treated animals as a function of time. Kaplan-Meier survival curves for mice (n=7) with s.c. MDA-MB-468 human breast cancer xenografts treated with a NPD incorporating 15 nm ^{177}Lu-AuNP (8.5 MBq, 3.52×10^{12} particles), unlabeled PEGylated AuNP or untreated mice. The median survival of mice treated with 15 nm ^{177}Lu-AuNP NPD was 73 d as compared to 49 d for unlabeled PEGylated AuNP (P=0.09) and 34 d for untreated control (P=0.02).

4.4.2 SPECT/CT IMAGING AND TUMOUR DOSIMETRY

SPECT/CT images (Fig. 4.3) revealed that radioactivity remained mainly in the NPD, but a greater amount was retained in the NPD incorporating 15 nm ^{177}Lu-AuNP than the NPD with 5 nm ^{177}Lu-AuNP at 7 d, suggesting greater release of 5 nm ^{177}Lu-AuNP from the NPD. This was confirmed by comparing the maximum doses [Gy per Bq administered (Gy/Bq)] delivered for the tumor dose distributions (Fig. 4.4) which revealed 1.7 fold greater dose for the 15 nm ^{177}Lu-AuNP NPD (maximum dose of 4.4×10^{-3} Gy/Bq) as compared to the 5 nm ^{177}Lu-AuNP NPD (maximum dose of 2.6×10^{-3} Gy/Bq). The one-dimensional dose profiles, along the x-axis intersecting the NPD center, in Gy/Bq as a function of x-position (mm) are shown in Fig. 4.3 (left panel) and illustrate the higher maximum dose for the NPD incorporating 15 nm ^{177}Lu-AuNP. When plotted on a logarithmic scale (Fig. 4.3; right panel), the dose at 3 mm from the NPD, near the tumor periphery is 10-fold greater for the NPD incorporating the 5 nm ^{177}Lu-AuNP than for the NPD incorporating 15 nm ^{177}Lu-AuNP. However, although the dose profiles demonstrate differences in intratumoral dose distributions, the overall tumor retention of radioactivity for both 15 nm and 5 nm ^{177}Lu-AuNP in the NPD were similar as shown in the biodistribution results.

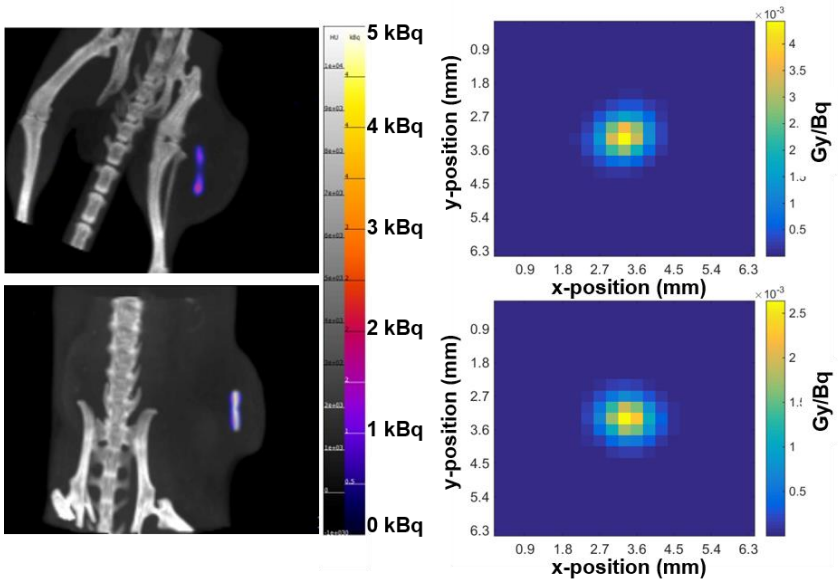

Figure 4.3 SPECT/CT image (left) at 7 days post-implantation and representative cross sectional maps of the dose distribution (right) in Gy per Bq administered (Gy/Bq) of a NPD incorporating 2.5 MBq of 15 nm ^{177}Lu-AuNP (top images) or 2.5 MBq of 5 nm ^{177}Lu-AuNP (bottom images) into a MDA-MB-468 human breast cancer xenograft in a NOD/SCID mouse. The representative z-slice chosen for the dose maps contains the maximum Gy/Bq in the tumour volume (5 nm: z=15, 15 nm: z=6). Note the difference in maximum dose (Gy/Bq) between dose distributions from 15 nm (top, right) and 5 nm (bottom, right) ^{177}Lu-AuNP.

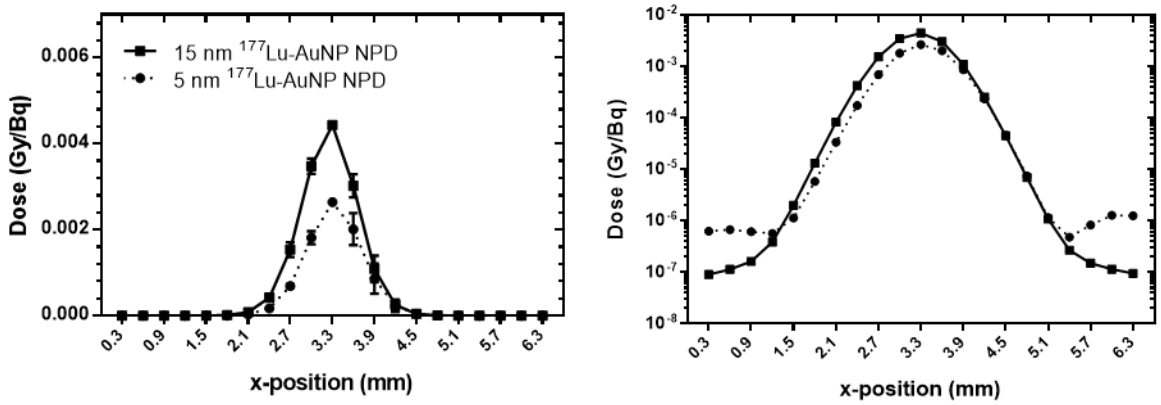

Figure 4.4 A one-dimensional dose profile intersecting the tumour and NPD at the location of maximum dose, in Gy per Bq administered (Gy/Bq) as a function of x-position (mm), plotted on a linear scale (left) and logarithmic scale (right), of the implanted 15 nm ^{177}Lu-AuNP NPD (solid line) and 5 nm ^{177}Lu-AuNP NPD (dashed line). Note the 2-fold difference in maximum dose (Gy/Bq) at x-position 3.3 mm between 15 nm and 5 nm ^{177}Lu-AuNP NPD, and 10-fold difference in peripheral dose (Gy/Bq) at x-position 0.3/6.3 mm.

4.4.3 BIODISTRIBUTION AND NORMAL ORGAN DOSIMETRY

Biodistribution studies (Fig. 4.5) revealed that the majority of radioactivity remained in the tumor up 15 days post implantation, with only minimal redistribution to other organs at 1 day post implantation for both 5 nm and 15 nm ^{177}Lu-AuNP NPD. For the 15 nm ^{177}Lu-AuNP treatment group tumor radioactivity at 1 day was 71±12 %IA/tumor and 44±4 %IA/g, which decreased by 15% and 25%, respectively at 15 days to 60±6 %IA/tumor ($P<0.0001$) and 33±7 %IA/g ($P<0.0001$). The liver had the highest normal organ uptake of radioactivity for mice receiving 15 nm ^{177}Lu-AuNP, with 2.1±2 %IA/organ and 2.2±2 %IA/g at 1 day post-implantation of the NPD. However liver radioactivity decreased to 0.2±0.1 %IA/organ and 0.16±0.1 %IA/g at 15 days. Kidney radioactivity was 0.3±0.2 %IA/organ and 1.0±0.6 %IA/g at 1 day which decreased to 0.033±0.007%IA/organ and 0.12±0.02 %IA/g, respectively, at 15 days. For the 5 nm ^{177}Lu-AuNP NPD treatment group, radioactivity in the tumor at 1 day was 73±7 %IA/tumor and 363±76 %IA/g, which decreased at 15 days to 71±1 %IA/organ and 51±15 %IA/g ($P<0.0001$), respectively. In contrast to mice receiving 15 nm ^{177}Lu-AuNP, the kidneys had the highest normal tissue uptake in mice receiving 5 nm ^{177}Lu-AuNP with 0.4±0.1 %IA/organ and 1.8±0.4 %IA/g at 1 day, which decreased to 0.11±0.02 %IA/organ and 0.39±0.04 %IA/g at 15 days. In contrast, the liver uptake at 1 day was very low with 0.6±0.3 %IA/organ and 0.5±0.2 %IA/g, which decreased to 0.03±0.01 %IA/organ and 0.03±0.01 %IA/g at 15 days.

The absorbed dose per unit administered radioactivity (Gy/Bq) to normal organs were calculated using S-values for mice from Bitar et al. (Bitar et al., 2007), and the doses absorbed by the tumor were calculated using OLINDA/EXM (Ver. 1.0) software (Stabin et al., 2005). These doses are summarized in Table 4.2. For mice treated with the 15 nm ^{177}Lu-AuNP incorporated into the NPD the absorbed dose to the tumor was 1.7±0.6 $\times 10^{-6}$ Gy/Bq and the highest normal organ doses were absorbed by the liver 0.17±0.06 $\times 10^{-6}$ Gy/Bq, followed by the kidneys ((0.07± 0.01) $\times 10^{-8}$ Gy/Bq). For the amount of radioactivity administered using the 15 nm ^{177}Lu-AuNP NPD (8.5 MBq), the absorbed dose (Gy) to the tumor was 14±5 Gy, to the liver was 1.4±0.5 Gy, and to the kidneys was 0.6±0.1 Gy. The absorbed dose to the tumor was 2.5±0.9 $\times 10^{-6}$ Gy/Bq in mice treated with 5 nm ^{177}Lu-AuNP and the highest normal organ doses were absorbed by the kidneys (0.20±0.01 $\times 10^{-6}$ Gy/Bq), followed by the liver (0.020±0.003 $\times 10^{-8}$ Gy/Bq). For the amount of radioactivity administered using the 5 nm ^{177}Lu-AuNP NPD (15 MBq), the absorbed dose (Gy) to the tumor was 38±14 Gy, to the kidneys was 3.1±0.2 Gy, and to the liver was 0.30±0.05 Gy. The average absorbed dose to the whole body was 8.5±0.3 $\times 10^{-10}$ Gy/Bq and 2.7±0.3 $\times 10^{-10}$ Gy/Bq, for the 15 nm ^{177}Lu-AuNP and 5 nm ^{177}Lu-AuNP treatment groups, respectively. A comparison of normalized organ doses (Gy/Bq) between mice treated with 15 nm or 5 nm ^{177}Lu-AuNP NPD revealed significant differences ($P<0.05$) between the absorbed doses delivered to the kidneys, liver, lungs, pancreas, spleen and stomach, but not to the tumor.

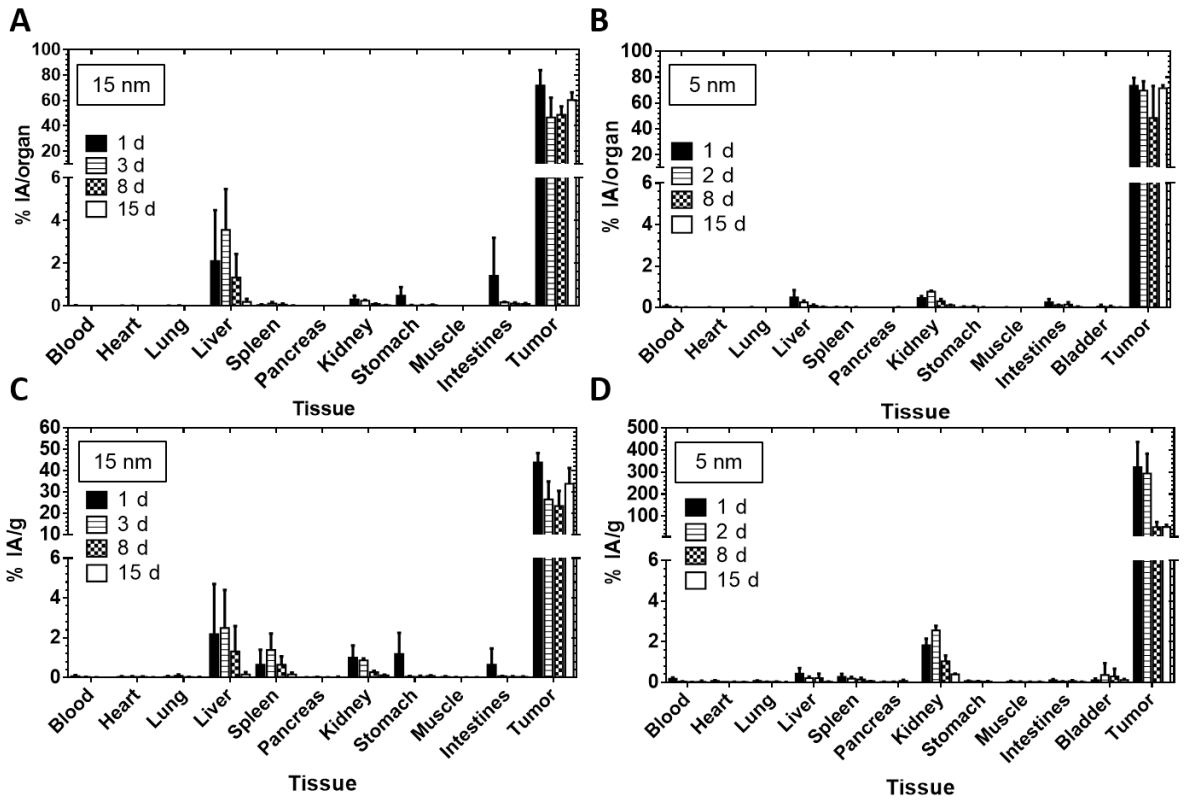

Figure 4.5 Biodistribution (%IA/organ) of ^{177}Lu-AuNP in selected organs up to 15 days post implantation of a NPD incorporating (a) 15 nm ^{177}Lu-AuNP or (b) 5 nm ^{177}Lu-AuNP. The corresponding %IA/g values for the tumour and normal tissues are shown in panels (c) and (d). Note the high accumulation of 15 nm and 5 nm ^{177}Lu-AuNP in the tumors. Note also the low normal tissue accumulation of 15 nm ^{177}Lu-AuNP in the liver, and 5 nm ^{177}Lu-AuNP in the kidneys.

Table 4.2 Organ doses in Gy per Bq administered (Gy/Bq) from biodistribution of 5 nm and 15 nm ^{177}Lu-AuNP NPD treated animals, determined using organ S-values obtained from Bitar et al.

	Absorbed dose (Gy/Bq)	
Tissue	5 nm ^{177}Lu-AuNP NPD	15 nm ^{177}Lu-AuNP NPD
Bladder	$(10\pm2)\times10^{-11}$	$(2\pm1)\times10^{-10}$
Brain *	$(6.0\pm0.7)\times10^{-12}$	$(2.3\pm0.9)\times10^{-11}$
Carcass *	$(2.8\pm0.3)\times10^{-10}$	$(8\pm3)\times10^{-10}$
Colon	$(9\pm1)\times10^{-9}$	$(2\pm1)\times10^{-8}$
Fat	$(1.35\pm0.09)\times10^{-9}$	$(9\pm4)\times10^{-10}$
Heart	$(2.0\pm0.2)\times10^{-9}$	$(3\pm1)\times10^{-9}$
Kidney (L)*	$(0.21\pm0.01)\times10^{-6}$	$(7\pm1)\times10^{-8}$
Kidney (R)*	$(0.20\pm0.01)\times10^{-6}$	$(7\pm1)\times10^{-8}$
Liver *	$(2.0\pm0.3)\times10^{-8}$	$(0.17\pm0.06)\times10^{-6}$
Lungs *	$(5.9\pm0.8)\times10^{-9}$	$(1.8\pm0.6)\times10^{-8}$
Marrow (L)	$(1.2\pm0.1)\times10^{-11}$	$(3\pm1)\times10^{-11}$
Marrow (R)	$(1.3\pm0.1)\times10^{-11}$	$(3\pm1)\times10^{-11}$
Ovary (L)	$(5.9\pm0.7)\times10^{-10}$	$(8\pm5)\times10^{-10}$
Ovary (R)	$(2.1\pm0.2)\times10^{-10}$	$(3\pm1)\times10^{-10}$
Pancreas *	$(1.2\pm0.2)\times10^{-8}$	$(7\pm2)\times10^{-9}$
Skull *	$(6.9\pm0.8)\times10^{-12}$	$(2\pm1)\times10^{-11}$
Small Intestines	$(7\pm1)\times10^{-9}$	$(2\pm1)\times10^{-8}$
Spinal cord *	$(5.8\pm0.5)\times10^{-11}$	$(1.4\pm0.6)\times10^{-10}$
Spleen *	$(10\pm2)\times10^{-9}$	$(4\pm2)\times10^{-8}$
Stomach wall *	$(9\pm2)\times10^{-9}$	$(4\pm2)\times10^{-8}$
Stomach contents *	$(8\pm1)\times10^{-9}$	$(3\pm2)\times10^{-8}$
Stomach *	$(1\pm0.1)\times10^{-8}$	$(4\pm2)\times10^{-8}$
Thyroid *	$(8\pm1)\times10^{-12}$	$(3\pm1)\times10^{-11}$
Uterus	$(1.4\pm0.2)\times10^{-10}$	$(3\pm2)\times10^{-10}$
Vertebrae *	$(7.9\pm0.7)\times10^{-11}$	$(1.7\pm0.7)\times10^{-10}$
Tumour	$(2.6\pm0.9)\times10^{-6}$	$(1.7\pm0.6)\times10^{-6}$

(*) Indicating significant differences between the absorbed dose (Gy/Bq) to the organs from 5 nm and 15 nm ^{177}Lu-AuNP NPD.

4.5 DISCUSSION

In this study, we investigated for the first time the effectiveness of ^{177}Lu-AuNP delivered via an implantable NPD system for inhibiting the growth of human BC xenografts in NOD/SCID mice. The NPD system is composed of a porous biodegradable calcium alginate seed which has dimensions similar to a permanent brachytherapy seed into which ^{177}Lu-AuNP are incorporated. The retention of ^{177}Lu-AuNP in the NPD combined with the 2 mm maximum range of the β-particles emitted by ^{177}Lu produced a conformal radiation field resulting in tumor growth arrest in NOD/SCID mice with s.c. MDA-MB-468 xenografts and moderate inhibition of the growth of MDA-MB-231 tumors in NOD/SCID mice (Fig. 4.1a,b). Treatment with unlabeled PEGylated AuNP did not inhibit tumor growth which was not significantly different than in the untreated control (Fig. 4.1a,b). These results confirm the findings of our previous study in which

we achieved strong tumor growth inhibition in athymic mice with s.c. MDA-MB-468 xenografts directly injected intratumorally (i.t.) with ^{177}Lu-AuNP (Yook et al., 2016a). However, delivery of ^{177}Lu-AuNP via a NPD is more clinically translatable than direct i.t. injection since it allows PSI techniques to be applied, which permits scaling to larger tumors in BC patients and precise placement of the NPD incorporating the ^{177}Lu-AuNP to deliver the prescribed dose and minimize dose heterogeneities.

Tumor xenografts were established by s.c. inoculation of MDA-MB-468 or MDA-MB-231 human BC cells that have higher and lower sensitivity in vitro to γ-radiation, respectively (Cai et al., 2008). MDA-MB-231 were less responsive than MDA-MB-468 tumors to treatment with a NPD incorporating ^{177}Lu-AuNP (Fig. 4.1). Tumor growth was arrested and survival prolonged in mice with MDA-MB-468 tumors implanted with a NPD incorporating 15 nm ^{177}Lu-AuNP (8.5 MBq; 3.5×10^{12} particles; Fig. 4.1a) while growth was only moderately inhibited in mice with MDA-MB-231 tumors treated with a NPD containing 5 nm ^{177}Lu-AuNP (15 MBq; 9.5×10^{13} particles) or 15 nm ^{177}Lu-AuNP (8.5 MBq; Fig. 4.1b). There were no significant differences in tumor growth inhibition in mice with MDA-MB-231 tumors treated with a NPD incorporating 5 nm or 15 nm ^{177}Lu-AuNP, despite the 2-fold higher administered amount of radioactivity for the 5 nm ^{177}Lu-AuNP. The absorbed dose delivered to MDA-MB-231 tumors implanted with a NPD with 5 nm ^{177}Lu-AuNP (15 MBq) was >2-fold higher (38 Gy vs. 15 Gy; Table 4.2) than deposited in MDA-MB-468 tumors treated with a NPD with 15 nm ^{177}Lu-AuNP (8.5 MBq), but the growth of MDA-MB-231 tumors was inhibited while MDA-MB-468 tumors were growth-arrested. This illustrates the differential radiation insensitivity of these two tumors. Due to the rapid growth of MDA-MB-231 tumors, mice were monitored for 14 days after treatment with ^{177}Lu-AuNP, while mice with MDA-MB-468 tumors were monitored for 78 days. Our results agree with those previously reported by our group which demonstrated that MDA-MB-468 xenografts were growth-arrested for >90 days after i.t. injection of ^{177}Lu-AuNP (4.5 MBq; 6×10^{11} particles) and all mice survived up to 120 days (Yook et al., 2016a). In our previous study, we did not evaluate the tumor growth inhibitory effects of ^{177}Lu-AuNP on MDA-MB-231 tumors, but in vitro clonogenic survival (CS) assays at 14 d post treatment revealed a 6-fold lower sensitivity of MDA-MB-231 cells compared to MDA-MB-468 cells to non-targeted ^{177}Lu-AuNP incubated for 16 h (CS = 51.6 ± 12.7% vs. 8.4 ± 3.3%) (Yook et al., 2015a). This difference in radiosensitivity between BC types have been speculated to arise from differences in gene expression for proteins responsible for regulation of cell cycle, DNA damage and repair such as BRCA1 and p53 (Yoshikawa et al., 2000). However, a study by Haldar et al. demonstrated that the p53 expression levels were the same between MDA-MB-231 and MDA-MB-468 BC (Haldar et al., 1994). Radiation resistance in MDA-MB-231 cells may be mediated by increased expression of Bcl-2 and Bcl-xL anti-apoptotic proteins (Li et al., 2012), or by overexpression of the distal-less homeobox2 (DLX2) transcription factor which has been found to increase the CS in vitro of MDA-MB-231 cells exposed to γ-radiation (Choi et al., 2016).

It may be possible to improve the response of MDA-MB-231 tumors, and other radiation resistant BC to ^{177}Lu-AuNP, by administration of higher radioactivity amounts, which should be feasible due to the highly conformal radiation field

delivered by β-particles emitted by ^{177}Lu (maximum range = 2 mm) which limit normal tissue exposure. We found no significant decrease in BWI in mice treated with a NPD incorporating 15 nm ^{177}Lu-AuNP (8.5 MBq; 3.5×10^{12} particles) or 5 nm ^{177}Lu-AuNP (15 MBq; 9.5×10^{13} particles) compared to mice receiving a NPD with unlabeled PEGylated AuNP or normal saline treated control mice (Fig. 1c,d), indicating no general normal organ toxicity. No normal tissue toxicities were observed in the MDA-MB-231 tumor bearing animals according to normalized changes in blood cell count or increases in serum Cr and ATL as compared to the control animals. These results are consistent with the hematology and serum biochemistry results reported by Yook et al. collected 15 d.p.i. following i.t. injection of 30 nm ^{177}Lu-AuNP (Yook et al., 2016a), as well as the serum Cr results reported by Vilchis-Juarez et al. which found no statistical differences between the treated and untreated control groups (Vilchis-Juarez et al., 2014). Lack of observed tissue toxicities correspond to the low activities measure from the biodistribution study, and low normal organ doses which were below tolerance doses. Moreover, in our previous study, we found no significant decrease in BWI, complete blood cell counts (CBC) or increases in serum alanine aminotransferase (ALT) or creatinine (Cr) indicative of liver or kidney toxicity at 15 days post i.t. injection of up to 4.5 MBq (6×10^{11} particles) of 30 nm ^{177}Lu-AuNP (Yook et al., 2016a). Nonetheless, it is possible that BC patients may experience some local radiation-induced toxicities from implantation of a NPD incorporating ^{177}Lu-AuNP such as erythema or telangiectasia as has been previously reported for PSI brachytherapy (Pignol et al., 2015)

The absence of significant normal tissue toxicity is likely due to retention of ^{177}Lu-AuNP at the intratumoral implantation site of the NPD which results in low accumulation in normal organs (Fig. 4.5) and low absorbed doses in these organs (Table 4.2). ^{177}Lu-AuNP (5 or 15 nm) incorporated into a NPD exhibited lower uptake of radioactivity in the liver and spleen compared to our previous study of directly i.t. injected 30 nm ^{177}Lu-AuNP (Yook et al., 2016a), but there was increased kidney uptake. Liver radioactivity after implantation of a NPD incorporating 15 nm or 5 nm ^{177}Lu-AuNP ranged from 2.2-2.5% IA/g and 0.2-0.5% IA/g, respectively (Fig. 4.5) from 1-3 days post-implantation compared to 8.5 ± 4.3 %IA/g at 2 days post-i.t. injection of 30 nm ^{177}Lu-AuNP (Yook et al., 2016a). Spleen uptake was lower for 15 nm ^{177}Lu-AuNP implanted into a tumor via the NPD (0.7-1.4% IA/g from 1-3 days; Fig. 4.5) compared to i.t. injected 30 nm ^{177}Lu-AuNP (5.4 ± 4.1% IA/g at 2 days) but not for 5 nm ^{177}Lu-AuNP (0.3-0.2% IA/g from 1-3 days) (Yook et al., 2016a). Kidney uptake was higher for both the 15 nm and 5 nm ^{177}Lu-AuNP (0.9-1.0%IA/g and 1.8-2.6%IA/g, respectively from 1-3 days) compared to i.t. injected 30 nm ^{177}Lu-AuNP (<1% IA/g at 48 h) (Yook et al., 2016a). There was higher kidney uptake in mice implanted with a NPD incorporating 5 nm ^{177}Lu-AuNP than 15 nm ^{177}Lu-AuNP, consistent with excretion of smaller AuNP by the kidneys with larger AuNP sequestered by the liver and spleen (Perrault et al., 2009).

The placement of the NPD was verified by SPECT/CT and dose maps were constructed to assess the intratumoral dose distribution based on Monte Carlo techniques (Lai et al., 2017). The dose distributions remained concentric around the NPD for both 5 nm and 15 nm ^{177}Lu-AuNP, but the NPD with 5 nm ^{177}Lu-AuNP had greater release of radioactivity

as previously reported (Lai et al., 2016). The consequence of greater release of 5 nm ^{177}Lu-AuNP from the NPD was a maximum dose 1.7-fold lower compared to a NPD incorporating 15 nm ^{177}Lu-AuNP. The dose (Gy/Bq) at the peripheries of the irradiated volume was also 10 fold higher for the NPD with 5 nm ^{177}Lu-AuNP than the 15 nm ^{177}Lu-AuNP. The intratumoral diffusion of ^{177}Lu-AuNP released from the NPD provides an advantage compared to conventional permanent brachytherapy seeds, since it may allow selection of a particular sized AuNP to achieve the desired radiation transport. Moreover, a more energetic and longer range β-emitter such as ^{90}Y (Eβ = 2.2 MeV; maximum range = 10-12 mm) may be selected to provide greater depth of radiation penetration within the tumor than achieved by the lower energy and shorter range β-particles emitted by ^{177}Lu (Eβ=0.6-0.7 MeV; maximum range = 2 mm) (Lai et al., 2017). The total absorbed doses in the tumor per Bq administered (Gy/Bq) were 1.7×10^{-6} Gy/Bq (15 ± 5 Gy) for a NPD incorporating 15 nm ^{177}Lu-AuNP (8.5 MBq; 3.5×10^{12} particles) and 2.5×10^{-6} Gy/Bq (38 ± 13 Gy) for a NPD containing 5 nm ^{177}Lu-AuNP (15 MBq; 9.5×10^{13} particles). These doses were similar to those deposited by direct i.t injection of 30 nm ^{177}Lu-AuNP (4.5 MBq; 6×10^{11} particles) in mice with MDA-MB-468 xenografts (22 Gy) (Yook et al., 2016a). A comparable dose (38 Gy) was deposited in C6 glioma xenografts in mice by i.t. injection of ^{177}Lu-AuNP (4 administrations of 2 MBq) (Vilchis-Juarez et al., 2014). These doses were lower than those typically prescribed for EBRT (50 Gy) of the breast and those prescribed to patients receiving permanent seed brachytherapy (90 Gy using ^{103}Pd or 124 Gy using ^{125}I) (Keller et al., 2005). However, the dose delivered is dependent on the amount of radiolabeled AuNP incorporated into the NPD and the radiation properties (e.g. β-particle energy, abundance and physical half-life) of the radionuclide. Keller et al. employed the time dose fractionation (TDF) formulation to determine equivalent doses of ^{103}Pd and ^{125}I which accounts for differences in dose rate, dependent on the rate of decay, and continuous dosing as to the conventional fractionation schedule of 2 Gy per day. Using the TDF formulation, we estimate that the required prescription dose for treatment of a BC patient following lumpectomy and using ^{177}Lu would be 71 Gy. If we assume an average of 71 NPD (*Section 1.3*) is required to adequately cover the treatment volume and the dose from 1 NPD delivers 1.7×10^{-6} Gy/Bq (*Section 4.4.3*), a specific activity of 0.59 MBq/3.52×10^{15} AuNP (1.67×10^{-10} Bq/AuNP) would be required. The $^{177}LuCl_3$ used in our experiments was obtained from Perkin Elmer, with a specific activity of 20 Ci/mg (2.15×10^{-10} Bq/^{177}Lu atom) at production. Assuming 57 PEG-*p*Glu(DOTA)$_8$-LA$_4$ per AuNP (*Section 3.3*) and 8 DOTA available for chelation to ^{177}Lu per PEG-*p*Glu(DOTA)$_8$-LA$_4$, the highest achievable specific activity is 9.80×10^{-5} Bq/AuNP, which is 5×10^5 times greater than the specific activity required to deliver 71 Gy to the treatment volume in a patient (1.67×10^{-10} Bq/AuNP). An even higher AuNP specific activity (5.03×10^{-4} Bq/AuNP) can be achieved using $^{177}LuCl_3$ obtained from ITG (Isotope Technologies Garching/Bruce Power, Garching, Germany), which has a specific activity of 103 Ci/mg at time of production.

Normal organ doses from a NPD incorporating ^{177}Lu-AuNP were very low (Table 4.2). The highest dose to the kidneys (3.1 ± 0.2 Gy, 2.0×10^{-7} Gy/Bq) was associated with a NPD incorporating 5 nm ^{177}Lu-AuNP (15 MBq; 9.5×10^{13} particles) while the highest dose to the liver (1.4 ± 0.5 Gy, 1.7×10^{-7} Gy/Bq) was deposited with a NPD containing 15 nm ^{177}Lu-AuNP (8.5 MBq; 3.5×10^{12} particles). These doses are higher than those previously reported for direct i.t. injection of 30 nm ^{177}Lu-AuNP (4.5 MBq; 6×10^{11} particles) which were 0.12 ± 0.05 Gy and 0.82 ± 0.49 Gy, due to the higher

administered radioactivity (Yook et al., 2016a). However, the normalized dose per amount of radioactivity (Bq) for direct i.t. injection of 30 nm ^{177}Lu-AuNP were similar for the liver (1.8×10^{-7} Gy/Bq), and over 10 times lower for the kidneys (2.7×10^{-8} Gy/Bq). Vilchis-Juarez et al., reported a dose of ~0.75 Gy to the kidneys and ~0.8-0.9 Gy to the liver following i.t. injection of 8 MBq ^{177}Lu-AuNP (20 nm AuNP) (Vilchis-Juarez et al., 2014). In humans the tolerance dose (TD; Gy) resulting in 5% complication rates over 5 years ($TD_{5/5}$) to the kidneys is 21.7 Gy from radionuclide therapy or 23 Gy for EBRT (Meredith et al., 2008). Similarly, the TD resulting in mild or no toxicity to the liver is 24 Gy for ^{90}Y-, ≤31 Gy for ^{131}I-, and 1.5 Gy for ^{186}Re-based therapies, while the $TD_{5/5}$ for EBRT is 30 Gy. The whole body doses to the mouse from NPD implantation incorporating 5 nm or 15 nm ^{177}Lu-AuNP were very low, at 0.0041 ± 0.0005 Gy (0.28 ± 0.03 mGy/MBq) and 0.007 ± 0.003 Gy (0.8 ± 0.4 mGy/MBq), respectively. The whole body dose limit generally accepted in humans is 2 Gy for radionuclide therapies to avoid radiation toxicity to the bone marrow (Forrer et al., 2009). However, extrapolation of these normal organ doses from mouse to humans is limited by the close proximity of organs in the mouse relative to each other, resulting in significant crossfire effects which may not occur in humans. Therefore, it is possible that whole body doses in humans would be even lower. Studies in humans will therefore be required to determine the normal organ dosimetry for patients with BC treated with a NPD incorporating ^{177}Lu-AuNP.

4.6 CONCLUSION

Treatment with 5 nm and 15 nm ^{177}Lu-AuNP NPD provided high tumor retention of radioactivity resulting in significant tumor growth inhibition as compared to the untreated control and unlabeled PEGylated AuNP groups, with no measurable differences in normal tissue toxicity as indicated by BWI. Lack of observable toxicities were consistent with the low doses delivered to the liver (1.4 Gy) and kidneys (3.1 Gy) using the NPD system. Mice bearing MDA-MB-468 tumors demonstrated enhanced tumor control, defined here as inhibition of tumor growth, with a 1.6-3.2 fold decrease in TGI, as compared to mice bearing MDA-MB-231 tumors, with a 1.3-1.6 fold decreased in TGI. Therefore, the use of the NPD system is clinically promising for treatment of BC as it can deliver therapeutically relevant doses while homogenizing the dose by releasing AuNP. Use of the NPD system also provides opportunities to use radionuclides with different radiation types (i.e. α particles) and energies that may not be suitable for i.v. administration or traditional brachytherapy.

4.7 ACKNOWLEDGEMENTS

The authors acknowledge Teesha Komal and Deborah Scollard at the Spatio-temporal Targeting and Amplification of Radiation Response (STTARR) Innovation Centre, University Health Network. P. Lai was also supported by an Alexander Graham Bell Canada Graduate Scholarship from the Natural Sciences and Engineering Research Council of Canada (NSERC) and a Centre for Pharmaceutical Oncology Graduate Scholarship. This study was supported by a grant from the Canadian Breast Cancer Foundation to R.M. Reilly and J.P. Pignol.

CHAPTER 5

5 SUMMARY AND FUTURE DIRECTIONS

5.1 SUMMARY OF FINDINGS

The objective of this thesis was to design, characterize, and validate the use of NPD for the delivery of AuNP labeled with e^- emitters, via a permanent brachytherapy technique for internal radiotherapy of localized breast cancers. In Chapter 2 a NPD was developed using sodium alginate, a biodegradable and biocompatible polymer used commonly in pharmaceutics, to facilitate controlled release of AuNP following implantation using permanent brachytherapy technique. NPD were constructed from various sizes of PEGylated AuNP (5 nm, 15 nm, 30 nm, and 50 nm) and concentrations of calcium alginate (6%, 8% and 10% w/v), in similar dimensions to conventional permanent brachytherapy seeds and implanted into tissue equivalent phantoms. NPD constructed from 6% w/v calcium alginate and 5 nm, 15 nm and 30 nm PEGylated AuNP were also implanted into MDA-MB-231 breast cancer xenografts. The rate of AuNP release from the NPD and AuNP spatial distributions were characterized in a phantom and *in vivo* in human BC xenografts using micro-CT imaging and silver-enhancement staining, and then compared to a Fickian diffusion model. Results from the phantom study revealed that the rates of AuNP release from the NPD were largely dependent on the AuNP size with no significant differences resulting from calcium alginate concentration. At 3 d p.i., the percentage of released for 5 nm, 15 nm, 30 nm, and 50 nm AuNP regardless of calcium alginate concentration were approximately 100%, 98%, 7% and 3.3% respectively. The high percentage of 5 nm and 15 nm AuNP released was in agreement with studies conducted by others (Klein et al., 1983, Cheetham et al., 1979) stating the pore sizes of 3-7% w/v calcium alginate ranges from 12-16 nm, and changes in concentration affects only the pore length and number of pores available. The spatial distribution of AuNP were concentric around the NPD, particularly for the 5 nm and 15 nm AuNP, which reached a radial distance of 5 mm from the NPD at 3 d and 7 d respectively. A comparison of the spatial distribution determined from the Fickian diffusion model to those obtained experimentally from the phantom study and *in vivo* revealed that the Fickian diffusion model greatly under predicts AuNP transport. In actuality, studies are suggesting that the main mechanism of particle transport in tumours is convection resulting from interstitial fluid flow (IFF) governed by interstitial fluid pressure (IFP) (Stapleton et al., 2013, Stapleton and Milosevic, 2013). Furthermore, the release and transport of AuNP *in vivo* was less accelerated (2.6-64.4 fold slower) and more heterogeneous than found in the phantom, likely as a results of the physiological and morphological complexities present in the tumour (Sykes et al., 2016), including heterogeneities in IFP (Stapleton et al., 2015). However, the implications of this work is that 5 nm and 15 nm AuNP, and any of the concentrations of calcium alginate investigated (6%-10% w/v), would be appropriate for NPD construction. The research conducted in Chapter 2 provides the groundwork for AuNP delivery using implantable depots, and additionally demonstrates the potential for NPD application in PSI brachytherapy. This work is significant in that it introduces a more clinically feasible avenue for local AuNP delivery that circumvents RES capture and dependence on EPR from systemically delivered AuNP, and provides

precision and predictability for interstitial delivery of AuNP that was lacking in i.t. administration of AuNP in suspension (Yook et al., 2016a).

The advantages of using the NPD for delivery of radiolabeled AuNP, compared to i.t. delivery of AuNP in suspension or as a conventional sealed source, was demonstrated by Monte Carlo computational dose simulations and experimentally in Chapter 3. The objective of this chapter was to evaluate the dose distribution surrounding the NPD resulting from spatially distributed radiolabeled AuNP in the tumour and the transport of radiation from the AuNP using image-based methods. In Chapter 2, NPD constructed from 15 nm AuNP were found to be suitable for implantation *in vivo*. Here, 15 nm AuNP were radiolabeled with ^{177}Lu, a β^- emitter with a mean energy of 0.13 MeV and penetration range of 0.17 cm, by chelation with DOTA bound to a PEG block and terminal lipoic acid (LA) groups for AuNP surface conjugation. The ^{177}Lu-AuNP were then injected intratumourally in a suspension of d.d.H_2O or incorporated into NPD and implanted into MDA-MB-231 human BC xenografts. Images of the tumour were acquired using micro-SPECT/CT at various times (1 h, 24 h, 48 h, and 7 d) post implantation and registered to determine the cumulative activity delivered to each voxel comprising the tumour. The dose and dose rate distributions were calculated by means of the convolution method using Monte Carlo (MCNP5) generated voxel dose kernels (VDK) containing S values for ^{177}Lu, ^{90}Y, and ^{111}In, which were validated by comparison with other published S values (Bolch et al., 1999, Lanconelli et al., 2012). Dose rate distributions surrounding the NPD were found to be consistently concentric while i.t. injected radiolabeled AuNP were irregularly distributed and varying temporally. To replicate the scenario where multiple NPD would be implanted, such as in larger human tumours, an array of 4 NPD spaced 4.5 mm apart containing ^{177}Lu-AuNP, ^{90}Y-AuNP, and ^{111}In-AuNP was simulated and the dose distributions calculated in the same previous manner. The DVH results demonstrated that the short penetration range of ^{177}Lu-AuNP and ^{111}In-AuNP emissions is unable to compensate for the low amount of AuNP redistribution, resulting in large fractions of the tumour volume receiving no dose (88.5% for ^{177}Lu-AuNP and 90.3% for ^{111}In-AuNP). However, use of ^{90}Y-AuNP, a β^- emitter with a mean energy of 0.93 MeV and penetration range of 1.1 cm, resulted in greater dose coverage and a more homogeneous dose distribution. A comparison to conventional sealed sources was also made to demonstrate effects of dose sparing to tissues immediately adjacent to the seed, which is commonly overdosed in permanent brachytherapy, from use of the NPD. A 3-fold decrease in maximum dose, attributed to the release of radiolabeled AuNP during the course of treatment, was determined through the simulations. This demonstrates an additional advantage to using NPD, particularly in clinical scenarios where seeds are implanted in close proximity to critical structures such as the skin or chest wall in breast cancer. The research presented in Chapter 3 has several implications; the use of NPD is more clinically feasible than i.t. injections of radiolabeled AuNP in suspension, greater distribution of AuNP is required to compensate for shorter range emitters such as ^{177}Lu and ^{111}In, however longer range emitters such as ^{90}Y are more appropriate for the current NPD design, and the clinical application of NPD in PSI brachytherapy can potentially reduce localized overdosing, or “hotspots”, by up to 3-fold.

The work from previous chapters have demonstrated that smaller AuNP are more readily released from the NPD, have greater penetration range in a tumour, and therefore may have superior reduction in "hotspots". In Chapter 4, 5 nm and 15 nm ^{177}Lu-AuNP were implanted into two different human BC xenograft models (MDA-MB-231 and MDA-MB-468) exhibiting low and high radiosensitivities (Cai et al., 2008) and the dosimetry, toxicity and treatment efficacy evaluated. Micro-SPECT/CT images of the tumours were acquired at various times post implantation (1 h, 24 h, 48 h, and 7 d) and registered, and the 3D dose distribution determined using the convolution method and VDK reported in Chapter 3. The SPECT images at 7 d.p.i. revealed greater release of 5 nm ^{177}Lu-AuNP and a decrease in maximum dose, centered at the NPD, by 1.7-fold in comparison to 15 nm ^{177}Lu-AuNP. The dose at the tumour periphery from 5 nm ^{177}Lu-AuNP, 3 mm from the NPD, was also 10-fold greater than 15 nm ^{177}Lu-AuNP. However the total percentage of radioactivity retained in the tumours using 5 nm and 15 nm ^{177}Lu-AuNP NPD were similar, as indicated by the biodistribution studies, demonstrating dose homogenization from use of 5 nm ^{177}Lu-AuNP NPD and no loss of radioactivity accounting for the differences in maximum dose and dose at the periphery. The organ level dose calculations (Stabin et al., 2005, Bitar et al., 2007) from the biodistribution studies also revealed low normal tissue exposures, with the highest absorbed dose measured in the liver ((0.17±0.06) $\times 10^{-6}$ Gy/Bq) followed by the kidneys ((0.07± 0.01) $\times 10^{-8}$ Gy/Bq) in animals treated with 15 nm ^{177}Lu-AuNP NPD, and the kidneys ((0.20± 0.01) $\times 10^{-6}$ Gy/Bq) followed by the liver ((0.020±0.003) $\times 10^{-8}$ Gy/Bq) in animals treated with 5 nm ^{177}Lu-AuNP NPD. The doses per unit radioactivity delivered to the liver and kidneys were very low in comparison to those delivered to the tumours ((1.7±0.6) $\times 10^{-6}$ Gy/Bq for 15 nm ^{177}Lu-AuNP NPD, and (2.5±0.9) $\times 10^{-6}$ Gy/Bq for 5 nm ^{177}Lu-AuNP NPD) and were in agreement with the lack of toxicity measured by BWI and in the hematology, ALT and serum Cr tests. Evaluation of TGI from 15 nm ^{177}Lu-AuNP NPD treated animals revealed tumour growth arrest up to 71 d for the MDA-MB-468 tumours and tumour growth inhibition for the MDA-MB-231 tumours resulting in a TGI 1.3-fold lower than untreated tumours. MDA-MB-231 tumours treated with 5 nm ^{177}Lu-AuNP NPD exhibited similar response with TGI 1.6-fold lower than untreated tumours, and no statistical differences were found between 15 nm ^{177}Lu-AuNP NPD and 5 nm ^{177}Lu-AuNP NPD treated groups. Therefore the research in Chapter 4 demonstrates proof of principle for application of radiolabeled AuNP NPD delivery by PSI brachytherapy, which has the potential to treat localized tumours without measurable toxicities to normal tissues, particularly to the liver and kidneys. Dose distributions with improved homogeneity can also be delivered with the use of smaller AuNP (5 nm) provided there is sufficient retention of radioactivity in the tumour and the exposure to organs at risk, such as the kidneys, are within tissue tolerance limits. In addition, the work here demonstrates the difference in treatment response from two human BC cells lines corroborating that the "one-size-fit-all" approach to cancer treatment is not effective for all patients. Instead, further research to demonstrate that treatment with radiolabeled AuNP NPD can support adjuvant therapies by conjugating to the AuNP surface, such as panitumumab monoclonal antibody therapy (Yook et al., 2015b), in order to targeting more radioresistant cancers is warranted.

Therefore in response to the specific aims outlined in Chapter 1, the conclusions of the research presented in this thesis are:

1. Controlled release and distribution of AuNP can be achieved using NPD as demonstrated in a tissue equivalent phantom and *in vivo*, however release and redistribution rates were highly dependent on the AuNP size and implantation media, with tumour tissue exhibiting slower release, and were less dependent on the calcium alginate concentration. The use of 5 nm AuNP resulted in the most homogeneous distribution, however heterogeneities in AuNP distribution were still observed experimentally in phantom and *in vivo*. The intratumoural distribution and heterogeneities were not successfully represented using the Fickian diffusion model, which ignores key components of particle transport in tissue such as convection from interstitial fluid flow. However the use of the NPD allowed for precise intratumoural delivery of AuNP and was compatible with permanent seed implantation brachytherapy.
2. Simulations of the dose distribution from an NPD demonstrated a reduction in maximum dose located at the "hotspots" by 3-fold when compared to conventional sealed seeds. An evaluation of electron emitting radionuclides (^{111}In, ^{177}Lu, and ^{90}Y) revealed that ^{90}Y-AuNP resulted in the most homogenous dose distribution both in simulation and *in vivo*, and could compensate for heterogeneities in radioactivity distribution. The intratumoural dose distribution for the ^{177}Lu-AuNP NPD were predictable and concentric, as compared to i.t. injections of ^{177}Lu-AuNP in suspension, which were irregular and redistributed outside the tumour quicker. Therefore our results suggest that NPD are clinically more feasible than i.t. administration of radiolabeled AuNP.
3. Treatment with 5 nm and 15 nm ^{177}Lu-AuNP NPD resulted in significant tumour growth inhibition with no normal tissue toxicity which was consistent with the high retention of radioactivity and dose delivered to the tumour (1.7-2.6 Gy/MBq) and low doses delivered to the liver (0.02-0.17 Gy/MBq) and kidneys (0.07-0.2 Gy/MBq). Use of the 5 nm ^{177}Lu-AuNP reduced the maximum dose by 1.7-fold and resulted in higher dose to the kidneys, while use of 15 nm ^{177}Lu-AuNP resulted in higher dose to the liver, which was consistent with elimination pathways for nanoparticles of that size range. Mice bearing MDA-MB-468 tumours demonstrated enhanced tumour control in comparison to mice bearing MDA-MB-231 tumours, with 1.6-3.2 fold decrease versus 1.3-1.6 fold decrease in TGI.

These findings demonstrate the feasibility of the NPD for delivery of radiolabeled gold nanoparticles, and lays the foundation for exploration of other nanoparticle types and surface modifications in future works. However, there are various caveats that must be noted in the presented research such as; the use of an animal xenograft model as opposed to an orthotopic or large animal model, the limited study of two BC cell lines, the implantation of a single NPD, and the simulated activity and dose distributions for ^{111}In and ^{90}Y using ^{177}Lu-AuNP distributions, to name a few. These limitations and assumptions should be addressed in future work.

5.2 FUTURE DIRECTIONS

5.2.1 NPD DESIGN IMPROVEMENT

The research presented in this thesis provides the framework for a novel form of nanoparticle delivery that utilizes existing PSI brachytherapy technique. There are various avenues that can be explored to improve on the design of radiolabeled AuNP NPD presented here such as;

Further optimization of AuNP size and NPD calcium alginate composition to manipulate the amount of AuNP available for redistribution. The results from Chapter 2 demonstrated that smaller AuNP (5 nm) were capable of penetrating the tumour to a greater degree than larger AuNP (15 nm, 30 nm, and 50 nm), however results from Chapter 4 revealed that much of the radioactivity was still retained within the NPD during the time period that the majority of the dose is delivered. To improve dose homogeneity, greater initial release of radioactivity can be achieved through the use of smaller AuNP, which will make more AuNP available for intratumoural redistribution in the earlier days post implantation. The caveat to using smaller AuNP is their greater potential to intravasate into tumour vasculature and redistribute elsewhere in the body. It would be reasonable to expect that the biodistribution of smaller AuNP (<5 nm) would be similar to the biodisitribution from 5 nm AuNP (Fig. 4.5b,d), but the %IA/g or %IA/organ would be greater at earlier time points, and therefore doses to certain normal tissues would be higher. An alternative to using smaller AuNP would be to alter the degradation rate of the calcium alginate hydrogel by using partially oxidized alginate to make the release of AuNP partially dependent on the degradation reaction (Lee and Mooney, 2012). The construction of the NPD outlined in Chapter 2 used the most stable form of alginate containing high guluronate content to ensure release of AuNP was not influenced by degradation.

Adjusting the surface charge of the AuNP to augment the rate and degree of intratumoural penetration. In Chapter 2, silver enhancement stained sections of PEGylated AuNP NPD implanted into tumour (Fig. 2.9) demonstrated 5 nm AuNP to have superior tumour penetration than larger AuNP (15 nm, 30 nm, and 50 nm). This was confirmed in Chapter 4 where the use of 5 nm ^{177}Lu-AuNP NPD resulted in a 10 fold higher dose than 15 nm ^{177}Lu-AuNP NPD at only 3 mm from the implant site (Fig. 4.4). However, the dose distributions generated in Chapter 4 revealed that greater and more rapid penetration of radiolabeled AuNP is required to achieve a homogeneous dose and avoid underdosing when using shorter range electron emitters such as ^{177}Lu. Therefore it would be prudent to investigate the impact of AuNP surface charge on intratumoural penetration. The zeta potential, or net surface charge, of an unmodified AuNP ranges from -30 to -40 eV, and research shows that negatively charged nanoparticles are capable of redistributing throughout the bulk of the tumour more rapidly, where positively charged nanoparticles are more readily internalized (Davis et al., 2008, He et al., 2010, Kim et al., 2010a). Tuning of the zeta potential has been accomplished by conjugating cationic materials, such as ammonium, or anion materials, such as carboxylate, to the AuNP surface (Goodman et al., 2004).

Investigating other biocompatible and biodegradable materials, such as PLGA, that are more robust and have greater rigidity for NPD construction. The formulation of the NPD outlined in this thesis utilizes very-low-viscosity high guluronate content alginate for its structural stability to form the NPD matrix and entrap AuNP. Alginate has been well-documented for use in various biomedical applications such as in tissue engineering and regeneration, wound dressing, cell culture, oral drug delivery, and as depot for tissue localized delivery of drugs and proteins (Lee and Mooney, 2012). The popularity of alginate is owed to its biocompatibility, low toxicity, commercial availability, ease of gelation, and ability to maintain a physiologically moist environment. However, there are limitations regarding the use of alginate for this application including its relatively soft construction compared to conventional brachytherapy sources, and its maintained moisture which poses a handling and contamination risk with regards to radiation safety. An alternative would be the use of PLGA, a synthetic biodegradable and biocompatible polymer that has greater mechanical strength and relies on degradation for release of encapsulated materials (Makadia and Siegel, 2011, Jain, 2000). Historically, PLGA has been used clinically to construct bioresorbable surgical devices such as sutures, however recently they have been investigated for fabrication of drug delivery devices and as scaffolds for tissue engineering. Theoretically, PLGA would be an appropriate surrogate for alginate if AuNP, which are water soluble, can be successfully incorporated into a PLGA matrix, which is hydrolyzed in the presence of water. Techniques, such as a double emulsion process, or water-in-oil-in-water emulsion methods used for encapsulating water-soluble drugs (i.e. peptides, proteins, vaccines) can be applied. In a similar manner to alginate hydrogels, the degradation rate and therefore the release of AuNP can be controlled by polymer composition, with higher glycolic acid proportion resulting in higher degradation rates (Makadia and Siegel, 2011).

5.2.2 SIMULATION OF CLINICAL SCENARIO USING MULTIPLE NPD

The work covered in this thesis has been limited to the implantation of single NPD *in vivo* due to the restraint set by tumour size, and a maximum of 4 NPD in simulation. Further investigation on the use of multiple NPD is required to evaluate clinical feasibility. As mentioned in Chapter 1, an average of 70 brachytherapy seeds are implanted in the treatment of BC and >100 seeds are typically implanted for the treatment of prostate cancer, both using different loading patterns to achieve an optimal dose coverage and tissue sparing. To investigate the impact of the NPD on dose coverage in a larger target volume, a preliminary study on the influence of NPD implantation distance on maximum (D_{max}) and minimum (D_{min}) dose from ^{177}Lu-AuNP, ^{90}Y-AuNP, and ^{111}In-AuNP NPD was explored and compared to conventional sealed sources (CSS) containing the same radionuclides. A 4 by 4 array totaling 16 NPD or 16 CSS was simulated with varying implantation distances, d (0.2-1.1 cm in 0.03 cm increments) (Fig. 5.1), and the 3D dose distribution estimated by convolution with Monte Carlo generated VDK from Chapter 3.

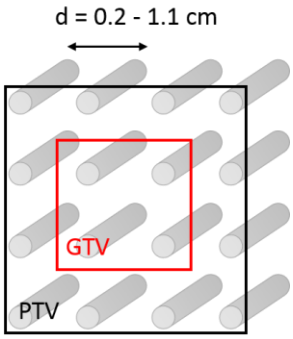

Figure 5.1 Illustration of 4 by 4 array of 16 NPD or 16 CSS, simulated with implantation distance, d, ranging from 0.2-1.1 cm with 0.03 cm increments, encompassing the planning target volume (PTV).

Dose volume histograms were generated to determine the proportion of the normalized target volume that was receiving a certain dose (Gy/Bq) for each implantation distance. Lastly, the dose homogeneity index (DHI) was calculated using Equation 5.1, where V100 and V150 are the relative volumes of the PTV receiving at least 100% and 150% of the prescribed dose, respectively. The DHI parameter is commonly used in interstitial brachytherapy to assess the volume of tissue that is overdosed relative to the treated volume (Wu et al., 1988).

$$DHI = \frac{V100 - V150}{V100} \quad (5.1)$$

5.2.2.1 INFLUENCE OF NPD DISTANCE ON MINIMUM AND MAXIMUM DOSE

Figure 5.2 displays representative ^{111}In-AuNP NPD and ^{111}In CSS arrangements with implantation distances of 1.1 cm. Note the difference in maximum dose between ^{111}In-AuNP NPD (4.25×10^{-5} Gy/Bq) and ^{111}In CSS (8.25×10^{-5} Gy/Bq), demonstrating a 1.9-fold decrease in maximum dose resulting from release of ^{111}In-AuNP from the NPD. In Figure 5.3, the maximum and minimum doses (Gy/Bq) are plotted as a function of implantation distance, d. There were no observable differences between minimum dose (Fig. 5.3a, b, c) from the NPD and CSS at implantation distances beyond 0.27 cm, although both D_{min} from the NPD and CSS decreased with increasing implantation distance for all radionuclides. This decreasing trend in D_{min} at greater implantation distances fails for ^{111}In CSS at d>0.75 cm, likely as a result of under sampling from the extremely small amounts of radiation the voxels were receiving at greater implantation distances due to the limited penetration range of ^{111}In, and lack of AuNP distribution. Note that this is not present in the ^{111}In-AuNP NPD D_{min} curve, suggesting the redistribution of ^{111}In-AuNP results in consistent radiation exposure even at greater implantation distances. Recall the mean emission energies and penetration ranges of the radionuclides, ^{90}Y: 0.93 MeV (β^-), 1.1 cm penetration range, ^{177}Lu: 0.13 MeV (β^-), 0.17 cm penetration range, and ^{111}In: 0.18 MeV (IC electron), 0.93 keV (AE), 0.06 cm penetration range. At small implantation distances (<0.27 cm),

particularly for shorter range emitters (^{177}Lu and ^{111}In), the minimum dose when using radiolabeled AuNP NPD was greater due to AuNP redistribution. The shorter the range of the emitter, the greater the impact of implantation distance on D_{min}. For instance, at the implantation distance of 0.2 cm the increase in D_{min} resulting from the use of the NPD for ^{90}Y was 1.09-fold, while the increase in D_{min} for ^{177}Lu and ^{111}In was 9.4-fold and 385-fold, respectively. In contrast, the maximum dose (Fig. 5.3d, e, f) resulting from the use of the NPD was consistently 2.1-fold and 1.9-fold less than the CSS for ^{177}Lu and ^{111}In, respectively, while D_{max} ranged from 1.4-fold to 1.5-fold less than the CSS at increasing implantation distances for ^{90}Y. The increase in D_{min} and decrease in D_{max} from use of the NPD indicates homogenization of dose. The impact of the NPD implantation distance on D_{min} and D_{max} is greater at smaller implantation distances particularly for short range emitters where dose heterogeneity is inherently greater. However, there is a significant reduction in D_{max} regardless of the implantation distance for all radionuclides. This reduction in "hotspots" is clinically impactful for permanent implants near critical structures such as the urethra for treatment of the prostate.

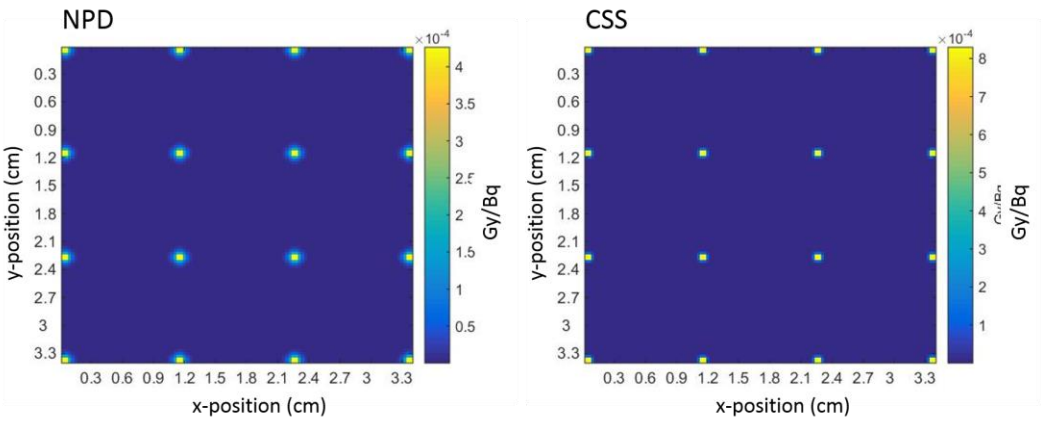

Figure 5.2 Representative 4 by 4 array of ^{111}In-AuNP NPD (left) and ^{111}In CSS (right) with 1.1 cm implantation distance. Note the 2-fold lower maximum dose (Gy/Bq) in the NPD dose distribution in comparison to the CSS.

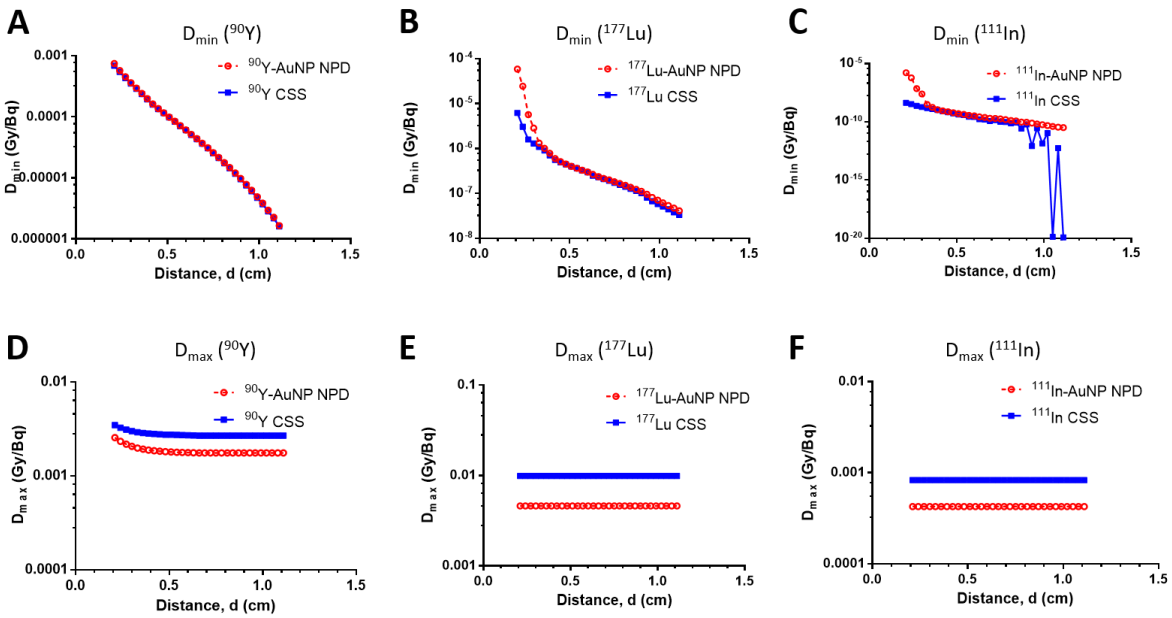

Figure 5.3 Minimum and maximum dose vs. implantation distance. Minimum dose (Gy/Bq) plotted on a logarithmic scale as a function of distance (cm), d, for (a) ^{90}Y, (b) ^{177}Lu, and (c) ^{111}In radiolabeled AuNP NPD and CSS. Maximum dose (Gy/Bq) plotted on a logarithmic scale as a function of distance (cm), d, for (d) ^{90}Y, (e) ^{177}Lu, and (f) ^{111}In radiolabeled AuNP NPD and CSS.

5.2.2.2 HISTOGRAM OF DOSE DISTRIBUTION IN NPD AND CSS

Dose volume histograms were generated for ^{90}Y-AuNP, ^{177}Lu-AuNP, and ^{111}In-AuNP NPD and ^{90}Y, ^{177}Lu, ^{111}In CSS, as shown in Figure 5.4, where each line represents a different implantation distance. The dashed blue line represents an implantation distance of 0.2 cm and the dashed red line represents an implantation distance of 1.1 cm. The histogram of the dose distribution can be interpreted as the proportion of volume, or relative volume (RV), that is receiving a certain dose (Gy/bq). For instance in Figure 5.4a in reference to the dashed blue line (implantation distance of 0.2 cm), 15% of the volume is receiving a dose of 0.0012 Gy/Bq. The corresponding red line (implantation distance of 1.1 cm) indicates that 75% of the volume is receiving 0 Gy/Bq. The ideal histogram would be a vertical line at the prescription dose indicating that every portion of the target volume is receiving the same prescribed dose. This is never observed in clinical practice but the histogram is still used as an indicator of dose homogeneity and coverage. A comparison of the radiolabeled AuNP NPD dose distribution histogram with the corresponding CSS dose distribution histogram, particularly for ^{177}Lu and ^{111}In, revealed that at closer implantation distances use of the NPD resulted in smaller volumes receiving no dose (RV<0.1) while large volumes were still receiving no dose using the CSS (RV>0.7). However, these results suggest that greater distribution of AuNP is required when treating with ^{177}Lu and ^{111}In in order to achieve a homogeneous dose distribution, as indicated by the wide range of doses delivered to the volume. Implantation distances of 0.2 cm is also clinically impractical. For volumes implanted with ^{90}Y-AuNP NPD and ^{90}Y CSS, the ideal implantation distance would be ~0.75 cm. At this distance the dose distribution is the narrowest, and up to

70% of the RV would receive the same dose (0.0002 Gy/Bq). The amount of radioactivity could then be scaled appropriately to deliver the proper prescription dose.

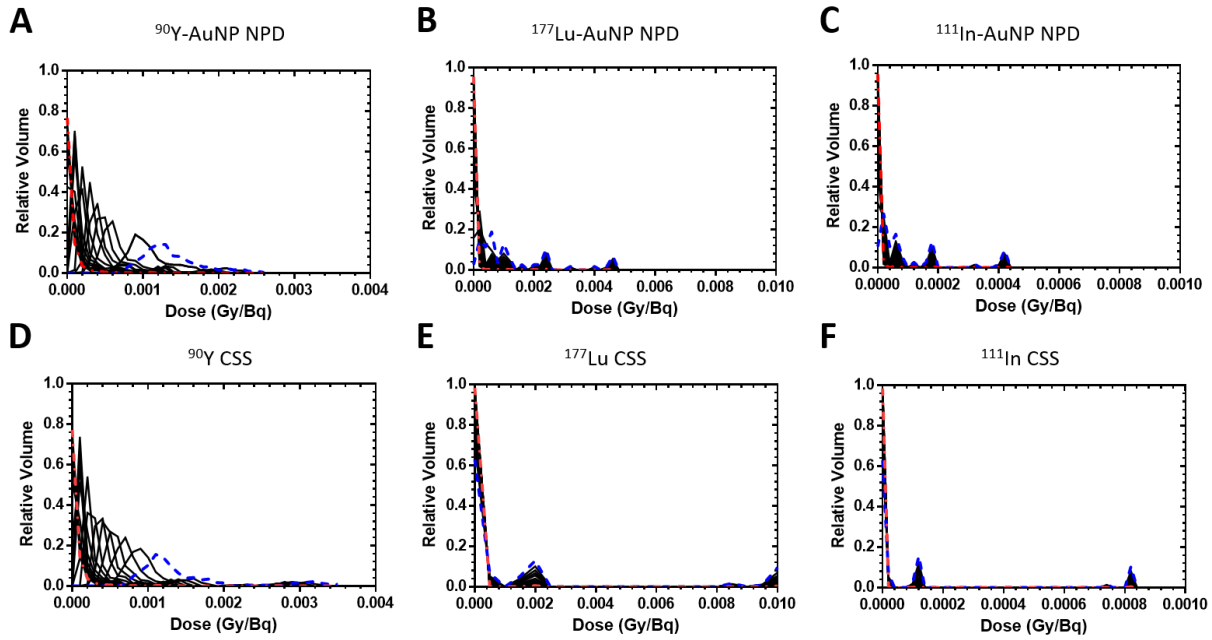

Figure 5.4 Histograms of dose distributions at various implantation distances. The relative volume (RV) plotted against dose (Gy/Bq) for (a) ^{90}Y, (b) ^{177}Lu, and (c) ^{111}In radiolabeled AuNP NPD and (d) ^{90}Y, (e) ^{177}Lu, and (f) ^{111}In CSS. The various lines represent the different implantation distances. The dashed red line represents the furthest implantation distance (1.1 cm) while the dashed blue line represents the closest implantation distance (0.2 cm).

5.2.2.3 DOSE HOMOGENEITY INDEX AS A FUNCTION OF IMPLANTATION DISTANCE

The mean high dose volumes V150 and V300, which show the proportion of the PTV receiving 150% and 300% of the prescribed dose, are dosimetric parameters commonly used in brachytherapy and are often used to indicate the level of dose uniformity. Here, the parameters V150, V300 and DHI are plotted as a function of implantation distance (Fig. 5.5). Since the goal of brachytherapy treatments is to deliver 100% of the prescribed dose to the entire PTV, the minimum dose (Gy/Bq) determined from the simulation (Fig. 5.3) was set as the prescription dose. Therefore, V150 and V300 were volumes receiving 150% or 300% of the minimum dose. The ideal treatment plan in brachytherapy delivers a uniform dose (DHI=1) where the entire PTV receives 100% of the prescription dose, and 0% of the PTV receives anything more than 100%. Clinically this is never the case given the nature of dose deposition from internal sources, which decreases rapidly at increasing distances. Therefore the optimal implantation distance of NPD should aim for a DHI of 1, and V150 and V300 of 0 on the normalized index. From Figure 5.5, the DHI is maximum at 0.33-0.48 cm for ^{90}Y-AuNP NPD (DHI=0.30), and 0.84-0.87 cm for ^{177}Lu-AuNP NPD (DHI=0.59). The DHI curve for ^{111}In-AuNP NPD was more irregular but had a maximum at 0.6 cm (DHI=0.23). Although these results seem to conflict with those

from Chapter 3, which found that large proportions of the target volume were receiving effectively no dose given an implantation distance of 4.5 mm, the implanted activity from the study was fixed (^{90}Y: 1.8 MBq, ^{177}Lu: 2.5 MBq, and ^{111}In: 25.1 MBq) resulting in very low minimum doses. Here, the minimum dose (Gy/Bq) has been scaled such that it is equivalent to the prescription dose. The DHI reported in clinical studies on permanent brachytherapy of the prostate using ^{103}Pd and ^{125}I have ranged from 0.3 to 0.5 (Wang et al., 2006, Van Gellekom et al., 2005, Williams et al., 2004). The DHI for ^{111}In-AuNP NPD is lower than the lowest DHI clinically reported, which was expected given its ultra-short penetration range. However, the DHI from ^{90}Y-AuNP NPD and ^{177}Lu-AuNP NPD when implanted at optimal separation distances are within the clinically acceptable ranges.

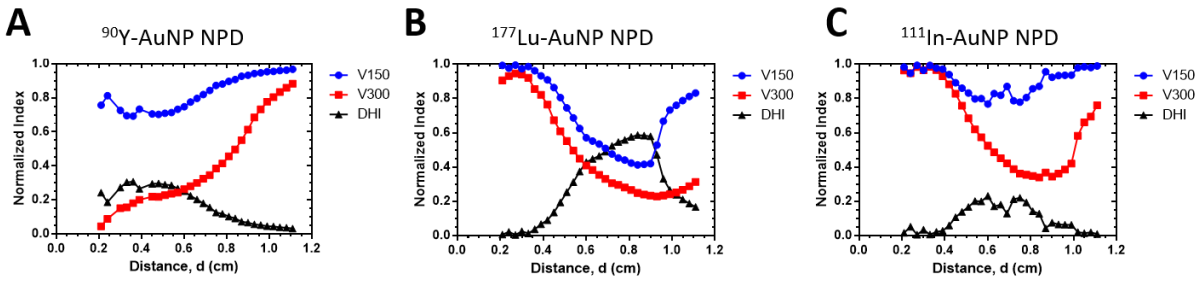

Figure 5.5 Dosimetric parameters V150, V300 and DHI plotted as a function of implantation distance (cm) for (a) ^{90}Y-AuNP, (b) ^{177}Lu-AuNP, and (c) ^{111}In-AuNP NPD.

There are other metrics for quantitative analysis of implant quality in permanent brachytherapy. One of the advantages of using electron emitting radionuclides is their finite range in tissue, and abrupt decrease in tissue dose deposition. This impacts the dose coverage by improving radiation conformity, which can be interpreted as the amount of the target volume that is in the irradiated volume. This can be quantified using the conformal or conformity index (CI) of which there are a few variations such as Equation 5.2 and 5.3. In the CI defined by 5.2, PTV_{ref} is the volume of the PTV receiving 100% or more of the prescribed dose, V_{PTV} is the volume of the PTV, and V_{ref} is the total volume that is treated with 100% or more of the prescribed dose (Wang et al., 2006). In the CI defined by 5.3, V_{PTV} is the planning target volume and $V_{95\%}$ is the volume enclosed by the 95% isodose (Knoos et al., 1998). Of these two equations, Equation 5.2 would more accurately describe the conformity of a treatment since Equation 5.3 does not take into account whether the volume receiving 95% of the prescribed dose actually coincides with the PTV. A CI equal to 1 is considered an ideal dose coverage, while a CI >1 indicates that the treated volume exceeds the target volume resulting in irradiation of healthy tissues. However, a CI<1 is typically observed in clinical practice. In general, interstitial brachytherapy is understood to be more conformal than external radiation treatments due to its tissue sparing quality. Conformity indices of 0.5 to 0.6 have been reported in PSI brachytherapy of the prostate (Wang et al., 2006), 0.9 for interstitial brachytherapy of the cervix (Sharma et al., 2013), and 0.7 for HDR interstitial brachytherapy

of the breast (Zourari et al., 2015). In whole breast external radiotherapy, CI of 1.4 have been reported (Petrova et al., 2017), while the CI from 3D-CRT of the breast and prostate are reported around 0.5-0.6 (Knoos et al., 1998) similar to the CI from PSI brachytherapy.

$$CI = \left(\frac{PTV_{ref}}{V_{PTV}}\right) \times \left(\frac{PTV_{ref}}{V_{ref}}\right) \tag{5.2}$$

$$CI = \frac{V_{PTV}}{V_{95\%}} \tag{5.3}$$

Other dosimetric parameters include D90 and D100, which are the doses that cover 90% and 100% of the target volume, respectively and the dose non-uniformity ratio, DNR, which is determined as 1-DHI.

5.2.3 ^{90}Y-AUNP NPD FOR TREATMENT OF BREAST CANCER

In Chapter 3, Monte Carlo simulations of radiolabeled AuNP NPD containing electron emitting radionuclides (^{111}In, ^{177}Lu, and ^{90}Y) revealed the necessity for radionuclides with longer penetrating range emissions, such as ^{90}Y, for the given NPD formulation (15 nm, 6% w/v calcium alginate). This would allow the NPD to be implanted at distances from each other that were clinically comparable (>4.5 mm) to PSI brachytherapy while ensuring tissues between the NPD were receiving sufficient dose. Additionally, results from Chapter 4 demonstrated further homogenization of dose distribution through the use of 5 nm AuNP, which reduced the maximum dose by 1.7-fold and increased tumour peripheral dose, 3mm from the NPD, by 10-fold. Therefore it would be impactful to explore a formulation of NPD that utilized smaller sized AuNP such as 5 nm, and longer range β^- emitter such as ^{90}Y, and investigate the dose distribution surrounding single or arrays of implanted 5 nm ^{90}Y-AuNP NPD. This could be achieved through computational simulations as conducted in Chapter 3, using the VDK and convolution method. A more homogeneous radioactivity distribution and a higher energy (0.93 MeV), longer range (1.1 cm) emitter may increase the implantation distance between NPD and allow the use of fewer NPD thereby minimizing the invasiveness of the procedure. A study on treatment response and toxicity should also be conducted as the higher energy β^- particle may be more detrimental to normal tissues, particularly the liver and kidneys, if there is sufficient uptake of radioactivity in these tissues. However, the challenge with using a mouse model for toxicity studies is that the range of the β^- particle relative to the size of the organs is large enough to result in organ cross-fire, such that tissues neighboring those where ^{90}Y-AuNP may accumulate, like the liver and kidneys, will also receive radiation exposure. This could result in inaccurately predicting the toxicity in humans in which these tissues are remote from the source of the ^{90}Y-AuNP NPD. Therefore, *in vivo* studies should ideally be conducted in larger animals using orthotopic models.

5.2.4 OTHER BIOMEDICAL APPLICATIONS, ADJUVANT THERAPIES AND APPLICATION IN OTHER TYPES OF CANCER

There are exciting research opportunities to expand on the therapeutic applications for NPD nanoparticle delivery. Depending on the clinical application, it may be possible to adjust the NPD formula and AuNP surface modifications. AuNP can be multifunctionalized to bind to biological targets present in cancers for targeted therapy, or act as delivery vehicles for drugs, proteins, or DNA (Tiwari et al., 2011). For instance, Yook et al. conjugated panitumumab to ^{177}Lu-AuNP to target EGFR overexpression in triple negative breast cancers, and found better retention of the targeted ^{177}Lu-AuNP in the tumours as compared to the non-targeted ^{177}Lu-AuNP following i.t. administration (Yook et al., 2015b, Yook et al., 2016a). Targeted ^{177}Lu-AuNP also resulted in greater internalization of the particles in the cells *in vitro* allowing improved localization of radioactivity to the cell nucleus. The outcome was a significant decrease in CS demonstrating greater radiobiological effectiveness of targeted ^{177}Lu-AuNP. In a study by Kim et al., an AuNP gene delivery system was developed to deliver nucleic acids into the nucleus of tumour cells to modulate the gene expression (Kim et al., 2011). Mice bearing LoVo human colon cancer xenografts were i.t. injected with AuNP-αRNA I-AS MCL-1 resulting in increased expression of cell death-inducing protein MCL-1S, reduced expression of cell survival promoting protein MCL-1L, and overall tumour growth inhibition. In both these studies, application of the NPD for delivery of their functionalized AuNP would improve the precision of AuNP placement and the retention of the therapeutic agent within the tumour.

There are also opportunities for adjuvant therapies by exploiting the characteristics of AuNP such as their; (1) *Radiation enhancing qualities*: their interaction with radiation and high atomic number resulting in generation of locally damaging photoelectric products, and (2) *Hyperthermic qualities*: their interaction with excitation sources (near-infrared light, radiowaves, alternating magnetic fields) that allow them to absorb incident energy and convert it to heat. Although there are no studies that have investigated radiolabeled AuNP with hyperthermia-based treatments or for radiation enhancement, there are studies that have proposed applications of these nano-based therapies in combination with brachytherapy (Ngwa et al., 2012, Cho et al., 2009). For instance, Cho *el al*. investigated the dosimetric feasibility of gold nanoparticle-aided brachytherapy and demonstrated dose enhancement >100% in gold nanoparticle loaded tumours (18 mg Au/g). In a phase I study by Wust et al., magnetic thermotherapy was used in combination with ^{125}I permanent brachytherapy of the prostate to deliver simultaneous application of heat and radiation (Wust et al., 2006). Transperineal injection of iron oxide nanoparticles in suspension were achieved to create magnetic fluid depots in the prostate, which were then exposed to a magnetic field for heat generation. Overall the temperatures that were achieved were hyperthermic, however, the quality of the nanoparticle distribution was variable and deviated greatly from the planned distribution, which negatively impacted the temperature distribution (Fig. 5.6). Nevertheless, Wust et al. successfully demonstrated the feasibility of nanoparticle-based thermotherapy in combination with permanent brachytherapy.

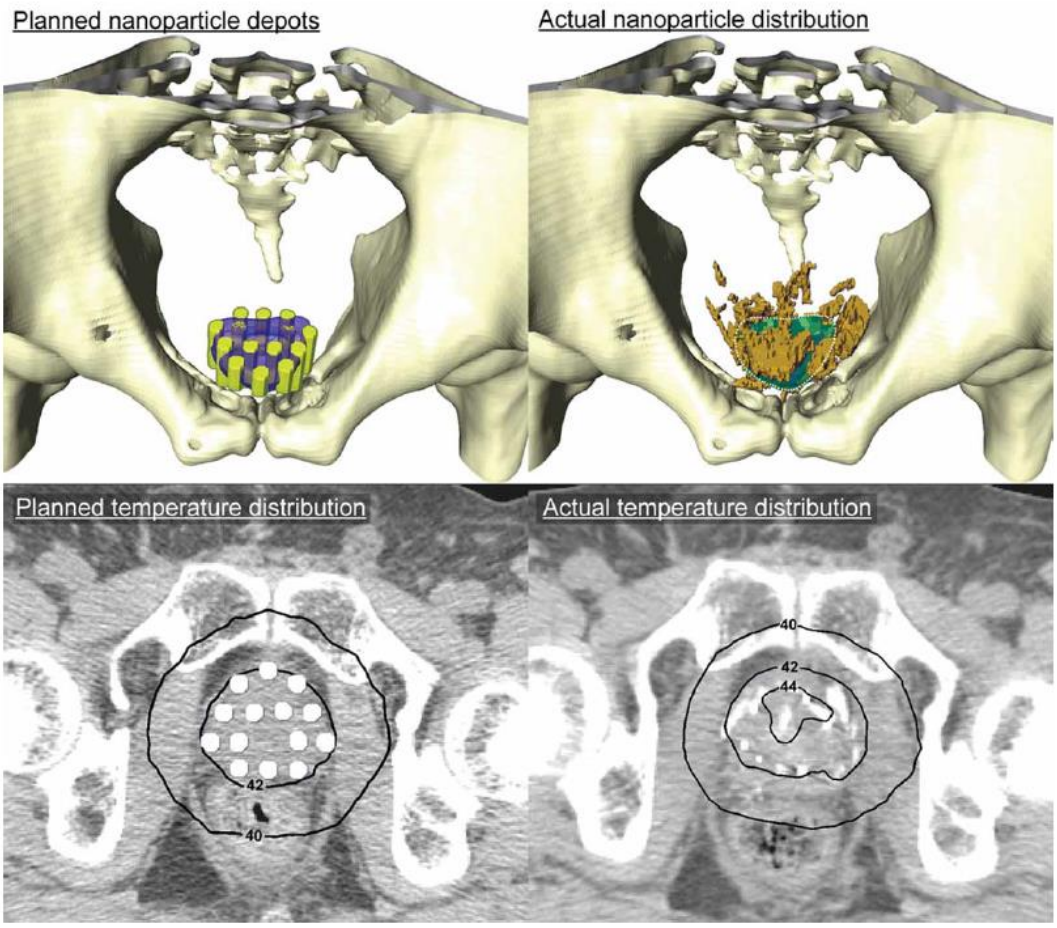

Figure 5.6 Planned placement (*top left*) and temperature distribution (*bottom left*), and actual nanoparticle distribution (*top right*) and temperature distribution (*bottom right*) from magnetic nanoparticle depots for treatment of prostate carcinoma (Wust et al., 2006). The top images are 3-dimensional reconstructions of CT images taken pre-implantation (*left*) for planning of depot positions and puncture tracks, and post-implantation (*right*) for analysis of implantation quality, nanoparticle distribution and temperature distribution. The bottom images are representative CT images illustrating the temperature distributions, and area of tissue receiving the target temperature of 42 degrees Celcius. *Reprinted with permission.*

In this thesis we have limited the discussion to gold nanoparticle delivery for treatment of breast cancer, however application of NPD is possible for other types of nanoparticles and in other cancers that are treated with permanent brachytherapy. For instance, in the example of nanoparticle thermotherapy in brachytherapy by Wust et al., it would be possible to use the NPD instead of fluid depots to achieve a more uniform distribution of nanoparticles in the prostate, and therefore a more predictable temperature distribution. Permanent seed brachytherapy has also been used to treat patients with primary or metastatic brain tumours (Bogart et al., 1999, Gutin et al., 1981) and cervical cancers (Monk et al., 2002), and would be appropriate candidates for nanoparticle delivery by NPD implantation.

5.2.5 CONCLUSION AND PERSPECTIVES ON THE FUTURE OF GOLD NANOPARTICLE DELIVERY

In recent years, AuNP have demonstrated enormous therapeutic potential through the development of functional groups and moieties, such as proteins, drugs and antibodies, which modify the AuNP surface and impart therapeutic effects. Their unique surface chemistry combined with their high surface to volume ratio, has made AuNP attractive vehicles for transporting agents to target tissues. Furthermore, other studies have exploited their radiation enhancing properties during radiation therapy to deliver a more localized lethal dose to the target volume. It is clear that AuNP are an important class of material. However, an important challenge for the continued development of AuNP is their successful delivery to the disease site, or tumour. Early systemic targeting strategies relied on the EPR effect, which demonstrated differential accumulation of nanoparticles in the tumour as a result of poor vascular function and lymphatic drainage. Unfortunately, concentrations of the nanoagents at the disease site were often insufficient in generating a therapeutic effect. Other active targeting strategies were developed such as antibodies targeting for surface receptors overexpressed in the diseased tissue, but these strategies were challenged with nonspecific uptake and extensive sequestration by the mononuclear phagocyte system. To circumvent these obstacles and improve translation into a clinical setting, direct administration into the target site is being recognized as a potential avenue to introduce therapeutic nanoparticles. This thesis outlines the development of an implantable depot capable of facilitating controlled release of radiolabeled AuNP following delivery using existing permanent brachytherapy techniques. In addition to bypassing the biodistribution challenges associated with systemic administration, and inconsistencies in particle distribution from intratumoural administration of AuNP suspensions, implantation of a depot for nano-based radiotherapy offers a solution to dose heterogeneities in permanent brachytherapy by reducing high dose-receiving regions, or “hotspots”. Use of the NPD in permanent brachytherapy also improves the robustness of the technique to implantation errors or seed drifting, particularly near critical structures, which may reduce patient morbidity. If we widen our perspective further and consider the impact that this work has beyond radiolabeled gold nanoparticles, we can begin to see the endless potential for its application such as with nanoparticles from various classes of materials, cofunctionalized or multifuntionalized to deliver a desired therapeutic effect, or even potentially using the depot for combined delivery of drugs or sensitizers, such as for hormone therapy (i.e. goserelin) in certain prostate cancer treatments which require continuous drug administration. Undeniably, there are exciting research opportunities on the horizon that will aid in moving the field of nanomedicine closer to clinical practice, where patients will finally benefit from the continued efforts of researchers who have developed innovative nanotherapies.

REFERENCES

2005. *Radiation Oncology Physics: A Handbook for Teachers and Students,* Vienna, Austria, International Atomic Energy Agency.

2009. *Basic Clinical Radiobiology,* London, Edward Arnold

2017. *NCD mortality and morbidity* [Online]. World Health Organization. Available: http://www.who.int/gho/ncd/mortality_morbidity/en/.

ABRAHAM, G. E. 2008. Clinical applications of gold and silver nanocolloids. *The Original Internist*, 132-157.

ABRAHAM, G. E. & HIMMEL, P. B. 1997. Management of Rheumatoid Arthritis: Rationale for the Use of Colloidal Metallic Gold. *Journal of Nutritional and Environmental Medicine,* 7, 295-305.

AFSHARPOUR, H., RENIERS, B., LANDRY, G., PIGNOL, J. P., KELLER, B. M., VERHAEGEN, F. & BEAULIEU, L. 2012. Consequences of dose heterogeneity on the biological efficiency of (1)(0)(3)Pd permanent breast seed implants. *Phys Med Biol,* 57, 809-23.

AMATO, E., ITALIANO, A., MINUTOLI, F. & BALDARI, S. 2013. Use of the GEANT4 Monte Carlo to determine three-dimensional dose factors for radionuclide dosimetry. *Nuclear Instruments and Methods in Physics Research A,* 708, 15-18.

AMENDOLA, V. & MENEGHETTI, M. 2009. Size evaluation of gold nanoparticles by UV-vis spectroscopy. *J. Phys. Chem.,* 113, 4277.

ARNIDA, JANAT-AMSBURY, M. M., RAY, A., PETERSON, C. M. & GHANDEHARI, H. 2011. Geometry and surface characteristics of gold nanoparticles influence their biodistribution and uptake by macrophages. *Eur J Pharm Biopharm,* 77, 417-23.

ATTIX, F. H. 2004. *Introduction to radiological physics and radiation dosimetry,* Weinheim, Wiley-VCH.

BALASUBRAMANIAN, S. K., JITTIWAT, J., MANIKANDAN, J., ONG, C. N., YU, L. E. & ONG, W. Y. 2010. Biodistribution of gold nanoparticles and gene expression changes in the liver and spleen after intravenous administration in rats. *Biomaterials,* 31, 2034-42.

BAO, C., CONDE, J., PAN, F., LI, C., ZHANG, C., TIAN, F., LIANG, S., FUENTE, J. M. D. L., CUI, D. & 2016. Gold nanoprisms as a hybrid in vivo cancer theranostic platform for in situ photoacoustic imaging, angiography, and localized hyperthermia. *Nano Research,* 9, 1043-1056.

BERENATO, S., AMATO, E., FISCHER, A. & BALDARI, S. 2016. Influence of voxel S factors on three-dimensional internal dosimetry calculations. *Phys Med*.

BERNAL, M. A., BORDAGE, M. C., BROWN, J. M., DAVIDKOVA, M., DELAGE, E., EL BITAR, Z., ENGER, S. A., FRANCIS, Z., GUATELLI, S., IVANCHENKO, V. N., KARAMITROS, M., KYRIAKOU, I., MAIGNE, L., MEYLAN, S., MURAKAMI, K., OKADA, S., PAYNO, H., PERROT, Y., PETROVIC, I., PHAM, Q. T., RISTIC-FIRA, A., SASAKI, T., STEPAN, V., TRAN, H. N., VILLAGRASA, C. & INCERTI, S. 2015. Track structure modeling in liquid water: A review of the Geant4-DNA very low energy extension of the Geant4 Monte Carlo simulation toolkit. *Phys Med,* 31, 861-74.

BITAR, A., LISBONA, A., THEDREZ, P., SAI MAUREL, C., LE FORESTIER, D., BARBET, J. & BARDIES, M. 2007. A voxel-based mouse for internal dose calculations using Monte Carlo simulations (MCNP). *Phys Med Biol,* 52, 1013-25.

BLASKO, J. C. 2000. Brachytherapy. *Urology,* 55, 306-8.

BOGART, J. A., UNGUREANU, C., SHIHADEH, E., CHUNG, T. C., KING, G. A., RYU, S., KENT, C. & WINFIELD, J. A. 1999. Resection and permanent I-125 brachytherapy without whole brain irradiation for solitary brain metastasis from non-small cell lung carcinoma. *J Neurooncol,* 44, 53-7.

BOLCH, W. E., BOUCHET, L. G., ROBERTSON, J. S., WESSELS, B. W., SIEGEL, J. A., HOWELL, R. W., ERDI, A. K., AYDOGAN, B., COSTES, S., WATSON, E. E., BRILL, A. B., CHARKES, N. D., FISHER, D. R., HAYS, M. T. & THOMAS, S. R. 1999. MIRD pamphlet No. 17: the dosimetry of nonuniform activity distributions--radionuclide S values at the voxel level. Medical Internal Radiation Dose Committee. *J Nucl Med,* 40, 11S-36S.

BOVI, J., QI, X. S., WHITE, J. & LI, X. A. 2007. Comparison of three accelerated partial breast irradiation techniques: treatment effectiveness based upon biological models. *Radiother Oncol,* 84, 226-32.

BROWN, J. M. C. & CURRELL, F. J. 2017. A local effect model-based interpolation framework for experimental nanoparticle radiosensitisation data. *Cancer Nanotechnol,* 8, 1.

CAI, Z., CHATTOPADHYAY, N., YANG, K., KWON, Y. L., YOOK, S., PIGNOL, J. P. & REILLY, R. M. 2016. 111In-labeled trastuzumab-modified gold nanoparticles are cytotoxic in vitro to HER2-positive breast cancer cells and arrest tumor growth in vivo in athymic mice after intratumoral injection. *Nucl Med Biol,* 43**,** 818-826.

CAI, Z., CHEN, Z., BAILEY, K. E., SCOLLARD, D. A., REILLY, R. M. & VALLIS, K. A. 2008. Relationship between induction of phosphorylated H2AX and survival in breast cancer cells exposed to 111In-DTPA-hEGF. *J Nucl Med,* 49**,** 1353-61.

CAI, Z., YOOK, S., LU, Y., BERGSTROM, D., WINNIK, M. A., PIGNOL, J. P. & REILLY, R. M. 2017. Local Radiation Treatment of HER2-Positive Breast Cancer Using Trastuzumab-Modified Gold Nanoparticles Labeled with 177Lu. *Pharm Res,* 34**,** 579-590.

CAO, J., WANG, Y., YU, J., XIA, J., ZHANG, C., YIN, D. & HAFELI, U. O. 2004. Preparation and radiolabeling of surface-modified magnetic nanoparticles with rhenium-188 for magnetic targeted radiotherapy. *Journal of Magnetism and Magnetic Materials,* 277**,** 165-174.

CHATTOPADHYAY, N., CAI, Z., KWON, Y. L., LECHTMAN, E., PIGNOL, J. P. & REILLY, R. M. 2013. Molecularly targeted gold nanoparticles enhance the radiation response of breast cancer cells and tumor xenografts to X-radiation. *Breast Cancer Res Treat,* 137**,** 81-91.

CHATTOPADHYAY, N., CAI, Z., PIGNOL, J. P., KELLER, B., LECHTMAN, E., BENDAYAN, R. & REILLY, R. M. 2010. Design and characterization of HER-2-targeted gold nanoparticles for enhanced X-radiation treatment of locally advanced breast cancer. *Mol Pharm,* 7**,** 2194-206.

CHATTOPADHYAY, N., FONGE, H., CAI, Z., SCOLLARD, D., LECHTMAN, E., DONE, S. J., PIGNOL, J. P. & REILLY, R. M. 2012a. Role of Antibody-Mediated Tumor Targeting and Route of Administration in Nanoparticle Tumor Accumulation in Vivo. *Mol Pharm*.

CHATTOPADHYAY, N., FONGE, H., CAI, Z., SCOLLARD, D., LECHTMAN, E., DONE, S. J., PIGNOL, J. P. & REILLY, R. M. 2012b. Role of Antibody-Mediated Tumor Targeting and Route of Administration in Nanoparticle Tumor Accumulation in Vivo. *Mol. Pharm.,* 9**,** 2168-2179.

CHEETHAM, P. S. J., BLUNT, K. W. & BUCKE, C. 1979. Physical studies on cell immobilization using calcium alginate gels. *Biotechnology and Bioengineering* XXI**,** 2155-2168.

CHEN, Y. S., HUNG, Y. C., LIAU, I. & HUANG, G. S. 2009. Assessment of the In Vivo Toxicity of Gold Nanoparticles. *Nanoscale Res Lett,* 4**,** 858-864.

CHEN, Z. J., BROADDUS, W. C., VISWANATHAN, R. R., RAGHAVAN, R. & GILLIES, G. T. 2002. Intraparenchymal drug delivery via positive-pressure infusion: experimental and modeling studies of poroelasticity in brain phantom gels. *IEEE Trans Biomed Eng,* 49**,** 85-96.

CHIBANI, O. & LI, X. A. 2002. Monte Carlo dose calculations in homogeneous media and at interfaces: a comparison between GEPTS, EGSnrc, MCNP, and measurements. *Med Phys,* 29**,** 835-47.

CHITHRANI, D. B., JELVEH, S., JALALI, F., VAN PROOIJEN, M., ALLEN, C., BRISTOW, R. G., HILL, R. P. & JAFFRAY, D. A. 2010. Gold nanoparticles as radiation sensitizers in cancer therapy. *Radiat Res,* 173**,** 719-28.

CHO, S. H., JONES, B. L. & KRISHNAN, S. 2009. The dosimetric feasibility of gold nanoparticle-aided radiation therapy (GNRT) via brachytherapy using low-energy gamma-/x-ray sources. *Phys Med Biol,* 54**,** 4889-905.

CHOI, Y. J., BAEK, G. Y., PARK, H. R., JO, S. K. & JUNG, U. 2016. Smad2/3-Regulated Expression of DLX2 Is Associated with Radiation-Induced Epithelial-Mesenchymal Transition and Radioresistance of A549 and MDA-MB-231 Human Cancer Cell Lines. *PLoS One,* 11**,** e0147343.

COMYN, J. (ed.) 1985. *Introduction to Polymer Permeability and the Mathematics of Diffusion, In: Polymer Permeability,* London: Chapman & Hall Inc. .

CRANK, J. 1975. *The Mathematics of Diffusion,* London, Clarendon Press.

CRISTY, M. & ECKERMAN, K. F. 1987a. Specific absorbed fractions of energy at various ages from internal photon sources. I. Methods. Oak Ridge National Laboratory Rep.

CROOK, J., MCLEAN, M., CATTON, C., YEUNG, I., TSIHLIAS, J. & PINTILIE, M. 2002. Factors influencing risk of acute urinary retention after TRUS-guided permanent prostate seed implantation. *Int J Radiat Oncol Biol Phys,* 52**,** 453-60.

CUI, L., HER, S., BORST, G. R., BRISTOW, R. G., JAFFRAY, D. A. & ALLEN, C. 2017. Radiosensitization by gold nanoparticles: Will they ever make it to the clinic? *Radiother Oncol,* 124**,** 344-356.

DANIEL, M. C. & ASTRUC, D. 2004. Gold nanoparticles: assembly, supramolecular chemistry, quantum-size-related properties, and applications toward biology, catalysis, and nanotechnology. *Chem Rev,* 104**,** 293-346.

DAUER, L. T., KOLLMEIER, M. A., WILLIAMSON, M. J., ST GERMAIN, J., ALTAMIRANO, J., YAMADA, Y. & ZELEFSKY, M. J. 2010. Less-restrictive, patient-specific radiation safety precautions can be safely prescribed after permanent seed implantation. *Brachytherapy,* 9**,** 101-11.

DAVIS, M. E., CHEN, Z. G. & SHIN, D. M. 2008. Nanoparticle therapeutics: an emerging treatment modality for cancer. *Nat Rev Drug Discov,* 7**,** 771-82.

DE JONG, W. H., HAGENS, W. I., KRYSTEK, P., BURGER, M. C., SIPS, A. J. & GEERTSMA, R. E. 2008. Particle size-dependent organ distribution of gold nanoparticles after intravenous administration. *Biomaterials,* 29**,** 1912-9.

DEMANN, E. T., STEIN, P. S. & HAUBENREICH, J. E. 2005. Gold as an implant in medicine and dentistry. *J Long Term Eff Med Implants,* 15**,** 687-98.

DEVLIN, P. M. 2007. *Brachytherapy: Applications and Techniques,* Philadelphia, USA, Lippincott Williams & Wilkins.

DEWARAJA, Y. K., WILDERMAN, S. J., LJUNGBERG, M., KORAL, K. F., ZASADNY, K. & KAMINISKI, M. S. 2005. Accurate dosimetry in 131I radionuclide therapy using patient-specific, 3-dimensional methods for SPECT reconstruction and absorbed dose calculation. *J Nucl Med,* 46**,** 840-9.

DIAGARADJANE, P., SHETTY, A., WANG, J. C., ELLIOTT, A. M., SCHWARTZ, J., SHENTU, S., PARK, H. C., DEORUKHKAR, A., STAFFORD, R. J., CHO, S. H., TUNNELL, J. W., HAZLE, J. D. & KRISHNAN, S. 2008. Modulation of in vivo tumor radiation response via gold nanoshell-mediated vascular-focused hyperthermia: characterizing an integrated antihypoxic and localized vascular disrupting targeting strategy. *Nano Lett,* 8**,** 1492-500.

DICKER, A. P., MERRICK, G., GOMELLA, L., VALICENTI, R. K. & WATERMAN, F. (eds.) 2005. *Basic and advanced techniques in prostate brachytherapy,* United Kingdom: Martin Dunitz Ltd, Taylor & Francis Group plc.

DREADEN, E. C., ALKILANY, A. M., HUANG, X., MURPHY, C. J. & EL-SAYED, M. A. 2012. The golden age: gold nanoparticles for biomedicine. *Chem Soc Rev,* 41**,** 2740-79.

DREADEN, E. C., MWAKWARI, S. C., SODJI, Q. H., OYELERE, A. K. & EL-SAYED, M. A. 2009. Tamoxifen-poly(ethylene glycol)-thiol gold nanoparticle conjugates: enhanced potency and selective delivery for breast cancer treatment. *Bioconjug Chem,* 20**,** 2247-53.

EARLY BREAST CANCER TRIALISTS' COLLABORATIVE, G., DARBY, S., MCGALE, P., CORREA, C., TAYLOR, C., ARRIAGADA, R., CLARKE, M., CUTTER, D., DAVIES, C., EWERTZ, M., GODWIN, J., GRAY, R., PIERCE, L., WHELAN, T., WANG, Y. & PETO, R. 2011. Effect of radiotherapy after breast-conserving surgery on 10-year recurrence and 15-year breast cancer death: meta-analysis of individual patient data for 10,801 women in 17 randomised trials. *Lancet,* 378**,** 1707-16.

ECKERMAN, K. F. & ENDO, A. 2008. *MIRD: Radionuclide Data and Decay Schemes,* Reston, VA, The Society of Nuclear Medicine.

EHLERDING, E. B. & CAI, W. 2016. Smaller Agents for Larger Therapeutic Indices: Nanoscale Brachytherapy with 177Lu-Labeled Gold Nanoparticles. *J Nucl Med,* 57**,** 834-5.

EIKENES, L., TARI, M., TUFTO, I., BRULAND, O. S. & DE LANGE DAVIES, C. 2005. Hyaluronidase induces a transcapillary pressure gradient and improves the distribution and uptake of liposomal doxorubicin (Caelyx) in human osteosarcoma xenografts. *Br J Cancer,* 93**,** 81-8.

EL-SAYED, I. H., HUANG, X. & EL-SAYED, M. A. 2006. Selective laser photo-thermal therapy of epithelial carcinoma using anti-EGFR antibody conjugated gold nanoparticles. *Cancer Lett,* 239**,** 129-35.

ENGLAND, C. G., GOBIN, A. M. & FRIEBOES, H. B. 2015. Evaluation of uptake and distribution of gold nanoparticles in solid tumors. *Eur Phys J Plus,* 130.

FERLAY, J., SOERJOMATARAM, I., DIKSHIT, R., ESER, S., MATHERS, C., REBELO, M., PARKIN, D. M., FORMAN, D. & BRAY, F. 2015. Cancer incidence and mortality worldwide: sources, methods and major patterns in GLOBOCAN 2012. *Int J Cancer,* 136**,** E359-86.

FISCHBACH, A. J., SAUSE, W. T. & PLENK, H. P. 1980. Radiation therapy for skin cancer. *West J Med,* 133**,** 379-82.

FORRER, F., KRENNING, E. P., KOOIJ, P. P., BERNARD, B. F., KONIJNENBERG, M., BAKKER, W. H., TEUNISSEN, J. J., DE JONG, M., VAN LOM, K., DE HERDER, W. W. & KWEKKEBOOM, D. J. 2009. Bone marrow dosimetry in peptide receptor radionuclide therapy with [177Lu-DOTA(0),Tyr(3)]octreotate. *Eur J Nucl Med Mol Imaging,* 36**,** 1138-46.

GHOSH, P., HAN, G., DE, M., KIM, C. K. & ROTELLO, V. M. 2008. Gold nanoparticles in delivery applications. *Adv Drug Deliv Rev,* 60**,** 1307-15.

GIASUDDIN, A., JHUMA, K. & HAQ, A. M. 2012. Use of Gold Nanoparticles in Diagnostics, Surgery and Medicine: A Review. *Bangladesh J Med Biochem,* 5**,** 56-60.

GIBSON, J. D., KHANAL, B. P. & ZUBAREV, E. R. 2007. Paclitaxel-functionalized gold nanoparticles. *J Am Chem Soc,* 129**,** 11653-61.

GOODMAN, C. M., MCCUSKER, C. D., YILMAZ, T. & ROTELLO, V. M. 2004. Toxicity of gold nanoparticles functionalized with cationic and anionic side chains. *Bioconjug Chem,* 15**,** 897-900.

GRIMES, J. & CELLER, A. 2014. Comparison of internal dose estimates obtained using organ-level, voxel S value, and Monte Carlo techniques. *Med Phys,* 41**,** 092501.

GUTIN, P. H., LEIBEL, S. A., HOSOBUCHI, Y., CRUMLEY, R. L., EDWARDS, M. S., WILSON, C. B., LAMB, S. & WEAVER, K. A. 1987. Brachytherapy of recurrent tumors of the skull base and spine with iodine-125 sources. *Neurosurgery,* 20**,** 938-45.

GUTIN, P. H., PHILLIPS, T. L., HOSOBUCHI, Y., WARA, W. M., MACKAY, A. R., WEAVER, K. A., LAMB, S. & HURST, S. 1981. Permanent and removable implants for the brachytherapy of brain tumors. *Int J Radiat Oncol Biol Phys,* 7**,** 1371-81.

HAINFELD, J. F., LIN, L., SLATKIN, D. N., AVRAHAM DILMANIAN, F., VADAS, T. M. & SMILOWITZ, H. M. 2014. Gold nanoparticle hyperthermia reduces radiotherapy dose. *Nanomedicine,* 10**,** 1609-17.

HAINFELD, J. F., SLATKIN, D. N. & SMILOWITZ, H. M. 2004. The use of gold nanoparticles to enhance radiotherapy in mice. *Phys Med Biol,* 49**,** N309-15.

HAKKINEN, H. 2012. The gold-sulfur interface at the nanoscale. *Nat Chem,* 4**,** 443-55.

HALDAR, S., NEGRINI, M., MONNE, M., SABBIONI, S. & CROCE, C. M. 1994. Down-regulation of bcl-2 by p53 in breast cancer cells. *Cancer Res,* 54**,** 2095-7.

HANNOUN, B. J. & STEPHANOPOULOS, G. 1986. Diffusion coefficients of glucose and ethanol in cell-free and cell-occupied calcium alginate membranes. *Biotechnol Bioeng,* 28**,** 829-35.

HE, C., HU, Y., YIN, L., TANG, C. & YIN, C. 2010. Effects of particle size and surface charge on cellular uptake and biodistribution of polymeric nanoparticles. *Biomaterials,* 31**,** 3657-66.

HENRY, A. M., AL-QAISIEH, B., GOULD, K., BOWNES, P., SMITH, J., CAREY, B., BOTTOMLEY, D. & ASH, D. 2010. Outcomes following iodine-125 monotherapy for localized prostate cancer: the results of leeds 10-year single-center brachytherapy experience. *Int J Radiat Oncol Biol Phys,* 76**,** 50-6.

HEPEL, J. T. & WAZER, D. E. 2012. A comparison of brachytherapy techniques for partial breast irradiation. *Brachytherapy,* 11**,** 163-75.

HU, M., NOVO, C., FUNSTON, A., WANG, H., STALEVA, H., ZOU, S., MULVANEY, P., XIA, Y. & HARTLAND, G. V. 2008. Dark-field microscopy studies of single metal nanoparticles: understanding the factors that influence the linewidth of the localized surface plasmon resonance. *J Mater Chem,* 18**,** 1949-1960.

HUANG, K., SNEED, P. K., KUNWAR, S., KRAGTEN, A., LARSON, D. A., BERGER, M. S., CHAN, A., POULIOT, J. & MCDERMOTT, M. W. 2009. Surgical resection and permanent iodine-125 brachytherapy for brain metastases. *J Neurooncol,* 91**,** 83-93.

HUANG, P., BAO, L., ZHANG, C., LIN, J., LUO, T., YANG, D., HE, M., LI, Z., GAO, G., GAO, B., FU, S. & CUI, D. 2011. Folic acid-conjugated silica-modified gold nanorods for X-ray/CT imaging-guided dual-mode radiation and photo-thermal therapy. *Biomaterials,* 32**,** 9796-809.

HUANG, X., JAIN, P. K., EL-SAYED, I. H. & EL-SAYED, M. A. 2008. Plasmonic photothermal therapy (PPTT) using gold nanoparticles. *Lasers Med Sci,* 23**,** 217-28.

HUANG, X., QIAN, W., EL-SAYED, I. H. & EL-SAYED, M. A. 2007. The potential use of the enhanced nonlinear properties of gold nanospheres in photothermal cancer therapy. *Lasers Surg Med,* 39**,** 747-53.

HUGUET, M. L. & DELLACHERIE, E. 1996. Calcium alginate beads coated with chitosan: effect of the structure of encapsulated materials on their release. 31**,** 745-751.

ICRU 1989. Tissue Substitutes in Radiation Dosimetry and Measurement. Bethesda, MD: International Commission on Radiation Units and Measurements.

JACKSON, P. A., BEAUREGARD, J. M., HOFMAN, M. S., KRON, T., HOGG, A. & HICKS, R. J. 2013. An automated voxelized dosimetry tool for radionuclide therapy based on serial quantitative SPECT/CT imaging. *Med Phys,* 40**,** 112503.

JAIN, R. A. 2000. The manufacturing techniques of various drug loaded biodegradable poly(lactide-co-glycolide) (PLGA) devices. *Biomaterials,* 21**,** 2475-90.

JANSEN, N., DENEUFBOURG, J. M. & NICKERS, P. 2007. Adjuvant stereotactic permanent seed breast implant: a boost series in view of partial breast irradiation. *Int J Radiat Oncol Biol Phys,* 67**,** 1052-8.

JIMENEZ-MANCILLA, N., FERRO-FLORES, G., SANTOS-CUEVAS, C., OCAMPO-GARCIA, B., LUNA-GUTIERREZ, M., AZORIN-VEGA, E., ISAAC-OLIVE, K., CAMACHO-LOPEZ, M. & TORRES-GARCIA, E. 2013. Multifunctional targeted therapy system based on (99m) Tc/(177) Lu-labeled gold nanoparticles-Tat(49-57)-Lys(3) -bombesin internalized in nuclei of prostate cancer cells. *J Labelled Comp Radiopharm,* 56**,** 663-71.

JIN, G. H., CHEN, L. X., DENG, X. W., LIU, X. W., HUANG, Y. & HUANG, X. B. 2013. A comparative dosimetric study for treating left-sided breast cancer for small breast size using five different radiotherapy techniques: conventional tangential field, filed-in-filed, tangential-IMRT, multi-beam IMRT and VMAT. *Radiat Oncol,* 8**,** 89.

JONES, B. L., KRISHNAN, S. & CHO, S. H. 2010. Estimation of microscopic dose enhancement factor around gold nanoparticles by Monte Carlo calculations. *Med Phys,* 37**,** 3809-16.

KELLER, B., SANKREACHA, R., RAKOVITCH, E., O'BRIEN, P. & PIGNOL, J. P. 2005. A permanent breast seed implant as partial breast radiation therapy for early-stage patients: a comparison of palladium-103 and iodine-125 isotopes based on radiation safety considerations. *Int J Radiat Oncol Biol Phys,* 62**,** 358-65.

KELLER, B. M., RAVI, A., SANKREACHA, R. & PIGNOL, J. P. 2012. Permanent breast seed implant dosimetry quality assurance. *Int J Radiat Oncol Biol Phys,* 83**,** 84-92.

KHLEBTSOV, N. & DYKMAN, L. 2011. Biodistribution and toxicity of engineered gold nanoparticles: a review of in vitro and in vivo studies. *Chem Soc Rev,* 40**,** 1647-71.

KIM, B., HAN, G., TOLEY, B. J., KIM, C. K., ROTELLO, V. M. & FORBES, N. S. 2010a. Tuning payload delivery in tumour cylindroids using gold nanoparticles. *Nat Nanotechnol,* 5**,** 465-72.

KIM, B. Y., RUTKA, J. T. & CHAN, W. C. 2010b. Nanomedicine. *N Engl J Med,* 363**,** 2434-43.

KIM, D. W., KIM, J. H., PARK, M., YEOM, J. H., GO, H., KIM, S., HAN, M. S., LEE, K. & BAE, J. 2011. Modulation of biological processes in the nucleus by delivery of DNA oligonucleotides conjugated with gold nanoparticles. *Biomaterials,* 32**,** 2593-604.

KIM, M. R., GILLIES, R. J. & REJNIAK, K. A. 2013. Current advances in mathematical modeling of anti-cancer drug penetration into tumor tissues. *Front Oncol,* 3**,** 278.

KING, C. R. 2002. LDR vs. HDR brachytherapy for localized prostate cancer: the view from radiobiological models. *Brachytherapy,* 1**,** 219-26.

KLEIN, J., STOCK, J. & VORLOP, D. 1983. Pore size and properties of spherical Ca-alginate biocatalysts. *European journal of applied microbiology and biotechnology,* 18**,** 86-91.

KNOOS, T., KRISTENSEN, I. & NILSSON, P. 1998. Volumetric and dosimetric evaluation of radiation treatment plans: radiation conformity index. *Int J Radiat Oncol Biol Phys,* 42**,** 1169-76.

KONO, Y., KUBOTA, K., ARUGA, T., ISHIBASHI, A., MOROOKA, M., ITO, K., ITAMI, J., KANEMURA, M., MINOWADA, S. & TANAKA, T. 2010. Swelling of the prostate gland by permanent brachytherapy may affect seed migration. *Jpn J Clin Oncol,* 40**,** 1159-65.

KRAMER, B. A., ARTHUR, D. W., ULIN, K., SCHMIDT-ULLRICH, R. K., ZWICKER, R. D. & WAZER, D. E. 1999. Cosmetic outcome in patients receiving an interstitial implant as part of breast-conservation therapy. *Radiology,* 213**,** 61-6.

KUMAR, A., MA, H., ZHANG, X., HUANG, K., JIN, S., LIU, J., WEI, T., CAO, W., ZOU, G. & LIANG, X. J. 2012. Gold nanoparticles functionalized with therapeutic and targeted peptides for cancer treatment. *Biomaterials,* 33**,** 1180-9.

KUMAR, A., ZHANG, X. & LIANG, X. J. 2013. Gold nanoparticles: emerging paradigm for targeted drug delivery system. *Biotechnol Adv,* 31**,** 593-606.

KUMAR, R., BELZ, J., MARKOVIC, S., JADHAV, T., FOWLE, W., NIEDRE, M., CORMACK, R., MAKRIGIORGOS, M. G. & SRIDHAR, S. 2015. Nanoparticle-based brachytherapy spacers for delivery of localized combined chemoradiation therapy. *Int J Radiat Oncol Biol Phys,* 91**,** 393-400.

LAI, P., CAI, Z., PIGNOL, J. P., LECHTMAN, E., MASHOUF, S., LU, Y., WINNIK, M. A., JAFFRAY, D. A. & REILLY, R. M. 2017. Monte Carlo simulation of radiation transport and dose deposition from locally released gold nanoparticles labeled with (111)In, (177)Lu or (90)Y incorporated into tissue implantable depots. *Phys Med Biol,* 62**,** 8581-8599.

LAI, P., LECHTMAN, E., MASHOUF, S., PIGNOL, J. P. & REILLY, R. M. 2016. Depot system for controlled release of gold nanoparticles with precise intratumoral placement by permanent brachytherapy seed implantation (PSI) techniques. *Int J Pharm,* 515**,** 729-739.

LANCONELLI, N., PACILIO, M., LO MEO, S., BOTTA, F., DI DIA, A., AROCHE, A. T., PEREZ, M. A. & CREMONESI, M. 2012. A free database of radionuclide voxel S values for the dosimetry of nonuniform activity distributions. *Phys Med Biol,* 57**,** 517-33.

LARSON, D. A., SUPLICA, J. M., CHANG, S. M., LAMBORN, K. R., MCDERMOTT, M. W., SNEED, P. K., PRADOS, M. D., WARA, W. M., NICHOLAS, M. K. & BERGER, M. S. 2004. Permanent iodine 125 brachytherapy in patients with progressive or recurrent glioblastoma multiforme. *Neuro Oncol,* 6**,** 119-26.

LECHTMAN, E., CHATTOPADHYAY, N., CAI, Z., MASHOUF, S., REILLY, R. & PIGNOL, J. P. 2011. Implications on clinical scenario of gold nanoparticle radiosensitization in regards to photon energy, nanoparticle size, concentration and location. *Phys Med Biol,* 56**,** 4631-47.

LEE, K. Y. & MOONEY, D. J. 2012. Alginate: properties and biomedical applications. *Prog Polym Sci,* 37**,** 106-126.

LETTMAIER, S., KREPPNER, S., LOTTER, M., WALSER, M., OTT, O. J., FIETKAU, R. & STRNAD, V. 2011. Radiation exposure of the heart, lung and skin by radiation therapy for breast cancer: a dosimetric comparison between partial breast irradiation using multicatheter brachytherapy and whole breast teletherapy. *Radiother Oncol,* 100**,** 189-94.

LI, J. Y., LI, Y. Y., JIN, W., YANG, Q., SHAO, Z. M. & TIAN, X. S. 2012. ABT-737 reverses the acquired radioresistance of breast cancer cells by targeting Bcl-2 and Bcl-xL. *J Exp Clin Cancer Res,* 31**,** 102.

LIANG, J. J., ZHOU, Y. Y., WU, J. & DING, Y. 2014. Gold nanoparticle-based drug delivery platform for antineoplastic chemotherapy. *Curr Drug Metab,* 15**,** 620-31.

LIN, L., PATEL, R. R., THOMADSEN, B. R. & HENDERSON, D. L. 2008. The use of directional interstitial sources to improve dosimetry in breast brachytherapy. *Med Phys,* 35**,** 240-7.

LIU, S. Y., LIANG, Z. S., GAO, F., LUO, S. F. & LU, G. Q. 2010. In vitro photothermal study of gold nanoshells functionalized with small targeting peptides to liver cancer cells. *J Mater Sci Mater Med,* 21**,** 665-74.

LIU, Y., YANG, M., ZHANG, J., ZHI, X., LI, C., ZHANG, C., PAN, F., WANG, K., YANG, Y., MARTINEZ DE LA FUENTEA, J. & CUI, D. 2016. Human Induced Pluripotent Stem Cells for Tumor Targeted Delivery of Gold Nanorods and Enhanced Photothermal Therapy. *ACS Nano,* 10**,** 2375-85.

LJUNGBERG, M., SJOGREEN, K., LIU, X., FREY, E., DEWARAJA, Y. & STRAND, S. E. 2002. A 3-dimensional absorbed dose calculation method based on quantitative SPECT for radionuclide therapy: evaluation for (131)I using monte carlo simulation. *J Nucl Med,* 43**,** 1101-9.

LLEVOT, A. & ASTRUC, D. 2012. Applications of vectorized gold nanoparticles to the diagnosis and therapy of cancer. *Chem Soc Rev,* 41**,** 242-57.

MAEDA, H. 2012. Vascular permeability in cancer and infection as related to macromolecular drug delivery, with emphasis on the EPR effect for tumor-selective drug targeting. *Proc Jpn Acad Ser B Phys Biol Sci,* 88**,** 53-71.

MAEDA, H., WU, J., SAWA, T., MATSUMURA, Y. & HORI, K. 2000. Tumor vascular permeability and the EPR effect in macromolecular therapeutics: a review. *J Control Release,* 65**,** 271-84.

MAKADIA, H. K. & SIEGEL, S. J. 2011. Poly Lactic-co-Glycolic Acid (PLGA) as Biodegradable Controlled Drug Delivery Carrier. *Polymers (Basel),* 3**,** 1377-1397.

MANSON, J., KUMAR, D., MEENAN, B. J. & DIXON, D. 2011. Polyethylene glycol functionalized gold nanoparticles: the influence of capping density on stability in various media. *Gold Bulletin,* 44**,** 99-105.

MARTINEZ-MONGE, R., NAG, S., NIERODA, C. A. & MARTIN, E. W. 1999. Iodine-125 brachytherapy in the treatment of colorectal adenocarcinoma metastatic to the liver. *Cancer,* 85**,** 1218-25.

MARTINEZ-MONGE, R., PAGOLA, M., VIVAS, I. & LOPEZ-PICAZO, J. M. 2008. CT-guided permanent brachytherapy for patients with medically inoperable early-stage non-small cell lung cancer (NSCLC). *Lung Cancer,* 61**,** 209-13.

MCMAHON, S. J., HYLAND, W. B., MUIR, M. F., COULTER, J. A., JAIN, S., BUTTERWORTH, K. T., SCHETTINO, G., DICKSON, G. R., HOUNSELL, A. R., O'SULLIVAN, J. M., PRISE, K. M., HIRST, D. G. & CURRELL, F. J. 2011. Biological consequences of nanoscale energy deposition near irradiated heavy atom nanoparticles. *Sci Rep,* 1**,** 18.

MEIGOONI, A. S., ZHANG, H., PERRY, C., DINI, S. A. & KOONA, R. A. 2003. Theoretical and experimental determination of dosimetric characteristics for brachyseed Pd-103, model Pd-1, source. *Appl Radiat Isot,* 58**,** 533-41.

MEREDITH, R., WESSELS, B. & KNOX, S. 2008. Risks to normal tissues from radionuclide therapy. *Semin Nucl Med,* 38**,** 347-57.

MONK, B. J., TEWARI, K. S., PUTHAWALA, A. A., SYED, A. M., HAUGEN, J. A. & BURGER, R. A. 2002. Treatment of recurrent gynecologic malignancies with iodine-125 permanent interstitial irradiation. *Int J Radiat Oncol Biol Phys,* 52**,** 806-15.

MORTON, D., HILTS, M., BATCHELAR, D. & CROOK, J. 2016. Seed Placement in Permanent Breast Seed Implant Brachytherapy: Are Concerns Over Accuracy Valid? *Int J Radiat Oncol Biol Phys,* 95**,** 1050-7.

NAG, S., BEYER, D., FRIEDLAND, J., GRIMM, P. & NATH, R. 1999. American Brachytherapy Society (ABS) recommendations for transperineal permanent brachytherapy of prostate cancer. *Int J Radiat Oncol Biol Phys,* 44**,** 789-99.

NAG, S., SHASHA, D., JANJAN, N., PETERSEN, I., ZAIDER, M. & AMERICAN BRACHYTHERAPY, S. 2001. The American Brachytherapy Society recommendations for brachytherapy of soft tissue sarcomas. *Int J Radiat Oncol Biol Phys,* 49**,** 1033-43.

NETTI, P. A., BERK, D. A., SWARTZ, M. A., GRODZINSKY, A. J. & JAIN, R. K. 2000. Role of extracellular matrix assembly in interstitial transport in solid tumors. *Cancer Res,* 60**,** 2497-503.

NGWA, W., MAKRIGIORGOS, G. M. & BERBECO, R. I. 2012. Gold nanoparticle-aided brachytherapy with vascular dose painting: estimation of dose enhancement to the tumor endothelial cell nucleus. *Med Phys,* 39**,** 392-8.

NICOLAE, A. M., VENUGOPAL, N. & RAVI, A. 2016. Trends in targeted prostate brachytherapy: from multiparametric MRI to nanomolecular radiosensitizers. *Cancer Nanotechnol,* 7**,** 6.

NIKJOO, H., EMFIETZOGLOU, D., LIAMSUWAN, T., TALEEI, R., LILJEQUIST, D. & UEHARA, S. 2016. Radiation track, DNA damage and response-a review. *Rep Prog Phys,* 79**,** 116601.

NIKJOO, H., UEHARA, S., EMFIETZOGLOU, D. & CUCINOTTA, F. A. 2006. Track-structure codes in radiation research. *Radiation Measurements,* 41**,** 1052-1074.

NIKJOO, H., UEHARA, S., WILSON, W. E., HOSHI, M. & GOODHEAD, D. T. 1998. Track structure in radiation biology: theory and applications. *Int J Radiat Biol,* 73**,** 355-64.

NORI, D., MERIMSKY, O., OSIAN, A. D., HEFFERNAN, M., CORTES, E. & TURNER, J. W. 1996. Palladium-103: a new radioactive source in the treatment of unresectable carcinoma of the pancreas: a phase I-II study. *J Surg Oncol,* 61**,** 300-5.

OLIVOTTO, I. A., WHELAN, T. J., PARPIA, S., KIM, D. H., BERRANG, T., TRUONG, P. T., KONG, I., COCHRANE, B., NICHOL, A., ROY, I., GERMAIN, I., AKRA, M., REED, M., FYLES, A., TROTTER, T., PERERA, F., BECKHAM, W., LEVINE, M. N. & JULIAN, J. A. 2013. Interim cosmetic and toxicity results from RAPID: a randomized trial of accelerated partial breast irradiation using three-dimensional conformal external beam radiation therapy. *J Clin Oncol,* 31**,** 4038-45.

PACILIO, M., AMATO, E., LANCONELLI, N., BASILE, C., TORRES, L. A., BOTTA, F., FERRARI, M., DIAZ, N. C., PEREZ, M. C., FERNANDEZ, M., LASSMANN, M., GIL, A. V. & CREMONESI, M. 2015. Differences in 3D dose distributions due to calculation method of voxel S-values and the influence of image blurring in SPECT. *Phys Med Biol,* 60**,** 1945-64.

PACIOTTI, G. F., KINGSTON, D. G. I. & TAMARKIN, L. 2006. Colloidal Gold Nanoparticles: A Novel Nanoparticle Platform for Developing multifunctional Tumor-Targeted Drug Delivery Vectors. *Drug Development Research,* 67**,** 47-54.

PACIOTTI, G. F., MYER, L., WEINREICH, D., GOIA, D., PAVEL, N., MCLAUGHLIN, R. E. & TAMARKIN, L. 2004. Colloidal gold: a novel nanoparticle vector for tumor directed drug delivery. *Drug Deliv,* 11**,** 169-83.

PAN, Y., LEIFERT, A., RUAU, D., NEUSS, S., BORNEMANN, J., SCHMID, G., BRANDAU, W., SIMON, U. & JAHNEN-DECHENT, W. 2009. Gold nanoparticles of diameter 1.4 nm trigger necrosis by oxidative stress and mitochondrial damage. *Small,* 5**,** 2067-76.

PATEL, R. R., BECKER, S. J., DAS, R. K. & MACKIE, T. R. 2007. A dosimetric comparison of accelerated partial breast irradiation techniques: multicatheter interstitial brachytherapy, three-dimensional conformal radiotherapy, and supine versus prone helical tomotherapy. *Int J Radiat Oncol Biol Phys,* 68**,** 935-42.

PEKKANEN, A. M., DEWITT, M. R. & RYLANDER, M. N. 2014. Nanoparticle enhanced optical imaging and phototherapy of cancer. *J Biomed Nanotechnol,* 10**,** 1677-712.

PERRAULT, S. D., WALKEY, C., JENNINGS, T., FISCHER, H. C. & CHAN, W. C. 2009. Mediating tumor targeting efficiency of nanoparticles through design. *Nano Lett,* 9**,** 1909-15.

PETROVA, D., SMICKOVSKA, S. & LAZAREVSKA, E. 2017. Conformity Index and Homogeneity Index of the Postoperative Whole Breast Radiotherapy. *Open Access Maced J Med Sci,* 5**,** 736-739.

PIGNOL, J.-P. & KELLER, B. M. 2009a. Permanent Breast Seed Implants. *In:* WAZER, D. E., ARTHUR, D. W. & VICINI, F. A. (eds.) *Accelerated Partial Breast Irradiation: Techniques and Clinical Implementation.* 2nd ed. Verlag Berlin Heidelberg: Springer.

PIGNOL, J. & KELLER, B. M. 2009b. Permanent Breast Seed Implants. *In:* WAZER, D. E. (ed.) *Accelerated Partial Breast Irradiation.* New York: Springer-Verlag Berlin Heidelberg.

PIGNOL, J. P., CAUDRELIER, J. M., CROOK, J., MCCANN, C., TRUONG, P. & VERKOOIJEN, H. A. 2015. Report on the Clinical Outcomes of Permanent Breast Seed Implant for Early-Stage Breast Cancers. *Int J Radiat Oncol Biol Phys,* 93**,** 614-21.

PIGNOL, J. P., KELLER, B., RAKOVITCH, E., SANKREACHA, R., EASTON, H. & QUE, W. 2006. First report of a permanent breast 103Pd seed implant as adjuvant radiation treatment for early-stage breast cancer. *Int J Radiat Oncol Biol Phys,* 64**,** 176-81.

PIGNOL, J. P., RAKOVITCH, E., KELLER, B. M., SANKREACHA, R. & CHARTIER, C. 2009. Tolerance and acceptance results of a palladium-103 permanent breast seed implant Phase I/II study. *Int J Radiat Oncol Biol Phys,* 73**,** 1482-8.

PODGORSAK, E. B. 2006. *Radiation Physics for Medical Physicists,* Germany, Springer-erla Berlin Heidelberg.

PORRAZZO, M. S., HILARIS, B. S., MOORTHY, C. R., TCHELEBI, A. E., MASTORAS, C. A., SHIH, L. L., STABILE, L. & SALVARAS, N. 1992. Permanent interstitial implantation using palladium-103: the New York Medical College preliminary experience. *Int J Radiat Oncol Biol Phys,* 23**,** 1033-6.

PORTER, A. T., BLASKO, J. C., GRIMM, P. D., REDDY, S. M. & RAGDE, H. 1995. Brachytherapy for prostate cancer. *CA Cancer J Clin,* 45**,** 165-78.

POTTERS, L., KLEIN, E. A., KATTAN, M. W., REDDY, C. A., CIEZKI, J. P., REUTHER, A. M. & KUPELIAN, P. A. 2004. Monotherapy for stage T1-T2 prostate cancer: radical prostatectomy, external beam radiotherapy, or permanent seed implantation. *Radiother Oncol,* 71**,** 29-33.

PRABHAKAR, U., MAEDA, H., JAIN, R. K., SEVICK-MURACA, E. M., ZAMBONI, W., FAROKHZAD, O. C., BARRY, S. T., GABIZON, A., GRODZINSKI, P. & BLAKEY, D. C. 2013. Challenges and key considerations of the enhanced permeability and retention effect for nanomedicine drug delivery in oncology. *Cancer Res,* 73**,** 2412-7.

PRAT, A., PINEDA, E., ADAMO, B., GALVAN, P., FERNANDEZ, A., GABA, L., DIEZ, M., VILADOT, M., ARANCE, A. & MUNOZ, M. 2015. Clinical implications of the intrinsic molecular subtypes of breast cancer. *Breast,* 24 Suppl 2**,** S26-35.

RAHMAN, W. N., BISHARA, N., ACKERLY, T., HE, C. F., JACKSON, P., WONG, C., DAVIDSON, R. & GESO, M. 2009. Enhancement of radiation effects by gold nanoparticles for superficial radiation therapy. *Nanomedicine,* 5**,** 136-42.

RAVI, A., KELLER, B. M. & PIGNOL, J. P. 2011. A comparison of postimplant dosimetry for (103)Pd versus (131)Cs seeds on a retrospective series of PBSI patients. *Med Phys,* 38**,** 6046-52.

RAY, P. C., YU, H. & FU, P. P. 2009. Toxicity and environmental risks of nanomaterials: challenges and future needs. *J Environ Sci Health C Environ Carcinog Ecotoxicol Rev,* 27**,** 1-35.

REINER, D., BLAICKNER, M. & RATTAY, F. 2009. Discrete beta dose kernel matrices for nuclides applied in targeted radionuclide therapy (TRT) calculated with MCNP5. *Med Phys,* 36**,** 4890-6.

RENIERS, B., VYNCKIER, S. & SCALLIET, P. 2002. Dosimetric study of a new palladium seed. *Appl Radiat Isot,* 57**,** 805-11.

REYNAERT, N., PALMANS, H., THIERENS, H. & JERAJ, R. 2002. Parameter dependence of the MCNP electron transport in determining dose distributions. *Med Phys,* 29**,** 2446-54.

RILEY, R. S. & DAY, E. S. 2017. Gold nanoparticle-mediated photothermal therapy: applications and opportunities for multimodal cancer treatment. *Wiley Interdiscip Rev Nanomed Nanobiotechnol,* 9.

RIVARD, M. J., COURSEY, B. M., DEWERD, L. A., HANSON, W. F., HUQ, M. S., IBBOTT, G. S., MITCH, M. G., NATH, R. & WILLIAMSON, J. F. 2004. Update of AAPM Task Group No. 43 Report: A revised AAPM protocol for brachytherapy dose calculations. *Med Phys,* 31**,** 633-74.

SADAUSKAS, E., DANSCHER, G., STOLTENBERG, M., VOGEL, U., LARSEN, A. & WALLIN, H. 2009. Protracted elimination of gold nanoparticles from mouse liver. *Nanomedicine,* 5**,** 162-9.

SAHGAL, A. & ROACH, M., 3RD 2007. Permanent prostate seed brachytherapy: a current perspective on the evolution of the technique and its application. *Nat Clin Pract Urol,* 4**,** 658-70.

SAITO, S., NAGATA, H., KOSUGI, M., TOYA, K. & YOROZU, A. 2007. Brachytherapy with permanent seed implantation. *Int J Clin Oncol,* 12**,** 395-407.

SAKATA, D., INCERTI, S., BORDAGE, M. C., LAMPE, N., OKADA, S., EMFIETZOGLOU, D., KYRIAKOU, I., MURAKAMI, K., SASAKI, T., TRAN, H., GUATELLI, S. & IVANTCHENKO, V. N. 2016. An implementation of discrete electron transport models for gold in the Geant4 simulation toolkit. *Journal of Applied Physics* 120.

SALLOUM, M., MA, R. H., WEEKS, D. & ZHU, L. 2008. Controlling nanoparticle delivery in magnetic nanoparticle hyperthermia for cancer treatment: experimental study in agarose gel. *Int J Hyperthermia,* 24**,** 337-45.

SCHWARZ, S. B., THON, N., NIKOLAJEK, K., NIYAZI, M., TONN, J. C., BELKA, C. & KRETH, F. W. 2012. Iodine-125 brachytherapy for brain tumours--a review. *Radiat Oncol,* 7**,** 30.

SHANKAR, S. S., AHMAD, A., PASRICHAA, R. & SASTRY, M. 2003. Bioreduction of chloroaurate ions by geranium leaves and its endophytic fungus yields gold nanoparticles of different shapes. *Journal of Materials Chemistry,* 13**,** 1822-1826.

SHARMA, D. N., GANDHI, A. K., SHARMA, S., RATH, G. K., JAGADESAN, P. & JULKA, P. K. 2013. Interstitial brachytherapy vs. intensity-modulated radiation therapy for patients with cervical carcinoma not suitable for intracavitary radiation therapy. *Brachytherapy,* 12**,** 311-6.

SHUKLA, R., CHANDA, N., ZAMBRE, A., UPENDRAN, A., KATTI, K., KULKARNI, R. R., NUNE, S. K., CASTEEL, S. W., SMITH, C. J., VIMAL, J., BOOTE, E., ROBERTSON, J. D., KAN, P., ENGELBRECHT, H., WATKINSON, L. D., CARMACK, T. L., LEVER, J. R., CUTLER, C. S., CALDWELL, C., KANNAN, R. & KATTI, K. V. 2012. Laminin receptor specific therapeutic gold nanoparticles (198AuNP-EGCg) show efficacy in treating prostate cancer. *Proc Natl Acad Sci U S A,* 109**,** 12426-31.

SINHA, N., CIFTER, G., SAJO, E., KUMAR, R., SRIDHAR, S., NGUYEN, P. L., CORMACK, R. A., MAKRIGIORGOS, G. M. & NGWA, W. 2015. Brachytherapy application with in situ dose painting administered by gold nanoparticle eluters. *Int J Radiat Oncol Biol Phys,* 91**,** 385-92.

SMITH, B. D., ARTHUR, D. W., BUCHHOLZ, T. A., HAFFTY, B. G., HAHN, C. A., HARDENBERGH, P. H., JULIAN, T. B., MARKS, L. B., TODOR, D. A., VICINI, F. A., WHELAN, T. J., WHITE, J., WO, J. Y. & HARRIS, J. R. 2009. Accelerated partial breast irradiation consensus statement from the American Society for Radiation Oncology (ASTRO). *Int J Radiat Oncol Biol Phys,* 74**,** 987-1001.

SMITH, G. L., XU, Y., BUCHHOLZ, T. A., GIORDANO, S. H., JIANG, J., SHIH, Y. C. & SMITH, B. D. 2012. Association between treatment with brachytherapy vs whole-breast irradiation and subsequent mastectomy, complications, and survival among older women with invasive breast cancer. *JAMA,* 307**,** 1827-37.

STABIN, M. G. 1996. MIRDOSE: personal computer software for internal dose assessment in nuclear medicine. *J Nucl Med,* 37**,** 538-46.

STABIN, M. G., SPARKS, R. B. & CROWE, E. 2005. OLINDA/EXM: the second-generation personal computer software for internal dose assessment in nuclear medicine. *J Nucl Med,* 46**,** 1023-7.

STAPLETON, S., JAFFRAY, D. & MILOSEVIC, M. 2017. Radiation effects on the tumor microenvironment: Implications for nanomedicine delivery. *Adv Drug Deliv Rev,* 109**,** 119-130.

STAPLETON, S., MILOSEVIC, M., ALLEN, C., ZHENG, J., DUNNE, M., YEUNG, I. & JAFFRAY, D. A. 2013. A mathematical model of the enhanced permeability and retention effect for liposome transport in solid tumors. *PLoS One,* 8**,** e81157.

STAPLETON, S., MILOSEVIC, M., TANNOCK, I. F., ALLEN, C. & JAFFRAY, D. A. 2015. The intra-tumoral relationship between microcirculation, interstitial fluid pressure and liposome accumulation. *J Control Release,* 211**,** 163-70.

STAPLETON, S. & MILOSEVIC, M. F. 2013. Pressure gradients in solid tumors. *Cancer Targeted Drug Delivery.* Springer.

STATISTICS, C. C. S. S. A. C. O. C. 2017. Canadian Cancer Statistics *In:* PUBLIC HEALTH AGENCY OF CANADA, P. T. C. R. (ed.). Toronto, ON: Canadian Cancer Society

STEICHEN, S. D., CALDORERA-MOORE, M. & PEPPAS, N. A. 2013. A review of current nanoparticle and targeting moieties for the delivery of cancer therapeutics. *Eur J Pharm Sci,* 48**,** 416-27.

STRNAD, V., OTT, O. J., HILDEBRANDT, G., KAUER-DORNER, D., KNAUERHASE, H., MAJOR, T., LYCZEK, J., GUINOT, J. L., DUNST, J., GUTIERREZ MIGUELEZ, C., SLAMPA, P., ALLGAUER, M., LOSSL, K., POLAT, B., KOVACS, G., FISCHEDICK, A. R., WENDT, T. G., FIETKAU, R., HINDEMITH, M., RESCH, A., KULIK, A., ARRIBAS, L., NIEHOFF, P., GUEDEA, F., SCHLAMANN, A., POTTER, R., GALL, C., MALZER, M., UTER, W., POLGAR, C., GROUPE EUROPEEN DE CURIETHERAPIE OF EUROPEAN SOCIETY FOR, R. & ONCOLOGY 2016. 5-year results of accelerated partial breast irradiation using sole interstitial multicatheter brachytherapy versus whole-breast

irradiation with boost after breast-conserving surgery for low-risk invasive and in-situ carcinoma of the female breast: a randomised, phase 3, non-inferiority trial. *Lancet,* 387**,** 229-38.

SYKES, E. A., DAI, Q., SARSONS, C. D., CHEN, J., ROCHELEAU, J. V., HWANG, D. M., ZHENG, G., CRAMB, D. T., RINKER, K. D. & CHAN, W. C. 2016. Tailoring nanoparticle designs to target cancer based on tumor pathophysiology. *Proc Natl Acad Sci U S A,* 113**,** E1142-51.

TANG, P. & TSE, G. M. 2016. Immunohistochemical Surrogates for Molecular Classification of Breast Carcinoma: A 2015 Update. *Arch Pathol Lab Med,* 140**,** 806-14.

TIMMERMAN, R., PAULUS, R., GALVIN, J., MICHALSKI, J., STRAUBE, W., BRADLEY, J., FAKIRIS, A., BEZJAK, A., VIDETIC, G., JOHNSTONE, D., FOWLER, J., GORE, E. & CHOY, H. 2010. Stereotactic body radiation therapy for inoperable early stage lung cancer. *JAMA,* 303**,** 1070-6.

TIWARI, P. M., VIG, K., DENNIS, V. A. & SINGH, S. R. 2011. Functionalized Gold Nanoparticles and Their Biomedical Applications. *Nanomaterials (Basel),* 1**,** 31-63.

UENO, H., NISHIKAWA, S., IINO, R., TABATA, K. V., SAKAKIHARA, S., YANAGIDA, T. & NOJI, H. 2010. Simple dark-field microscopy with nanometer spatial precision and microsecond temporal resolution. *Biophys J,* 98**,** 2014-23.

VAN GELLEKOM, M. P., MOERLAND, M. A., VAN VULPEN, M., WIJRDEMAN, H. K. & BATTERMANN, J. J. 2005. Quality of life of patients after permanent prostate brachytherapy in relation to dosimetry. *Int J Radiat Oncol Biol Phys,* 63**,** 772-80.

VILCHIS-JUAREZ, A., FERRO-FLORES, G., SANTOS-CUEVAS, C., MORALES-AVILA, E., OCAMPO-GARCIA, B., DIAZ-NIETO, L., LUNA-GUTIERREZ, M., JIMENEZ-MANCILLA, N., PEDRAZA-LOPEZ, M. & GOMEZ-OLIVAN, L. 2014. Molecular targeting radiotherapy with cyclo-RGDFK(C) peptides conjugated to 177Lu-labeled gold nanoparticles in tumor-bearing mice. *J Biomed Nanotechnol,* 10**,** 393-404.

WANG, Y., SANKREACHA, R., AL-HEBSHI, A., LOBLAW, A. & MORTON, G. 2006. Comparative study of dosimetry between high-dose-rate and permanent prostate implant brachytherapies in patients with prostate adenocarcinoma. *Brachytherapy,* 5**,** 251-5.

WARTERS, R. L., HOFER, K. G., HARRIS, C. R. & SMITH, J. M. 1978. Radionuclide toxicity in cultured mammalian cells: elucidation of the primary site of radiation damage. *Curr Top Radiat Res Q,* 12**,** 389-407.

WILHELM, S., TAVARES, A. J., DAI, Q., OHTA, S., AUDET, J., DVORAK, H. F. & CHAN, W. C. W. 2016. Analysis of nanoparticle delivery to tumours. *Nat Rev Materials,* Published online-April 22, 2016.

WILLIAMS, S. G., MILLAR, J. L., DUCHESNE, G. M., DALLY, M. J., ROYCE, P. L. & SNOW, R. M. 2004. Factors predicting for urinary morbidity following 125iodine transperineal prostate brachytherapy. *Radiother Oncol,* 73**,** 33-8.

WU, A., ULIN, K. & STERNICK, E. S. 1988. A dose homogeneity index for evaluating 192Ir interstitial breast implants. *Med Phys,* 15**,** 104-7.

WUST, P., GNEVECKOW, U., JOHANNSEN, M., BOHMER, D., HENKEL, T., KAHMANN, F., SEHOULI, J., FELIX, R., RICKE, J. & JORDAN, A. 2006. Magnetic nanoparticles for interstitial thermotherapy--feasibility, tolerance and achieved temperatures. *Int J Hyperthermia,* 22**,** 673-85.

YOOK, S., CAI, Z., LU, Y., WINNIK, M. A., PIGNOL, J. P. & REILLY, R. M. 2015a. Radiation Nanomedicine for EGFR-Positive Breast Cancer: Panitumumab-Modified Gold Nanoparticles Complexed to the b-Particle-Emitter, Lu. *Mol Pharm,* 12**,** 3963-3972.

YOOK, S., CAI, Z., LU, Y., WINNIK, M. A., PIGNOL, J. P. & REILLY, R. M. 2015b. Radiation Nanomedicine for EGFR-Positive Breast Cancer: Panitumumab-Modified Gold Nanoparticles Complexed to the beta-Particle-Emitter, (177)Lu. *Mol Pharm,* 12**,** 3963-72.

YOOK, S., CAI, Z., LU, Y., WINNIK, M. A., PIGNOL, J. P. & REILLY, R. M. 2016a. Intratumorally Injected 177Lu-Labeled Gold Nanoparticles: Gold Nanoseed Brachytherapy with Application for Neoadjuvant Treatment of Locally Advanced Breast Cancer. *J Nucl Med,* 57**,** 936-42.

YOOK, S., LU, Y., JEONG, J. J., CAI, Z., TONG, L., ALWARDA, R., PIGNOL, J. P., WINNIK, M. A. & REILLY, R. M. 2016b. Stability and Biodistribution of Thiol-Functionalized and (177)Lu-Labeled Metal Chelating Polymers Bound to Gold Nanoparticles. *Biomacromolecules,* 17**,** 1292-302.

YOSHIKAWA, K., OGAWA, T., BAER, R., HEMMI, H., HONDA, K., YAMAUCHI, A., INAMOTO, T., KO, K., YAZUMI, S., MOTODA, H., KODAMA, H., NOGUCHI, S., GAZDAR, A. F., YAMAOKA, Y. & TAKAHASHI, R. 2000. Abnormal expression of BRCA1 and BRCA1-interactive DNA-repair proteins in breast carcinomas. *Int J Cancer,* 88**,** 28-36.

YU, Y., ANDERSON, L. L., LI, Z., MELLENBERG, D. E., NATH, R., SCHELL, M. C., WATERMAN, F. M., WU, A. & BLASKO, J. C. 1999. Permanent prostate seed implant brachytherapy: report of the American Association of Physicists in Medicine Task Group No. 64. *Med Phys,* 26**,** 2054-76.

ZELEFSKY, M. J., YAMADA, Y., MARION, C., SIM, S., COHEN, G., BEN-PORAT, L., SILVERN, D. & ZAIDER, M. 2003. Improved conformality and decreased toxicity with intraoperative computer-optimized transperineal ultrasound-guided prostate brachytherapy. *Int J Radiat Oncol Biol Phys,* 55**,** 956-63.

ZHANG, C., LI, C., LIU, Y., ZHANG, J., BAO, C., LIANG, S., WANG, Q., YANG, Y., FU, H., WANG, K. & CUI, D. 2015. Gold nanoclusters-based nanoprobes for simultaneous fluorescence imaging and targeted photodynamic therapy with superior penetration and retention behaviour in tumors. *Adv. Funct. Mater.,* 25**,** 1314-1325.

ZHANG, G., YANG, Z., LU, W., ZHANG, R., HUANG, Q., TIAN, M., LI, L., LIANG, D. & LI, C. 2009. Influence of anchoring ligands and particle size on the colloidal stability and in vivo biodistribution of polyethylene glycol-coated gold nanoparticles in tumor-xenografted mice. *Biomaterials,* 30**,** 1928-36.

ZHANG, Y. N., POON, W., TAVARES, A. J., MCGILVRAY, I. D. & CHAN, W. C. 2016a. Nanoparticle-liver interactions: Cellular uptake and hepatobiliary elimination. *J Control Release*.

ZHANG, Y. N., POON, W., TAVARES, A. J., MCGILVRAY, I. D. & CHAN, W. C. W. 2016b. Nanoparticle-liver interactions: Cellular uptake and hepatobiliary elimination. *J Control Release,* 240**,** 332-348.

ZOURARI, K., MAJOR, T., HEREIN, A., PEPPA, V., POLGAR, C. & PAPAGIANNIS, P. 2015. A retrospective dosimetric comparison of TG43 and a commercially available MBDCA for an APBI brachytherapy patient cohort. *Phys Med,* 31**,** 669-76.

ZYGMANSKI, P. & SAJO, E. 2016. Nanoscale radiation transport and clinical beam modeling for gold nanoparticle dose enhanced radiotherapy (GNPT) using X-rays. *Br J Radiol,* 89**,** 20150200.

APPENDICES

A. CHARACTERIZATION OF ^{177}LU-AUNP STABILITY

The stability of ^{177}Lu-AuNP in the NPD with respect to loss of radiometal was studied in three test solutions; d.d. H_2O, phosphate buffered saline (PBS, pH 7.4) and Dulbecco's Modified Eagle Medium (DMEM). Single NPD were submerged in microcentrifuge tube containing 500 µL of d.d. H_2O, PBS or DMEM, and incubated at 37˚C with gentle shaking to promote release of ^{177}Lu-AuNP. The same NPD was then transferred to new microcentrifuge tubes containing fresh test solutions at 1, 2, 3, 4, 24, 48 hr and 7 days and incubated at 37˚C with gentle shaking to collect ^{177}Lu-AuNP from various time points that have been released from the NPD. The microcentrifuge tubes containing released ^{177}Lu-AuNP were ultracentrifuged at 15,000 × g for 45 min at 4˚C to separate the supernatant containing free PEG-*p*Glu(DOTA)$_8$-LA$_4$-^{177}Lu. The radioactivity of the pellet containing ^{177}Lu-AuNP and the supernatant were measured in a γ-counter (Wizard Model 1480; PerkinElmer Inc., Akron, OH, USA) to determine the percent dissociation of radioactivity from the ^{177}Lu-AuNP. Free ^{177}Lu-AuNP, in the absence of the NPD, in d.d. H_2O, PBS and DMEM were used as controls.

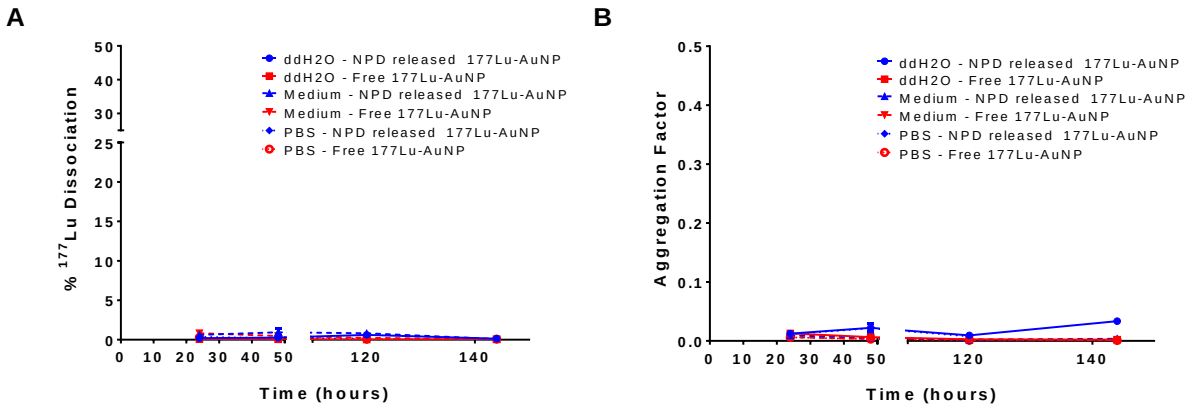

Figure A 1 (a) Percent dissociation of ^{177}Lu from AuNP from incubation in ddH_2O, DMEM cell culture medium, and PBS, at various time points (h), and (b) the aggregation factor of 177Lu-AuNP in ddH_2O, DMEM cell culture medium, and PBS, at various time points (h).

An aggregation assay was also conducted on ^{177}Lu-AuNP not incorporated into the NPD and ^{177}Lu-AuNP released from the NPD in d.d. H_2O, PBS or DMEM after incubation at 37˚C for 1, 2, 3, 4, 24, 48 h and 7 d. Triplicates of each sample collected from each time point (150 µL) were deposited into wells of a UV-Star 96 well microplate (Sigma-Aldrich) and the absorbance at 615 nm and 524 nm, the surface plasmon resonance band, was measured using a BioTek Synergy 2 microplate reader (Fisher Scientific, Waltham, MA, USA). An aggregation factor (AF) was calculated as the ratio of

the 615 nm to 524 nm absorbance and was plotted as a function of time (Yook et al., 2016b). The stability of ^{177}Lu-AuNP incorporated and released from the NPD in d.d. H_2O, PBS and DMEM was compared to non-incorporated ^{177}Lu-AuNP by calculating the area under the curve (AUC) for AF versus time using Prism 6.01 software (GraphPad Software Inc., San Diego, CA, U.S.A.).

The binding stability of PEG-*p*Glu(DOTA)$_8$-LA$_4$-^{177}Lu to the AuNP surface as a function of time is illustrated in Figure A 1a, and compares dissociation of the metal chelating polymers (MCP) from NPD-released and free (control) ^{177}Lu-AuNP in d.d. H_2O, PBS or DMEM. The results demonstrate instabilities in the MCP binding during the first 3 hours followed by minimal dissociation of MCP after 24 hours for all incubation media. The initial binding instability of MCP was greater (0.6-3.4 times at 1 hour) in ^{177}Lu-AuNPs incorporated into NPD when compared to their free ^{177}Lu-AuNPs counterparts but were not statistically different at longer time points. ^{177}Lu-AuNP in DMEM exhibited the greatest MCP binding instability out of the three incubation media tested.

Dissociation of MCP resulted in AuNP aggregation which was detected using UV-visible absorption. The AF was calculated as the ratio of absorbance at 615 nm to 524 nm and is plotted up to 144 hours in Figure A 1b. The absorbance at 615 nm was greatest at 1 hr as indicated by a larger AF, and decreased at subsequent time points suggesting that most of the aggregation occurred earlier in time. The AF was integrated from 1 hour to 144 hour to determine the AUC, which was then used to compare the stability of MCP-AuNP constructs in d.d. H_2O, PBS and DMEM. All MCP-AuNP constructs incorporated into NPD were stable when compared to their respective controls, and exhibited no significant differences in AUC (3.4 ± 0.3 AF×*h* vs. 2.14 ± 0.01 AF×*h*, 1.7 ± 0.1 AF×*h* vs. 2 ± 1 AF×*h*, and 3.2 ± 0.4 AF×*h* vs. 1.04 ± 0.02 AF×*h* for NPD versus their controls in d.d. H_2O, DMEM and PBS respectively). There were also no statistical differences in AUC between MCP-AuNP constructs in d.d. H_2O, DMEM and PBS.

B. SUPPLEMENTAL MATERIAL FOR CHAPTER 3

Table B 1 Radionuclide decay properties of ^{90}Y, ^{177}Lu, and ^{111}In.

		β^- [a]		γ [a] /X [a]		AE [a] /IC [a]	
	Half-life (d)	Mean Energy (MeV)	Yield (%)	Mean Energy (MeV)	Yield (%)	Mean Energy (MeV)	Yield (%)
^{90}Y	2.68	0.93	100	2.19^{γ}	1.40×10^{-6}	5.1×10^{-4} AE	0.13
				8.19×10^{-4} X	0.15	1.75 IE	0.012
^{177}Lu	6.64	0.13	100	0.18^{γ}	18.0	1.01×10^{-3} AE	112
				2.58×10^{-3} X	137	0.087 IE	15.5
^{111}In	2.80	n/a	n/a	0.21^{γ}	185	9.26×10^{-4} AE	743
				2.1×10^{-3} X	950	0.18 IE	15.9

[a] Auger electron (AE), internal conversion electron (IC), beta minus particle (β^-), gamma radiation (γ), and X radiation (X).

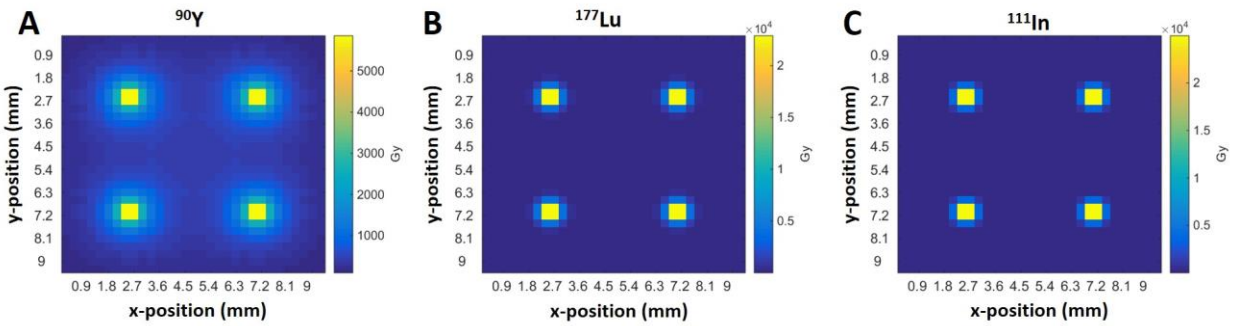

Figure B 1 Dose maps of 4 conventional seeds spaced 4.5 mm apart (center-to-center) in a square formation. The seed contained either (a) ^{90}Y, (b) ^{177}Lu, or (c) ^{111}In. Dose maps were generated from axial cross sections (slice z=11) of the 3-dimentional dose distributions. Note the difference in the dose intensity scales.

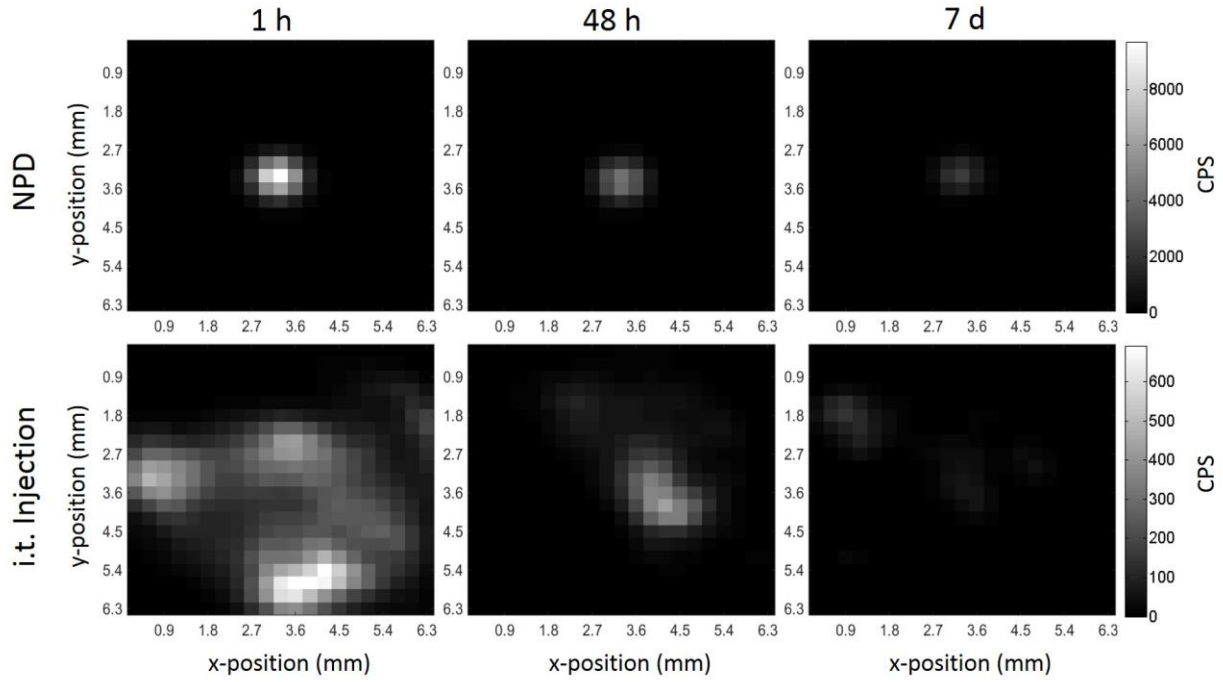

Figure B 2 Representative slice from 3D SPECT image for tumours (a) implanted with NPD and (b) injected intratumourally (i.t.) with ^{177}Lu-AuNP, at 1 h, 48 h and 7 d. Images have been corrected for radioactive decay.

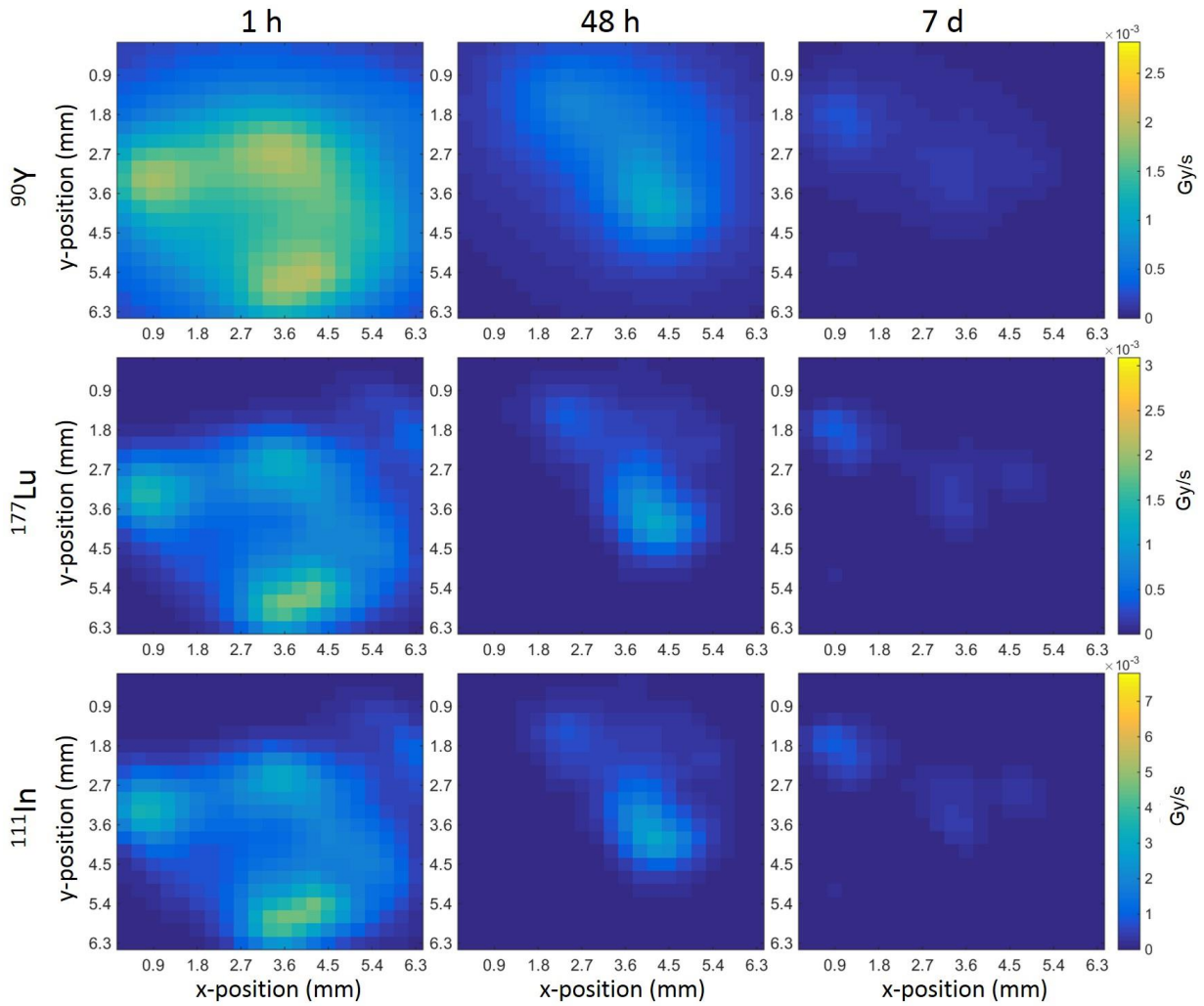

Figure B 3 Dose rate distributions generated by convolving representative 3D SPECT images of i.t. injected tumours, from 1 h, 48 h and 7 d, with the voxel dose kernels for ^{90}Y *(top row)*, ^{177}Lu *(middle row)*, or ^{111}In *(bottom row)*. Note the difference in intensity scales.

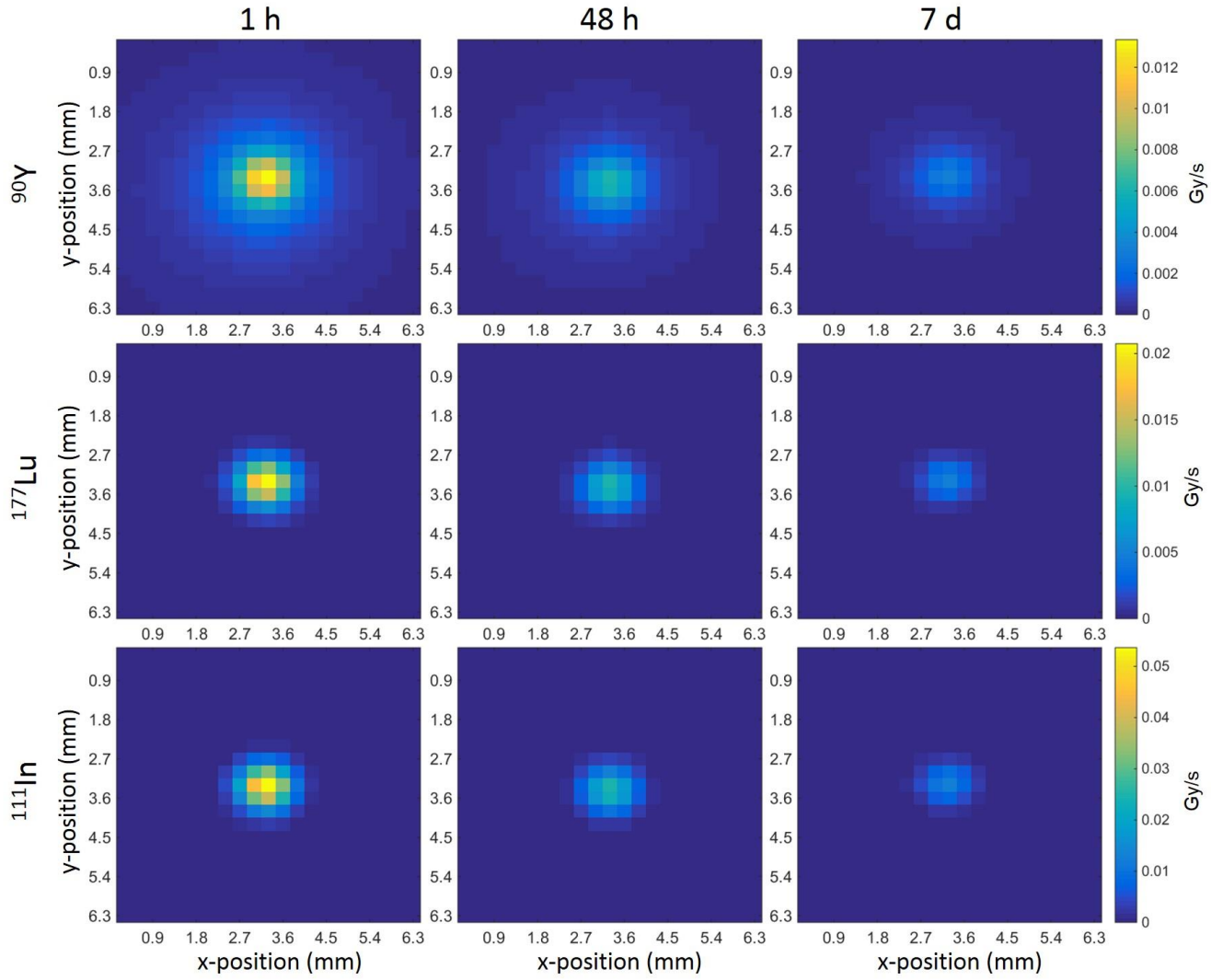

Figure B 4 Dose rate distributions generated by convolving representative 3D SPECT images of tumours implanted with a NPD at 1 h, 48 h and 7 d, with the VDK for ^{90}Y *(top row)*, ^{177}Lu *(middle row)*, or ^{111}In *(bottom row)*. Note the difference in intensity scales.

The counts in the VOI on the SPECT images (Fig. B 1) were converted to radioactivity using the following conversion factors: 112 cps/MBq, 80 cps/MBq, and 8 cps/MBq for NPD implanted in the tumour and 214 cps/MBq, 153 cps/MBq, and 15 cps/MBq for i.t. injection for ^{90}Y, ^{177}Lu, and ^{111}In respectively. The dose rate maps, generated from select axial slices of the 3D dose rate distributions, are shown in Figure B 2 for i.t. injected radiolabeled AuNP and in Figure B 3 for a tumour implanted with a NPD. Dose rate maps are presented for 1 h, 48 h and 7 d time points and have been corrected for radioactive decay to illustrate the impact of radiolabeled AuNP redistribution and radionuclide (^{90}Y, ^{177}Lu

or ^{111}In) on dose rate. Dose rate distribution from the single i.t. injection of ^{177}Lu-AuNP in Figure B 2 is heterogeneous as a result of the variable distribution of ^{177}Lu-AuNP. The dose rate distributions in Figure B 3 remained concentric about the NPD for all time points and radionuclides, however the dose deposition from ^{177}Lu (middle row) and ^{111}In (bottom row) are limited to the voxels in close proximity to the NPD due to the short range of the electrons emitted by these radionuclides. At 1 h, voxels at the peripheries of the cubic volume received dose rates as low as 1.3×10^{-7} Gy/s and 4.1×10^{-9} Gy/s, for ^{177}Lu and ^{111}In respectively, as compared to 3.7×10^{-5} Gy/s for ^{90}Y.

The dose rate distributions for i.t. injected radiolabeled AuNP (Fig. B 2) are variable and appear to change in profile between time points. Multiple regions receiving high dose can be observed at each time point regardless of the radionuclide (^{90}Y, ^{177}Lu or ^{111}In). Although there was greater overall diffusion of radioactivity from i.t. injection than for radiolabeled AuNP incorporated into NPD, the lowest dose rate delivered to a voxel in the cubic volume at 1 h was 4.2×10^{-5} Gy/s, 1.3×10^{-7} Gy/s and 4.2×10^{-9} Gy/s, for ^{90}Y, ^{177}Lu and ^{111}In respectively, which were not different from the lowest dose rates for tumours implanted with NPD (P=0.3). However, the differences in the maximum dose rates received by a voxel between tumours implanted with a NPD and i.t. injected tumours at 1 h were significantly different (P=0.005) with NPD implants delivering higher dose rates (1.3×10^{-2} Gy/s vs. 2.8×10^{-3} Gy/s, 2.1×10^{-2} Gy/s vs. 3.1×10^{-3} Gy/s, 5.4×10^{-2} Gy/s vs. 7.8×10^{-3} Gy/s for ^{90}Y, ^{177}Lu and ^{111}In respectively).

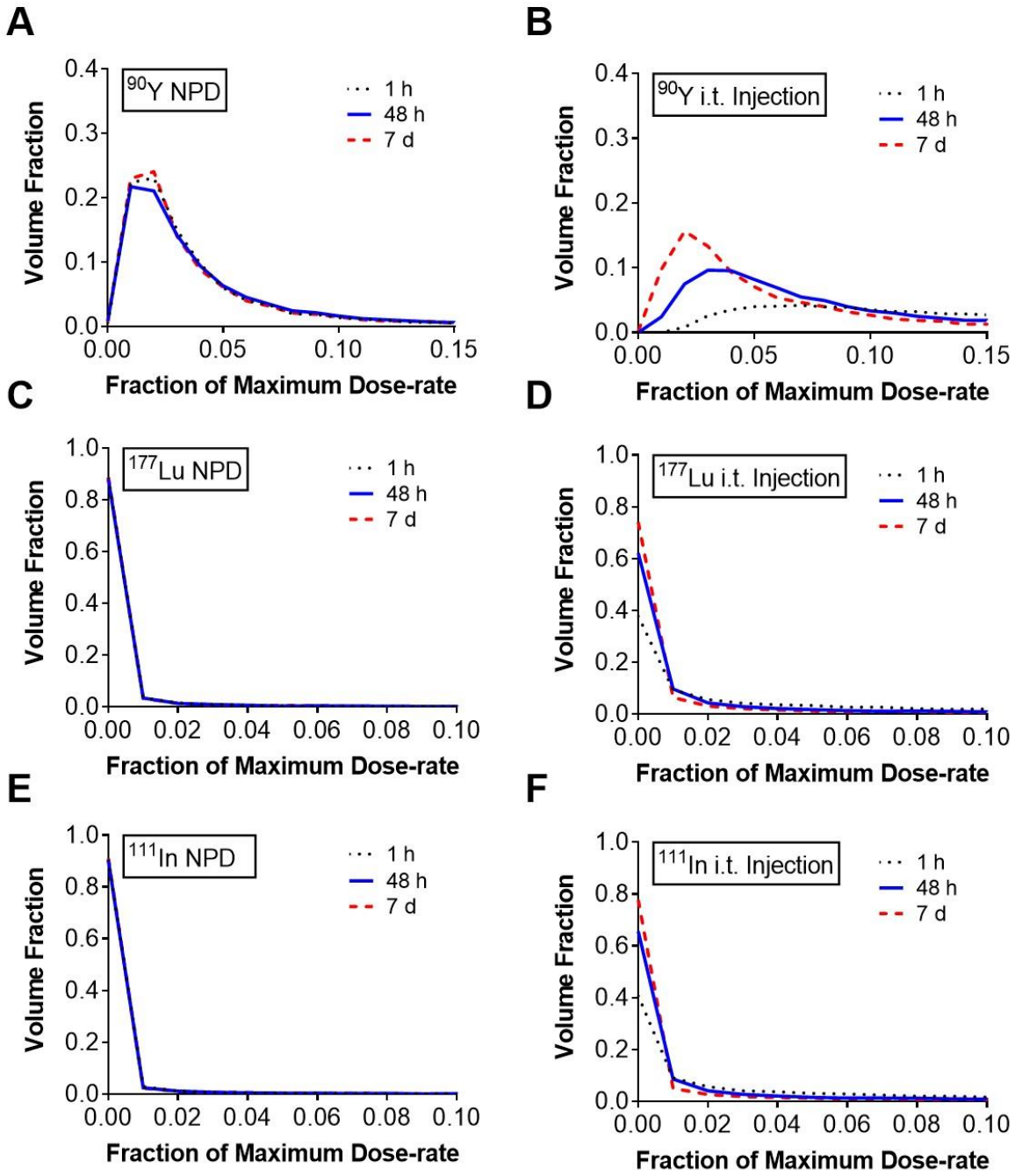

Figure B 5 Discrete dose rate volume histograms (DrVH) corresponding to the simulated dose rate distributions from *in vivo* SPECT images at 1 h, 48 h or 7d, for NPD implanted and i.t. injected AuNP labeled with ^{90}Y [(a) and (b) respectively], ^{177}Lu [(c) and (d) respectively], and ^{111}In [(e) and (f) respectively].

The DrVH for the dose rate distributions shown in Figure B 2 and Figure B 3, are presented in Figure B 4 for NPD implanted and i.t. injected AuNP labeled with ^{90}Y (*top row*), ^{177}Lu (*middle row*), or ^{111}In (*bottom row*). The distribution in dose rate from ^{90}Y in both NPD implanted (Fig. B 4a) and i.t. injected (Fig. B 4b) tumour volumes appear to be more homogeneous than ^{177}Lu (Fig. B 4c and B 4d) and ^{111}In (Fig. B 4e and B 4f), with <0.8% (NPD) and <0.2% (i.t.) of the volume fraction receiving a dose rate between 0 ± 0.005% of the maximum dose rate (0.02 Gy/s and 0.003 Gy/s respectively) at all time points. On the contrary, an average of 88.4 ± 0.4% and 90.6 ± 0.4% of the volume fraction received a dose rate between 0 ± 0.005% of the maximum dose rate (0.01 Gy/s and 0.05 Gy/s) for ^{177}Lu and ^{111}In incorporated in a NPD, respectively). The distribution in dose rate as indicated by the shape of the histogram remained consistent between 1 h, 48 h and 7 d, for NPD implanted volumes. The DrVH for i.t. injected AuNP were more variable between time points due to the increased diffusion of radioactivity, but the volume fraction receiving a dose rate between 0 ± 0.005% of the maximum dose rate were lower (37.9%, 62.2%, and 74.1% for ^{177}Lu, and 40.7%, 65.6%, and 77.7% for ^{111}In, at 1 h, 48 h and 7 d respectively).

C. RADIONUCLIDE PRODUCTION AND DECAY

Iodine-125 is artificially manufactured using a reactor through neutron capture by xenon-124 (^{124}Xe), a process where a neutron collides with and is absorbed into the nucleus of another atom forming a heavier nucleus. From this process xenon-125 (^{125}Xe) is produced and decays by electron capture to create ^{125}I (Eq. 5.4). Iodine-125 decays by electron capture (Eq. 5.5), a process where an inner shell (K or L shell) electron is absorbed by a proton, converting the nuclear proton into a neutron. The daughter nuclide will transition from an excited state to ground state tellurium-125 (^{125}Te) and in the process, emit a γ-ray. The vacancy left by the absorbed electron is filled by an outer shell electron resulting in the emission of one or multiple characteristic X-rays. In the case of ^{125}I, Auger electrons are also produced when the inner-shell vacancy is filled and the excess energy is transferred to the emission of an outer shell electron instead of a characteristic X-ray. Iodine-125 is most commonly used in prostate permanent brachytherapy, although it has also been applied towards treatment of brain cancers (Schwarz et al., 2012, Huang et al., 2009).

$$(5.4) \qquad {}^{124}_{54}Xe + {}^{1}_{0}n \rightarrow {}^{125m}_{54}Xe / {}^{125}_{54}Xe \rightarrow {}^{125}_{53}I$$

$$(5.5) \qquad {}^{125}_{53}I + {}^{0}_{-1}\beta \rightarrow {}^{125}_{52}Te + \overline{\nu_e}$$

Palladium-103 is produced by proton collision of rhodium-103 (^{103}Rh) in a cyclotron resulting in the products ^{103}Pd and an ejected neutron (Eq. 5.6). Similar to ^{125}I the mode of decay is by electron capture of an inner shell electron to ^{103}Rh, and emission of a characteristic X-ray (Eq. 5.7). Palladium-103 is most commonly applied in prostate brachytherapy although there are reports of ^{103}Pd seeds for clinical trial applications in permanent breast seed implantation (Pignol et al., 2006, Pignol et al., 2015).

(5.6) $$^{103}_{45}Rh + ^{1}_{1}p \rightarrow ^{103}_{46}Pd + ^{1}_{0}n$$

(5.7) $$^{103}_{46}Pd + ^{0}_{-1}\beta \rightarrow ^{103}_{45}Rh + \overline{\nu_e}$$

Lutetium-177 is a popular radionuclide for targeted radionuclide therapies in nuclear medicine. It is produced by neutron irradiation of ^{176}Lu (direct method) or ^{176}Yb (indirect method) (Eq. 5.8 and 5.9), however the indirect method requires separation of ^{177}Lu from target ^{176}Yb atoms. It decays by beta minus decay to hafnium-177 (^{177}Hf), where a neutron is converted into a proton resulting in the creation of a β^- particle and electron antineutrino (Eq. 5.10). The β^- particles have a maximum energy of 497 keV (78.6%) when ^{177}Lu decays to the ground state of ^{177}Hf, and energies of 384 keV (9.1%) and 176 keV (12.2%) when ^{177}Lu decays to an excited state of ^{177}Hf, which transitions to the ground state with a gamma emission (113 keV (6.6%), 208 keV (11%)).

(5.8) $$^{176}_{71}Lu + ^{1}_{0}n \rightarrow ^{177}_{71}Lu$$

(5.9) $$^{176}_{71}Yb + ^{1}_{0}n \rightarrow ^{177}_{71}Lu$$

(5.10) $$^{177}_{71}Lu \rightarrow ^{0}_{-1}\beta + ^{177}_{72}Hf + \bar{\nu}_e$$

Yttrium-90 has been used as a therapeutic medical isotope most commonly in targeted radionuclide therapies in nuclear medicine, and in resin microspheres for selective internal radiation therapy of liver tumours. It is produced by neutron irradiation of ^{89}Y (Eq. 5.11) or, more frequently, from β^- decay of strontium-90 (^{90}Sr, t1/2=28.78 y, 546 keV) (Eq. 5.12). Strontium-90 is the product of uranium-235 (^{235}U) fission reaction, and is therefore produced in large amounts in nuclear reactors around the world, making production of ^{90}Y widely accessible. Yttrium-90 also decays by nearly pure β^- emission with a maximum energy of 2.28 MeV into stable ^{90}Zr (Eq. 5.13).

(5.11) $$^{89}_{39}Y + ^{1}_{0}n \rightarrow ^{90}_{39}Y$$

(5.12) $$^{90}_{38}Sr \rightarrow ^{0}_{-1}\beta + ^{90}_{39}Y + \bar{\nu}_e$$

(5.13) $$^{90}_{39}Y \rightarrow ^{0}_{-1}\beta + ^{90}_{40}Zr + \bar{\nu}_e$$

Indium-111 is typically used in diagnostic applications coupled with planar or SPECT imaging due to its gamma emission (245.4 keV). However it also emits AE and IC which has generated interest for its application as a therapeutic, due to the highly localized deposition of dose from these low energy, short ranged electrons. Indium-111 is produced by proton bombardment of cadmium-112 (^{112}Cd) (Eq. 5.14), and decays by electron capture leaving a cadmium-111 nucleus in an excited state. The ^{111}Cd transitions to a stable state following the emission of gamma radiation (171 keV and 245 keV) or emits an IC (144keV and 218 keV) (Eq. 5.15).

(5.14) $$^{112}_{48}Cd + ^{1}_{1}H \rightarrow ^{111}_{49}In + 2^{1}_{0}n$$

(5.15) $$^{111}_{49}In + ^{0}_{-1}\beta \rightarrow ^{111}_{48}Cd + \overline{\nu_e}$$